UNIVERSIDAD DE CHILE
FACULTAD DE CIENCIAS
DEPARTAMENTO DE QUÍMICA

BAND ALIGNMENT IN $Cu_2O/CH_3NH_3PbI_3$ INTERFACES

TESIS PARA OPTAR AL GRADO ACADÉMICO DE
MAGÍSTER EN CIENCIAS QUÍMICAS

LUCAS NICOLÁS LODEIRO MORAGA

PROFESOR GUÍA:
DR. EDUARDO MENÉNDEZ PROUPIN
PROFESOR GUÍA 2:
DR. RENATO CONTRERAS RAMOS

MIEMBROS DE LA COMISIÓN:
DR. FERNANDO MENDIZABAL
DR. ANTONIO GALDAMEZ
DR. PABLO JAQUE

Este trabajo ha sido parcialmente financiado por los proyectos FONDECYT 11180984, 1171807, 3150174 y por CONICYT–PFCHA Magíster Nacional 2019, 22190138. Powered@NLHPC: Esta tesis fue parcialmente apoyada por la infraestructura de supercómputo del NLHPC (ECM-02).

SANTIAGO DE CHILE
JUNIO 2022

FACULTAD DE CIENCIAS
UNIVERSIDAD DE CHILE

INFORME DE APROBACIÓN
TESIS DE MAGÍSTER

Se informa a la Escuela de Postgrado de la Facultad de Ciencias que la Tesis de Magíster presentada por el candidato

Lucas Nicolás Lodeiro Moraga

ha sido aprobada por la Comisión de Evaluación de la Tesis como requisito para optar al grado de Magíster en Ciencias Químicas, en el examen de Defensa de Tesis rendido el día 4 de Octubre de 2022.

Director de Tesis

Dr. Eduardo Menéndez Proupin ______________________

Co–Director de Tesis

Dr. Renato Contreras Ramos ______________________

Comisión de Evaluación de la Tesis

Dr. Fernando Mendizabal ______________________

Dr. Antonio Galdamez ______________________

Dr. Pablo Jaque ______________________

RESUMEN DE TESIS PARA OPTAR AL GRADO ACADÉMICO DE:
MAGÍSTER EN CIENCIAS QUÍMICAS
POR: LUCAS NICOLÁS LODEIRO MORAGA
FECHA: JUNIO 2022
DIRECTOR DE TESIS: DR. EDUARDO MENÉNDEZ PROUPIN
CO–DIRECTOR DE TESIS: DR. RENATO CONTRERAS RAMOS

ALINEAMIENTO DE BANDAS EN INTERFACES $Cu_2O/CH_3NH_3PbI_3$

La generación de energía utilizando la radiación solar como suministro es una de las tecnologías más prometedoras para poder enfrentar el calentamiento global y el aumento de la concentración de CO_2 en la atmósfera, permitiendo a futuro reemplazar las energías basadas en combustibles fósiles. La forma mas extendida de uso de la energía solar se efectúa mediante celdas solares fotovoltaicas que producen electricidad aprovechando el efecto fotovoltaico en diferentes materiales semiconductores. Particularmente, durante la última década las tecnologías fotovoltaicas basadas en haluros híbridos orgánico–inorgánicos con estructura de perovskita (HOIHP) han mostrado un aumento en su eficiencia de fotoconversión sin precedentes (25.7%), logrando eficiencias similares a las clásicas basadas en Silicio. Este material no solo es prometedor por su alta eficiencia, si no que también por su bajo costo y simple fabricación. Aún así, presentan dificultades que todavía tienen que ser solucionadas, como la inestabilidad/descomposición al exponerse al ambiente, y los posibles materiales transportadores de carga complementarios que pueden solucionar y mejorar su desempeño. Particularmente, celdas fotovoltaicas basadas en perovskitas que utilizan Cu_2O como material transportador de agujeros han mostrado un buen desempeño de fotoconversión y por sobre todo una estabilidad comparativamente mayor.
Considerando la complejidad de los experimentos a escala atómica, necesarios para entender y continuar mejorando el desempeño, los estudios computacionales de primeros principios son una fuente en información relevante para comprender estos fenómenos a escala atómica.

En esta investigación hemos utilizando cálculos de primeros principios a escala atómica mediante la Teoría del Funcional de la Densidad en conjunto con la aproximación de frontera periódica, para estudiar el alineamiento de niveles energéticos de la interfaz entre Cu_2O y $CH_3NH_3PbI_3$ (la más estudiada de la familia de HOIHP). Para ello hemos utilizado sistemas tipo baldosa para ambos materiales y alineado sus niveles energéticos mediante dos metodologías: usando procedimiento indirecto del nivel de vacío como referencia, y posteriormente, generando explícitamente las interfaces entre ambos materiales para aquellas superficies que mostraron un alineamiento y geometrías adecuadas para la formación de la interfaz. Esto nos permitió realizar una exploración de distintas superficies en primera instancia, para después estudiar detallada y explícitamente las interfaces seleccionadas. Además utilizamos dos metodologías distintas para determinar las energías de los estados de máxima de valencia y mínimo de conducción, esto es: mediante cálculos de campo autoconsistente con funcional híbrido, y mediante la extrapolación desde el material extendido utilizando el potencial electrostático promedio como referencia.
Utilizando estas aproximaciones y metodologías, hemos obtenido información relevante sobre ambos materiales como también de la interfaz $Cu_2O/CH_3NH_3PbI_3$ respecto del alineamiento de niveles electrónicos, geometrías atómicas y estados trampa. Esta información es relevante para mejorar la eficiencia y estabilidad de celdas fotovoltaicas basadas en HOIHP, particularmente $CH_3NH_3PbI_3$ con Cu_2O como material transportador de agujeros.

THESIS' ABSTRACT FOR THE DEGREE OF:
MASTER OF SCIENCE CHEMISTRY
BY: LUCAS NICOLÁS LODEIRO MORAGA
DATE: JUNE 2022
THESIS' DIRECTOR: DR. EDUARDO MENÉNDEZ PROUPIN
THESIS' CO–DIRECTOR: DR. RENATO CONTRERAS RAMOS

BAND ALIGNMENT IN $Cu_2O/CH_3NH_3PbI_3$ INTERFACES

Energy generation employing solar radiation as a supply is one of the most promising technologies for tackling global warming and the increasing of CO_2 concentration in the atmosphere, enabling in the future to replace fossil fuel–based energies. The most extended way of solar energy use is through photovoltaic solar cells that produce electricity by exploiting the photovoltaic effect in different semiconductor materials. Particularly, during the last decade, photovoltaic technologies based on Halide Organic–Inorganic Hybrid Perovskites (HOIHP) have shown an unprecedented increase in photo–conversion efficiency (25.7%), achieving similar efficiencies to classical silicon–based photovoltaic. This material is not only promising for its high efficiency, but also for its low cost and simple fabrication. However, presents difficulties that still need to be solved, such as instability/decomposition upon exposure to the environment, and possible complementary charge transport materials that can solve and improve their performance. In particular, perovskite–based photovoltaic cells using Cu_2O as a hole transport material have shown good performance efficiencies and a comparatively higher stability.

Considering the complexity of atomic–scale experiments, needed to understand and further improve performance, computational first–principles studies are a source of relevant information to understand these atomic–scale phenomena.

In this research we have employed atomic–scale first–principles calculations through Density Functional Theory and periodic boundary condition approximation, to study the energy level alignment at the interface of Cu_2O and $CH_3NH_3PbI_3$ (the most studied of the HOIHP family). We have used slab systems for both materials and aligned their energy levels by two methodologies: using the indirect procedure of vacuum level as a reference, and afterwards, explicitly generating the interfaces between the two materials for those surfaces that showed suitable alignment and geometries for interface formation. This allowed us to explore different surfaces in the first instance, and subsequently to study the selected interfaces in detail and explicitly. In addition, we used two different methodologies to determine the energies of the valence maximum and conduction minimum states, *i.e.*, by self–consistent field calculations with hybrid functional, and by extrapolation from the extended material using the average electrostatic potential as a reference.

Using these approaches and methodologies, we have obtained relevant information on both materials as well as on the $Cu_2O/CH_3NH_3PbI_3$ interface about electronic level alignment, atomic geometries and trap states. This information is relevant to improve the efficiency and stability of HOIHP–based photovoltaic cells, particularly $CH_3NH_3PbI_3$ with Cu_2O as hole transport material.

A mis padres, quienes despertaron y mantuvieron en mí
las ansias por intentar comprender el mundo.

Agradecimientos

Quisiera partir agradeciendo al profesor Eduardo Menéndez Proupin por su apoyo incondicional desde el momento que comencé el programa de Magíster hasta el día de hoy. Durante estos años he aprendido mucho de usted, no solo de Ciencia, su experiencia y disposición son invaluables. Le agradezco el apoyo e impulso para participar en congresos y escuelas durante estos años, que me han permitido nutrirme de conocimientos.
Al profesor Renato Contreras, por seguir apoyándome a pesar de haber cambiado el área de investigación durante los años. Desde temprano en mi camino en la Ciencia, y mucho antes de comenzar a investigar, he podido aprender de su experiencia y rigor.

A Ana Montero, Jesús Castellanos y Tomáš Rauch, principales colaboradores y compañeros de investigación, gracias a los cuales buena parte de la investigación y publicaciones realizadas fueron posibles. Ha sido un placer colaborar mano a mano con ustedes y aprender de su trabajo.

Agradecer al financiamiento y apoyo económico recibido de proyectos FONDECYT 11180984, 1171807, 3150174, especialmente durante mi primer año de Magíster, como también para participar de congresos y escuelas.
Al ICTP por su completo apoyo económico, a mi como a estudiantes de todo el mundo, para poder asistir al congreso organizado el año 2019.
Muchas gracias a CONICYT–PFCHA Magíster Nacional 2019, 22190138, por el financiamiento otorgado durante el año 2019, que me permitió enfocarme completamente en el programa de Magíster.
A la infraestructura de supercómputo del NLHPC (ECM–02) y al personal que trabaja en ella siempre con una amabilidad y predisposición magnánimas, sin ambas buena parte de los cálculos realizados en esta tesis no hubieran sido posibles.

Agradecer a los profesores que desde que inicié en el pregrado y hasta hoy me han enseñado y apoyado, permitiéndome encontrar mi camino en este mundo llamado Ciencia. Muchisimas gracias profesores/as Irma Crivelli, Alicia Labra, Alexander Vargas, Fernando Mendizabal, Paul Jara, Sergio Muñoz, Carlos Cardenas, Antonio Galdamez, Marcelo Vilches, Cecilia Rojas, Victor Vargas, Richard Toro, Miguel Kiwi, Gonzalo Gutiérrez, Luis Foá, su persona ha marcado una diferencia en mi desarrollo personal, educacional y científico.
Un especial y gigante agradecimiento a la profesora Cecilia Labbe y al profesor Nicolás Yutronic, que cada vez que requerí ayuda personal o académica estuvieron ahí, su humanidad y magnanimidad han marcado y marcan una diferencia en la Facultad.

Agradecer a los funcionarios del Departamento de Química, Departamento de Física, Facultad de Ciencias y Campus JGM de la Universidad de Chile, que desempeñan las labores fundamentales que permiten el funcionamiento de todas las actividades que se realizan, cada uno de ellos son parte de la ciencia que se realiza en nuestra Facultad. En especial a Maryorett, Ximena, Don Segundo, muchas gracias.

Un especial saludo y agradecimiento a la profesora Luisa Melo, quién en el colegio me enseñó Química, mostrándome el camino que más tarde seguiría. También al Tío Lucho y los profesores/as Vania, Kelly, Pato, Sara, Delia, Claudia, Lidia, que marcaron mi desarrollo escolar.

A los habitantes de GNM, Karla, Pipa, Mati, Carvacho; Química Teórica, Bruno, Seba R., Seba G., Rodrigo, Andrés, Jazmín; y el Departamento de Física, Trinidad, Andres, César, por esos momentos de distensión, café, discusión y conspiración, a lo largo de estos años y tardes que se hacían noche estudiando e investigando.

A todas las personas con las que compartí en las distintas actividades y proyectos en la universidad. Agradecer a los integrantes de Natación JGM, en especial a Katt y Salva. Agradecer al TIP, a las jefas Caren Vega y Constanza Berrios, y compañeros tutores: Dani, Luis Felipe, Pato, Consuelo, Magda, fue una instancia muy formadora. Agradecer a esos ayudantes que marcaron la diferencia teniendo vocación de enseñanza y apoyo: Geraldine, Maricarmen, José Mella, Daniela Bobadilla, Vikingo, Nathalie, Bruno Loch, Mariana, Camilo.

A las amistades del colegio y la vida, Alvaro, Fabi, JP, Mayo, Feña por los momentos de distensión, paseos y enseñanzas. A los compañeros de camino en la Ciencia, Maire, Nayareth, Mati, Vicky, León, un placer haber compartido cada momento de desarrollo académico y personal.
Un especial agradecimiento y abrazo a mis compañeros de Ciencia y amigos Nicolás, Orlando y Tomás, por el mutuo y desinteresado apoyo que los caracteriza. Con ustedes la Ciencias es más divertida.

Por último, pero no menos importante, a mis padres Patricia y Pedro, que me han apoyado y acompañado durante toda la vida, algunas veces a distancia. Ustedes han sido el principal fomento para seguir aprendiendo y desarrollándome en la vida. Muchas gracias por apoyarme incondicionalmente.

Contents

List of Tables

List of Figures

Notations

Here some useful notations to understand the manuscript are presented. They are listed in alphabetical order to facilitate the search. Greek letters and Latin letters used for functions, potentials and coordinates are listed at the end of the list.

AIMD	*Ab Initio* MD
BM	Birch–Murnaghan equation of the state
BOMD	Born–Oppenheimer MD
CBM	Conduction Band Minimum, immediately higher band to the Fermi level
CP2K	CP2K is a DFT–, GPW– and PP–based code
DFA	Density Functional Approximation
DFT	Density Functional Theory
DOS	Density Of States
EA	Electron affinity
GGA	Generalized Gradient Approximation level of theory of DFT
Gt	Giga–ton (10^{12} kg)
HF	Hartree–Fock, could be used as super– or sub–scripts
HOCO	Highest Occupied Crystal Orbital
HSE	Heyd–Scuseria–Ernzerhof short–range hybrid PBE based functional
IP	Ionization Potential
KS	Kohn–Sham, could be used as super– or sub–scripts
LDA	Local Density Approximation level of theory of DFT
LDOS	Local Density Of States
LUCO	Lowest Unoccupied Crystal Orbital
MA^+	$CH_3NH_3{}^+$
MAPI	$CH_3NH_3PbI_3$ perovskite
MD	Molecular Dynamics
N_A	Avogadro Number
NCPP	Norm–Conserving Pseudo–Potentials
PAW	Projector Augmented Wave method
PBE	Perdew–Burke–Ernzerhof functional, at GGA level of theory
PBEsol	modified PBE functional for surface and solids
PBE0	hybrid PBE based functional
PBE0(α)	PBE0 functional with tuned α fraction of exact exchange
PBC	Periodic Boundary Condition
PCE	Photo–Conversion Efficiency

PDOS	Projected Density Of States
PP	Pseudo–Potential
PW	Plane Wave functions, basis set
QC	Quantum Confinement
QE	Quantum–ESPRESSO is a DFT–, PW– and PP–based code
SCF	Self–Consistent Field procedure
SIE	Self–Interaction Error
SOC	Spin–Orbit Coupling
SQL	Shockley–Queisser Limit
USPP	Ultra–Soft Pseudo–Potentials
VASP	Vienna *Ab initio* Simulation Package is a DFT–, PW– and PP–based code
VBM	Valence Band Maximum, immediately lower band to the Fermi level
WFN	Wavefunction

$\mathbf{r}$	electron space coordinate
$\mathbf{R}$	nuclei space coordinate
σ	electron spin coordinate
$\mathbf{Q}$	normal coordinate for *nuclear configuration*
E_F or μ_F	Fermi level or chemical potential of electrons
$\mathbf{k}$	Brillouin Zone point
$\mathbf{G}$	reciprocal translation vector
$\Psi(\{\mathbf{r}_i\}, \{\mathbf{R}_I\})$	N–electron M–nuclei wavefunction
$\psi(\{\mathbf{r}_i\}; \{\mathbf{R}_I\})$	N–electron wavefunction, with $\{\mathbf{R}_I\}$ as parameters
$\chi(\{\mathbf{R}_I\})$	M–nuclei wavefunction
$\varphi_j(\mathbf{r}\sigma)$	one–electron wavefunction of state j.
ϵ_j	energy of one–electron state j corresponding to wavefunction $\varphi_j(\mathbf{r}\sigma)$
$\rho(\mathbf{r})$	total electronic charge density
$\upsilon_{KS}(\mathbf{r})$	Kohn–Sham effective–potential
$\upsilon_{ext}(\mathbf{r})$	external potential
$\upsilon_h(\mathbf{r})$	Hartree potential
$\upsilon_{xc}(\mathbf{r})$	exchange–correlation potential
$\Sigma_x(\mathbf{r}\sigma, \mathbf{r}'\sigma')$	Fock exchange operator, so–called exact exchange

How to Read This Thesis

This thesis is structured in five chapters.
It starts with the introduction (Chapter 1) regarding global warming and photovoltaic energy sources. The properties and characteristics of semiconductor and the Halide Organic–Inorganic Hybrid Perovskite–based solar cells are introduced, with new hole transport materials such as Cu_2O and its efficiency results. An extensive literature review of $CH_3NH_3PbI_3$ perovskite and Cu_2O materials is shown.
Before moving on to the studies carried out for both materials, a theoretical background of electronic structure calculation (Chapter 2) is presented, where the main points of interest and concepts about the calculations are summarized. Mean–field and Born–Oppenheimer approximations on the Schrödinger Equation are discussed to afford polyatomic and polyelectronic systems. Hartree–Fock and Density Functional Theory are displayed. Periodic Boundary Condition is introduced to deal with solid state systems (bulk and slabs). Finally, the problem about the reference potential is discussed, and the two–step procedure is introduced to deal with the system–dependent reference potential.
The following two chapters deal with bulk and slab systems of $CH_3NH_3PbI_3$ (Chapter 3) and Cu_2O (Chapter 4) materials separately. Here we analyze different calculation setups to explore their electronic structure, and subsequently, we study bulk electronic structure of both materials with different functionals to achieve a good description of the band gap and band edges. Later, we construct and study slab systems with different surfaces. The convergence of different quantities with respect to slab thickness is studied. Band alignment using the vacuum level as the reference potential and the two–step procedure are displayed for both materials.
Finally, the explicit interface systems are studied (Chapter 5) for those surfaces that present an optimal band alignment, epitaxial growth and geometrical match. Discussion about energetic alignment and interactions at the interface to search for the optimum ones is the main topic. Their electronic properties are presented by means of projected and local density of states, band alignment, charge transfer, interface states, and energy of adhesion.
Computational details and convergence studies of calculation parameters are left to the Appendix.

This thesis presents unpublished and published results. Three publications are product of the work of this thesis and collaborations: “Methodological Issues in First–Principle Calculations of $CH_3NH_3PbI_3$ Perovskite Surfaces: Quantum Confinement and Thermal Motion” ACS Omega, 5, 45, 29477–29491, 2020 [1], L. Lodeiro, A. Montero–Alejo and E. Menéndez–Proupin are the main authors, L. Lodeiro as corresponding author in the submission and response to the journal. “Atomic–Scale Model and Electronic Structure of $Cu_2O/CH_3NH_3PbI_3$ Interfaces in Perovskite Solar Cells” ACS Appl. Mater. Interfaces, 12, 40, 44648–44657, 2020 [2], J. Castellanos–Águila,

L. Lodeiro and E. Menéndez–Proupin are the main authors and contributed equally to this work. “DensityTool: A Post–Processing Tool for Space– and Spin–Resolved Density of States from VASP” Comput. Phys. Commun., 277, 108384, 2022 [3], L. Lodeiro and T. Rauch are the authors.

In order not to leave gaps in the presentation of results and discussions, collaborative work is also showed in this thesis. Chapter 3 starts with unpublished bulk calculations of $CH_3NH_3PbI_3$, and continues with surface and slab results published in Ref. [1]. Chapter 4 presents unpublished results and discussions. Finally, Chapter 5 starts with unpublished discussion which links the two previous chapters, and continues to the explicit interfaces published in Ref. [2].

DensityTool program published in Ref. [3] was used to compute the local density of state function for interface models in Chapter 5. Convergence studies of calculation parameters in Appendix A.2 were carried out taking into account previous results in Karla Jiménez’s thesis.

Chapter 1

Introduction

Contents

Climate change is an immediate problem that humankind must address. High CO_2 atmospheric concentration due to the use of fossil fuels will change drastically the world, and must be reduced or deleted by transitioning to renewable energy sources, such as solar energy. Photovoltaic solar cells became an interesting and competitive alternative as energy source. These technologies have been developed for more than 80 years, exploring new device types and absorption materials to make them a worldwide accessible energetic source.
The so–called perovskite solar cells based on Hybrid organic–inorganic halide perovskite have shown high efficiencies, becoming "the raising star of photovoltaics". But, some weakness need to be afforded to impulse them to the large–scale market. New hole transport materials (as Cu_2O) and the study of these new interfaces is an important and necessary step to tune up these emerging technologies.

1.1 Global Warming and CO_2

Human activity on Earth is today, without a doubt, one of the most important issues to be dealt within global policies. The strong and excessive effect of industrialized humanity has had on the planet, emitting pollutants and producing synthetic compounds, jeopardize our future.

The climate system can respond to changes in external forcing, which disturb the natural energy balance of the planet. The change in incident solar radiation, the doubling of atmospheric CO_2 and the emission of other atmospheric pollutants are an example of this. Rapid climate change is the realization that Earth is out of energy balance, caused mainly by greenhouse effect as a result of the high concentrations of CO_2 in the atmosphere, which exceed 400 ppm since 2016. This is a highly harmful value for the global climate, the life on the planet and for the humankind [4, 5].

Nowadays, the humankind must confront collectively the effects of our industrial civilization: the uncomfortable fact that we are the main contributor to climate change and global warming. Certain effects have begun to seem inevitable in recent years, such as the impact of ocean acidification, the loss of fresh water supply, the change of climatic zones, among others. If humanity wishes to preserve a planet and climate similar to the one in which civilization developed, and not to cause a massive extinction, it is required that most of the remaining fossil carbon is not emitted into the atmosphere. This is the main realistic way to drastically reduce CO_2 emissions; in addition to changing the energy matrix of the planet, within the framework of the Paris Agreement [6].

1.1.1 Effects and Implications

The effects of global warming are diverse, and most of them interrelate. For example, the ice melting increases the sea level (affecting smaller islands and coastal cities) and decreases sea salinity affecting marine life, which are one of the main CO_2 captors by organic routes. Other example is the carbon cycle on the oceans, gaseous CO_2 is absorbed as inorganic carbonate, but this process acidifies the ocean affecting sea life and promoting the release of CO_2 from sediments, or the water cycle and acid rain. Also human and economic future of countries are threatened.

If the current CO_2 pollution persist with an increase rate of 2.5 ppm per year, the climate changes will be irreversible [7].

Evidence suggests that stabilization of the Arctic Sea ice sheet requires restoration of the planetary energy balance. For this, the amount of CO_2 must be reduced to 350 ppm, ideally 300 ppm to recover the sea ice of 30 years ago [7].

Almost a decade ago, a limit of 1 °C for global warming was advocated, with the aim of preventing the ice sheet from being practically irreversibly reduced and the loss of species continuing to increase. Currently the discussion is about a limit of 1.5 °C or 2 °C, this would imply a maximum limit of 430 or 450 ppm of CO_2, respectively (before humanity becomes carbon neutral) [8], but with the current rate of increase we will reach before 2040, as observed in the trend in Fig. 1.1. Also, this global temperature rise could affect the carbon sources in

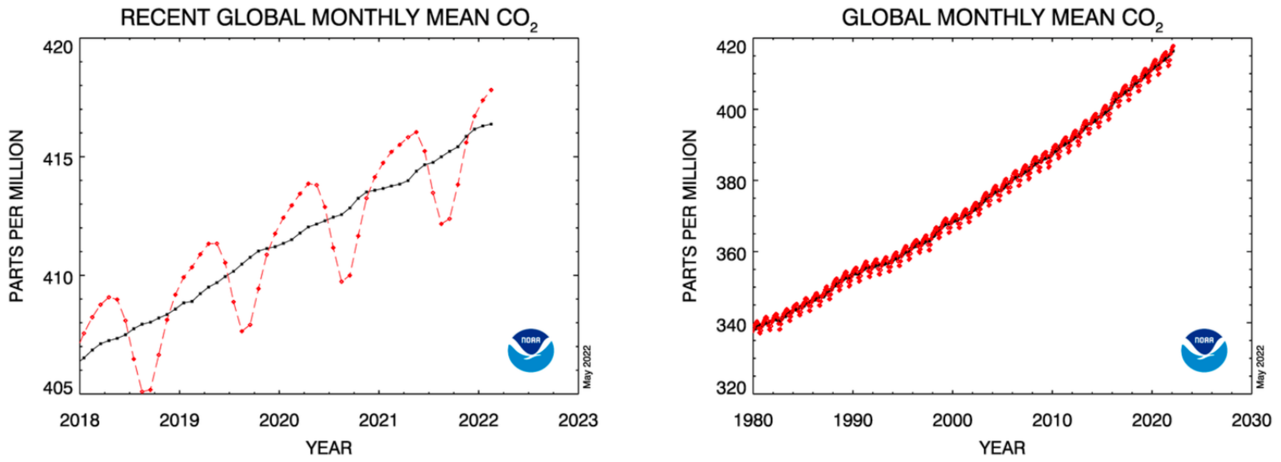

Figure 1.1: Global mean CO_2 atmospheric concentration in ppm. Left panel shows recent years. Right panel shows last four decades. Dashed red line with diamond symbols represents the monthly mean values, centered on the middle of each month. Black line with square symbols represents the same, after correction for the average seasonal cycle. May 2022, NOAA.

the soil and cause its release into the atmosphere, which will undoubtedly intensify the crisis and the effects of climate change [9].
If a CO_2 concentration of the order of 450 ppm or more is maintained for a long time, it would push Earth towards an ice–free state. Such a level of CO_2 would likely trigger dynamic responses (storms, floods, desertification, extreme climates, among others) that could be beyond humanity's control.

1.1.2 Confrontation and Energy Production

To stabilize this scenario, it is required that net CO_2 emissions approach to zero, due to CO_2 is too stable and has a long life on the atmosphere ($\sim$ 100 years).
The SARS–COVID–19 pandemic and its effect paralyzing the planetary industry and humankind activities, had a diminishing effect on global CO_2 emissions, but it was just an interannual fluctuation, since the long term increasing trend persist. Similar behaviours were observed in previous global crises such as: oil crises of 1974, 1980–1982, and 1992, and the financial crisis of 2008. In 2020 the global net CO_2 emission was reduced to a value similar to that of a decade ago, but in 2021 it rebounded to a similar value of 2019, which definitely not decreased the net concentration in the atmosphere. At the current global emissions (35 $GtCO_2$), the remaining CO_2 budget to limit global warming to 1.5 °C will be reached in less than a decade [10].

A large part of CO_2 emissions from burning fossil fuels remains in the air for a long time. Therefore, a moderate reduction in the use of fossil fuels will not appreciably mitigate human caused climate change in the long term. In practical terms, fossil fuel reserves should not be exploited without a plan to recover and remove the resulting atmospheric CO_2 [11].

Despite the current rapid growth of atmospheric CO_2 concentration, it has been shown that it is conceivable to reduce it in this century to less than current amount, but only through rapid changes in public policies related to the environment [7, 12].

The desire to reduce atmospheric CO_2 raises the question whether it can be artificially removed from the atmosphere. As of today there are no large–scale technologies for capture, but these technologies represent a developing field today.
The capture of CO_2 by the soil, and by different types of solvents have been deployed today as one of the main methods. Nevertheless, the ability to make CO_2 reactive is quite poor, due to its low reactivity. It is generally necessary to activate it by means of electrochemical over–potentials [13], the use of catalysts [14] and task specific green solvents, such as ionic liquids [15–17] as well as deep eutectic solvents [18, 19].
All of these methods require energy and/or materials for their application, which is in itself the problem we have to deal with.

Nowadays, the main source of electric energy production are the fossil fuels (∼ 80 %), which are also the main source of CO_2 produced by the humankind (∼ 60 %) [20]. Moreover, the fossil fuels are the main energy source for human and cargo transportation systems as well as industry and domestic heating, which are the main source of CO_2 emission and its annual growth [10].
Electric energy consumption, industry and transport are essential in our life and society. To maintain our living standard and technology, we have to change the energy source of our production and transport systems. Humanity's energy demand is continually increasing due to population growth, and rising *per capita* requirements.
It is worth mentioning that energy consumption and CO_2 emissions are drastically different between developed and developing countries, the former being the most important contributors. The main issue of the coming years for humankind is to find and implement new energy production policies, to survive the global warming.

Renewable energies are currently one of the most important and feasible field to produce cost effective energy. They can contribute to solving, at least partially, the supply difficulties that are likely to arise in a not too distant future. Unfortunately, they are still responsible for a low percentage of worldwide energy production (∼ 10 %) [20]. Renewable energies are those that are produced continuously and are inexhaustible on a human–scale. They also have the additional advantage of being able to complement each other, favoring integration between them. Renewable energies are in agreement with Sustainable Development Goals (UN 2030 Agenda).
They are environmentally friendly and even if they cause negative effects on the environment, they are minimal in comparison with fossil fuel sources. Renewable energy sources are diverse and depends on the capacities and availability of each country or territory, some examples of them are: hydroelectric energy, wind energy, biofuel energy, geothermic energy, tides and ocean current energy, thermal concentrator solar energy, photovoltaic solar energy, among others. Most of them produce electric energy that can be distributed, locally or commercially, and used for transport, industry or domestic heating, among others.
As mentioned, the availability of many of these renewable energies depend on the existence of the source, and its persistence in order to ensuring energy supply and provisioning, to make them applicable on a large–scale.

Solar energy is a widely available source anywhere in the world in practice, and solar radiation

is a high persistent source, as the popular expression said: “every day the sun rises”. Solar radiation over Earth’s surface depends on Earth’s latitudinal position and the weather, so it oscillates along the year’s seasons.
Places located between tropics or near the equatorial line, with dry environment and without clouds, such as deserts, are appropriate places for photovoltaic solar energy. Although, other places also can use and produce energy by means of solar energy. This makes it a well suited technology for large–scale energy production, including other renewable energies as secondary and cooperative sources, such as simultaneous and direct production of renewable fuels and electrical power from sunlight through hybrid photo–electrochemical and photovoltaic devices [21]. Also solar energy can produce electricity locally without the need for long distribution systems, for both large– and small–scale.
The most extended way of solar energy use is through photovoltaic solar cells that produce electricity by exploiting the photovoltaic effect in different semiconductor materials. Powered by new record photo–conversion efficiencies near 30 %, diversification of material and types of photovoltaic cells, more efficient ways of production, among others, have made photovoltaic energy an interesting and competitive alternative. Particularly, the energy production prices have decreased rapidly, reducing 18 times its cost in a decade [22].

Chilean energy policy over the last half century was based mainly on fossil fuels, based on the general policy that by maximizing economic development would give welfare to the people an communities. This general policy did not have in mind the environment damage or the harmful effects on communities. The sustainability and equity concepts were integrated to energy policy at the 1990s. Subsequently, energy supply security concept was integrated due to previous energy and supply crises.
Major changes were not made until the creation of the Ministry of Energy, when the first guidelines of a long term energy policy with environmental point of view were made. These policies take into account the community participation, environment impact and the global warming effects, pointing to expand renewable energy production and the goal of becoming carbon neutral.
It is projected a 60 % of renewable energy at 2035, and 70 % at 2050. Chilean renewable energy sources are wide and varied. Solar radiation is an important source in our country, specially in desert zones, enabling to be a leadership in solar energy production.

1.2 Photovoltaic Energy

Photovoltaic energy generation is the process of transforming the solar radiation directly into electric current. Photovoltaic effect was discovered by Becquerel in 1839 using an electrochemical cell, he explain this phenomena as: "the production of an electric current when two plates of platinum or gold immersed in an acid, neutral, or alkaline solution are exposed in an uneven way to solar radiation" [23].
Modern explanation of photovoltaic effect is conceived very similarly to photoelectric effect. In both cases electromagnetic waves (light) are absorbed, in quantum packages called photons, provoking the excitation of electrons to higher energy states. Photovoltaic effect refers to excitation to states into the same absorber material, such as conduction bands in semiconductors, while, photoelectric effect refers to excitation to out–material states (electron ejection outside the material, free electrons). In both cases an electric potential is generated, which can be used as electromotive force and electric current, and thus some of the light energy is converted into electric energy.
Regarding to the quantified nature of matter, incident photons must have sufficient energy to overcome the potential barrier for excitation. A photo–excited electronic state, consists of an electron in the conduction band (photo–excited electron) and a hole (electron–empty) state in the valence band, which must be persistently generated and separated by diffusion and filtering to generate electromotive force [24].

Solar radiation irradiance over Earth planet is around 1400 Wm^{-2}, known as solar constant, with a variation of ±3 % throughout the year due to the ellipticity of Earth's orbit. Solar spectrum distribution resemble a black body emission at 6000 K average temperature. Atmosphere reflects and absorbs a part of solar radiation, so solar radiation irradiance at Earth's sea level is around 1000 Wm^{-2} ($\sim$ 70 % of solar constant).
Atmospheric absorption is not homogeneous, big part of ultraviolet radiation is absorbed by chemical reactions, radical formation and mainly by O_3. Also particular energy windows of infrared radiation are almost completely absorbed by vibrational modes of main molecular compounds of atmosphere (N_2, H_2O, O_2 and CO_2).
Therefore, the composition of solar radiation irradiance at Earth's sea level is approximately: 5 % of ultraviolet radiation (380 nm and lower wavelengths), 45 % visible radiation (between 380 nm and 780 nm) and 50 % infrared radiation (780 nm and higher wavelengths) [25, Chapter 1].

1.2.1 Semiconductors

The photovoltaic generation depends mainly on the absorption material. Best suited materials for this purpose are semiconductors, which have conduction properties between metal and insulator materials.
Metals are materials without band gap (energy window without electronic states between occupied and unoccupied states, *i.e.*, valence and conduction bands) where valence and conduction bands are energy overlapped, or small band gap materials (below $\sim$ 0.3 eV, which can be eliminated by natural defects/impurities states, also called semimetals). Therefore, electrons can be promoted to higher energy states by small perturbations, such as phonon and thermal motion,

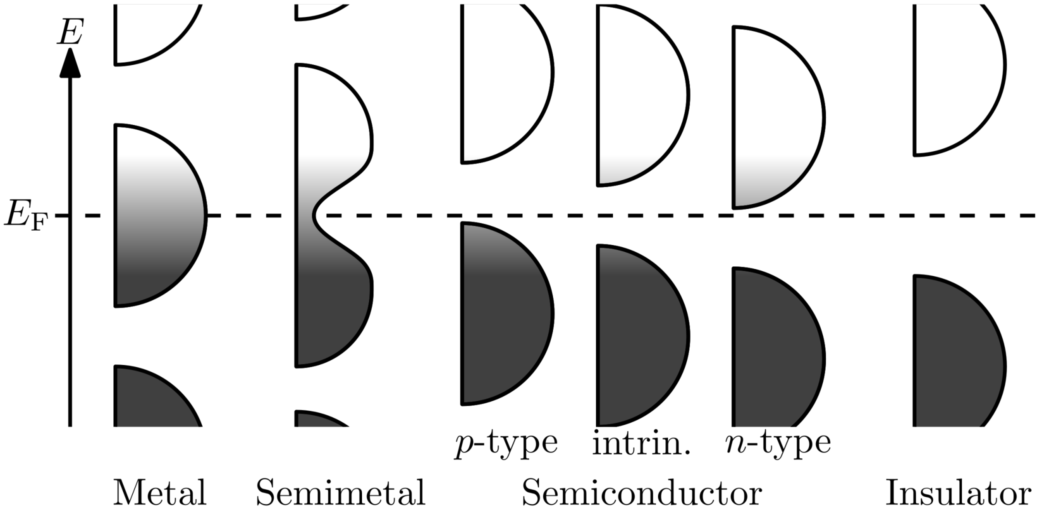

Figure 1.2: Comparative bands diagram of different type of materials, classified by its electrical conduction properties. State population at equilibrium, by Fermi–Dirac distribution, is shown by colors: black means fully occupied states, white means fully unoccupied states, and gray–scale partially (fractional) occupied states. Extracted from Wikipedia [27].

migrating within the material, so metals are very good electrical conductors.
On the other hand, insulator are materials with extremely wide band gap (above $\sim$ 4.0 eV), therefore electron promotion from valence to conduction bands is not possible in normal conditions, so insulators are bad electrical conductors.

Then semiconductors are materials with band gap between 0.3–4.0 eV range approximately, therefore small amounts of electrons can be promoted at room temperature from valence to conduction bands, so its electrical conduction properties are intermediate and can be modified. Band gap determines the minimum photon energy to trigger the photovoltaic effect, *i.e.*, produce an electronic excitation [26, Chapter 12]. Fig. 1.2 shows a comparative diagram of the different material types.

A proper way to define semiconductor materials, is the possibility to modify its electrical conduction properties by means of doping. These modifications generate three types of semiconductor categories (intrinsic, n–type and p–type semiconductors), depending on the relative position of the Fermi level in the band gap, defining the electrical behaviour of the material. The Fermi level E_F, also called chemical potential of electrons μ_F, is a hypothetical electronic energy level with a half probability of being occupied at thermodynamic equilibrium as given by the Fermi–Dirac distribution, which describes the average electronic state occupation. The Fermi level is useful to differentiate between conductors and semiconductors.
In conductors (metals) E_F lies over bands of the material making them thermally active, while in semiconductors E_F lies in the band gap or energetically near to the band edges, *i.e.*, Valence Band Maximum (VBM) or Conduction Band Minimum (CBM), allowing just a low amount (diluted concentration) of carriers (promoted electrons to conduction bands and holes in valence bands) [26, Chapter 13] [28, Chapter 3].

Semiconductor categories depends on the relative position of the Fermi level in the band gap, what determines the band edges (frontier bands, mainly VBM and CBM) activity.
The intrinsic semiconductors are materials where the electron (in the conduction band) and

hole (in the valence band) carrier concentrations are equal at room temperature. As donor and acceptor defects and impurities in semiconductors can produce a different concentration of carriers when they do not balance each other, it is said that most intrinsic semiconductors have low defects and impurities.

This ideal situation does not necessarily apply to all semiconductors. Some of them have natural constitutional and thermal defects or natural impurities that do not balance each other, so have a predominant acceptor (p–type) or donor (n–type) character, which defines the semiconductor behaviour. Also, this imbalance can be produced artificially in a controlled manner by doping the semiconductor, adding impurities in small amounts replacing semiconductor atoms [26, Chapter 12]. Defects and impurities make semiconductors interesting.

If a semiconductor atom is replaced by an atom with more valence electrons, *i.e.*, a donor impurity, the semiconductor enhance its n–type behaviour. Conversely, if a semiconductor atom is replaced by an atom with less valence electrons, *i.e.*, an acceptor impurity, the semiconductor enhance its p–type behaviour.

In this way, p–type semiconductors present a higher hole carrier concentration with respect to electron carrier concentration, and *vice versa*, n–type semiconductors present a higher electron carrier concentration with respect to hole carrier concentration. These characteristics also cause changes in the position of band energy levels with respect to E_F (which is not necessarily affected). p–type semiconductors have their VBM close to E_F, meanwhile n–type semiconductors have their CBM close to E_F. Fig. 1.2 shows an schematic diagram of different semiconductor behaviours [26, Chapter 13] [28, Chapter 3].

The semiconductor character has consequences when carrier conduction is considered. p–type/n–type semiconductors have in general higher hole/electron conductivity. When a hole/-electron is injected into it from another material, it has lower probability of carrier recombination due to its counter carrier, *i.e.*, electron/hole carrier, has lower concentration. Another consequence is that band energy levels can be tuned within an energy window (which depends on the material), to match the band edges with other material band edges.

1.2.2 Technical Aspects of Solar Cells

Photoelectric effect is just the beginning of the photovoltaic generation, due to the photo–excited electrons in conduction bands and holes in valence bands can annihilate each other by means of electron–hole recombination. Recombination can be radiative (emitting photons) or non–radiative. The former is most common when electron “jumps” directly from conduction to valence bands, and the later is most common when defects/intermediate states are present in the band gap, also called in–gap states.

When sunlight or other sufficiently energetic light is incident upon the semiconductor, the electrons present in the valence band absorb energy and, being excited, “jump” to the conduction band, leaving a hole in the valence band. Sometimes the photo–excited electron and hole remain bound, *i.e.*, exciton quasiparticle, which does not make possible free and unlinked diffusion of charge carriers. In order to separate the exciton into free charge carriers, additional energy is needed. Some materials have a high exciton energy binding, such as Cu_2O, which hinder separation and generates excitons with long half–life. Conversely, materials with low exciton energy binding, such as $CH_3NH_3PbI_3$ perovskite, enables easy separation and short half–life excitons [28, Chapter 6].

Since the moment that generated carriers are free, they undergo random and independent diffusion across the semiconductor. In order to make use and collect these carriers to generate a usable photo–current, a driving force is necessary to give direction to the carrier flux. To reduce the electron–hole recombination, these are directed in opposite directions by means of rectifying junction which generates a built-in potential (Galvani potential). Rectifying junctions are made with n–type/p–type semiconductor to collect and transport the electron/hole carriers, then they receive the name of Electron/Hole Transport Materials (ETM/HTM).

When the absorption material is a p–type/n–type semiconductor, just one junction is needed with a counter character semiconductor, *i.e.*, n–type/p–type semiconductor. This n–p or p–n cell designs, depending on the growth order with respect to the transparent electrode through which the light will enter the device, are a diode junction. Meanwhile, when the absorption material is an intrinsic semiconductor, two junctions with opposite character are needed to collect both carriers at different sides. Then devices with p–i–n or n–i–p order, depending on the growth order, are generated [28, Chapter 3]. Fig. 1.3 shows intrinsic semiconductor–based solar cell ordering, particularly for $CH_3NH_3PbI_3$ perovskite.

The junctions in the device must have some minimal characteristics to be efficient carrier

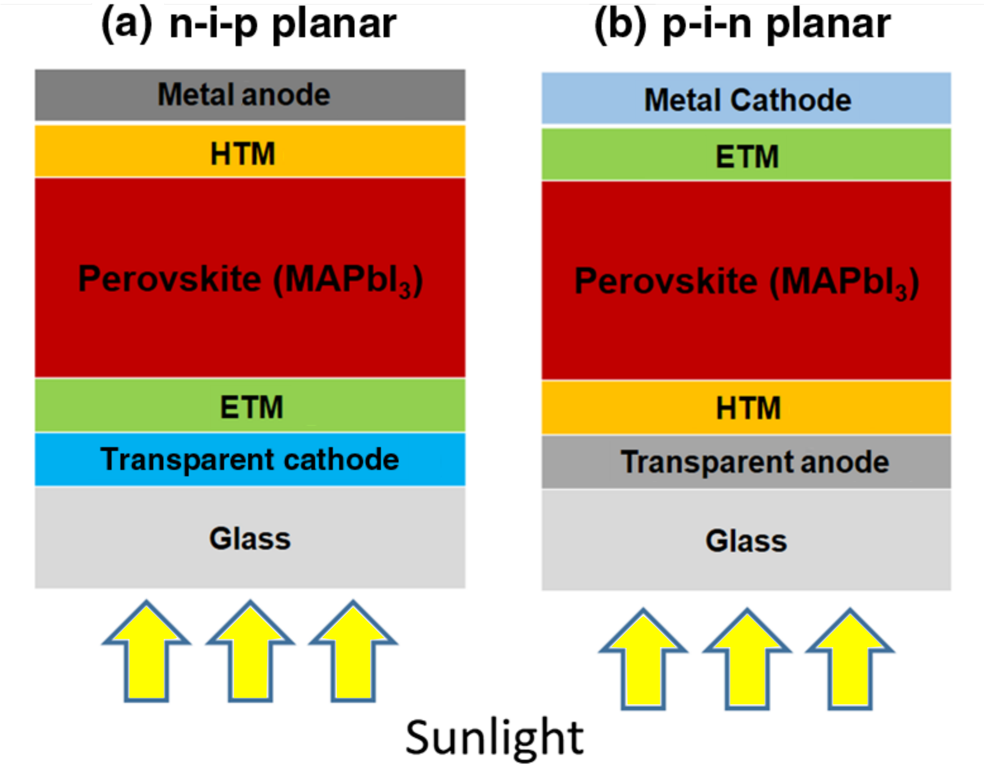

Figure 1.3: Schematic representation of solar cell devices with $CH_3NH_3PbI_3$ intrinsic semiconductor absorber (MA^+ correspond to $CH_3NH_3{}^+$) and planar junctions: (a) n–i–p device growth order and (b) p–i–n device growth order. Carriers are collected at opposite directions (with respect to the transparent electrode, *i.e.*, anode or cathode) depending on the device ordering. Extracted and modified from Ref. [29]

collectors. The interface at the junction must not have interfacial/localized energy states in the band gap because they can act as trap states, not allowing carrier diffusion and increasing the possibility of recombination. Harmful hole trap states are energetically located above the VBM at the junction, while electron trap states are located below the CBM at the junction. Therefore, in–gap interfacial states must be avoided. To maximize the injection current across the interface, the VBM/CBM levels of absorber material and HTM/ETM must be aligned for efficient hole/electron collecting [26, Chapter 14]. Although temperature and pressure have negligible effect on the bulk band structure of semiconductors, in the common temperature an pressure ranges, they affect to a larger extent to interface characteristics [30].

The ideal alignment does not possess an energetic step between carrier active band edges of both materials (*i.e.*, VBM at HTM interface and CBM at ETM interface, of both materials must be equal), but this situation is difficult to achieve. Also the interface must have an energy barrier for the counter carrier at the opposite band edge of both materials (*i.e.*, CBM at HTM interface and VBM at ETM interface) to avoid the flux of both carrier to the same direction, blocking them (*i.e.*, HTM blocking photo–excited electrons and ETM blocking holes). This is easily achieved using HTM and ETM with bigger band gap than of absorption material, and aligning correctly the corresponding band edges. In other words, the ETM and HTM act as filters for the photo–generated charge carriers. The described alignment at both interfaces is a Type II alignment [31, Chapter 9].

If the misalignment, of the corresponding band edges at the interface, reduce the device band gap with respect to absorption material band gap, the maximum achievable open circuit voltage is mainly affected reducing it, and the density current also is lowered slightly by carrier quantum scattering. The opposite situation, if the misalignment increases the device band gap with respect to absorption material band gap, the density current is mainly affected lowering it, by carrier classic scattering (due to the additional energy needed by the carrier to cross the interface) but also by quantum scattering, and the maximum achievable open circuit voltage is slightly increased. Let us recall that hole transfer between materials is really electron transfer in the opposite direction, so the energetic analysis/flux of holes carriers is the opposite of electron carriers [26, Chapter 14].

The energetic disorder and defects of the absorber material will only have a minor effect in the absorption, because the carrier separation and carrier transport take place at the interface, outside the absorber material. In contrast, the distribution of energetic states in the transport materials have an effect changing transport due to the population of band edges [32,33]. The objective is enhance the electron and hole transport and diminish the electron–hole recombination, improving carrier collection. This happens when exists grain boundary free direct pathways towards the external circuit. In consequence, optimization of absorber material, hole/electron transport material, and interfaces is an important task for designing efficient photovoltaic solar cells. Characterization and control of surfaces and interfaces are critical for photovoltaic applications.

The selection of optimal interfaces should consider commensurable vectors (epitaxy) to avoid stress, favorable crystal structure and atomic termination in the junctions that prevent dangling bonds, and barrier–free charge transport, *i.e.*, electronic state alignment between both materials. Therefore, a first step to the correct design of an interface requires knowing details of the structure and energy level of each part.

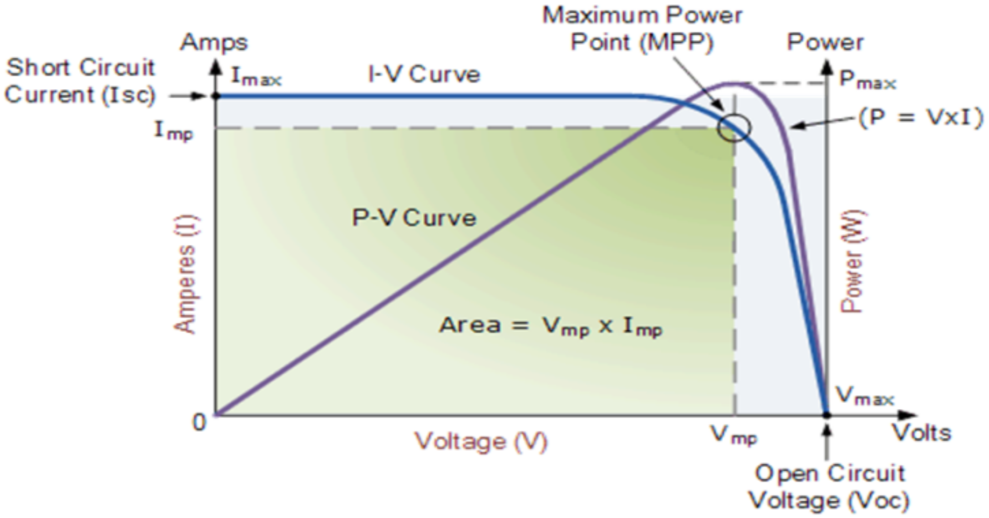

Figure 1.4: Solar cell I–V (current–potential) characteristic curve, with its corresponding P–V (power–potential) curve. Extracted from Ref. [34].

The device efficiency performance is measured by electrical parameters. Briefly, the main electric parameters are the open circuit photo–voltage V_{OC} and short circuit photo–current I_{SC}, both measured through I–V curve. V_{OC} is the electrical potential difference between both device electrodes when they are disconnected (*i.e.*, without photo–current between them). I_{SC} is the current that flows between both device electrodes when the voltage across the solar cell device is zero. Fig. 1.4 shows schematically I–V curve, I_{SC} and V_{OC}. Both parameters correspond to the higher possible voltage and current, respectively, at which the device can operate. If the solar cell device were to operate fictitiously at the I_{SC} or V_{OC}, no electrical power would be generated. I–V curves are measured using standard radiation irradiance conditions, using the Air Mass constant (AM). AM characterize the solar radiation irradiance at different latitudes, taking into account light travel length towards sea level are different. AM 1.5G is the most common standard, corresponding to a sun zenith angle of $\sim 48°$. It has a radiation irradiance of 1000 Wm^{-2}, which includes direct radiation and diffuse radiation (dispersed radiation by atmosphere, mainly visible light) [28, Chapter 7].

The Maximum Power Point (MPP) is the ideal operation condition of the device. This is the operational condition for the solar cell to deliver the maximum power. Electrical power is given by the product of current and voltage, $P = I \times V$. Therefore, P_{MP} corresponds to the highest possible area of any rectangle inscribed within the I and V axes, and the I–V curve (green rectangle in Fig. 1.4), where its vertex is positioned near the bend in the I–V characteristics curve. The voltage and current of this point are defined as maximum power photo–voltage V_{MP} and maximum power photo–current I_{MP}. They typically range between 0.80–0.90 and 0.85–0.95 times the V_{OC} and I_{SC}, respectively. Fig. 1.4 shows schematically I_{MP}, V_{MP}, and, P–V curve and P_{MP}.

With these four parameters is possible to label the solar cell performance by two definitions.

The Fill Factor (FF) is the ratio between the P_{MP} and $V_{OC} \times I_{SC}$ product. FF measures the quality of the solar cell and is a measure of how square/rectangle the curve is. Typical values range between 0.70–0.85, and 1.0 is the optimal value.

Photo–Conversion Efficiency (PCE) is the percentage ratio between the device electric power produced (usually P_{MP}) and solar incident power. Most of the solar cells devices and designs made to date do not exceed 10 % of PCE, being categorized as concept test devices. Only a few have exceeded the 20 % PCE barrier, which are the outstanding for large–scale solar cell generation.

The solar cell PCE is limited by thermodynamics, *e.g.*, defects, impurities, recombination process; and astronomical conditions, *e.g.*, the solar spectrum and the zenith angle of the sun with respect to the ground. Also photons with lower energy than the band gap are lost, *i.e.*, cannot be exploited, consequently not all solar spectrum radiation can be used. These limitations have their own optimal values that cannot be reached altogether, so a balance must be achieved between them in order to achieve maximum efficiency.
For a solar cell composed of a single absorber, the maximum PCE is ~ 33 %, for an absorbent material with a band gap of 1.34 eV. This is known as the Shockley–Queisser Limit (SQL), which applied for single absorber solar cells [35]. A not so strict optimal band gap definition is an band gap range between 1.2 and 1.5 eV. In practice, the maximum efficiency is further reduced by loss mechanisms in the cells. Currently, the solar cells closer to the SQL are based on GaAs semiconductor, which have been demonstrated 28 % PCE. Several other solar cells are over the 20 % PCE barrier [36]. These technologies are still making progress and it is expected some gain of a few percents to approach the SQL.
Multi–junction, also called tandem, solar cells can exceed the theoretical limit of single absorber solar cells (SQL), because they use two or more staggered absorber materials at the same device.

The nature of the absorber material band gap is important because it determines the absorption rates (absorption coefficient). Light absorption along a material is governed by Lambert–Beer law, which establishes that intensity of transmitted light decrease in an exponential rate as it passes through the material. If I_0 is the incident light intensity (of a particular frequency) perpendicular to the surface material, the transmitted light intensity I can be determined as $I = e^{-\alpha L} I_0$, where α is the frequency dependent absorption coefficient, and L the length traveled by light.
Absorption coefficient describes the transition probability at a particular photon energy. In semiconductors, as a band gap between occupied and unoccupied states exists, a zero absorption coefficient is observed for photon energies lower than band gap energy. Above band gap energy the absorption coefficient takes non–zero and its value depends on the nature of the electronic transition between semiconductor bands, *i.e.*, Joint Density Of States (JDOS) and the transition matrix elements.

Band gap nature of different semiconductors can be of four types: direct, direct symmetry–forbidden, indirect and indirect symmetry–forbidden.
Direct band gap refers that the lower energy electronic transition occurs by vertical (in momentum space) excitation, which maintain almost constant the crystal momentum. This type of band gap nature enables to have high absorption coefficient just above the band gap energy. Meanwhile, indirect band gap refers to the feature that the lowest energy electronic transition occurs by non–vertical excitation, which does not maintain the crystal momentum by itself. This transitions needs phonon–electron coupling to transfer/absorb momentum to/from the electron from/to the crystal vibration modes to conserve the total momentum in the absorption process. This phenomena is a low probability process because many particles (photon–phonon–electron) have to interact altogether. So this type of band gap nature have low absorption coefficient

just above the band gap energy until the first direct (higher energy) transition appears in the spectrum.
On the other hand, the transitions (direct or non–direct ones) can be allowed or forbidden by symmetry. Allowed transitions occur with significant probability, unlike forbidden transition have low probability of occurrence [26, Chapter 12].

As a consequence of this, symmetry–forbidden transitions have low absorption coefficients, so if they are the electronic transition at the band gap, the absorption coefficient just above the band gap energy will be low (with respect to an allowed similar transition, *i.e.*, direct or indirect) until the first allowed (higher energy) transition appears.
Therefore, indirect symmetry–forbidden band gap semiconductors are not suitable for solar radiation absorption. Meanwhile, direct band gap semiconductors are the best suited for this purpose. Nevertheless, direct symmetry–forbidden and indirect band gap materials, *e.g.*, silicon, have been successfully used for photovoltaic solar cells, but thicker films need to be used to achieve similar absorption rates with respect to direct band gap materials. From another point of view, direct band gap semiconductors allows to use thinner films and reduce material costs.

1.2.3 Photovoltaic Solar Cell Devices

The first solar cell, consisting of a layer of selenium covered with a thin film of gold, was experimented by Charles Fritts in 1884, but it had a very poor efficiency (below 1 %) [37]. It took many decades for the first solar cells with efficiencies above 1 % to appear in 1950s [38]. Before 2000s, solar cell technology was not a domestic/large–scale technology, and it use was restricted to aerospace and science purposes. Along the years, many different semiconductor materials were used to produce photovoltaic solar cells, with different technologies, implementations and efficiencies. These different type of solar cells are traditionally categorized into three family generations. This is shown in Fig. 1.5.

Currently large–scale photovoltaic generation is based on the first generation solar cells, made of crystalline silicon wafers, which are those investigated for the longest time since 1950s [38], been essentially unchanged since they were invented. They typically demonstrate PCE of 15–20 % (27.6 % record efficiency) [36] and high stability, allowing them to currently dominate the solar cell generation market, and also their use in domestic rooftops.
The shortcomings of this family are their high rigidness and high energy production cost due to the need of purification for pristine crystalline silicon films with extremely low impurities and defects, and its indirect band gap forces to use more material to growth thick films ($\sim$ 0.5 mm thick).

The second generation of solar cells are based on thin films (with respect to silicon wafers) semiconductors, which employ light absorbers made of gallium arsenide (GaAs), cadmium telluride (CdTe), copper indium gallium selenide (CIGS), amorphous silicon, and many others materials. They typically demonstrate PCE of 15 % (27.8 % GaAs–, 23.4 % CIGS–, 22.1 % CdTe– and 14.0 % amorphous silicon–based record efficiencies) [36].
The advantage of this family of solar cells are their lower material consumption, reducing the production costs, due to they have direct band gap, which allows to thinner films ($\sim$ 3 μm thick) achieving good absorption rates. Also, they are flexible to some degree. However, the

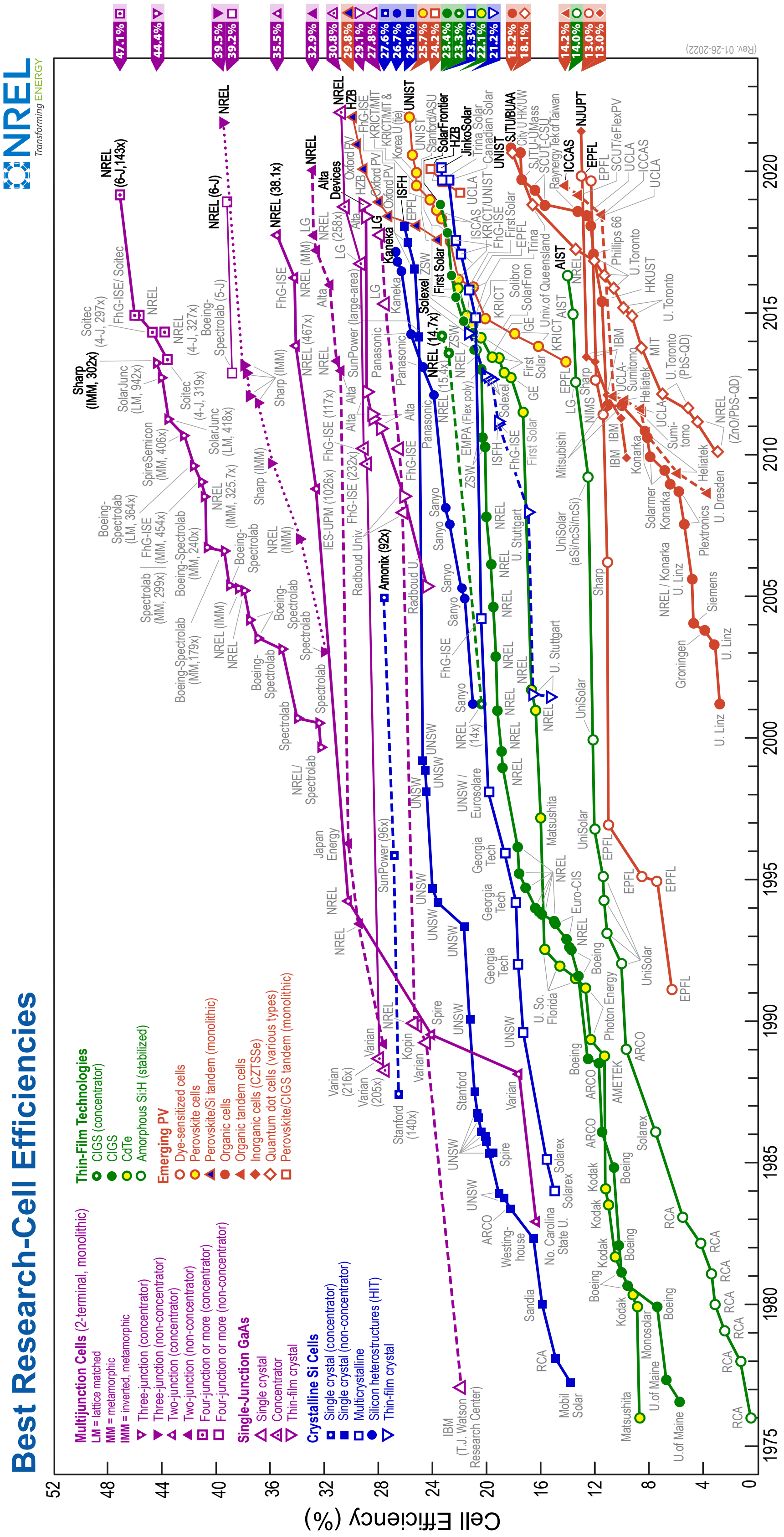

Figure 1.5: Best Research–Cell Efficiency line time, since 1976 until January 23th, 2022 [36].

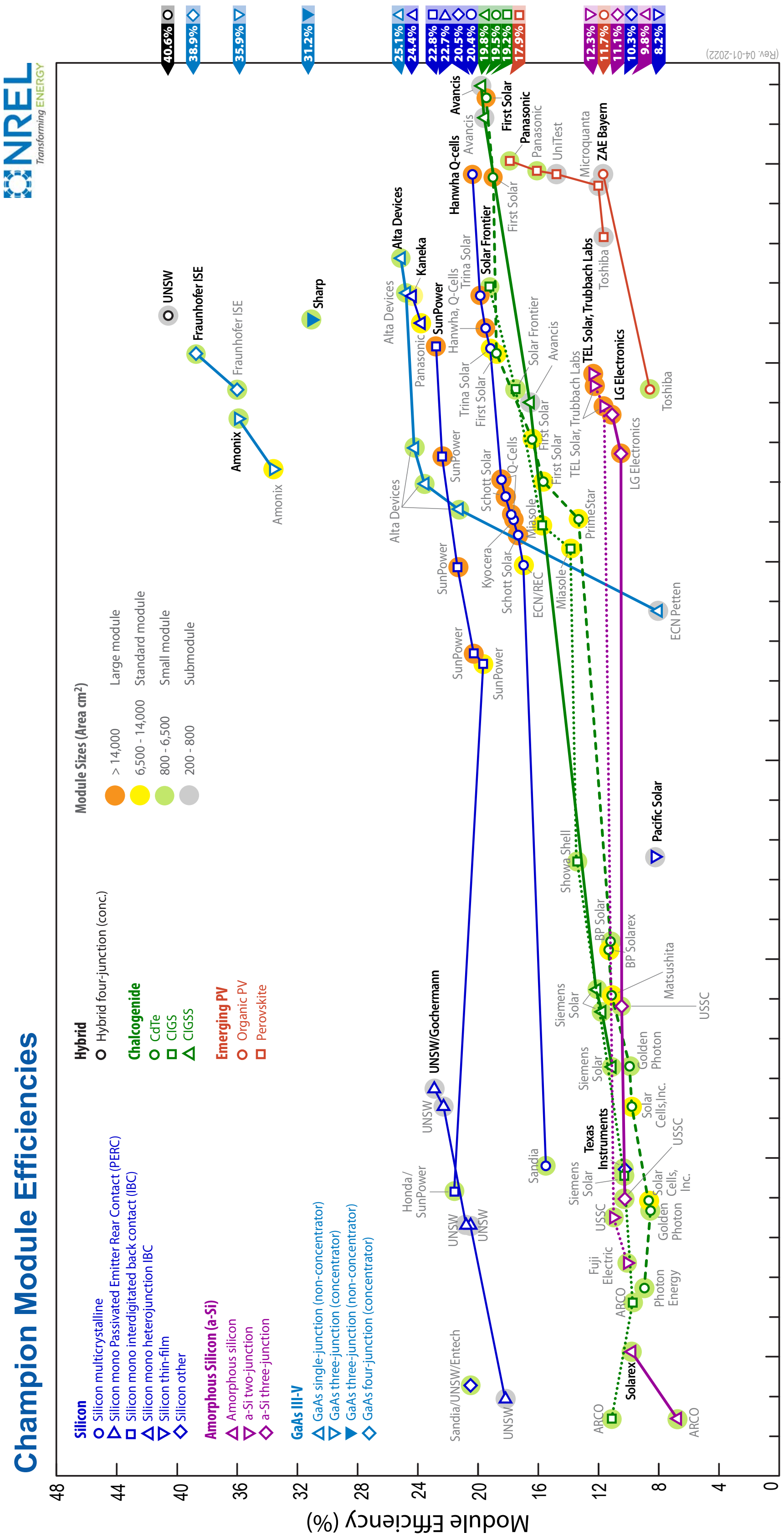

Figure 1.6: Champion Module Efficiencies line time, since 1988 until April 1st, 2022 [39].

production process still needs some complex process, such as vacuum and high temperature treatments, consequently the energy production cost is still large, and more over they need carrier materials to give mechanical stability. Also, most of these thin film solar cells are made of scarce elements limiting them in price, making them dependent on energy production price to be economically viable, although they have a share in the global photovoltaic market.

The third generation of solar cells are based on organic materials, inorganic materials, small molecules, polymers, dye–sensitized, Halide Organic–Inorganic Hybrid Perovskites (HOIHP), quantum dots, among many others. High performance devices using different tandem solar cells are in this family, reaching record PCE and exceeding the SQL, but most tandem solar cells are highly expensive relegating them to scientific research purposes. This family demonstrate varied PCE depending on the absorber nature, for example: 25.7 % HOIHP–, 18.2 % organic–, 18.1 % quantum dots–, and 13.0 % dye–sensitized– and inorganic–based solar cells [36].

Most of this solar cell generation offers a wide variety of advantages, such as simple and inexpensive large–scale production, use of already available and potentially inexpensive materials and industrial “printing” fabrication, direct band gap, among others. The main disadvantage of this solar cell generation is still their limited stability with respect to first and second generation, but nevertheless, their high record PCE and fast performance growth reinforce their great potential.

Particularly, HOIHP–based solar cells have shown the greatest PCE of these generation with just over a decade of research, reaching similar record performance of silicon solar cells. Sometimes HOIHPs are called “the raising star of photovoltaics” thanks to their advantageous optoelectronic properties. The optimization of absorber, hole transport and electron transport materials allows for further improvements in performance and stability to tune up these emerging technologies [40].

Despite the high efficiencies reached by several solar cell technologies, as shown in Fig. 1.5, these best research efficiencies are achieved by solar cell devices with very small area (< 1 cm^2). These tiny devices are not of practical use for large–scale energy production. Hence, just reaching high efficiencies is not enough, it is necessary to produce devices with high efficiencies and, at the same time, be larger in size. This is an even bigger challenge, which only a few solar cell technologies have successfully overcome, as shown in Fig. 1.6.

Fig. 1.6 show the champion module efficiencies for large–scale production solar cells. It is evident that achieve solar cells with areas bigger than 800 cm^2 (equivalent to a square tile of $\sim$30 cm of side) is a difficult frontier to cross. Particularly, during the last few years HOIHP–based solar cells have succeed in produce devices of high efficiency and size.

1.3 Halide Organic–Inorganic Hybrid Perovskites

Halide organic–inorganic hybrid perovskites are a family of original intrinsic semiconductor materials with perovskite crystalline structure. HOIHP show a rich phenomenology from the point of view of semiconductor physics and crystallography. They are powerful light absorber materials with interesting optoelectronic properties used as optical detectors and mainly in photovoltaic solar cell devices as absorbers. Synthesized HOIHP presents a wide range of compositions between different organic cations, halogen anions and metallic centers, and also non–stoichiometric mixtures/alloys of these different compositions have been described [41].

1.3.1 Properties and Electronic Structure

HOIHPs exhibit a perovskite crystalline structure, with ABX_3 general formula. Perovskite structure is a general structure of many metal oxide minerals, such as the first discovered in 1839, $CaTiO_3$, by Gustav Rose who named it perovskite in honor to Lev Aleksevich von Perovski. Perovskite crystalline structure of HOIHP shows a framework of octahedral cages, formed by halogens anions at the corners ($X^- = I^-$, Br^- or Cl^-) with a metal cation in the center ($B = Pb^{+2}$ or Sn^{+2}). This framework has negative charge which is compensated by organic protonated cations ($A^+ = CH_3NH_3{}^+$ or $HC(NH_2)_2{}^+$). These organic protonated cations are located at the interstices of octahedral framework, see Fig. 1.7. Additionally, exist halide all–inorganic perovskite compounds, which replace the organic protonated cations with alkaline metal cations, *e.g.*, inorganic cesium and rubidium [42]. Recent developments include mixtures of different halogens and cations (random alloys of the pure compounds), with the goal of optimizing the absorption to improve their properties. As a consequence of this wide variability of compositions, their structural and electronic properties can be tuned widely.

The semiconductor unique features of HOIHP include long carrier diffusion lengths [43], high carrier mobility, low recombination losses by means of electron–hole recombination, low sensitivity to defects, low material and fabrication costs without rare elements, high absorption coefficients with a direct band gap (enabling thin film devices) in the optimum range of SQL, and high band gap tuning capacity through changes in its composition.
Therefore, HOIHP–based solar cells under research have emerged as a strong promise for efficient and cheap solar cells.

Methylammonium lead iodide, $CH_3NH_3PbI_3$, $MAPbI_3$ or MAPI, is by far the most experimentally and theoretically studied material of HOIHP family, making it the main study model. Many studies have been modeled their structure, optoelectronic properties [44] and the effect of thermal motion on them [45].
In the perovskite structure, the A–, B–, and X–sites are occupied by the ions MA^+, Pb^{+2}, and I^-. MAPI shows two phase transitions at 163 and 327 K [46], among the three different crystalline structures. The stable phases are the orthorhombic structure at low temperatures, the tetragonal structure at room temperature, and finally the cubic structure at high temperature [47, 48]. The main difference between these structures is the relative position between the octahedra. Cubic structure shows aligned octahedra without tilt between them, meanwhile orthorhombic and tetragonal structure presents a tilt/rotation of octahedra framework, chang-

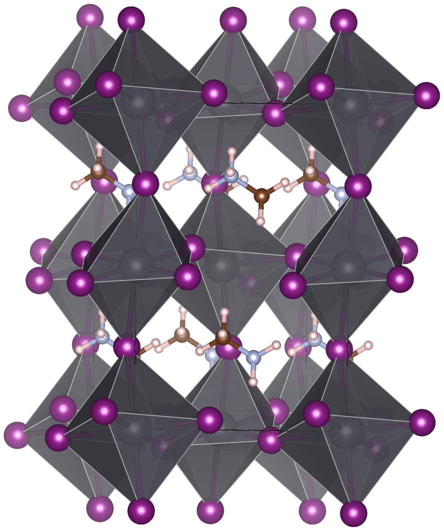

Figure 1.7: Crystal tetragonal structure model of $CH_3NH_3PbI_3$ perovskite unit cell. Iodine atoms as violet spheres, lead atoms as black spheres, both forming the octahedra framework, and, carbon atoms as brown, nitrogen atoms as light blue and hydrogen atoms as white spheres, forming MA^+. Image generated with VESTA [50].

ing the shape of the interstices where organic cations are located. In orthorhombic/tetragonal structure this distortion is in phase/anti–phase for consecutive octahedra framework planes [49].

Tetragonal structure has experimental lattice constant of 8.76 Å for a and 12.39 Å for c cell vectors (c/a constant of 1.41) [49]. Structure model is shown in Fig. 1.7. Theoretical research have shown that dispersion corrected non–local functionals improve the geometry structures obtained by GGA functionals, in excellent agreement with experiment, but its use is not mandatory, and GGA results are also reliable [44, 45]. However, non–local functionals cannot be used with the Spin–Orbit Coupling (SOC), which modifies the band structure of the $CH_3NH_3PbI_3$ perovskite.

MAPI has a nominal band gap of $\sim$ 1.6 eV, with a range of values 1.5–1.7 eV depending on the amount of bromine and chlorine doping ions replacing iodine atoms. Theoretical calculations using GGA functional reproduce this values [44, 51] due to error cancellation between SOC and GGA underestimation band gap due to SIE. SOC reduces the band gap by almost 1.0 eV while the underestimation error is also almost 1.0 eV. Then when GGA functionals without SOC are used, the lack of SOC fortuitously compensate the GGA band gap error, and band gap appears to be well described [44]. However as both errors do not affect equally VBM and CBM energies, their relative energy may not be correct even if the band gap is. The inclusion of SOC reduces the band gap mainly stabilizing conduction states and to a lesser extent destabilizing valence states. Conversely, the inclusion of exact exchange through hybrid functionals or using GW approximation, increase the band gap mainly stabilizing valence bands and in lesser extent destabilizing conduction bands. Both effects in conjunction produce practically the same band gap of GGA functionals, but the band edge energy levels are reduced in a range of 0.5–1.0 eV [44].
SOC is crucial to describe the CBM, which is composed mainly from lead 6p subshell, and in some cases present interesting effects like the Rashba splitting. Hybrid functionals together

with SOC, allow to accurately describe the band structure of MAPI, with a correct description of band edges and band dispersion [44]. Also GW approximation using G_0W_0+SOC is a useful approach to obtain correct band gap and band structure [52].
Valence bands show a dominant composition of iodine states, mainly 5p subshell, and a smaller composition of lead states, 6p subshell in the deeper valence states and 6s subshell near the valence edge. Conduction bands show a dominant composition of lead 6p subshell, and a smaller amount of iodine 5p subshell, in a wide energy range of conduction states. The high lead composition of conduction bands explains why SOC mainly affect them, meanwhile valence bands are less affected by SOC by their low amount of lead composition [51, 53].
For a detailed review of the theoretical methods of electronic structure calculations see Chapter 2: Electronic Structure Calculations.

MAPI shares the advantageous properties of HOIHP family with an extended use in experimental solar cells as a powerful light absorber. Particularly, MAPI has a direct band gap with a nominal energy of 1.6 eV, which is close to the optimal band gap for single junction solar cells, according to SQL. The direct band gap entails a high absorbance just above the band gap energy, allowing to use just a few micrometers of the material to absorb photons with the band gap and higher energies, making it very attractive as photovoltaic light harvesters.

1.3.2 $CH_3NH_3PbI_3$ Solar Cells and Surfaces

Perovskite solar cells have achieved efficiencies that compete with silicon photovoltaic cells, starting with 3.8 % PCE in 2009 [40] and increasing up to 25.7 % at the present time [36]. Also, HOIHP can be used to boost the PCE of single junction solar cells such as CIGS or silicon, in tandem solar cells architecture, which have been produced with 24.2 % and 29.8 % PCE records, respectively. Particularly, silicon/HOIHP–based tandem solar cells reached higher PCE than standalone silicon– and HOIHP–based single junction solar cells [40].

The firsts HOIHP–based solar cells were fabricated using MAPI as the light absorber material. While, the current use of alloys of HOIHPs is the standard and extended methodology. The use of mixtures of organic cations does not change the band gap directly, because they are not part of the valence and conduction band edges wavefunctions, but, they disturb the octahedra framework changing indirectly the band gap. Also mixtures of halogens are used. Halogen composition determine directly the band gap and mainly VBM energy, due to halogen atoms are the main contributor to VBM wavefunctions.

The use of MAPI (and HOIHP family) on large–scale solar cells is still limited due to a significant weakness. MAPI is barely stable against decomposition/degradation into lead iodide and methylammonium iodide produced by the environment wetness. Acid–base reactions on methylammonium and iodide with water molecules and photo–decomposition, causes the degradation of the material, and consequently of the devices [54, 55].
MAPI degradation is accompanied by toxicity risks due to lead content. Therefore, much research has been done to replace lead in MAPI, and to increase stability. While lead replacement (mainly by Sn^{+2}) always cause a large decrease in the band gap [56] and in the solar cell PCE, therefore there are significant achievements in the stability by means of interface engineering by

confining it from the environment using different transporting materials [57], and by alloying the cations [58].

In planar interface solar cells (as shown in Fig. 1.3), the HOIHP light absorber is sandwiched between a p–type and a n–type semiconductor (HTM and ETM, respectively) films [59]. Sunlight absorption takes place at the HOIHP, inducing the generation of photo–excited electrons and holes, which are separated at the interfaces with the HTM and the ETM, respectively [60, 61]. Transparent conducting materials as Indium Thin Oxide (ITO), Fluoride Thin Oxide (FTO) and organic polymers as poly(3,4–ethylenedioxythiophene), also called PEDOT, are used also to complete the device.

Experimental advances have been critical to produce HOIHP–based solar cells with the required degree of crystallinity to provide high solar cell performance. However, in the practice of building these solar cells, very little information is available on the characteristics of the surfaces obtained, neither their composition nor their energy levels. The same is true for their interfaces. By reviewing the electronic energy levels of perovskite films, determined essentially by combining ultraviolet photoelectron spectroscopy (UPS) and inverse photoemission spectroscopy (IPES), it is possible to realize that the reports differ greatly [62]. The differences are associated not only with the preparation methods and the ratio of precursors, but also with the substrates and the exposure of the prepared films, air, light, and the thermal conditions [62,63]. Particularly in MAPI, variations of up to 0.7 eV in energy levels are reported changing the ratio of their precursors. However, most of the studies looking for alignments with MAPI levels still consider the reported VBM energy for bulk (-5.4 eV), and project the CBM energy at -3.7 or -3.9 eV, depending on the band gap considered [62–66].

By scanning tunneling microscopy (STM) and spectroscopy, it was possible to elucidate the atomic rearrangement of the surface and the density of state of the valence band of an ultrathin film of MAPI [67]. The measurements corresponded to the orthorhombic phase and it was concluded that the surface ends in a layer rich in methylammonium iodide (MAI) in the plane (001), with two rearrangements of iodine coexisting. With this experiment a real image of defects is shown for the first time, although large areas of surface without defects are mostly observed. The computational model explains the influence of organic cations on the rearrangements of the observed atoms. The STM technique also provided the surface description of $CH_3NH_3PbBr_3$ and other HOIHP mixed compositions used to improve the cell stability [68–70]. However, in all cases the information is limited to the low temperature phase that is far from the experimental conditions in which the solar cells are manufactured.

The elemental composition of the MAPI surface obtained by X–ray photoelectron spectroscopy (XPS), under controlled humidity conditions, has recently been reported for photo–catalytic applications [71]. The analysis indicates that below 35 % humidity the MAI type composition of the surface predominates, and at higher humidity the surface is PbI_2 type. However, the authors found no photo–conversion activity on the MAPI surface in humidity conditions above 35 %. The report supports that the MAI–terminated surface exhibits photo–catalytic behaviour because moisture generates surface defects exposing surface lead atoms as active–sites.

Prior to the STM [67] and XPS [71] results, theoretical models of the surfaces of each of the three MAPI phases had already been attained, including some defect proposals. For the orthorhombic phase, the (100) and (001) slab models appear with the lowest surface energies, which correlates with the largest coordination number of the surface lead atoms [72]. In agreement to the subsequent STM experiment, the surfaces show MAI–terminated terminations and the interactions between organic cations and iodine atoms are a stabilizing factor.

Surface models corresponding to a pseudo–cubic unit cell have also been anticipated, this time to study the adsorption of a molecule that simulate hole transport layers in solar cells [73]. The slabs representative of the (001) surfaces included the MAI and PbI_2 termination types, both stoichiometric. Again, the orientation of the surface MA^+ influences the stabilization mechanism of the slabs. Binding energy calculations predict the preferred conformation of the adsorbed molecule on the surface, although energy level alignment was not considered.

The surface of the tetragonal phase has been more studied since it is the phase most stable at room temperature, and several stoichiometric and non–stoichiometric (with defects) models have been proposed [66, 74–77]. These studies suggest that the MAI–terminated (110) and (001) surfaces are energetically favored, although PbI_2 type terminations are still possible. The greater stability of the MAI–terminated slab is again associated with the NH_3^+ group of MA^+ interacting with the iodine atoms, configuration where the CH_3 group is oriented outward, namely top–C [77]. The relative instability of the PbI_2–terminated surface at vacuum could favor their energy of adhesion with any transporting layers in the cell [75].
MAPI(001) surfaces are formed by alternating layers with MAI and PbI_2 composition, but not both at the same time per (100) surface unit cell. Each layer has a neutral charge. Thus, a two–plane repeat unit of MAI and PbI_2 layers is necessary to maintain stoichiometry. This situation causes the (001) surface to be neutral but with dipole, categorizing it as a Tasker class II surface [78]. In order to balance the total system dipole, the system needs two equal and opposite surfaces canceling its dipoles, breaking the stoichiometry of the system.

In addition to the differences in the stability of the surface termination, reports show that electronic properties of each surface are highly sensitive to the slab thickness and the relative orientation of MA^+ within each slab. An initial report estimated the convergence in surface energy by modeling slabs up to five layers thick, where each layer extent half unit cell [75]. The surface terminated by MAI did not reach convergence with respect to the band gap for these slab thickness, whereas PbI_2–terminated surface revealed a constant band gap. Other models show that both the band gap and the energies of the frontier states with respect to the vacuum level change if the CH_3 or NH_3^+ ends of the MA^+ are regularly oriented towards the vacuum or if an apolar configuration of these cations is imposed within the entire slab [77]. Despite finding these variations, the agreement between the calculated frontier electronic states and the experimental data was reasonably achieved including spin–orbit coupling effects as *a posteriori* correction.

Regarding MAPI, it is one of the semiconductor materials that have presented excellent properties for achieving good PCE in different solar cell arrangements and can be relatively easily obtained by chemical methods well described in the literature. On the other hand, the high cost of hole transport materials based on organic compounds raises the need for more economic alternatives for long term large–scale application.
Information at interfaces of MAPI and HTM/ETM is more sparse, and highly important to achieving high quality solar cells. The alignment of energy levels is just one of the conditions

required for a good and efficient interface. Other requirements are: high carrier mobility, absence of trap states, adhesion, chemical stability, non–toxicity or encapsulation, and finally costs. Some of these requirements, are contradictory and not obvious at all. For example, the use of spiro–OMeTAD (2–7,7–tetrakis (N,N–di–p–methoxypheny–lamine)–9,9–spirobifluorene) as HTM allowed the highest cell efficiencies, but it was later found to be part of the mechanism of degradation of the device [79]. The high cost of spiro–OMeTAD, compared to the inorganic p–type semiconductors and the perovskite itself, is one of the limitations for further large–scale applications.

The p–type semiconductors that we are considering are copper–based inorganic materials. These materials are candidates to replace the organic spiro–OMeTAD that is usually employed in HOIHP and dye–sensitized solar cells at laboratory–scale. Compared with organic HTMs, inorganic p–type semiconductors appear to be an ideal choice given their properties. Inorganic p–type semiconductors appear as good choice given their high mobility, stability, easy synthesis and low cost.

In this sense, it is interesting for our country to explore the performance of copper–based semiconductors. Perovskite solar cells using copper iodide and copper thiocyanate have been reported as HTM in lead halide perovskite solar cells, showing 6 % [80] and 12 % [81] of PCE, respectively. Cu_2O is another p–type semiconductor with high hole mobility. Cu_2O has many of the desired requirements, therefore it is expected it can act as a efficient HTM in HOIHP–based solar cells.

1.4 Cu_2O

Cu_2O, cuprite, cuprous oxide or copper(I) oxide is a red solid, diamagnetic, non–toxic, low cost and Earth–abundant mineral with different crystal habits: cube, octahedron, dodecahedron, and combinations of them. Is one of the most studied semiconductor since is the oldest material of semiconductor electronics [82]. Currently its use is extended: nanoelectronics, spintronics [83], photo–catalysis [84–86] and photovoltaics [87, 88]. Cu_2O is one of the three stable phases of copper oxide compounds (the others are Cu_4O_3 and CuO). Cuprite natural crystals have been found worldwide, most of them as a small red crystals, but high quality gem size crystals with low density of structural defects and inclusions stem were found in Zaire (Africa) [89].

1.4.1 Properties and Electronic Structure

Cuprite crystal is a simple cubic Bravais lattice (O_h^4 space group), 6 atom unit cell (Cu_4O_2 atomic composition), with an experimental lattice constant of 4.2696±0.0010 Å [90]. It is formed by two sublattices: the copper face–centered cubic (fcc) sublattice and the oxygen body–centered cubic (bcc) sublattice [91].
Selecting an oxygen atom as the Cartesian origin, the copper atom positions are $(\frac{1}{4},\frac{1}{4},\frac{1}{4})$, $(\frac{1}{4},\frac{3}{4},\frac{3}{4})$, $(\frac{3}{4},\frac{1}{4},\frac{3}{4})$ and $(\frac{3}{4},\frac{3}{4},\frac{1}{4})$ in terms of lattice constant, as Fig. 1.8 shows. The coordination number for the metallic atoms (copper) is unusual, due to it is linearly coordinated by two neighboring oxygen atoms. Meanwhile, oxygen atoms occupy tetrahedral interstitial positions relative to the copper sublattice with fourfold coordination. Also, the short Cu–O bond length is smaller than the sum of any pair of ionic radii of Cu^+ and O^{-2}, an unusual situation [92], which suggest

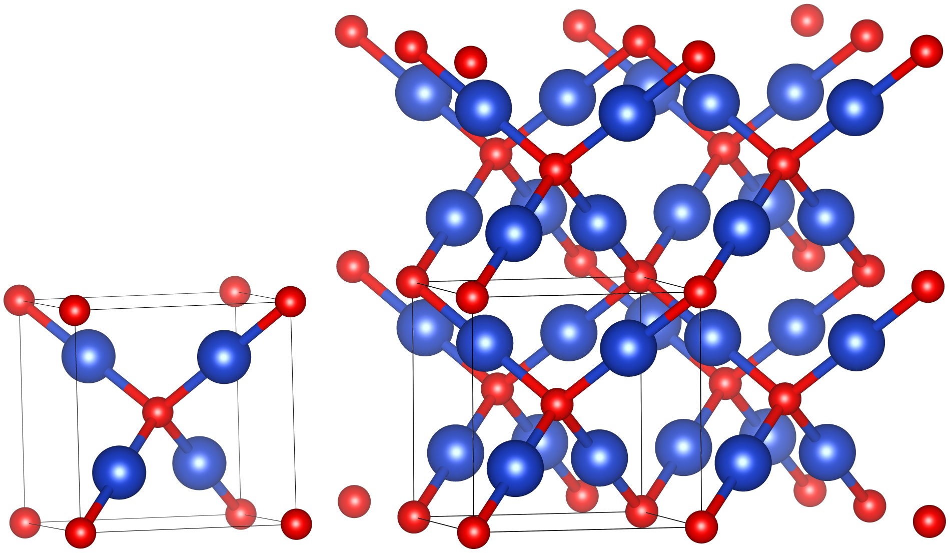
(a) Cu_2O unit cell (b) Cu_2O supercell

Figure 1.8: Crystal structure models of Cu_2O. Oxygen atoms as red, and copper atoms as blue spheres. (a) Unit cell, (b) a 2 × 2 × 2 supercell, *i.e.*, 8 unit cell structure. Images generated with VESTA [50].

a covalent–like bond. A consequence of this characteristic is the presence of an anisotropy at the copper atom, due to the hybridization of 3d (mainly $3d_{z^2}$ due to symmetry) and 4s orbitals, which causes electronic holes on 3d subshell. Also the hybridization causes the valence bands present some non–negligible copper 4s character, while the conduction bands present some non–negligible copper 3d character [93, 94].

The Cu_2O electronic structure has been of interest for a long time [95,96] because exhibits an unusual exciton spectrum, with a long series of exciton transitions, starting from a symmetry–forbidden line [97–99]. Many experimental studies were carried on Cu_2O in order to analyze its electronic structure [100, 101].

Cu_2O has been extensively investigated theoretically using Density Function Theory based calculations [95, 102–105]. Most of these studies achieved a good description and can reproduce the experimentally observed electronic structure, but they need constant energy shifts to match experiments. This drawback is related with the poor description of Cu_2O band gap for almost all theoretical frameworks, which has immediate implications for the energetic of point defects and photovoltaics.

Cu_2O has an experimental band gap of 2.17 eV and the first allowed optical transition at 2.62 eV [106,107], with a experimental *macroscopic* dielectric constant of 7.5 [108]. Many theoretical research have been made, showing that LDA/GGA based calculations give a low fraction of the experimental band gap, ranging 0.4–0.7 eV [102, 109]. Hartree–Fock based calculations give wider (4.5 times) band gap with respect to experimental one [110]. Other type of frameworks as LDA+SIC [111], GGA+U [112], hybrid functionals [103, 113] and GW [114] could achieve band gap with an error of 0.3 eV or less than 0.1 eV. A general conclusion of these studies suggests to go beyond the standard DFT schemes to obtain reliable electronic structure results, which in many cases is very expensive and unaffordable. The electronic on–site correlation is expected to be low, due to the closed shell d^{10} configuration of copper atom (in the picture of ionic model Cu+), with respect to other transition metal oxides.

Conversely, computed lattice parameter and mechanical properties of GGA results are close to experimental values. The calculated *macroscopic* dielectric constant at GGA level is about 6.7, slightly smaller than experimental value [115], while GW calculations obtain 5.7, even farther away [116]. Despite the failure of LDA/GGA functional to describe electronic structure of Cu_2O, the orbital composition of bands is correctly described. Valence bands show a dominant composition of copper states, mainly 3d subshell (with a non–vanishing copper 4s and 4p subshell distributions), and a smaller composition of oxygen 2p subshell. Conduction bands show a dominant composition of copper 4s subshell and oxygen 2p subshell at the edge, while at higher energies the copper 4p subshell turns dominant (non–vanishing copper 3d subshell distributions is observed at CBM and higher energies) [115]. The high copper 3d subshell composition of valence bands explains the high dispersive structure compared with other oxide semiconductors with high oxygen 2p subshell composition and localized valence bands. SOC affects slightly the electronic structure of Cu_2O, as expected for systems with non–heavy atoms, with very small changes in terms of energy. The main change is related with the VBM, which is predicted as a threefold degenerated without SOC, which split into a twofold degenerated VBM and a non–degenerated smaller band with an energy difference of 0.13 eV, when SOC is applied.

For a detailed review of the theoretical methods of electronic structure calculations see Chapter 2: Electronic Structure Calculations.

As all crystals, Cu_2O presents point defects at equilibrium, such as constitutional and thermal defects. Some typical point defects are: copper or oxygen sublattice vacancy and anti–site copper/oxygen atom on the oxygen/copper sublattice. These point defects have important influence on the electronic properties. The electronic properties also can be controlled through the preparation conditions: partial oxygen pressure and temperature, among others [117].
The predominant defects in a wide range of conditions are the cation vacancies, due to low formation energy, turning Cu_2O as an intrinsically copper deficient, p–type semiconductor, with a low non–stoichiometric composition (losing ~ 1 per 1000 corresponding copper atoms) [112]. It is worth mentioning that at very low partial oxygen pressure and controlled conditions, oxygen vacancies appear to become dominant [118], reaching self–compensation with intrinsic defects [119], but not enough to reach a n–type Cu_2O.

The Cu_2O conduction behaviour is non–classical. It is based on polaronic hopping mechanism [120, 121], due to copper atom vacancies which causes an excess of oxygen atoms. These copper vacancies act as shallow and efficient hole producers (acceptors centers) located at the VBM, that give rise to the so–called electronic sub–band. The oxygen vacancies cannot act as a potential hole killer because they do not have in–gap transition levels, then cannot annihilate holes. Other point defects that can act as hole killers have high formation energy and deep transitions levels turning them incapable to be efficient hole annihilators [112], The presence of defects and their energy level have been measured through Deep Level Transient Spectroscopy. This explains why Cu_2O is a natural intrinsic p–type semiconductor, with high hole mobility through phonon scattering (high temperature) and ionized impurity scattering (low temperature, below 200K) [122], The p–type and hole mobility can be controlled by fabrication conditions favoring the formation of copper vacancies and avoiding formation of donor defects. Also the acceptor defects concentration can be tuned by extrinsic acceptor as nitrogen doping (replacing some oxygen atoms), enhancing the hole density by two orders of magnitude [123, 124].

1.4.2 Fabrication, Applications and Surfaces

Cu_2O fabrication is a widely studied area. Currently there exist many documented routes, with different and versatile techniques.
Bulk synthetic crystal fabrication of Cu_2O has been reported by oxidizing copper sheets, by melt growth, by floating zone growth, by hydrothermal growth [89], among others.
Moreover, thin films can be fabricated by many techniques, for example: electrochemical reduction of lactate or citrate Cu(II) complexes onto conductive substrates [125], direct thermal oxidation of copper [126], copper anodization [127], electrodeposition, sol–gel, spray or sputtering [106], dip coating [128], among others. This thin film can be tens to hundred nanometers of grain size, with polycrystalline structure controlled by fabrication technical conditions.

Cuprite was used extensively in the past for different electronic devices, as diodes and photovoltaic absorber material. Its photovoltaic performance was poor, due to limited PCE. This behaviour was explained because a low open circuit voltage with respect to its SQL [106]. Old Cu_2O–based photovoltaic devices reached 1.8 % of PCE and foreseen 3 % with further development. Higher (6 %–10 %) PCE required new designs [87]. Currently, Cu_2O–based photovoltaic devices are under attention, a new thin film and transparent devices were fabricated using impurity controlled technology, reaching a record PCE of 8.4 % and a potential to reach an efficiency over 10 %. The cell was conceived for use in electric vehicles and high altitude platform station applications. Also, tandem solar cells offers the promise of more efficient solar modules, such as Cu_2O–Si tandem cell for which is estimated a PCE of 27.4 % [88]. Anyway, Cu_2O is not a prominent material for solar cell absorber, because its bang gap (2.17 eV) is too much high with respect to optimal ones, according with SQL for single junction cells. This situation predicts an upper limit PCE of 20 %. Also, the direct symmetry–forbidden band gap nature, entails a low absorbance just above the band gap energy and up to 2.62 eV, where the first allowed optical transitions begin. The mentioned energy range presents the green, blue and indigo exciton series of Cu_2O [99].

Cu_2O has been an important focus of attention in the search for p–type oxide semiconductors [129] to use them as HTM in photovoltaic solar cells, based on Cu_2O characteristics: abundant, non–toxic, low cost, high hole mobility, and, wider band gap and similar ionization potential with respect to used absorber materials.

Particularly, Cu_2O nominal ionization potential is very similar to that of $CH_3NH_3PbI_3$ perovskite, so it has been conceived as a potential alternative to traditional organic hole transport materials [130, 131] in HOIHP–based solar cells.

Ionization potential of Cu_2O was investigated theoretically and experimentally, achieving similar results: 5.25 eV by *in situ* electrochemical STM (corrected to pH 7.0) [132], 5.66 eV by photoemission spectroscopy [133], 5.49 eV by DFT calculations on $Cu_2O(111)$ surface [134] and 5.3–6.0 eV range by different DFT methods on $Cu_2O(111)$ surface [135, 136].

Ionization potential and band edges energies are surface termination dependent, therefore it can be tuned by its composition. Many studies were made on different surface terminations [102, 104, 105, 109, 135, 137–139], mainly focused on their potential for photo–catalysis. Low index surfaces of Cu_2O, *i.e.*, (111), (110) and (100), have been investigated showing that surface $Cu_2O(111)$ with oxygen termination is the most stable one in most conditions [135]. This surface shows a minimal surface vectors with hexagonal shape (120°) and $\sqrt{2}$ times bulk Cu_2O lattice vector length, so is probably not present in interfaces with MAPI because it poor epitaxial match with MAPI will would cause stress and could not satisfy a good atomic terminations at the interface.

Similar situation occur with $Cu_2O(110)$ surface. It presents orthogonal vectors with 1 and $\sqrt{2}$ times bulk Cu_2O lattice vector length, which does not allow for a good epitaxy.

$Cu_2O(100)$ surface would allow a good epitaxy with low stress because it is a square surface, it is indeed a face of the simple cubic cell of Cu_2O. This surface has a quarter of surface area of MAPI(001) surface area, then a 2×2 $Cu_2O(100)$ surface unit cell will match in the first instance with MAPI. This surface is formed by alternating layers with one oxygen and two copper atoms (but not both at the same time) per (100) surface unit cell, with a charge of -2 and $+2$, respectively. Thus, a two–plane repeat unit of copper and oxygen layers is necessary to maintain stoichiometry and charge neutrality. This situation causes the (100) surface to be polar, categorizing it as a Tasker class III surface [78], which difficulties their simulation. In order to balance the total system dipole, the system needs two equal and opposite surfaces canceling its dipoles, breaking the stoichiometry of the system.

Microcrystal cubic habits of Cu_2O and cubic nanoparticles of Cu_2O presents $Cu_2O(001)$ surfaces [140–142], therefore the presence of this surface and its formation into interfaces with MAPI is a possibility, mainly if Cu_2O layers are synthesized by nanoparticle deposition.

Different studies on $Cu_2O(100)$ surface have been made [104, 105, 135, 137–139] showing that copper and oxygen surface terminations are possible. Terminations depends strongly on the sample preparation conditions, *e.g.*, temperature, annealing time and controlling gaseous oxygen pressure from poor, near zero, to rich conditions. Also, defects are present at the surface. Surface defects do not originate from bulk defects, where the most common is the copper vacancy. Most prevalent surface defect is an oxygen vacancy producing two separated rows of oxygen atoms at the surface, and introduce electronic states in the band gap, which play an important role in surface reactivity. $Cu_2O(100)$ surface structure determination has shown a greater difficulty of study with respect to other surface indices.

1.4.3 $CH_3NH_3PbI_3$–Based Solar Cells with Cu_2O as Hole Transport Material

Experimental HOIHP–based solar cells with CuO, Cu_2O or CuO_x as HTM have been reported [142–151], with a maximum PCE of 17 %, as well as improved stability with respect to control solar cells that used spiro–OMeTAD. Nitrogen doped Cu_2O has been proposed for tunnel recombination junction on tandem Si/HOIHP–based solar cells [152], as well as for single junction cells [153]. Improved 19 % PCE has been achieved by the combination $CuO_x/MAPbI_{3-y}Cl_y$ [154]. Liu *et al.* [141] achieved a high 18.9 % efficiency using Cu_2O nanocubes deposited from solution on a mixed perovskite $Cs_{0.05}FA_{0.81}MA_{0.14}PbI_{2.55}Br_{0.45}$. Other interesting realization has been the use of Cu_2O as HTM with a buffer layer of spiro–OMeTAD [153, 155, 156], leading to champion PCE over 17 %. Reviews of the experimental achievements using copper oxides and other copper based compound HTMs can be found elsewhere [157, 158]. Device simulations [130, 159–163] predict different efficiencies for MAPI solar cells using Cu_2O as HTM, the most optimistic value of which is 28 %. Despite these perspectives, the development of Cu_2O/perovskite solar cells has not yet boosted. We think that one difficulty relies in the control of interface properties.

Device simulations predict record efficiencies using this semiconductor, but experimental results do not yet show this trend. More detailed knowledge about the Cu_2O/perovskite interface is mandatory to improve the PCE. We shall explore several routes to increase the PCE of HOIHP–based solar cells. Optimizing interfaces is one of the critical tasks that has a direct effect on the performance of solar cells [63]. Characterization of Cu_2O/perovskite interfaces is absent in the still brief literature about this topic.

1.5 Hypothesis and Objectives

Atomic–scale calculations using DFT allow the study of band structure and energy levels of $CH_3NH_3PbI_3$ and Cu_2O materials, as well as the study of the interface between them.

Knowledge of the band alignment with respect to vacuum level and the relative band alignment between both materials is necessary to validate the viability of using Cu_2O as a HTM in perovskites solar cells. Moreover, we intend to determine which surface types are convenient in the junction zone. This will provide information about the necessary conditions to produce favorable interfaces to increase the photo–conversion efficiency of this type of solar cell.

The main objective of this work is evaluate the band alignment between the $CH_3NH_3PbI_3$ as light absorber material and Cu_2O as hole transport material, using different surfaces of them. The aim of these studies are contribute to the knowledge of this type of solar cells and materials, and provide information about its band alignment for the production of more efficient solar cells. Throughout this work the next specific objectives are addressed:

1. To carry out a convergence study of the calculation parameters for the different bulk materials, as well as for slab–type systems.
2. To optimize the bulk structures of both materials and obtain their band structure and electronic alignment at different levels of theory.
3. To optimize slab–type systems of both materials for different surface types, perform its band alignment against vacuum and the comparison between materials.
4. To generate the explicit interface between both materials for surfaces that allow epitaxial growth and present an optimal band alignment.

Chapter 2

Electronic Structure Calculations

Contents

The concept "Electronic Structure" is a polymorphic expression, because it covers a wide range of electronic properties of matter. As an example, it can refer to the electronic density (number of electrons at space point $\mathbf{r}$); to the energy needed/gain to extract/add an electron to the system, this is ionization–potential/electronic–affinity; among many others. These properties characterize the electronic structure of matter in different aspects and states. Electronic properties are of a wide variety, being either ground–state or excited–states properties, conserved/non–conserved particle quantity, among others. They can be experimentally measured, *e.g.*, by direct and inverse photoemission spectroscopy, optical absorption spectroscopy, electron energy loss spectroscopy, electrochemistry, etc. In parallel, they can be calculated or predicted from a theoretical description in distinct frameworks (known as *ab initio* or First Principle Methods). The latter will be the way to study our systems, and gives the name to this chapter: Electronic Structure Calculations.

2.1 General Glance to Schrödinger Equation

The description of mutually interacting electrons and nuclei in matter is a colossal task. The Schrödinger equation is the famous non–relativistic motion equation for particles (electrons and/or nuclei) in Quantum Mechanics, known for decades. Atoms, molecules, clusters, surfaces and extended solids could be, in principle, solved in the same way using the Schrödinger equation. The Hamiltonian for a generalized polyatomic and polyelectronic system is

$$\mathscr{H} = \sum_{i}^{N} -\frac{\hbar^2\nabla_i^2}{2m_e} + \sum_{I}^{M} -\frac{\hbar^2\nabla_I^2}{2M_I} + \frac{1}{2}\sum_{i\neq j}^{N} \frac{k_e e^2}{|\mathbf{r}_i - \mathbf{r}_j|} + \frac{1}{2}\sum_{I\neq J}^{M} \frac{k_e Z_I Z_J e^2}{|\mathbf{R}_I - \mathbf{R}_J|} - \sum_{i,I}^{N,M} \frac{k_e Z_I e^2}{|\mathbf{r}_i - \mathbf{R}_I|} \qquad (2.1)$$

where the index i runs over N electrons and I runs over M nuclei. The terms, in order, are: kinetic energy operator for electrons and nuclei, instantaneous spin–independent interaction between electron–electron, nuclei–nuclei and electron–nuclei pairs through the Coulomb potential. The relativistic correction terms (spin–dependent as SOC, and others) will be included only when necessary. The index exclusion in the summation is to avoid the self–interaction terms, and the double counting is corrected with 1/2 factor. We will introduce the atomic units henceforth to simplify the expressions, that is: $\hbar = e = m_e = k_e = 1$, thus the atomic units (a.u.) for lengths, energy and mass will be Bohr radius, Hartree and electron mass, respectively.

To obtain the stationary states for this Hamiltonian, it is necessary to solve the Schrödinger equation in the time–independent approach. First, we need to diagonalize the secular determinant to obtain the energies, and subsequently solve secular equation to obtain the solution or wavefunction to each energy. We said before, *"could be, in principle, solved"*, because the wavefunctions, $\Psi(\{\mathbf{r}_i\}, \{\mathbf{R}_I\})$, are dependent of all nuclei coordinates ($\{\mathbf{R}_I\} = \mathbf{R}_1,\ldots,\mathbf{R}_M$) and all–electron coordinates ($\{\mathbf{r}_i\} = \mathbf{r}_1,\ldots,\mathbf{r}_N$). This Hamiltonian is a $(N + M)$–particle problem with an exceptionally complicated "solution".
Moreover, when $N+M \geq 3$, there are not an analytical solution due to the three–body problem. This is the case of simplest He or H_2^+ systems. This is more complex in molecules, clusters and much more in a periodic crystal with $\sim N_A$ particles.

There are only a few systems where an analytical solution exists to Schrödinger equation, some of these are: hydrogen atom, harmonic oscillator, decoupled harmonic oscillators, Morse oscillator, rigid rotor, infinite potential well, periodic hydrogen chain and non–interacting electrons in an atom. Several of these are ideal systems or approximated systems to reality.

This is an issue, because interesting systems to study are not directly solvable, therefore we need to do some simplifications and approximations to solve it. In the following sections we will present these different approaches.

2.2 Born–Oppenheimer Approximation: Electronic Hamiltonian

The Born–Oppenheimer approximation [164], a particular case of adiabatic approximation, is fundamental in the atomistic description of matter for, it enables decoupling the nuclear and electronic movements, and makes the problem soluble, generating the classical concept of *nuclear configuration*. It is an approximation since it assumes some particular conditions that we will review. The starting point is an evident fact: the mass ratio between the nuclei and the electron is large. Particularly, the smallest mass ratio is in the case of Hydrogen nuclei and the electron, with a value around 1836.

This situation leads to suppose that electrons move much faster than the nuclei. In other words, electrons are in a stationary state of the instantaneous field of fixed nuclei, or analogously, the nuclei move slowly in a distribution of the electron cloud that adapts instantaneously to the changes of the nuclear coordinates. This allows to neglect the nuclear kinetic energy term (assuming it as a perturbation to the system), and have a constant nuclear repulsion term. The problem is simplified in two steps. The first step is generate a new Hamiltonian with $\{\mathbf{r}_i\}$ as variables and $\{\mathbf{R}_I\}$ as parameters, the electronic Hamiltonian, plus the constant nuclear repulsion term. Since constant terms added to an operator only adds to the operator eigenvalues and has no effect on the operator eigenfunctions, then the solutions are electronic wavefunctions of the electronic Hamiltonian, and depends parametrically on the nuclei coordinates. In other words, there is a complete set of electronic wavefunction, electronic energy and nuclear repulsion for each nuclei arrangement [165, Chapter 2]. That is

$$\mathscr{H}_{ele} = \sum_{i}^{N} -\frac{\nabla_i^2}{2} + \frac{1}{2}\sum_{i\neq j}^{N} \frac{1}{|\mathbf{r}_i - \mathbf{r}_j|} - \sum_{i,I}^{N,M} \frac{Z_I}{|\mathbf{r}_i - \mathbf{R}_I|} \qquad \text{and} \qquad \mathscr{V}_{NN} = \frac{1}{2}\sum_{I\neq J}^{M} \frac{Z_I Z_J}{|\mathbf{R}_I - \mathbf{R}_J|} \tag{2.2}$$

where the time–independent Schrödinger equation and its solutions are

$$\mathscr{H}_{ele}\psi(\{\mathbf{r}_i\};\{\mathbf{R}_I\}) = \mathscr{E}_{ele}\psi(\{\mathbf{r}_i\};\{\mathbf{R}_I\}) \qquad \text{with} \qquad \mathscr{E}_{ele} = \mathscr{E}_{ele}(\{\mathbf{R}_I\}) \tag{2.3}$$

and the total energy in the Born–Oppenheimer approximation is $\mathscr{E}_{tot} = \mathscr{E}_{ele} + \mathscr{V}_{NN}$.

As $\mathscr{E}_{ele}$ and $\mathscr{V}_{NN}$ are parametric terms of nuclei coordinates, then $\mathscr{E}_{tot} = \mathscr{E}_{tot}(\{\mathbf{R}_I\})$, as shows Fig. 2.1(A). This quantity is the potential energy surface for nuclear motion, with this we can explore a nuclear Hamiltonian to complete the picture in the second step.

Using Eq. 2.1 and 2.2, the nuclear Hamiltonian is building on the basis of electronic terms (electronic Hamiltonian) and nuclei–nuclei repulsion are the potential energy surface in the Hamiltonian for nuclear motion, yields

$$\mathscr{H}_{nuc} = \sum_{I}^{M} -\frac{\nabla_I^2}{2M_I} + \left\langle \sum_{i}^{N} -\frac{\nabla_i^2}{2} + \frac{1}{2}\sum_{i\neq j}^{N} \frac{1}{|\mathbf{r}_i - \mathbf{r}_j|} - \sum_{i,I}^{N,M} \frac{Z_I}{|\mathbf{r}_i - \mathbf{R}_I|} \right\rangle + \mathscr{V}_{NN}$$

$$\mathscr{H}_{nuc} = \sum_{I}^{M} -\frac{\nabla_I^2}{2M_I} + \langle \mathscr{H}_{ele} \rangle + \mathscr{V}_{NN} = \sum_{I}^{M} -\frac{\nabla_I^2}{2M_I} + \mathscr{E}_{tot}(\{\mathbf{R}_I\}) \tag{2.4}$$

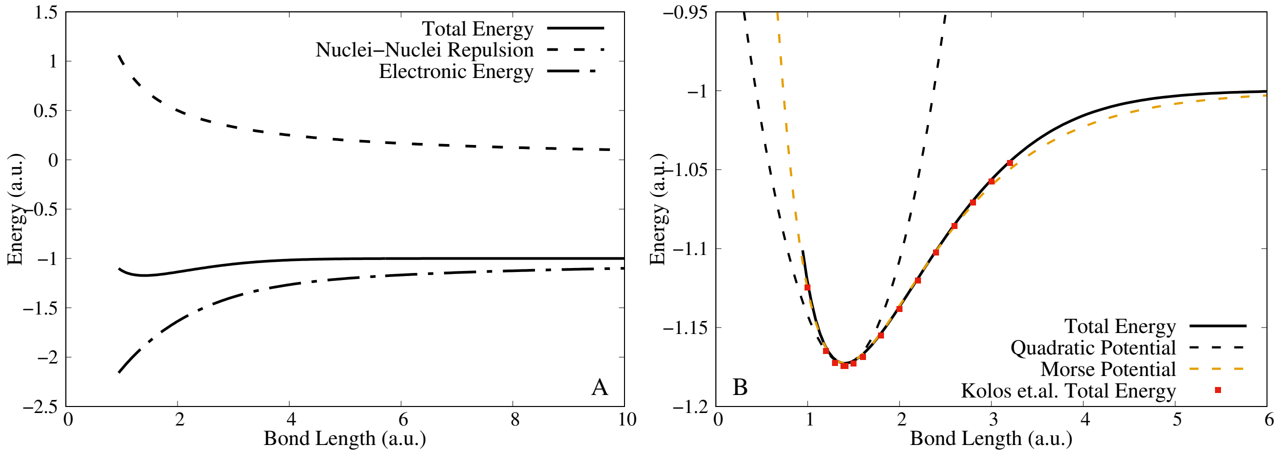

Figure 2.1: H_2 potential energy surface, at fullCI/aug–cc–pVTZ level of theory, as a function of bond length. (A) shows the decomposition of $\mathscr{E}_{tot}$. (B) shows the quadratic and Morse potential approximation, and energies from Kolos *et al.* [166].

If the expression for $\mathscr{E}_{tot}(\{\mathbf{R}_I\})$ is known, then the time–independent Schrödinger equation can be solved for $\mathscr{H}_{nuc}$, where the eigenfunctions are the nuclear wavefunctions and the energies are the nuclear energy (vibrations, rotations and translations) plus total energy (electronic plus nuclei–nuclei repulsion), namely

$$\mathscr{H}_{nuc}\chi(\{\mathbf{R}_I\}) = \mathscr{E}_{BO}\chi(\{\mathbf{R}_I\}) \qquad \text{with} \qquad \mathscr{E}_{BO} = \mathscr{E}_{nuc} + \mathscr{E}_{tot} \tag{2.5}$$

Finally, as the nuclei and electron are decoupled, the total wavefunction is a product of nuclear and electronic wavefunctions: $\Psi(\{\mathbf{r}_i\}, \{\mathbf{R}_I\}) = \chi(\{\mathbf{R}_I\})\psi(\{\mathbf{r}_i\}; \{\mathbf{R}_I\})$.

Unfortunately, there is not a generalized analytical expression for $\mathscr{E}_{tot}(\{\mathbf{R}_I\})$, even for diatomic systems. Some approximated expressions could be used as an approach, such as quadratic potential (harmonic oscillator) or Morse potential (anharmonic oscillator).
The first is the simplest potential and a very good approximation for stationary points on the potential energy surface (see Fig. 2.1(B)). Technically it is a second order Taylor series, where the first derivatives are zero (stationary point) and the Hessian (second derivative matrix) is diagonal in normal coordinates for *nuclear configuration* $(\{\mathbf{Q}_I\})$

$$\mathscr{E}_{tot} \approx \mathscr{E}_0 + \frac{1}{2}\sum_{I}^{M}\left(\frac{\partial^2\mathscr{E}_{tot}}{\partial\mathbf{Q}_I^2}\right)_{\mathscr{E}_0}(\mathbf{Q}_{I,e} - \mathbf{Q}_I)^2 \qquad \text{with} \qquad \left(\frac{\partial^2\mathscr{E}_{tot}}{\partial\mathbf{Q}_I^2}\right)_{\mathscr{E}_0} = k_I = \mu_I\omega_I^2 \tag{2.6}$$

where $\mathbf{Q}_{I,e}$, k_I, μ_I, ω_I are the equilibrium normal coordinate, oscillator constant, reduced mass and vibrational angular frequency for I^{th} oscillator, respectively, and $\mathscr{E}_0$ is the total energy at the stationary point, $\mathscr{E}_0 = \mathscr{E}_{tot}(\{\mathbf{Q}_{I,e}\})$. Second derivatives can be calculated analytically or numerically.
In a similar fashion, nuclear kinetic energy operator can be written in terms of $\{\mathbf{Q}_I\}$. This leads to M decoupled equations of harmonic oscillators. In molecular systems there are three normal modes for translations and two or three (linear or non–linear geometries) for rotations, with null oscillator constants. The infinite potential well and the pseudo–classical rigid rotor could be used for these modes to obtain statistical thermodynamic information. The $\chi(\{\mathbf{R}_I\})$ is a product of translation, rotation and vibration wavefunctions, $\chi(\{\mathbf{R}_I\}) = \chi_{tra}(\{\mathbf{Q}_I\})\chi_{rot}(\{\mathbf{Q}_I\})\chi_{vib}(\{\mathbf{Q}_I\})$,

and the nuclear energy is the summation of each component, $\mathscr{E}_{nuc} = \mathscr{E}_{tra} + \mathscr{E}_{rot} + \mathscr{E}_{vib}$.
For each non–zero oscillator constant modes, the solution of time–independent Schrödinger equation is one Harmonic wavefunction, and a Harmonic vibration energy. Replacing the nuclei kinetic energy operator in $\{\mathbf{Q}_I\}$ and Eq. 2.6 into Eq. 2.4, gives

$$\mathscr{H}_{vib} = \sum_I^M -\frac{\nabla_I^2}{2\mu_I} + \sum_I^M \frac{\mu_I \omega_I^2}{2}(\mathbf{Q}_{I,e} - \mathbf{Q}_I)^2 + \mathscr{E}_0 \qquad \text{and} \qquad \mathscr{H}_{vib}\chi_{vib}(\{\mathbf{Q}_I\}) = (\mathscr{E}_{vib} + \mathscr{E}_0)\,\chi_{vib}(\{\mathbf{Q}_I\})$$

$$\mathscr{E}_{vib} = \sum_I^M \hbar\omega_I \left(n_I + \frac{1}{2}\right) \qquad \text{and finally} \qquad \mathscr{E}_{ZPE} = \sum_I^M \frac{\hbar\omega_I}{2} \tag{2.7}$$

where n_I is the quantum vibrational number ($n_I = 0, 1, 2, \dots$) of I^{th} vibrational state. $\mathscr{E}_{ZPE}$ is the Zero–Point Energy (ZPE), or the residual vibrational energy, when all $n_I = 0$. Then, at zero kelvin (no thermal contribution), $\mathscr{E}_{BO} = \mathscr{E}_{ZPE} + \mathscr{E}_0$. In the dissociation process is important to use $\mathscr{E}_{BO}$ instead of $\mathscr{E}_0$. Concluding this approach, it is important to mention that the values of ω_I give important information of the stationary points. If all values are positive, a minimum energy point is found. If all minus one is positive (*i.e.*, one value is imaginary), a first order saddle point is found (if two values are imaginary, it is a second order saddle point, and so on). The first order saddle points are important, because they connect two or more minimum energy points, and are associated with transition states structures.

The quantitative procedure to prove the Born–Oppenheimer Approximation is complicated, and is explained in some books [167, Chapter 12] [168, Chapter 2]. Just some conditions and problems will be discussed.
The proposition of fixed nuclei and constant nuclear potential is a zero order Taylor series (in $\{\mathbf{Q}_I\}$) for the full nuclei–nuclei and electron–nuclei Coulomb potential. If higher order terms are considered to solve the nuclear Hamiltonian, $\mathscr{E}_{tot}$ must be corrected by vibronic interaction terms, that couples different electronic states. The total wavefunction is a summation of different products of nuclear and electronic wavefunctions: $\Psi(\{\mathbf{r}_i\}, \{\mathbf{R}_I\}) = \sum_j c_j \chi_j(\{\mathbf{R}_I\})\psi_j(\{\mathbf{r}_i\}; \{\mathbf{R}_I\})$, this is the Adiabatic Approximation. This terms can be neglected only in the absence of electronic degeneracy or pseudo–degeneracy (when the electronic energy difference between different states is in the order of vibrational transition energy). This is when the vibrational states are localized mainly in one electronic state, and they do not oscillate between two or more states mixing their wavefunctions. Moreover, if the full Taylor series is used to solve the electronic Hamiltonian, non–adiabatic terms appear. Now the electronic wavefunctions are explicit functions of $\{\mathbf{R}_I\}$, being affected by the nuclear kinetic energy operator.

Born–Oppenheimer approximation solve nuclei–nuclei and electron–nuclei interaction, but the electron–electron interaction in the electronic Hamiltonian remains a problematic term without exact solution. In other words, the one $(N + M)$–particle problem is reduced to one N–electron problem for each *nuclear configuration*. Now there are analytical solutions for one–electron plus M–nuclei systems, as is for H_2^+ systems.
Also the classical concept, *nuclear configuration*, allows the nuclei positions to temporarily evolve in a classical trajectory, as in classical Molecular Dynamics (MD). In *Ab Initio* MD approach (AIMD), the forces are calculated solving quantum mechanical equations. Particularly, Born–Oppenheimer MD (BOMD) solves the electronic Hamiltonian for each *nuclear configuration*. In both cases the quantum behaviour of nuclei is neglected and Zero–Point effects are not present.

2.3 N–electron problem: Many–Body Electron Theory

When the electronic system has two or more electrons, it is necessary to make more approximations due to the electron–electron interaction terms, in the electronic Hamiltonian, which do not allow exact solutions. These different approximations are called many–body electron theories, and they are necessary to face the problem to predict the electronic structure (ground–, but also, excited–states) of many–body electronic systems, such as atoms, molecules and condensed phases (liquids or solids), and investigate their properties, minimum energy structures, among others.

Many–body electron theories transform the N–electron problem, in the electronic Hamiltonian, into N one–electron problems, approximating electron–electron Coulomb interaction by means of a mean–field electronic potential approximation, also known as one–particle approximation [169–171]. Direct consequences of this approximation are: require an iterative procedure to find the solution of the coupled and non–linear N one–electron problems simultaneously, known as Self–Consistent Field procedure (SCF), which provide an orthonormal set of one–electron wavefunctions $\varphi_j(\mathbf{r}\sigma)$, also called spin–orbitals, and one–electron energy eigenvalues ϵ_j.
Electronic correlation, which contains the many–body electron effects, is not included in principle due to the use of a mean–field electronic potential, therefore it has to be recovered somehow. Those different approaches to recover the electronic correlation (spatial– and spin–correlation) are diverse, and are split into two main families: Wavefunction theories and Density Functional Theory.

Wavefunction based methods are Hartree–Fock (HF) [169, 170], Post–HF such as Møller–Plesset Perturbation Theory and Coupled Cluster, Multi–Configurational and Complete Active Space SCF, GW approximation, among others. Electronic density based method are the so–called Density Functional Theory (DFT) [172], which is applied through Kohn–Sham (KS) system (KS–DFT) [171] and different exchange–correlation functionals, also called KS–DFT.

In this research we have made extensive use of KS–DFT due to its equilibrium between accuracy and computational cost to deal with condensed phase periodic systems. Also we employ hybrid functionals, which is a type of "mixture" between KS–DFT and HF methods [165, 173]. Consequently, we will review both approaches and their characteristics. Before to start, we introduce the SOC term, which is necessary to describe the $CH_3NH_3PbI_3$ perovskite electronic structure.
SOC is a relativistic correction term, which adds an additional term to the electronic Hamiltonian that couples the Pauli spin operator $\vec{\sigma}$ (electronic spin operator $\vec{S}$) with the orbital angular momentum operator $\vec{L} = \vec{r} \times \vec{p}$ of electron. Its on–site approximation is: $\mathscr{H}_{SOC} \propto \vec{L} \cdot \vec{\sigma} \propto \vec{L} \cdot \vec{S}$. This term can be included as a first order perturbation or self–consistently into the SCF equations [44]. Since $\mathscr{H}_{SOC}$ is not diagonal in the spin–orbital basis set (collinear case), the basis set has to be transformed when SOC is included. The resulting basis set is no more an eigenfunction of electronic spin operator, but is an eigenfunction of the total electronic angular momentum operator $\vec{J}$ (non–collinear case), defined as: $\vec{J} = \vec{L} + \vec{S}$. Then the $\mathscr{H}_{SOC}$ can be rewritten using the relation $\vec{L} \cdot \vec{S} = \frac{1}{2}(\vec{J}^2 - \vec{L}^2 - \vec{S}^2)$.
In our research, when SOC is used, we include it self–consistently. Its effects becomes non–

negligible for elements with heavy nuclei, as is for iodine (I), and more important for lead (Pb).

2.3.1 Hartree–Fock Theory

Hartree theory [170] try to represent the N–electron (all–electron) wavefunction $\psi(\{\mathbf{r}_i\};\{\mathbf{R}_I\})$ as the best product (which minimize the system energy using variational principle) of N occupied one–electron wavefunction set $\varphi_j(\mathbf{r}\sigma)$, also called Hartree product. Here, the spin only plays a practical role just allowing to two electrons use the same spatial one–electron wavefunction if they have opposite spins.
Using this construction for the N–electron wavefunction, the properties and quantities of the system can be obtained, such as total electronic charge density

$$\rho(\mathbf{r}) = \sum_{j}^{N} |\varphi_j(\mathbf{r}\sigma)|^2 \tag{2.8}$$

The mean–field electronic potential (also called Hartree potential) approximates electron–electron Coulomb interaction, is constructed by all occupied one–electron wavefunctions of the system which are in fact the total electronic charge density. Then each electron moves in an effective–field formed by the charge distribution of electrons

$$\upsilon_h(\mathbf{r}) = \sum_{j}^{N} \int \frac{|\varphi_j(\mathbf{r}'\sigma')|^2}{|\mathbf{r}-\mathbf{r}'|}\, d\mathbf{r}' = \int \frac{\rho(\mathbf{r}')}{|\mathbf{r}-\mathbf{r}'|}\, d\mathbf{r}' \tag{2.9}$$

With this definition each electron interacts with itself, including a non–physical and spurious interaction, called Self–Interaction Error (SIE). It can be removed by rewriting Eq. 2.9 with $j \neq i$, been i the interacting electron with the potential. In this case the Hartree potential cannot be defined with the total electronic charge density.
Although, the most important issue is that Hartree product does not have the correct anti–symmetry character when two spatial–spin electron coordinates are interchanged, violating the Pauli principle, and making electron in the system distinguishable among them. Moreover, the Hartree theory does not recover electronic correlation at all, neither spatial– nor spin–correlation. Therefore, the results cannot be analyzed quantitatively, and the total energy error is usually too large, for example it cannot differentiate singlet and triplet states in terms of energy. This points made Hartree theory just an historical topic.

To solve these issues, Fock [169] proposed an approach where the all–electron wavefunction $\psi(\{\mathbf{r}_i\};\{\mathbf{R}_I\})$ is represented as a normalized linear combination of Hartree products of all possible two spatial–spin electron interchanged coordinates between one–electron wavefunctions, also called Slater determinant. This approach, Hartree–Fock theory (HF), fulfills the Pauli principle. It makes the wavefunction anti–symmetric and the electrons indistinguishable (identical) among them. Also, as it is a matrix determinant, if two electrons have the same spatial–spin coordinates (the same spin–orbital) the all–electron wavefunction turns zero, incorporating the spin–occupation rules naturally.
Most one–electron properties can be computed similarly to Hartree theory, such as total electronic charge density using Eq. 2.8. The main change into equations when the Slater determinant

is considered is the emergence of a new term in the mean–field electronic potential added to the Hartree potential. This new interacting term is called Fock exchange operator, it is a spin–dependent term which introduce electronic correlation only for electrons with the same spin, also called exchange (spin–correlation). Fock exchange operator $\Sigma_x(\mathbf{r}\sigma,\ \mathbf{r'}\sigma')$ is a non–local potential constructed similarly as Hartree potential, but interchanging spatial–spin coordinates of two one–electron wavefunctions, namely

$$\Sigma_x(\mathbf{r}\sigma, \mathbf{r}'\sigma')\varphi_i(\mathbf{r}\sigma) = -\sum_j^N \int \frac{\varphi_j^*(\mathbf{r}'\sigma')\varphi_i(\mathbf{r}'\sigma')}{|\mathbf{r}-\mathbf{r}'|}\varphi_j(\mathbf{r}\sigma)\ d\mathbf{r}' \tag{2.10}$$

This term introduces an energy correction for the mean–field interaction of same–spin electrons, giving lower total electronic energies for same–spin electron pairs with respect to different–spin electron pairs, enabling to differentiate singlet and triplet states.
An interesting point of Fock approach is related with the SIE, because the self–interaction through Hartree potential, is equal as the self–interaction through Fock exchange operator, they are the same quantity but with opposite sign. In fact they are the same term just with different sign, for example for the i^{th} electron

$$\upsilon_{h,(i)}(\mathbf{r})\varphi_i(\mathbf{r}\sigma) = \int \frac{\varphi_i^*(\mathbf{r}'\sigma')\varphi_i(\mathbf{r}'\sigma')}{|\mathbf{r}-\mathbf{r}'|}\varphi_i(\mathbf{r}\sigma)\ d\mathbf{r}' = -\Sigma_{x,(i)}(\mathbf{r}\sigma, \mathbf{r}'\sigma')\varphi_i(\mathbf{r}\sigma) \tag{2.11}$$

therefore, HF theory is free of SIE by construction and for this reason Fock exchange operator is also called exact exchange.

Finally, the one–electron problem can be written as a Schrödinger–like equation for the set of one–electron wavefunctions. This is the HF theory equation

$$\left[\frac{-\nabla_i^2}{2} + \upsilon_{ext}(\mathbf{r}) + \upsilon_h(\mathbf{r}) + \Sigma_x(\mathbf{r}\sigma, \mathbf{r}'\sigma')\right]\varphi_i(\mathbf{r}\sigma) = F\varphi_i(\mathbf{r}\sigma) = \epsilon_i\varphi_i(\mathbf{r}\sigma) \tag{2.12}$$

where $\upsilon_{ext}(\mathbf{r})$ represent the Coulomb potential of nuclei, also called external potential due to it depends only on the *nuclear configuration*, and F is the one–electron HF Hamiltonian.
This one–electron equation have to be solved simultaneously for the N one–electron occupied wavefunctions (or more, in order to obtain unoccupied one–electron wavefunctions). As they conform a coupled and non–lineal equation set, they have to be solved iteratively through a SCF approach, *i.e.*, until the set of occupied one–electron wavefunctions which generates the HF potential (Hartree potential and Fock exchange potential) is equal (minimal differences) to the produced set of occupied one–electron wavefunctions. When the latter happens, is said the equations and wavefunctions converged. The SCF convergence criteria is different between programs, ranging from minimal changes in the total electronic energy, minimal changes in the one–electron wavefunctions and/or minimal changes in the total electron charge density.
The way how this equations are solved is based on Lagrange's method of undetermined multipliers, the latter correspond to the set of energy eigenvalues ϵ_i due to the restriction of one–electron wavefunctions to be orthonormal among them. Lagrange's method minimum correspond to the minimum of the total electronic energy of the system, returning the best one–electron wavefunction set for the desired state (usually ground–state), approximated by a single Slater determinant.

The i^{th} one–electron wavefunction may or may not have the same spatial distribution for both spin–values. When the equivalence between them is mandated, is said to be a restricted calculation (RHF). Meanwhile, when the equivalence between them is not mandated is said to be a unrestricted calculation (UHF). This framework is used in the same way in KS–DFT, listed as RKS and UKS, respectively. Typically RHF calculations are used when an even number of electron is equally distributed for both spin–values, because for both spins the effective–potential is the same and spatial solution must be the same. Cases with odd number of electrons or even number of electrons unequally spin distributed, have different effective–potentials for each spin–value, due to the spin–dependent Fock exchange operator. Then the spatial solutions of one–electron wavefunctions with opposite spins will be different. This also produce two different energy eigenvalue sets for each spin–values.

Ground–state total electronic energy in HF theory (as in other many–body electron theories) is not simply the sum of N lowest occupied one–electron energy eigenvalues. If we consider just the sum, a double counting of interelectronic interaction terms would be considered (non–physical situation). Therefore, total electronic energy have to be constructed as the sum of all interaction terms separately without double counting, or as the sum of N lowest occupied one–electron energy eigenvalues minus the double counted interelectronic interaction terms.

One–electron energy eigenvalues have a physical interpretation because they are quasiparticle energy levels. The N lowest one–electron energy eigenvalues are the occupied states (ground–state), and their values refer to the binding energy of an electron in this energy state with the whole system that is, the energy needed to remove an electron from this state to a free particle state. The energy of the highest occupied state is the negative of ionization potential (IP). Conversely, one–electron energy eigenvalues higher than the first lowest N are the unoccupied (virtual) states, and refers to the needed energy to insert a free electron with no kinetic energy to the system in this energy state, *i.e.*, the negative of Electron Affinity (EA). The later is known as the Koopman's theorem, which is in principle exact (if the spatial–correlation of electron were considered), with the only error of not considering the orbital relaxation of the new electronic distribution when losing or capturing an electron.
Also this one–electron energy eigenvalues can be used to approximate the transition energy from ground–state to excited–states. It is just an approximation because it does not consider the Coulomb hole (correlation) and Fermi hole (exchange) generated by the electronic excitation.

In summary, HF theory gives the best variational wavefunction, written as a single Slater determinant for the all–electronic system. The main drawback is that it does not consider at all the spatial electronic correlation, strongly affecting the results and making them unreliable, if spatial–correlation is not included somehow. As the Slater determinants formed by a particular basis sets are orthonormal between them, it is reasonable to approximate the true all–electron wavefunction as a linear combination of Slater determinants (maybe millions of them).
This is the basic idea of Post–HF theories (such as Møller–Plesset Perturbation Theory and Coupled Cluster) and Multi–Configurational/Complete–Active–Space SCF, which recover most part of the spatial–correlation, reaching chemical accuracy. Unfortunately, for condensed phase systems it is complex and computational expensive use this type of methods.
A related approach to recover the electronic correlation in condensed phase systems is by means of GW approximation of Hedin's Equations [174]. It is also a single Slater determinant method, but uses a self–screened electronic potential through energy–dependent dielectric function of the medium, making the potential short ranged (non–static). If the screening is avoided, the Hartree–Fock Theory appears, then GW approximation is a screened version of HF, and by

means of the screening, the electronic correlation energy is recovered. This in principle ensures better results, and Koopman's theorem still applies. This approach can be used self–consistently [114] or perturbatively (G_0W_0) using HF or DFT one–electron wavefunction and eigenvalues sets as reference [175].

2.3.2 Density Functional Theory

Density Functional Theory (DFT) is an extremely successful approach, it uses the total electronic charge density $\rho(\mathbf{r})$ as the object of interest to solve the many–body electron problem, switching from the multidimensional all–electron wavefunction to the simple and 3–D $\rho(\mathbf{r})$ function.

DFT shows that the ground–state of a N–electronic system (energy and properties) can be described entirely in terms of its ground–state $\rho(\mathbf{r})$, bypassing the need to know the N–electron wavefunction. Hohenberg–Kohn theorem [172] demonstrates this approach, proving that for a non–degenerated ground–state all–electronic system at a particular *nuclear configuration* (fixed external potential $\upsilon_{ext}(\mathbf{r})$) there is a one–to–one correspondence between the ground–state $\rho(\mathbf{r})$ and the external potential acting on it, so external potential defines a unique $\rho(\mathbf{r})$ for the electronic system and it becomes the function of interest.
The main consequence of the one–to–one correspondence is the existence of a universal functional of the $\rho(\mathbf{r})$ to describe the energy of the system. Then, knowing the external potential of a particular *nuclear configuration* and the Hohenberg–Kohn universal functional, the picture is complete to describe the ground–state energy only with $\rho(\mathbf{r})$. Moreover, the procedure can be carried out in the opposite direction starting from a known $\rho(\mathbf{r})$ and using the Kato's cusp condition, then there is only one possible external potential related to it.
Also, Hohenberg–Kohn theorem shows that the variational principle can be used in conjunction with the external potential and the universal functional, starting from a guess $\rho(\mathbf{r})$, to minimize the ground–state electronic energy, as well as the exact ground–state $\rho_0(\mathbf{r})$.

Energy in DFT is a functional of $\rho(\mathbf{r})$, $E[\rho(\mathbf{r})]$, described by the sum of universal functional $F[\rho(\mathbf{r})]$ and the interaction of $\rho(\mathbf{r})$ with the external potential

$$E[\rho(\mathbf{r})] = F[\rho(\mathbf{r})] + \int \upsilon_{ext}(\mathbf{r})\rho(\mathbf{r})\ d\mathbf{r}\ . \tag{2.13}$$

The universal functional $F[\rho(\mathbf{r})]$ contains energetic terms that only consider the electrons, *i.e.*, the kinetic energy $T[\rho(\mathbf{r})]$ and the electron–electron Coulomb repulsion energy $E_{ee}[\rho(\mathbf{r})]$ of the electronic system in terms of the $\rho(\mathbf{r})$

$$F[\rho(\mathbf{r})] = T[\rho(\mathbf{r})] + E_{ee}[\rho(\mathbf{r})] = T[\rho(\mathbf{r})] + E_h[\rho(\mathbf{r})] + E_{xc}[\rho(\mathbf{r})]\ . \tag{2.14}$$

$E_{ee}[\rho(\mathbf{r})]$ can be expressed in terms of the Hartree potential energy $E_h[\rho(\mathbf{r})]$ (obtained by spatial integration of the product between $\upsilon_h(\mathbf{r})$ and $\rho(\mathbf{r})$) and the exchange–correlation energy term E_{xc}. The exact functional form of the exchange–correlation term is unknown, but it can be approximated with good accuracy using different approaches known as Density Functional Approximations, as explained below.
The main drawback of DFT is the kinetic energy term of the electronic system, because there

is no guess of how it can be obtained as a density functional. Many approaches and attempts were made along the years to approximate it, such as Thomas–Fermi and von Weizsäcker kinetic energy functionals, among others, but they does not approximate the kinetic energy with the required accuracy. For example, Thomas–Fermi kinetic energy functional approximates precisely the kinetic energy in the limit of $Z \rightarrow \infty$. Meanwhile, von Weizsäcker kinetic energy functional is exact only for a "Bosonic behaved" electronic system, such as Helium atom. Linear combination between both functionals or the addition of "Fermionic corrector" potentials to ensure a "Fermionic behaved" electronic distribution when von Weizsäcker kinetic energy functional is used, have failed to succeed.
This problem is related with high accuracy needed for kinetic energy approximation. As Virial theorem states, when the potential energy of the problem is proportional to the first power of the interparticle distance, the total energy and kinetic energy of the system have the same absolute value. Then a 1 % error in kinetic energy is a 1 % error in total energy, a huge quantity to allow describing chemical processes.

Hohenberg-Kohn theorem proves the existence of the universal and exact functional, but not its form. Then *a priori* its exact form is not know, making it an still open problem.

2.3.3 Kohn–Sham Electronic System

Kohn and Sham in 1965 [171] devised an approach to bypass the problem of the kinetic energy functional. This approach has its key point in the assumption of kinetic energy can be approximated as HF does, *i.e.*, computing it by means of one–electron wavefunctions. To achieve this, it is assumed that for each non–uniform ground–state $\rho(\mathbf{r})$ of an interacting electronic system, there exist a non–interacting electronic system with the same non–uniform ground–state $\rho(\mathbf{r})$. Then, a non–interacting electronic system (KS electronic system) is used as an auxiliary system to compute the kinetic energy term, meanwhile all other term (potential energy terms) are still computed via functional form with the $\rho(\mathbf{r})$ computed in the KS electronic system, as it is the same as the interacting electronic system. The assumption of $\rho(\mathbf{r})$ correspondence between interacting and non–interacting electronic systems has been successful, at least for non–pathological situation, enabling to use it in most cases.

In KS approach $\rho(\mathbf{r})$ is calculated as HF does, (see Eq. 2.8 for $\rho(\mathbf{r})$) using the non–interacting electronic system one–electron wavefunctions, resembling a single Slater Determinant method. But as the Slater Determinant is not constructed, the Pauli principle is satisfied by imposing an interval occupation restriction $[0, 1]$ on the one–electron wavefunctions, allowing KS–DFT to be useful in multireference electronic systems. Also the kinetic energy is computed by means of the one–electron wavefunctions, as is done in HF theory, using the non–interacting electronic system one–electron wavefunctions

$$T_{KS}[\rho(\mathbf{r})] = \sum_{i}^{N} \int \varphi_i^{*KS}(\mathbf{r}\sigma) \frac{-\nabla_i^2}{2} \varphi_i^{KS}(\mathbf{r}\sigma) \; d\mathbf{r} \tag{2.15}$$

The non–interacting electronic system one–electron wavefunctions $\varphi_j^{KS}(\mathbf{r}\sigma)$ are obtained from the Schrödinger–like KS equations (coupled and non–linear one–electron equations)

$$\left[\frac{-\nabla_i^2}{2} + \upsilon_{KS}(\mathbf{r})\right] \varphi_i^{KS}(\mathbf{r}\sigma) = \epsilon_i^{KS}\varphi_i^{KS}(\mathbf{r}\sigma) \tag{2.16}$$

where $\upsilon_{KS}(\mathbf{r}) = \upsilon_{ext}(\mathbf{r}) + \upsilon_h(\mathbf{r}) + \upsilon_{xc}(\mathbf{r})$ is the effective–potential of KS electronic system, composed of external, Hartree and exchange–correlation potentials, respectively. This effective–potential represents the electron interacting with the mean–field of the whole electronic system. $\upsilon_{xc}(\mathbf{r})$ is given by the functional derivative of exchange–correlation energy functional with respect to $\rho(\mathbf{r})$, namely

$$\upsilon_{xc}(\mathbf{r}) = \frac{\delta E_{xc}[\rho(\mathbf{r})]}{\delta\rho(\mathbf{r})} \ . \tag{2.17}$$

Finally, the electronic system total energy is computed via

$$E_{KS}[\rho(\mathbf{r})] = T_{KS}[\rho(\mathbf{r})] + E_h[\rho(\mathbf{r})] + E_{xc}[\rho(\mathbf{r})] + \int \upsilon_{ext}(\mathbf{r})\rho(\mathbf{r})\ d\mathbf{r} \tag{2.18}$$

where $E_{xc}[\rho(\mathbf{r})]$ is the exchange–correlation functional, which is mainly responsible to recover the spatial– and spin–correlation not included when the electron–electron Coulomb repulsion energy is approximated by the Hartree potential energy. Also it tries to correct the discrepancies that may exist between kinetic energy computed via KS approach and kinetic energy computed via functional form, because it is known that $T_{KS}[\rho(\mathbf{r})]$ is an upper bound of $T[\rho(\mathbf{r})]$. It is defined as

$$E_{xc}[\rho(\mathbf{r})] = (\ E_{ee}[\rho(\mathbf{r})] - E_h[\rho(\mathbf{r})]\ ) + (\ T[\rho(\mathbf{r})] - T_{KS}[\rho(\mathbf{r})]\ ) \ . \tag{2.19}$$

The minimization of KS energy, Eq. 2.18, is done in a similar way as in HF theory, using a SCF iterative procedure with Lagrange multipliers and variational principle with the occupied one–electron wavefunction set as the optimization parameters.

KS electronic system solves in principle the kinetic energy functional problem of DFT with the cost of reintroducing the N one–electron wavefunction problem, as it is in HF theory, but with the advantage of including the electronic correlation (spatial– and spin–correlation) in an approximate manner through $E_{xc}[\rho(\mathbf{r})]$, providing better results than HF theory at a lower cost. The form of exchange–correlation functional is not known exactly so it must be approximated in different ways.

2.3.4 Density Functional Approximation

In order to attack the many–body electron problem in a practical way with KS–DFT, the exchange–correlation functional must be approximated with reasonable accuracy.

Different ways and forms to approximate the exchange–correlation functional have been proposed, naming them as Density Functional Approximations (DFA). Most of them follows two generalizations. The first one is related with the partition of exchange–correlation functional into its two elements which has different physical origins, *i.e.*, the exchange and correlation functionals

$$E_{xc}[\rho(\mathbf{r})] = E_x[\rho(\mathbf{r})] + E_c[\rho(\mathbf{r})] \ . \tag{2.20}$$

Each term of this equation can be modeled separately, and in principle exchange and correlation functionals can be mixed between them using the different approximations that take each one. The second generalization is related with the functional form of the exchange and correlation functionals with respect to $\rho(\mathbf{r})$. Both take the following general form

$$E_i[\rho(\mathbf{r})] = \int \varepsilon_i[\rho(\mathbf{r})]F_i[\rho(\mathbf{r}), \nabla\rho(\mathbf{r}), \nabla^2\rho(\mathbf{r}), ...] \tag{2.21}$$

where $\varepsilon_i[\rho(\mathbf{r})]$ is the exchange or correlation (according to the case) energy density per electron, and $F_i[\rho(\mathbf{r}), \nabla\rho(\mathbf{r}), \nabla^2\rho(\mathbf{r}), ...]$ is the enhancement factor that modifies the energy density. The way as the enhancement factor is modeled (and its dependence on the $\rho(\mathbf{r})$) generates different approximation functionals and families. DFA families are conceptually positioned at levels or rungs, also called Jacob's ladder. It starts in the bottom rung called "Hartree hell" where no exchange–correlation functional is considered, and the following higher rungs start to consider exchange–correlation functionals which depend on $\rho(\mathbf{r})$, $\nabla\rho(\mathbf{r})$, $\nabla^2\rho(\mathbf{r})$, $\ldots$, and so on, as is going to upper rungs. The idea is that by adding higher derivative $\rho(\mathbf{r})$ terms to the functional, the accuracy will increase until reach the chemical accuracy. The three pure DFT rungs of the Jacob's ladder are: Local Density Approximation (LDA), Generalized Gradient Approximation (GGA) and meta–Generalized Gradient Approximation (metaGGA).

The first rung and the most simple is the LDA, which sets the enhancement factor to the unity, then the exchange and the correlation functionals only depend on the $\rho(\mathbf{r})$ through the energy density. The exchange and correlation energy density are modeled using the original idea of Thomas–Fermi–Dirac theory, considering the general inhomogeneous $\rho(\mathbf{r})$ as locally homogeneous, and writing the energy density terms as an exchange and correlation holes corresponding to a homogeneous/uniform electron gas or jellium.
Exchange is modeled with the Dirac exchange functional, meanwhile correlation is modeled by a fitted functional over Ceperley and Alder's Quantum Monte Carlo simulation of uniform electron gas [176]. The fitted correlation functional has different forms, receiving different names depending on the authors of the fitted approximation to the functional: Perdew and Zunger [177], Vosko, Wilk, and Nusair [178], Perdew and Wang [179]. All of them give the same practical results. Finally, exchange and correlation functionals depends only on the $\rho(\mathbf{r})$ at the coordinate where the functional is evaluated.
LDA is exact for a uniform electron gas, an ideal system, but most part of electronic systems have at least smooth changes in the $\rho(\mathbf{r})$. LDA gives surprisingly good and wide applicable results, mainly on metallic systems, where the $\rho(\mathbf{r})$ varies little throughout the system, and has a poorer performance on high polarized systems, ionic systems and molecules, where the $\rho(\mathbf{r})$ varies significantly throughout the system.

The second rung is the GGA. This type of functionals try to address the problem with the used assumption in LDA of a locally homogeneous $\rho(\mathbf{r})$. To do it, GGA functional uses $\rho(\mathbf{r})$ and $\nabla\rho(\mathbf{r})$ to construct enhancement factors that modifies the exchange and correlation energy densities used in LDA, to afford the variation of the $\rho(\mathbf{r})$ in the vicinity of the considered point. This enables GGA functionals to capture non–local effects at short distance ranges, considering the changes in $\rho(\mathbf{r})$ away from the coordinate where the functional is evaluated, constituting GGA functionals as semi–local approaches.
The criteria for constructing these enhancement factors are varied, and two main ways are observed. One of them is based on mathematical–physical criteria, *e.g.*, Perdew–Burke–Ernzerhof

functional (PBE) [180]. Meanwhile, the other uses a set of systems to parameterize them, *e.g.*, Becke exchange functional (B88) [181] and Lee–Yang–Parr correlation functional (LYP) [182].

The third rung is the metaGGA, it follows the same idea as GGA, and continues to incorporate the Laplacian of $\rho(\mathbf{r})$, *i.e.*, $\nabla^2\rho(\mathbf{r})$ (in practice the kinetic energy density), to construct the enhancement factor. The improvement of metaGGA is limited in comparison with GGA.

GGA functionals, specially PBE, are the most used ones, due to its low computational cost and moderate/good results. Particularly, geometries are in very good agreement in most cases, specially when a functional designed to the system characteristics is used. For example, the PBEsol functional is a variation of the PBE functional to give improved equilibrium properties of packed solids and their surfaces [183].

DFA has two main drawbacks. The first one is related with its poor capture of non–local effects at medium–large distance ranges, making DFA "short sighted". This drawback does not enable DFA to capture dispersion interactions. Dispersion interactions are extremely important in non–polar molecular systems, and moderately important in polar, covalent and ionic systems, to achieve chemical accuracy and good geometries. To fix this drawback exists two main ways, using force–field–like dispersion corrections, *e.g.*, the parameterized Grimme correction scheme –D3 [184] and –D3–BJ [185]. The other approach is based in non–local correlation functionals which uses a double spatial integration of a two coordinate–dependent functional, $E_{nl-c}[\rho(\mathbf{r}), \rho(\mathbf{r}')]$, also called Van der Waals functionals [186, 187].
The second drawback is related with the SIE. Exchange–correlation functionals do not fulfill the requirement of cancellation of the SIE due to the Hartree potential interaction, which results in more delocalized $\rho(\mathbf{r})$ and wavefunctions with respect to the exact ones. Direct effect of this is the underestimation of the band gap in condensed phases, computed as the difference between the Lowest Unoccupied Crystal Orbital (LUCO) energy and the Highest Occupied Crystal Orbital (HOCO) energy, with respect to the fundamental band gap, defined as the difference between the IP and EA. Also band position and band dispersion is affected. To mitigate this drawback different corrections and terms can be added to the functionals, *e.g.*, Hubbard correction [188] and self–interaction correction [177], but also it can be controlled by means of Hybrid functionals.

Hybrid functionals is the name for the generalized KS approach, where the exchange energy of a electronic system is computed as a combination of a fraction of DFA–based exchange and a fraction of non–local exact exchange (Hartree–Fock exchange, E_x^{HF}) calculated via the occupied KS one–electron wavefunctions, see Eq. 2.22. The theoretical motivation to apply this approach is based on the adiabatic connection formula between the non–interacting and interacting electronic system, but it did not establish the amount of E_x^{HF} needed. Another theoretical motivation is the one–electron discontinuity of exact energy functional in terms of the number of electrons. The DFA is a continuous and convex functional, while HF is a discontinuous and concave functional. Hence a linear combination of both can optimize the energy functional to obtain a discontinuous one which resemble the exact energy functional.

Exact exchange cancel exactly the SIE, correcting the inherent SIE in DFA, then the amount of it can be tuned to control the SIE cancellation. Also hybrid functionals improve the DFA performance enabling to obtain accurate system properties and energies, approaching to the chemical accuracy and competing with Post–HF methods. The way in which the amount (α)

of exact exchange is determined following the same GGA construction criteria: mathematical–physical or fitting. Also hybrid functional can be constructed in principle using any combination of exchange and correlation functionals. For example PBE0 [189, 190] hybrid functional uses a 25 % of exact exchange ($\alpha = 0.25$) and the PBE exchange–correlation functional.

$$E_{xc}^{Hybrid} = (1-\alpha)E_{x}^{DFA}[\rho(\mathbf{r})] + \alpha E_{x}^{HF}[\varphi_{occ}^{KS}(\mathbf{r}\sigma)] + E_{c}^{DFA}[\rho(\mathbf{r})]. \tag{2.22}$$

A more generalized form of hybrid functionals is the range–separated ones, which splits the two–electron operator used for exchange (using the error function and a new parameter) into a Short Range (SR) and Long Range (LR) portions, enabling to mix DFA exchange and exact exchange in different amounts at SR and LR, similarly is done in Eq. 2.22. An example of range–separated hybrid functional is HSE [191, 192], it uses a 25 % of exact exchange at SR, and, PBE exchange functional for the rest of SR exchange and full PBE exchange functional at LR, with a range–separated parameter of 0.2 Å^{-1}. Also the PBE correlation functional is used.

Both hybrid and range–separated hybrid functionals improve the band gap, correcting its underestimation mainly by the destabilization of unoccupied crystal orbitals (LUCO and higher), but the resulting band gap is highly dependent on the amount of exact exchange used.
To avoid this arbitrariness in the selection of the exact exchange amount, recent approaches motivated on COHSEX approximation defines the mixing fraction of exact exchange in PBE0 hybrid functional in terms of a physically motivated, non–empirical, and system–dependent way, by means of the inverse of the *macroscopic* dielectric constant ($\alpha = \varepsilon_{\infty}^{-1}$) [193–195]. This novel approach, called PBE0(α) gives better IPs and fundamental band gap in condensed phases with respect to general hybrid functionals. Also has been shown that PBE0(α) gives correct alignment between energy levels of different materials [195, 196]

KS one–electron energy eigenvalues do not have a physical interpretation because they are not quasiparticle energy levels. A direct consequence of it is that Koopman's theorem does not apply to it.
However in KS–DFT exists the Janak's theorem (sometimes called DFT–Koopman's theorem) which establish that the derivative of the total energy, as constructed in DFT, with respect to an occupied orbital occupation is equal to the eigenvalue of that orbital. This statement is valid independently of the detailed form of the exchange–correlation functional [197]. Then the eigenvalue of HOCO will correspond to the negative of IP, IP$= -\epsilon_{HOCO}$, as is in HF. In the case of EA, Janak's theorem does not establish its direct relation with the eigenvalue of LUCO because the derivative exhibits a "derivative discontinuity" in the exchange–correlation functional (Δ_{xc}), so can be argued that EA is the negative of LUCO eigenvalue plus the Δ_{xc}.
Δ_{xc} is known only for LDA (where is zero). It is the error source of band gap (E_g) determination, due to the latter is defined as E_g =IP$-$EA. Therefore, in the search for an easy and, in some point, accurate approach, the most used approach is to force EA be equal to the negative of LUCO eigenvalue, ensuring that the obtained system band gap, computed as the difference between the LUCO energy and the HOCO energy, is near the experimental one.
Hybrid functionals, particularly PBE0(α), are the most suitable to use with this approach, because the inclusion of exact exchange corrects the band gap underestimation of DFA. Finally KS–DFT IPs are better than HF ones, because the first includes the correlation energy and also consider the effect of orbital relaxation.

2.4 Periodic Boundary Condition and slabs

In this thesis we will refer to applications of DFT to periodic systems, which allows to use the implications of the Bloch theorem [198]. The systems are described in terms of periodic unit cells, which replicate an infinite periodic structure. Also the properties of these systems are periodic in space in the form $f(\mathbf{r}) = f(\mathbf{r}+\mathbf{T})$, where $\mathbf{T} = n_1\mathbf{a_1} + n_2\mathbf{a_2} + n_3\mathbf{a_3}$ is the translation vector formed by the linear combination of vectors forming the unit cell $\mathbf{a_i}$, with $n_i \in \mathbb{N}_0$. This is the Periodic Boundary Condition (PBC). With it, only is necessary to known the properties and functions in $\mathbf{r} = x_1\mathbf{a_1} + x_2\mathbf{a_2} + x_3\mathbf{a_3}$, with $x_i \in [0, 1[$, *i.e.*, only into the unit cell.
Particularly, the effective–potential for the electronic system is periodic in space. The one–electron wavefunctions resulting from this periodic Hamiltonian can be obtained as Bloch states, *i.e.*, a periodic function (dependent on the nuclear geometry) enhanced by a plane wave which modulates the periodic function

$$\varphi_{j,\mathbf{k}}(\mathbf{r}) = e^{-i\mathbf{k}\cdot\mathbf{r}} u_{j,\mathbf{k}}(\mathbf{r}) \ . \tag{2.23}$$

$u_{j,\mathbf{k}}(\mathbf{r})$ is a spatial periodic function, but not $\varphi_{j,\mathbf{k}}(\mathbf{r})$, due to the modulation plane wave does not have the periodicity of the unit cell. Since $\rho(\mathbf{r})$ must be periodic, $|\varphi_{j,\mathbf{k}}(\mathbf{r})|^2 = |u_{j,\mathbf{k}}(\mathbf{r})|^2$ satisfy the PBC.
Bloch states depend on a new quantum number $\mathbf{k}$, which is in fact the crystal momentum vector, a three dimensional continuous quantity. Therefore, for each pair of one–electron wavefunction $\varphi_j(\mathbf{r})$ and energy eigenvalue ϵ_j in non–PBC calculations, now there is a continuous set in $\mathbf{k}$ for one–electron wavefunction $\varphi_{j,\mathbf{k}}(\mathbf{r})$ and energy eigenvalue $\epsilon_{j,\mathbf{k}}$, this is a band.
Crystal momentum space is related with real space, so sometimes it is called reciprocal space, and has analogous PBC. Properties in reciprocal space also has periodicity in terms of momentum translation vector $\mathbf{G} = m_1\mathbf{g_1} + m_2\mathbf{g_2} + m_3\mathbf{g_3}$, so only it is necessary to know them in the reciprocal unit cell formed by the reciprocal unit cell vectors $\mathbf{g_i}$, with $m_i \in \mathbb{N}_0$.
The $\mathbf{k}$ sampling of properties $f(\mathbf{k})$ in Bloch states is only necessary within the reciprocal unit cell, also known as Brillouin Zone, *i.e.*, $\mathbf{k} = x_1\mathbf{g_1} + x_2\mathbf{g_2} + x_3\mathbf{g_3}$ with $x_i \in [0, 1[$. The inconvenience lies in the fact that there is not an analytical form to sample $\mathbf{k}$, then a discrete sampling selecting particular points into the Brillouin zone is necessary, which approximates the full and continuous sampling. This can be done by means of grid sampling using special $\mathbf{k}$–points, *e.g.*, the Monkhorst–Pack method [199].
If $\mathbf{k}$–point sampling is selected correctly containing the VBM and CBM, VBM matches with the HOCO, and CBM matches with the LUCO of the calculation. The energy of the VBM and the CBM, with respect to the vacuum level, are the negatives of the IP and the EA of the studied material, respectively. The study of energy levels in periodic systems is complex due to the multiple $\mathbf{k}$–point sampling, which generates many different energy levels. For this reason, indirect ways to study them are used, such as Density Of States (DOS), Projected Density Of States (PDOS) and Local Density Of States (LDOS), for a detailed description, application and implementation see Ref. [3]. Periodic unit cells may be also of artificial nature. This allows to describe with this approach also non–periodic materials like finite slabs with surfaces, 2D materials, molecules or interfaces.

How to get accurate slab/interface models? When surfaces and interfaces are studied by *ab initio* methods, computational cost restricts the slab thickness to a few nanometers, compared to the tens or hundreds nanometers in experimental cases. In this quantum well regime, the

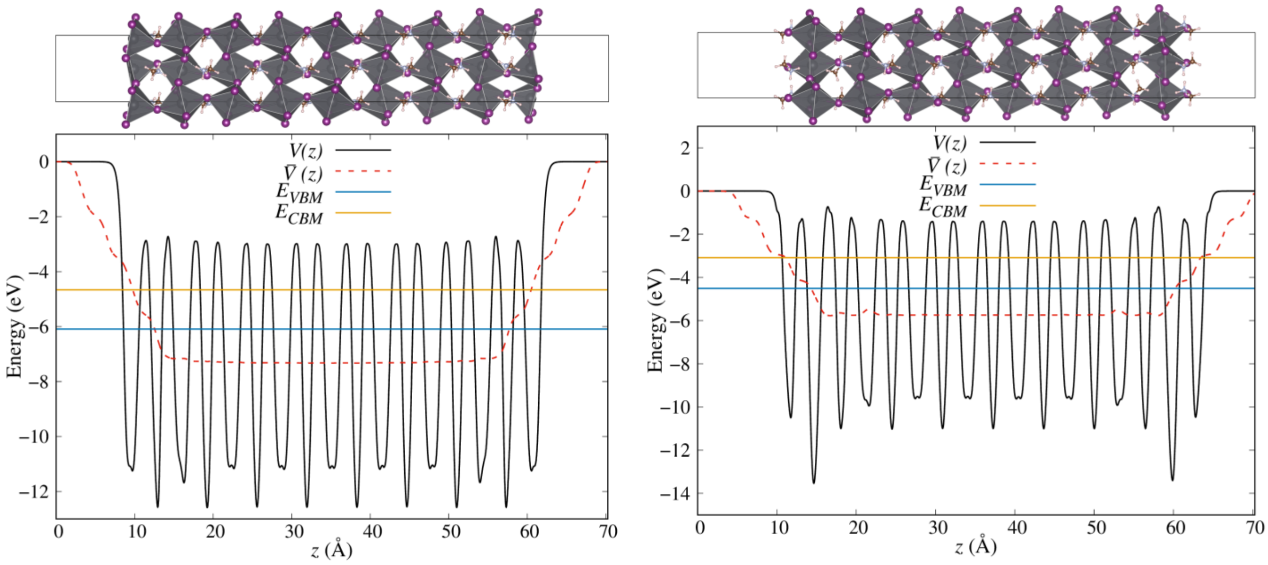

(a) MAPI(001)–PbI_2 (b) MAPI(001)–MAI

Figure 2.2: Planar–averaged ($V(z)$) and *macroscopic* ($\bar{V}(z)$) electrostatic potentials, VBM and CBM energies, with respect to vacuum level, for $(1 \times 1) \times 8$ slabs computed with PBEsol: (a) $(1 \times 1) \times 8$ MAPI(001)–PbI_2 and (b) $(1 \times 1) \times 8$ MAPI(001)–MAI.

electronic states are affected by Quantum Confinement (QC). The correct description of surface and inner, geometry and electronic structure, need to be studied, by means of electronic state energies, surface energy and band gap convergence with respect to slab thickness. Also, vacuum thickness is an important parameter when PBC is used for the three directions, due to the model has replicas in the cleavage direction, and the vacuum need to be long enough to avoid interaction with periodic replicas (see Appendix A.4).

As shown in Fig. 2.2, the simulation supercell contains a crystal volume (the slab), and a vacuum volume.

The crystal volume is continuous in two directions, namely, x and y, and the surface is normal to the third direction, z. PBC is used for the three directions. Therefore, this represents two infinite surfaces, which must be sufficiently separated not to interact. The separation of the surfaces is determined by both the slab and vacuum thicknesses. The effect of slab thickness will be studied in Chapter 3 and 4, and vacuum thickness in Appendix A.4.

2.4.1 Basis Sets, Pseudo–potentials and Programs

The periodic part of Bloch state $u_{j,\mathbf{k}}(\mathbf{r})$ must be expanded in terms of a known set (K) of functions, also called basis set,

$$u_{j,\mathbf{k}}(\mathbf{r}) = \sum_{\alpha}^{K} c_{j,\mathbf{k}}^{\alpha} \phi_{\alpha}(\mathbf{r}) \ . \tag{2.24}$$

The basis sets are divided into two main groups.

One group includes localized atom–centered functions, *e.g.*, Slater, Gaussian or numerical. The main characteristics are: require a low amount of functions per atom (tens to hundreds) to produce reasonable results; exhibit basis set superposition error; Gaussian functions enable fast computation of Fock exchange operator; there is no a systematic way to reach the basis set completeness; basis set is not orthogonal; among others.

The second group tries to exploit the periodic symmetry and properties of Bloch functions (modulation plane wave and $u_{j,\mathbf{k}}(\mathbf{r})$), then uses plane wave functions (PW). These plane waves are a selected set with crystal momentum vector equal to $\mathbf{G}$, *i.e.*, $\phi_{\mathbf{G}}(\mathbf{r}) = V^{-\frac{1}{2}}e^{-i\mathbf{G}\cdot\mathbf{r}}$. The main characteristics are: functions are not localized and do not depend on atom positions, so are free of basis set superposition error; require a very high amount of functions (thousands to millions) to produce reasonable results; computation of Fock exchange operator must be done numerically; there is a systematic way to reach the basis set completeness by adding higher momentum PW, which is controlled by the cutoff energy parameter equal to $|\mathbf{G}_{max}|^2/2$; presents a big advantage to compute Hartree and kinetic energy terms; requires Pseudo–Potentials (PPs) to deal with core electron in atoms; basis set is orthonormal by construction; among others.

There are programs which uses a mixture (GPW) between localized basis sets for wavefunctions and PW basis set to expand $\rho(\mathbf{r})$, such as CP2K code.

PPs are needed for PW basis sets because the singularity of the Coulomb potential of nuclei leads to issues. Also nodes in real wavefunctions is a complex situation for PW basis sets, requesting too high energy cutoff (too many PW functions) to approximate them. To solve these problems, core electrons are replaced by a mimic potential (pseudo–potential), which does not have singularity and enable to use nodeless wavefunctions (pseudo–wavefunctions) for valence electrons. The replacement of core electrons is possible because they are strongly localized around the nuclei, with small overlap to valence electron wavefunctions. Then the core electron distributions is poorly affected by the chemical environment of the atom, so they are somehow “frozen”. Moreover, the reduction of total number of electrons decrease the number of one–electron equations to solve, reducing the time and resources needed for the calculation. PP theory is a broad field, but briefly pseudo–wavefunctions are equal to all-electron wavefunctions outside the atom–centered spheres defined by cutoff radius, and the differences are within the cutoff radius. Depending on how is the pseudo–wavefunction in the inner region, different types of PPs are classified: Ultra–Soft Pseudo–Potentials (USPP), Norm–Conserving Pseudo–Potentials (NCPP), Projector Augmented Wave method (PAW), among others.

In this thesis three different PBC program packages were used to compute the electronic structure of studied systems: Quantum–ESPRESSO (QE) [200, 201] is a DFT–, PW– and PP–based code. Vienna *Ab initio* Simulation Package (VASP) [202–204] is a DFT–, PW– and PP–based code. CP2K [205,206] is a DFT–, GPW– and PP–based code. Computational details are shown in Appendix A.1.

2.5 Experiment/Theory Relation and Reference Potential

Different properties can be compared between experiment and theory, using previous theoretical approaches to predict them.

Mechanical properties and unit cell lattice vectors obtained by X–ray crystallography, can be compared with minimum energy structures of the total energy curve of cell simulation. Exploring the total energy curve adding stress/pressure to the system enables to obtain mechanical properties as bulk modulus B_0 by fitting the Birch–Murnaghan equation of state [207, 208] on the total energy curve.

$$E(V) = E_0 + \frac{9V_0B_0}{16}\left(\left[\left(\frac{V_0}{V}\right)^{\frac{2}{3}} - 1\right]^3 B_0' + \left[\left(\frac{V_0}{V}\right)^{\frac{2}{3}} - 1\right]^2 \left[6 - 4\left(\frac{V_0}{V}\right)^{\frac{2}{3}}\right]\right) \tag{2.25}$$

Birch–Murnaghan equation of state has four fitting parameters: minimum energy E_0, volume at the minimum energy V_0, bulk modulus B_0 and its pressure first derivative B_0'.
Electronic properties related with energy levels and bands structure can be compared with experimental results. Direct and inverse photoemission spectroscopy, using the photoelectric effect, enables to map the occupied states and the unoccupied states as a function of the energy. With them it is possible to access to IP and EA. These quantities can be obtained computationally by means of Koopman's or Janak's theorem using many–body electron theories to compare with experimental ones. Also angle–resolved photoemission spectroscopy allows to discriminate between different **k**–points on the reciprocal space to obtain band resolved electronic structure. The band gap energy can be determined from the IP and the EA, or using absorption spectroscopy, which allows to access directly to the optical gap. The optical gap differs from the band gap by the exciton binding energy, or due to symmetry–forbidden transitions. Hence determining the band gap from optical measurements is not always straightforward.

A direct consequence of PBC calculations is referred to the reference potential energy. Most molecular calculations uses non–PBC, ensuring that the reference potential energy (with respect to which the energy eigenvalues are referenced) is always the vacuum level. In contrast, PBC calculations have a reference potential energy that is not well defined, due to the electrostatic terms in the Hamiltonian, which are defined by a conditionally convergent series. Thus, the reference potential energy depends on the calculated system. This situation prevents band alignment directly between materials computed separately.
Alignment of the energy levels of two materials need a common reference in potential energy. Usually *macroscopic* electrostatic potential for each material and the vacuum level are used to determined VBM and CBM energy levels, by means of a two–step procedure [1,2,196,209–211]. First, some vacuum must be present in the simulation cell in order to obtain the vacuum level. This is done by means of slab calculation. From the slab or interface calculations, the electrostatic potential $V(x, y, z)$ is extracted and analyzed by means of two kinds of averages. The electrostatic potential $V(x, y, z)$ is the sum of the electrostatic Hartree energy, and the local part of the PPs, the latter of which implies some extent of arbitrariness.
Subsequently the planar–average electrostatic potential is obtained for the slab/interface model, as shown in Fig. 2.2 for PbI_2 and MAI surfaces of MAPI, and Fig. 2.3 for Cu_2O/MAPI interface, according to

$$V(z) = \frac{1}{A_{xy}} \iint V(x, y, z)\; dxdy + E_0 \quad , \tag{2.26}$$

where A_{xy} is the transverse area of the slab/interface. The constant E_0 is an energy shift applied to make $V(z) = 0$ in the vacuum region for slab systems. In this way, the zero of energy is set to the electrostatic potential energy in vacuum. The vacuum reference determination is a current research topic [212, 213]. When interface systems are used, the constant E_0 is avoided because is not necessary. Also, the convoluted *macroscopic* electrostatic potential is defined for slabs and bulk cells as

$$\bar{V}(z) = \frac{1}{c} \int_{-c/2}^{c/2} V(z + z')\; dz' \quad , \tag{2.27}$$

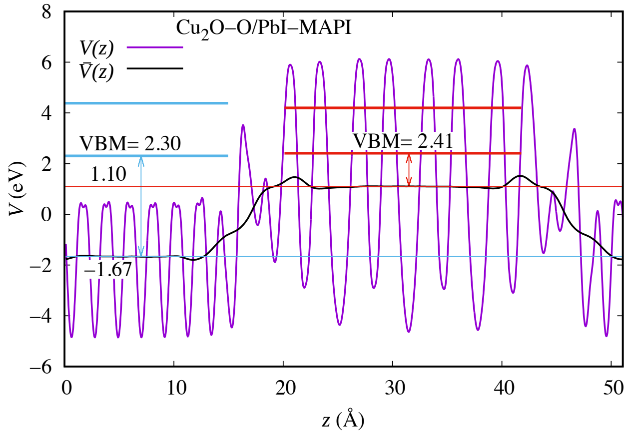

Figure 2.3: Electrostatic potential in an interface slab model, and band edges of the materials at each side of the interface. Each vertical arrow indicates the difference between the VBM and the average electrostatic potential for each material, as obtained from bulk calculations. See Chapter 5 for interface nomenclature.

where c is the lattice constant in the direction perpendicular to the slab surface, c has been set equal to one half of the lattice constant. As $V(z)$ is periodic inside the crystal, $\bar{V}(z)$ should be constant at the central part of the slab, represented as red dashed line in Fig. 2.2. Also, $\bar{V}(z)$ is strictly constant, and independent of the functional, when it is computed for a unit cell of the crystal, *i.e.*, without vacuum, as Fig. 2.4 shows.
In interface case, the *macroscopic* electrostatic potential is defined as a double convolution,

$$\bar{V}(z) = \frac{1}{c_1 c_2} \int_{-\frac{c_1}{2}}^{\frac{c_1}{2}} \int_{-\frac{c_2}{2}}^{\frac{c_2}{2}} V(z + z' + z'')\, dz' dz'' \,, \tag{2.28}$$

where c_1 and c_2 are the periodicity lengths of $V(z)$ in each of the bulk materials. For both

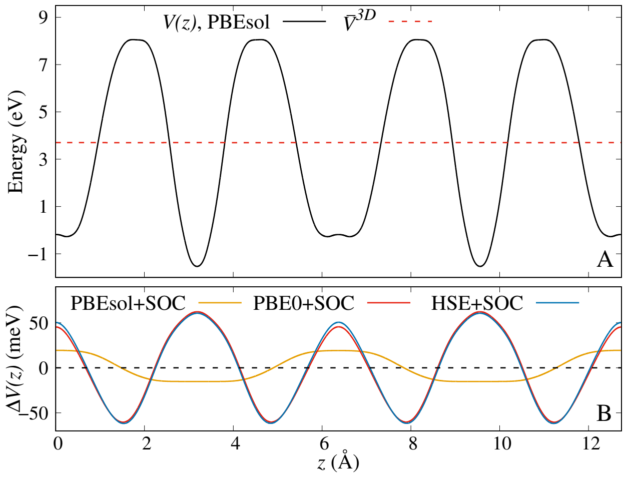

Figure 2.4: Planar–averaged and *macroscopic* electrostatic potential for the MAPI unit cell, along z, for different levels of theory and functionals. (A) PBEsol. (B) PBEsol+SOC and other functionals, as difference with respect to (A). Note the difference in the energy scales.

Cu_2O and MAPI, c_1 and c_2 have been set equal to one half of the lattice constant. $\bar{V}(z)$ is represented by the black line in Fig. 2.3. If the region occupied by each material is thick enough, $\bar{V}(z)$ displays a plateau at the central region. The approximately constant values of $\bar{V}(z)$ at the plateaus define the values $\bar{V}(z_{in,slab}^{(m)})$ ($m =$ Cu_2O, MAPI) in slab and interface systems. $\bar{V}(z_{in,slab}^{(m)})$ is precisely the reference used to transfer the VBM and CBM energies, from a three-dimensional (3D) crystal to a slab with vacuum or an interface. From a crystal calculation are obtained the average electrostatic potential $\bar{V}^{3D,(m)}$, and the energies $E_{VBM}^{3D,(m)}$ and $E_{CBM}^{3D,(m)}$. Finally, the VBM and CBM energies (with respect to the vacuum level in slab case, or with respect to particular reference level in interface case) are obtained as

$$E_{\alpha,slab}^{(m)} = \bar{V}(z_{in,slab}^{(m)}) + \left(E_{\alpha}^{3D,(m)} - \bar{V}^{3D,(m)}\right) \quad , \tag{2.29}$$

where $\alpha = VBM, CBM$. This $E_{\alpha}^{3D,(m)} - \bar{V}^{3D,(m)}$ difference is shown, for the VBM of both materials, by the vertical arrows in Fig. 2.3. Therefore, the VBMs and CBMs of both materials in the slab/interface energy–scale can be obtained using Eq. 2.29.

This two–step process, with the difference $E_{\alpha}^{3D} - \bar{V}^{3D}$ transferred from a bulk calculation with a primitive cell, allows to correct the errors in VBM and CBM energies (leading to gap underestimation in GGA), by means of higher level calculations, such as hybrid functionals or the GW approximation, over primitive bulk cell. The slab/interface calculation is prohibitively expensive with such high level methods, but it can be done with GGA functionals, assuming that the electrostatic potential is well described by GGA. This assumption is true in most cases, also in MAPI, as demonstrated Fig. 2.4 for calculations with and without SOC using three functionals, over bulk unit cell. Particularly, the different levels of theory and functionals do not change $\bar{V}(z)$ and $\bar{V}^{3D}$. There is just a small change in $V(z)$ profile (< 60 meV, as shown in Fig. 2.4), due to small changes in electron density. SOC shifts electron density from MAI layers to PbI_2 layer, while for both hybrid functionals, the shift is from inter layer space to MAI and PbI_2 layers. Notice, these changes in $V(z)$ also are periodic in space with positive and negative values, then the convolution result does not change.

To determine the interface potential barriers at VBM and CBM without the explicit interface, the previous two–step procedure is used, using the vacuum level as the common reference. This approach also allows to know in detail the shape of potential barrier and electronic states that can form on surface.

To obtain more precise values of potential barrier, an explicit model interface of the two materials is constructed.
Explicit calculation of an interface between two materials enables to compute and compare directly the energy levels of the system, where $E_{\alpha}^{(m)}$ ($m =$$Cu_2O$, MAPI) can be identified with the VBM and CBM wavefunction of which is delocalized over the central part of the region occupied by material m. The values $E_{\alpha}^{(m)}$ computed in this way depend on the width of the m–material slab, in some cases displaying the QC effect [1,31]. Hence, $E_{\alpha}^{(m)}$ should be computed for sufficiently wide slabs, which generally contain such a high number of atoms that prevents DFT calculations.

However, the VBM alignment across the interface can be determined by means of a two–step procedure to transfer the bulk VBM and CBM of both materials to the explicit interface system, using the averaged and *macroscopic* electrostatic potential in areas far from the interface. In addition to avoiding the QC effect, the two–step process has more advantages versus a direct slab calculation of $E_\alpha^{(m)}$, because $\bar{V}(z)$ converges quickly in terms of slab thickness [1]. $V(z)$ and $\bar{V}(z)$ depend weakly on the exchange–correlation functional, thus it can be computed using a non–expensive GGA functional, see Fig. 2.4. However, one must verify that the GGA error in the band edges do not cause a spurious charge transfer across the interface. On the other hand, E_α depends strongly on the functional, but it can be obtained at a high level of theory because the unit cell is a relatively small system.

The band offsets at the interface are defined as

$$(\Delta E_{VBM})_{int} = E_{VBM,slab}^{(\mathrm{Cu_2O})} - E_{VBM,slab}^{(\mathrm{MAPI})} = E_{VBM}^{(\mathrm{Cu_2O})} - E_{VBM}^{(\mathrm{MAPI})}, \tag{2.30}$$

$$(\Delta E_{CBM})_{int} = E_{CBM,slab}^{(\mathrm{Cu_2O})} - E_{CBM,slab}^{(\mathrm{MAPI})} = E_{CBM}^{(\mathrm{Cu_2O})} - E_{CBM}^{(\mathrm{MAPI})}. \tag{2.31}$$

for VBM and CBM energy level through two–step procedure or direct interface calculation, respectively. A positive sign of $(\Delta E_{CBM})_{int}$ means an energy barrier for the transfer of photo–excited electrons from MAPI to $\mathrm{Cu_2O}$. For hole transfer, an energy barrier is obtained when $(\Delta E_{VBM})_{int}$ is negative. Therefore, the ideal situation for $\mathrm{Cu_2O}$ as HTM is to has $(\Delta E_{VBM})_{int} \simeq 0$, and $(\Delta E_{CBM})_{int} > 0$. By construction, the band gap satisfy

$$E_g^{(m)} = E_{CBM}^{3D,(m)} - E_{VBM}^{3D,(m)} = E_{CBM,slab}^{(m)} - E_{VBM,slab}^{(m)}. \tag{2.32}$$

using the same functional data for both when two–step procedure is used in slab and interface cases.

Chapter 3

$CH_3NH_3PbI_3$ Electronic Structure

Contents

In this chapter we approach different computational methodologies in search of accurate representations of MAPI band structure from bulk model and MAPI surfaces from slab models. The surface energy levels are modeled by means of a method that refers the band energies of the bulk to the energy levels of the slab, considering hybrid functional and SOC. Furthermore, the results were validated with the SCF wavefunction of sufficiently large slabs under the same level of theory. Correspondingly, the convergence of these energy levels with respect to the size of the slab is also studied. Finally, the surface structures have been characterized including thermal motion, so we can include features that static models cannot address. The main results of this chapter are already published in Ref. [1]. For computational details, see Appendix A.1.

3.1 Bulk: Structure and Properties

The starting point is a model of the tetragonal crystal structure of MAPI [49], which is a 48 atom unit cell, named *Unpol* in Ref. [214]. The name *Unpol* refers to the null polarization associated to the orientation of the C–N bonds in all (001) MAI layers (see Fig.1.7). This structure represents a polymorphic configuration of the phase since the distortions are similar to those obtained within the configurational ensemble of this phase including thermal motion [45, 214]. The *Unpol* unit cell was optimized by means of variable–cell relaxation.

3.1.1 How to Proceed to the Computational Study of $CH_3NH_3PbI_3$?

Several computational setups can be used to study the the geometrical and the electronic structure. These different approaches has different strengths and disadvantages for different properties. We focus on two main areas: geometry and band edges.
To define which setup is the optimum in terms of accuracy and computational costs, we performed a study using three different computational setups with PBEsol exchange–correlation functional: USPP, NCPP and NCPP+SOC (see Method I and II in Table A.1). As a general rule, USPP requires a smaller PW basis set in comparison to NCPP, enabling faster calculations. Meanwhile, QE does not allow computations with SOC and USPP, in contrast to NCPP.

We check the effects and reliability of these three computational setups firstly in geometrical structure of MAPI.
For this purpose, we explored the total energy surface adding stress/pressure to the system. Particularly, we enforce the a length vector to certain values around ±5 % the equilibrium value, and we allow the c length vector to relax, with the aim of study possible stress effects in the description of MAPI(001) surfaces an interfaces. This was done by variable–cell relaxation in c using fixed a value, maintaining the orthogonality of the vectors and allowing the complete relaxation of the atoms in the system. It is important to note, calculations with SOC do not allow cell relaxation, so these calculations used NCPP optimized cells as starting point to complete atomic relaxation of the system, considering that SOC perturbation in cell and atom geometry is small.
Latter, the resulting total energy surfaces were fitted using Birch–Murnaghan equation of state (BM equation), setting $V_0 = a_0^2 c_0$ and $E_0 = 0$ for each computational setup, in order to compare them in the same–scale. B_0 and B_0' were left as adjustment variables.
Total energy surfaces and BM equation fit for three computational setups are shown in Fig. 3.1A

Table 3.1: BM equation fit parameters for MAPI bulk cell using USPP, NCPP and NCPP+SOC setup.

Setup	$a_0[c_0]$ (Å)	B_0 (Gpa)	B_0'
USPP	8.75[12.37]	7.72	3.64
NCPP	8.74[12.37]	7.81	3.93
NCPP+SOC	8.76[12.39]	7.50	4.00
Exp. [49, 215]	8.81[12.71]	13.9	~ 4.00

and B. Quantitative results are shown in Table 3.1.

From Fig. 3.1A it is clear that USPP and NCPP setup produce the same total energy profile, meanwhile SOC affect it slightly, shifting the minimum energy to larger a lengths (also c). This is clear with the data shown in Table 3.1. Despite this, in terms of mechanical properties and bulk cell volume, three computational setups show similar deviations underneath with respect to experimental values of a and c lattice length and bulk modulus. In this case, our bulk modulus value corresponds to a bi–axial (ab plane) stress over the MAPI cell, while experimental bulk modulus corresponds to isotropic stress. Taking into account that we have allowed the relaxation of simulation cell in c, lower bulk modulus is expected for our computation. Atomic and cell geometry are in good agreement with the experimental ones, enabling to use them as representative models. Moreover Fig. 3.1D shows the behaviour of c/a constant (the quotient between c and a lattice lengths) is also the same between USPP and NCPP setups, showing a negative slope with respect to a lattice constant.
Taking these results into account is justified to use USPP setup to compute geometry and cell optimization henceforth, without substantial loss of geometrical model accuracy.

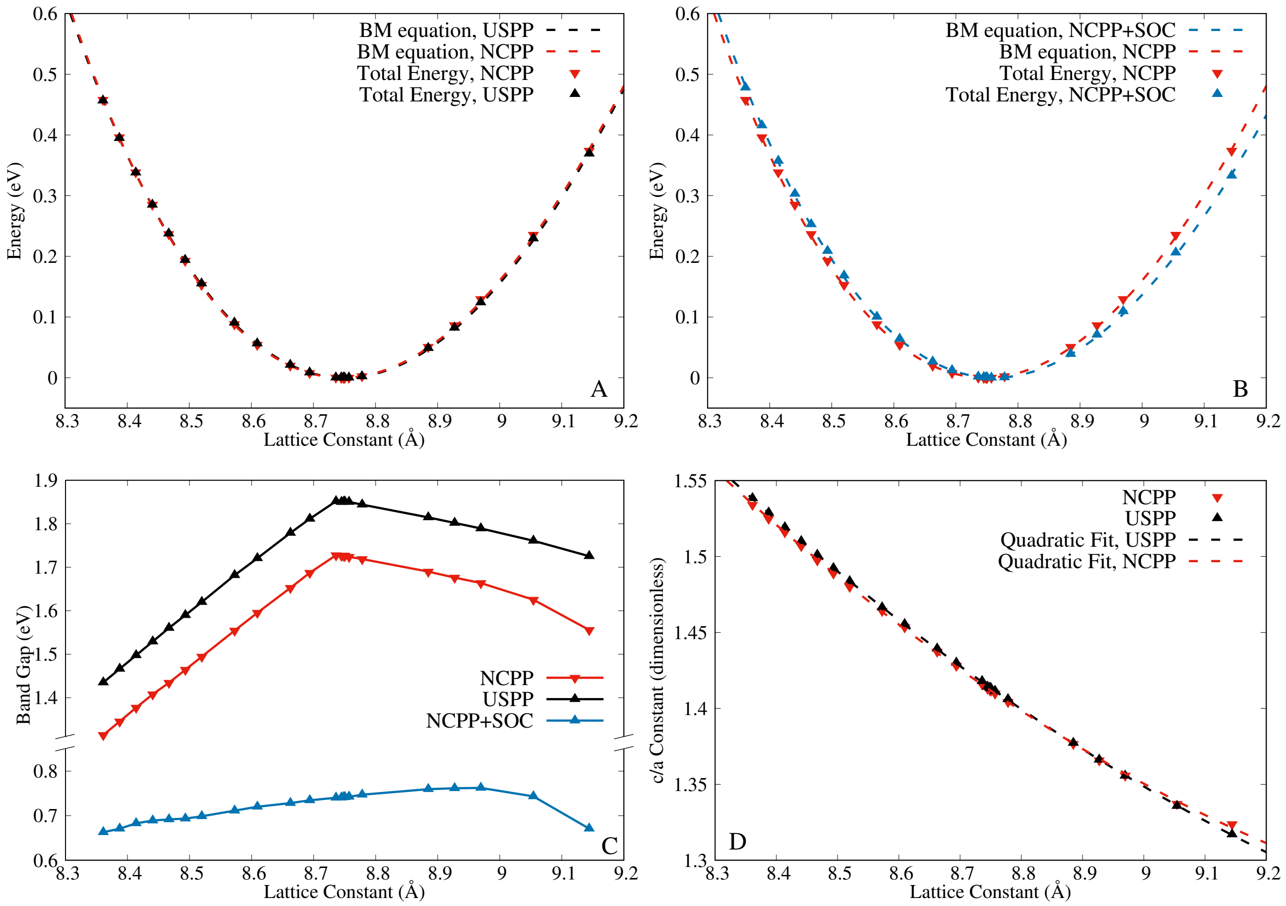

Figure 3.1: $CH_3NH_3PbI_3$ properties with respect to the lattice constant a. (A) total energy surface and BM equation fit for USPP and NCPP setups, (B) total energy surface and BM equation fit for NCPP and NCPP+SOC setups, (C) band gap for the three setups and (D) c/a dimensionless constant for USPP and NCPP setups.

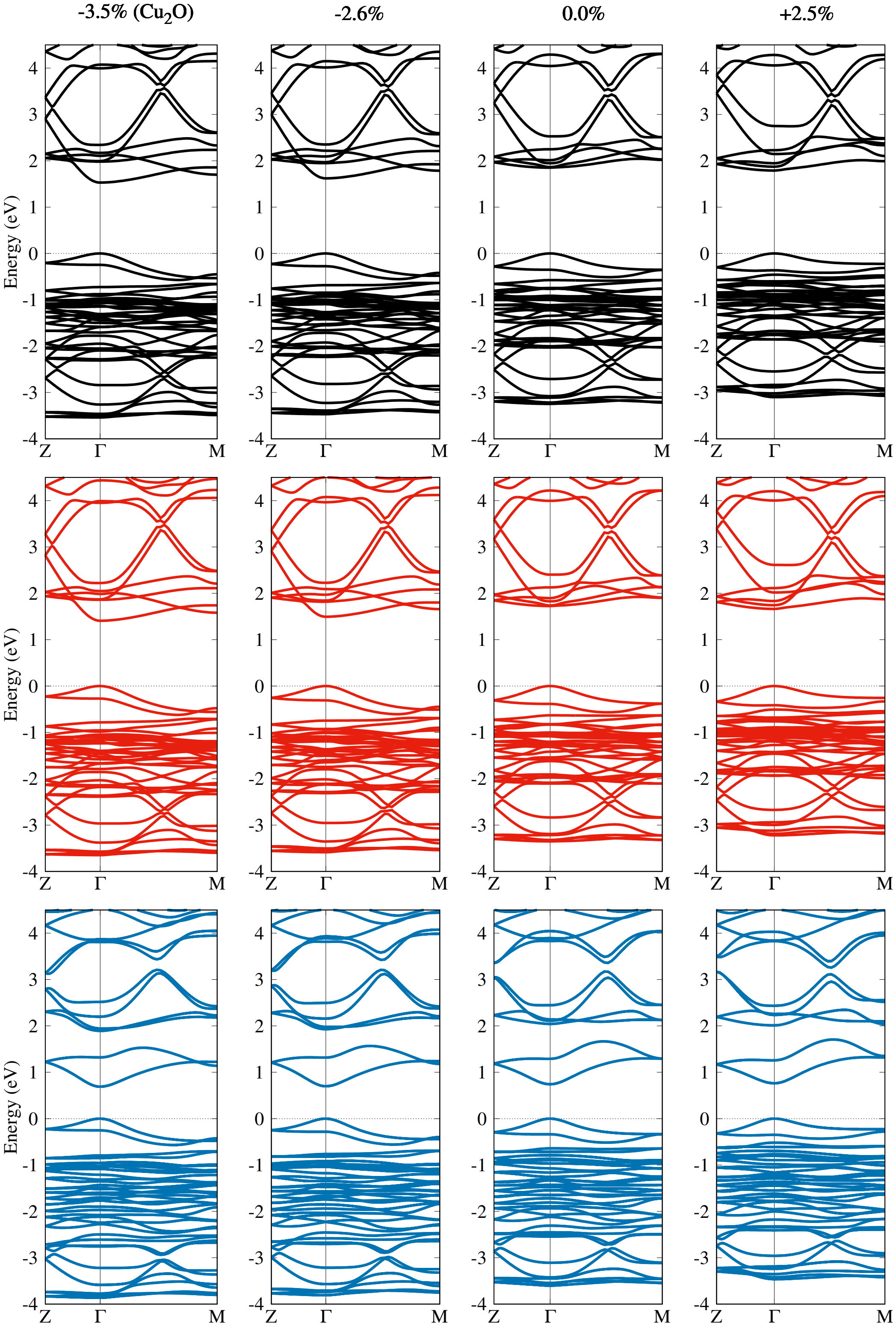

Figure 3.2: Band structure of tetragonal *Unpol* MAPI at minimum energy volume(0.0 %) and different stressed a lattice lengths, using different computational setups: black USPP, red NCPP and blue NCPP+SOC. **k**–points used: $\Gamma = (0,0,0)$, $\mathrm{Z} = (0,0,\frac{1}{2})$ and $\mathrm{M} = (\frac{1}{2},\frac{1}{2},0)$, in terms of reciprocal lattice vectors. Zero energy is defined as E_{VBM}.

The second important point is related with the electronic structure of the model: band edges, band gap and band dispersion. Fig. 3.1C shows the band gap, for different values of the lattice constant a of previous systems. Band gap is highly affected by compression but less by expansion of the (001) simulation cell face. In both cases the band gap is diminished by $\sim$ 0.4 and $\sim$ 0.2 eV, respectively, independent of using USPP or NCPP setups. Both setups show the same trends, with just $\sim$ 0.15 eV difference in band gap, almost constant over the entire study range. NCPP setup at the minimum energy geometry gives a closer band gap with respect to experimental one.
Meanwhile, when SOC is included, the effects of compression and expansion of (001) cell face become smaller in the study range, with values between 0.85 and 0.75 eV, exhibiting an underestimation of band gap. Also, there is no band gap cusp–point at the minimum energy geometry as is for USPP and NCPP.

To shed deeper insight on the electronic structure, we select four cell geometries and compute band structure in the path Z–Γ–M where the VBM, CBM and band gap are located (Γ–point), see Fig. 3.2. We use the minimum energy geometry, a expanded and compressed geometry and one with the $Cu_2O(001)$ surface area, using USPP, NCPP and NCPP+SOC setups. Zero energy is defined as E_{VBM} in order to use the same energy–scale to compare the results, as the reference potential is different in each case.
As can be seen, the USPP and NCPP setup band structure are in practice the same, exhibiting bands with the same distribution, dispersion and intercrossing for each geometry cell, and the unique difference is in E_{CBM} energy level, which is in practice the constant difference in band gap between USPP and NCPP setups. In addition, it can be seen at the minimum energy geometry the CBM belongs to different bands for negative and positive stress, and the band swap takes place at the null stress geometry, when both bands are degenerated at the Γ–point. This situation is responsible for the cusp–point in the band gap behaviour, in USPP and NCPP setups.
NCPP+SOC setup bands do not show the swap of CBM band, being the same band throughout the entire studied range that corresponds to the CBM. SOC affects strongly to the conduction bands, changing their order and dispersion/shape. This shows the big importance of the SOC in MAPI, so it is necessary to obtain a satisfactory and representative result.

It is worth mentioning that, the error cancellation between the lack of SOC and GGA underestimation band gap due to SIE allows to obtain a band gap result in agreement with experimental band gap, but the values of the band edges are not expected to be correct with respect to the vacuum level. Hence, hybrid functionals with SOC have to be introduced in order to correct both errors. This is done hereunder.

In conclusion, USPP setup is a reliable framework for obtaining cell geometries. The volume deviation with respect to the experimental value [49] reached −3.6 % and −0.2 % for PBEsol and vdW functionals, respectively. As shown, the SOC effect into geometries is insignificant, so from now on, we do not include SOC for geometric optimizations. Meanwhile, NCPP setup is necessary when electronic structure is needed, SOC must be included to obtain the band structure subsequently, with the companionship of hybrid functionals.

3.1.2 Electronic Structure of Bulk $CH_3NH_3PbI_3$

We proceed to compute the electronic structure of MAPI using NCPP and NCPP+SOC setups for over the minimum energy structure obtained with USPP setup, all of them in conjunction with PBEsol functional.
In order to get a detailed electronic structure, we compute band structure with a complete reciprocal space path (Z–Γ–M–X–R–Z–A–R–A–M), which pass over all high symmetry points in the Brillouin Zone for simple tetragonal symmetry. Also we compute the DOS, and, atomic and orbital PDOS using a denser **k**–point grid (see Appendix A.1). Results for NCPP and NCPP+SOC setups are shown in Fig. 3.3.

The band structure (left panel) shows that VBM and CBM are located at Γ–point for both setups. The valence band structure present low dispersion, with a densely populated zone around -1.0 eV, meanwhile the inclusion of SOC does not change the shape of valence bands,

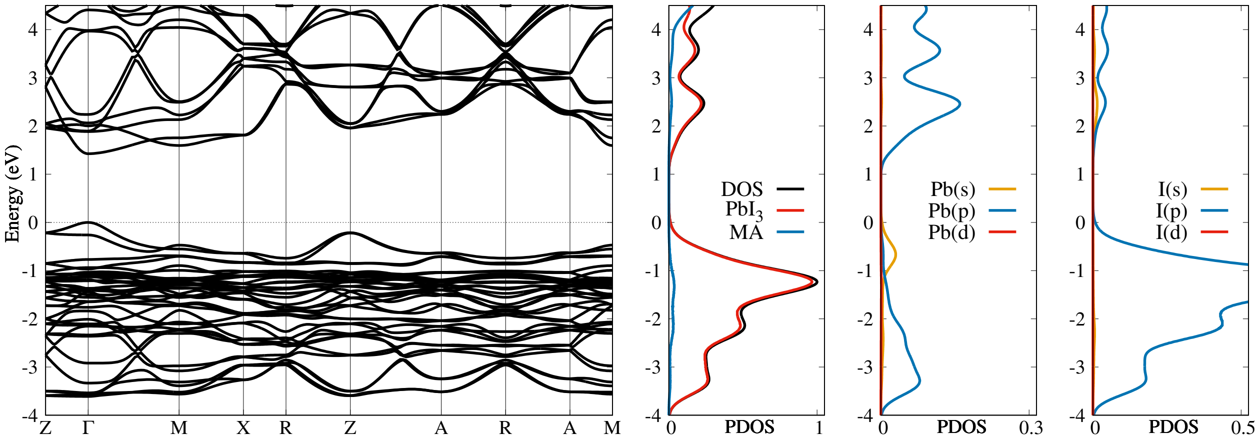

(a) without SOC

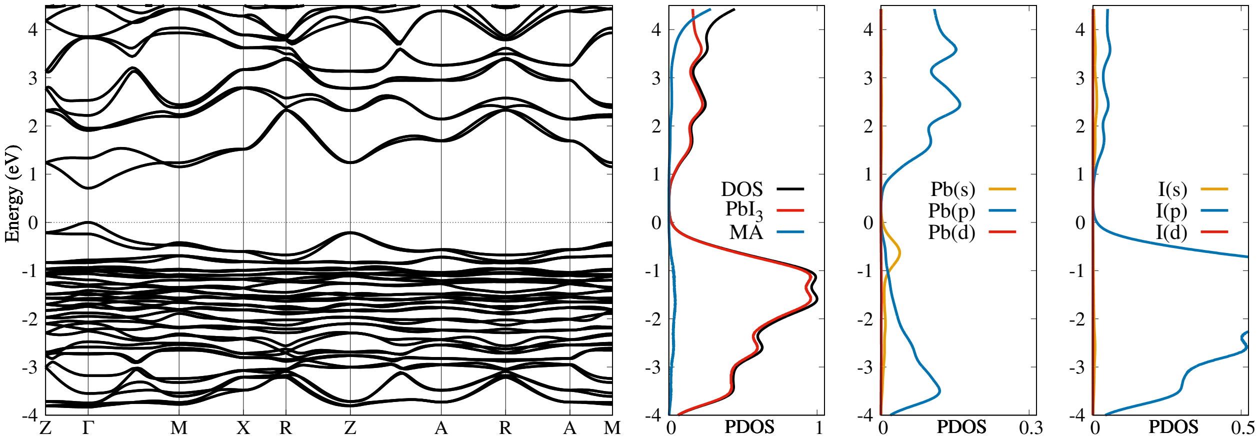

(b) with SOC

Figure 3.3: Band structure (left panel), and atom– and orbital–PDOS (right panels), of tetragonal *Unpol* MAPI at minimum energy volume: (a) without SOC and (b) with SOC. **k**–points used: $\Gamma = (0,0,0)$, $X = (0,\frac{1}{2},0)$, $M = (\frac{1}{2},\frac{1}{2},0)$, $A = (\frac{1}{2},\frac{1}{2},\frac{1}{2})$, $R = (0,\frac{1}{2},\frac{1}{2})$ and $Z = (0,0,\frac{1}{2})$, in terms of reciprocal lattice vectors. Zero energy is defined as E_{VBM}.

but decompress the densely populated zone. Conduction bands exhibit high dispersion as it is expected and the inclusion of SOC strongly affect the shape and dispersion of conduction bands, CBM is the most affected.
The DOS black line in right panels) is mainly and practically complete composed by PbI_3^- octahedra framework states, in the range shown in Fig. 3.3, with both setups. It is worth mentioning that, in this case the PDOS on MA^+ was calculated as the difference of DOS and PDOS on PbI_3^-, *i.e.*, $PDOS(MA^+) = DOS - PDOS(PbI_3^-)$, due to NCPP for carbon, nitrogen and hydrogen atoms did not have its corresponding atomic orbitals. To check it, we compute properly PDOS with USPP obtaining similar results. The valence states are composed mainly by iodine states, 5p subshell, and low amounts of lead states, 6p subshell in deeper valence states and 6s subshell at valence band edge. Conversely, conduction states are composed mainly by lead states, 6p subshell, and low amounts of iodine states, 5p subshell. This explains why conduction bands are highly affected by SOC, which effects are mainly located in heavy atoms, such as lead.
The band gap at this level of theory is, as previously mentioned, "correctly" estimated (1.72 eV) due to the error cancellation between SOC and GGA underestimation due to SIE. But when SOC is included, the underestimation of GGA is evident, resulting in a band gap of 0.74 eV. In order to correct the band gap, we explore different hybrid functionals and G_0W_0 over PBEsol reference. It is expected that the inclusion of exact exchange does not change the shape of band structure and DOS, destabilizing the conduction bands and stabilizing valence bands, moving them rigidly in energy. This can be checked by comparing different functionals in Ref. [44] Fig. 2. Taking this into account, we proceed to explore corrections for VBM and CBM (at Γ–point). As *macroscopic* electrostatic potential does not change when the functional is changed (see Fig. 2.4), we can compare directly the values of E_{VBM} and E_{CBM} computed with different levels of theory using the same cell structure.

VBM and CBM corrections are very different for different functionals, meanwhile band gap values do not change too much among them, as shown Table 3.2. It is worth mentioning that, PBE0(0.188) functional corresponds to the use of SCF *macroscopic* dielectric function of MAPI (5.32) [44]. This functional produces a reliable electronic structure with coinciding band gap for MAPI [44]. All hybrid functionals stabilize the valence bands and conduction bands, but, G_0W_0+SOC shows the most different trend stabilizing valence and conduction bands too much, mainly valence, also band gap is too wide. Probably due to its perturbational approach, which is not variational at all, the valence band is over–stabilized. We will check this computing band edge levels with respect to vacuum latter, see Fig. A.2. Other approaches, three hybrid functionals exhibit similarities and differences among them. HSE+SOC and PBE0(0.188)+SOC produce practically the same valence band correction, meanwhile a different conduction band

Table 3.2: E_{VBM} and E_{CBM} energy corrections for PBEsol computations, using different levels of theory with the minimum energy cell structure. Energy corrections ($E_{\alpha,corr}$ informed as: $E_\alpha(i) - E_\alpha(\text{PBEsol})$*. All values in the Table are in eV.

Functional	HSE+SOC	G_0W_0+SOC	PBE0(0.188)+SOC	PBE0+SOC
$E_{VBM,corr}$	−0.44	−1.42	−0.48	−0.75
$E_{CBM,corr}$	−0.95	−1.16	−0.70	−0.70
E_g	1.24	2.10	1.54	1.80

* Reference energy levels computed with PBEsol without SOC.

corrections. Conversely, PBE0(0.188)+SOC and PBE0+SOC produce practically the same conduction band correction, meanwhile a different valence band corrections. HSE+SOC and PBE0+SOC does not produce similar corrections at all.

Taking this into account, and checking for the best band gap predicted in comparison with nominal band gap of 1.60 eV, tuned PBE0(0.188)+SOC functional is the best suited for this purpose. Also HSE+SOC functional will produce reliable results for valence band energy, meanwhile conduction band energy will be lower in energy underestimating the band gap in ~ 0.3 eV.

3.2 Surfaces: Structure, Properties and Thickness Convergence

We modeled MAPI surfaces as slab models constructed by replication of MAPI unit cell. Slab models of MAPI(001) surfaces were obtained cleaving bulk supercells at selected atomic planes with orientation (001). Let us define the slab stoichiometric unit as a couple of adjacent MAI and PbI_2 (001) planes that span half of a unit cell with thickness $c/2$. Mind that $c/2$ roughly equals the lattice parameter of the cubic phase of MAPI. Henceforth, the number of stoichiometric units define the slab thickness, as well as the number of MAI and PbI_2 planes. An additional PbI_2 or MAI plane was added to each slab in order to have two symmetric surfaces (breaking the system stoichiometry but not the charge stoichiometry), and to avoid internal electric field. Hence, a MAPI(001)–PbI_2 slab of n stoichiometric units has a total of n MAI layers, and $n+1$ PbI_2 layers, while for MAPI(001)–MAI the numbers are permuted.
The lattice vectors parallel to the surface can be linear combinations of the primitive vectors, allowing for surface reconstruction. Hence, we employ the slab nomenclature $(m \times m) \times n$ for the slab models, were m indicate the unit cell multiplication in each orthogonal direction along the surface. The index n indicates the number of stoichiometric units along the direction [001]. All the atomic coordinates within the slabs were relaxed with the a and b cell vectors fixed at their bulk values. The cell vector perpendicular to the surface was also kept fixed.
In order to avoid using dipole correction [216,217], the slabs and their surfaces were constructed and relaxed, canceling the dipoles presented in surfaces, mainly, by MA^+ rotations. We did not enforce the use of symmetry elements (mirror planes, inversion, for example) on the calculation, albeit the crystal geometry remained very close to its symmetric structure, which presents these elements of symmetry.

3.2.1 Slab Thickness Convergence

We study the convergence of the electronic state energies, band gap, surface energies, and structural parameters, with respect to the slab thickness, for $(1 \times 1) \times n$ slab without and with the SOC. Also convergence of vacuum width is studied in Appendix A.4. We have classified the different slab states, through inspection of spatial localization of squared wavefunctions, into surface states and bulk confined states (VBM and CBM). The electronic states were studied at the Γ–point, obeying the position of the bulk VBM and CBM (see the band structure diagrams in Fig. 3.4).

The first checked item was the convergence of the energy levels with respect to the slab thickness. Fig. 3.5 shows, for MAPI(001)–PbI_2 and MAPI(001)–MAI slabs, the dependence of the frontier energy levels (relative to the vacuum level). The blue and sky blue symbols correspond to the quantum confined states of CBM (top plot), and the VBM (bottom plot). The CBM is the LUCO for both surface types. In MAPI(001)–PbI_2, the HOCO and the next (HOCO-1) are surface states, which are doubly degenerate because this slab model has two equivalent surfaces. Thus, the VBM is the HOCO-2. This is consistent with previous reports [74]. The surface states are caused by the cleavage of iodine octahedra around surface lead atom, which generates naked lead atoms with dangling bonds. For MAPI(001)–MAI, the

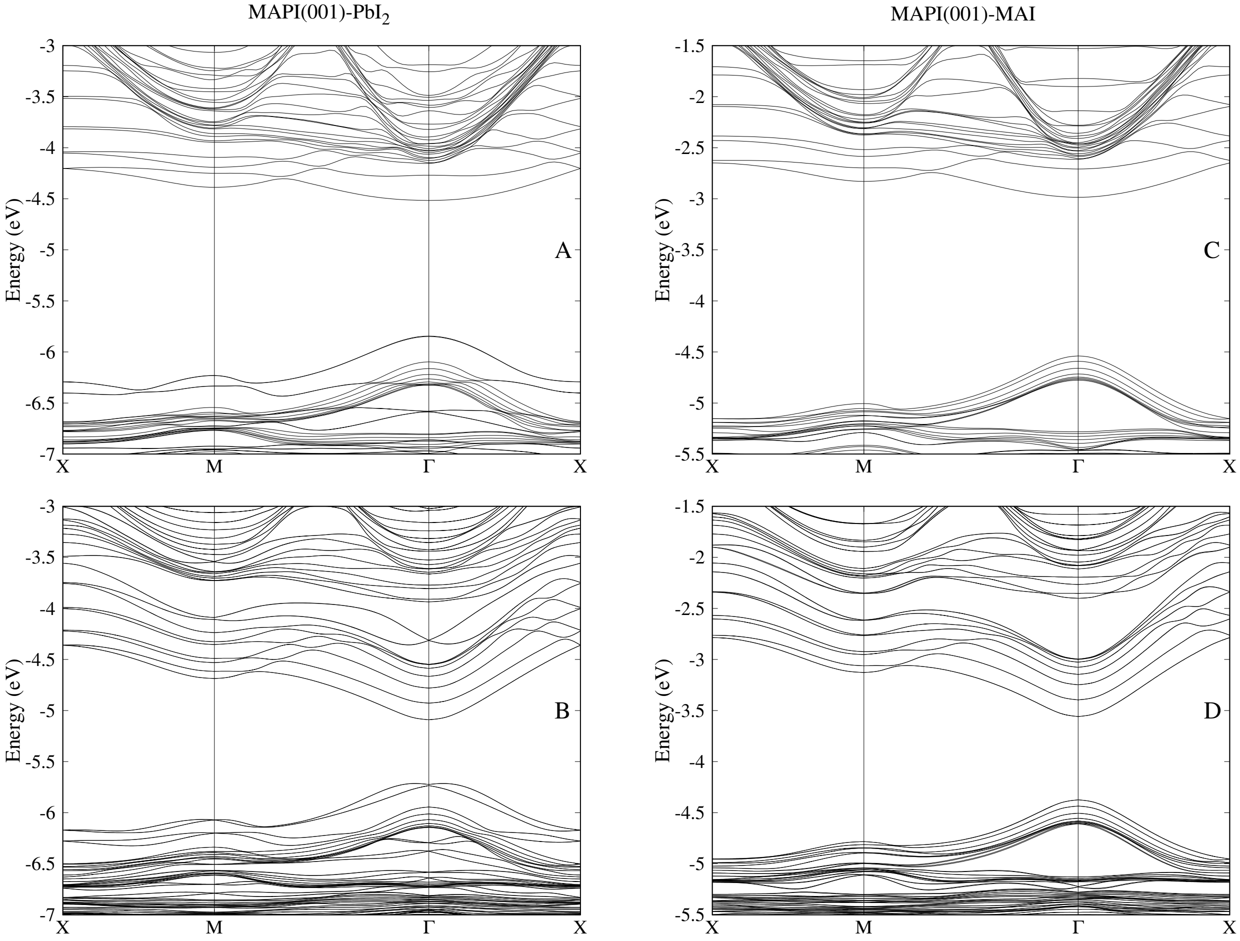

Figure 3.4: Band structure diagrams of $(1 \times 1) \times 8$ MAPI(001)–PbI$_2$ and MAPI(001)–MAI. (A) and (C) PBEsol. (B) and (D) PBEsol+SOC. Energies with respect to vacuum level. The occupied in–gap surface states of MAPI(001)–PbI$_2$ are located at Γ–point. Particularly, when the SOC is included, a small splitting of surface states along crystal momentum axis is observed. **k**–points used: $\Gamma = (0,0,0)$, X$= (0, \frac{1}{2}, 0)$ and M$= (\frac{1}{2}, \frac{1}{2}, 0)$.

VBM confined state is the HOCO, no surface state has energy within the gap. The red and black symbols correspond to the CBM and VBM energies, respectively, obtained from the two–step procedure explained in Chapter 2, Section 2.5. Its dependence on the slab thickness follows the behaviour of the average electrostatic potential at slab center $\bar{V}(z_{in})$, from which they differ in constant values (Eq. 2.29).

Geng *et al.* [75] have reported that the MAPI(001)–PbI$_2$ band gap depends weakly on slab thickness, also being smaller than the band gap of MAPI(001)–MAI. Our results show that the HOCO and HOCO−1 in MAPI(001)–PbI$_2$ are surface states, which explain the weak dependence and reduced band gap value (see Fig. 3.6). Moreover, surface state (HOCO) and CBM (LUCO) present a similar energy variation with respect to the slab thickness, leading to a nearly independent HOCO–LUCO gap (in the thinner slab thickness regime).

Fig. A.4 and A.5 show several squared wavefunctions (HOCO, LUCO, etc.) and their energies for $(1 \times 1) \times 8$, MAPI(001)–PbI$_2$ and MAPI(001)–MAI, respectively, averaged like Eq. 2.26. Here,

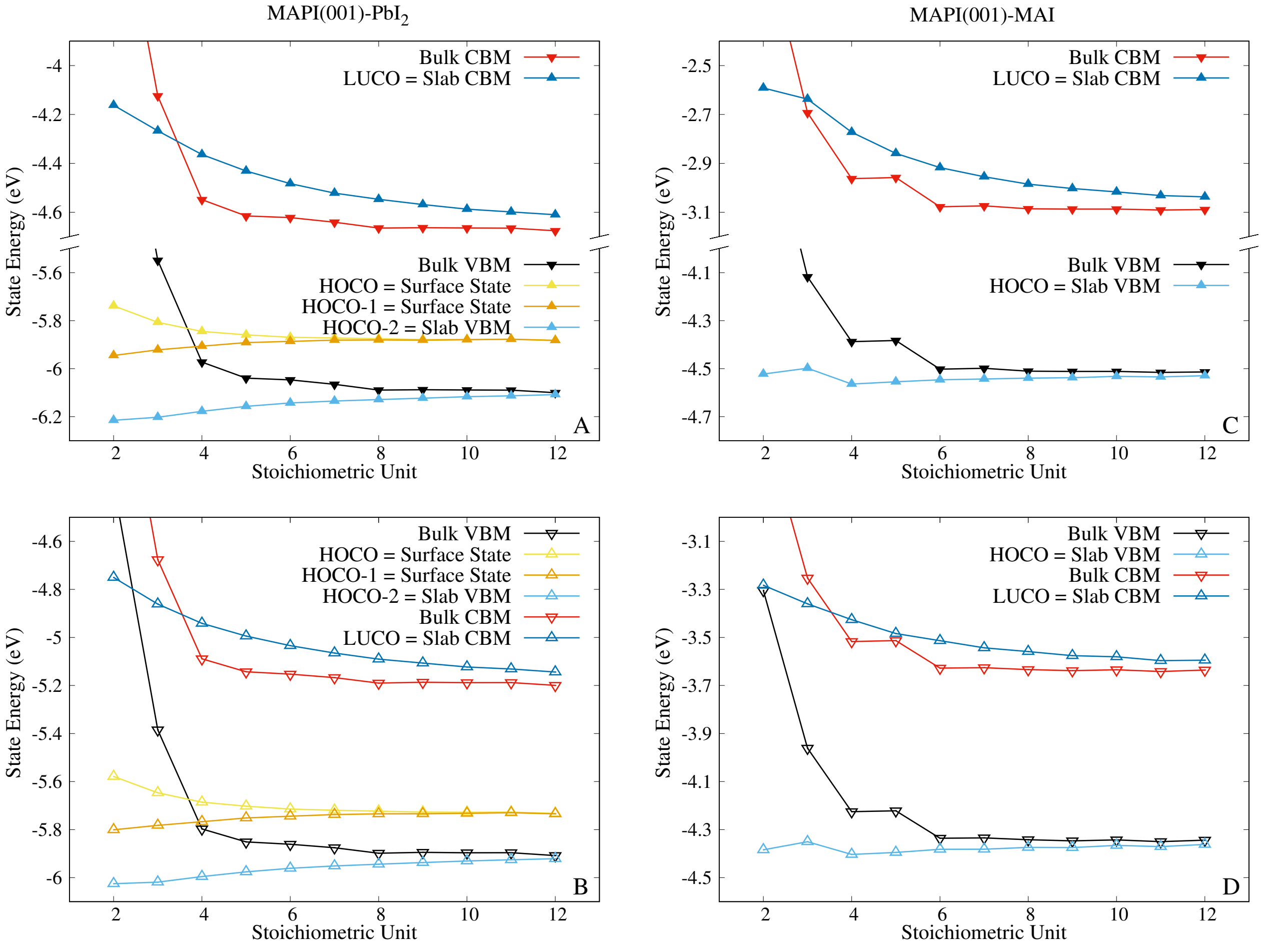

Figure 3.5: Convergence of energy slab levels, at Γ–point, with respect to slab thickness. (A) and (C) PBEsol. (B) and (D) PBEsol+SOC. Energies with respect to vacuum level

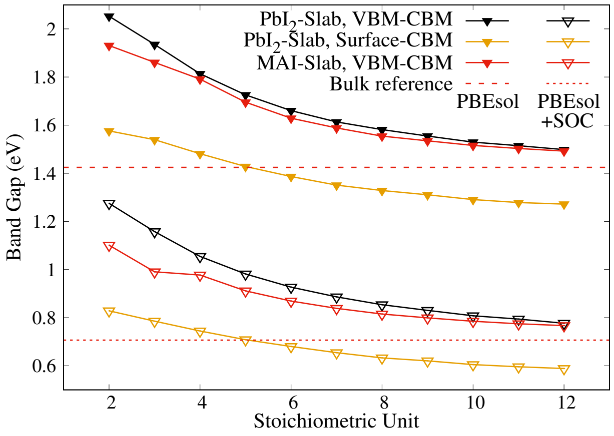

Figure 3.6: Convergence of MAPI(001)–PbI_2 and MAPI(001)–MAI band gap (for inner slab bands and surface slab bands) with respect to slab thickness.

the surface character of the HOCO and HOCO−1 are clearly appreciated in MAPI(001)–PbI_2 case. These states are localized mainly on the surface PbI_2 layers. For the other states, the bulk character and the QC effect are clearly appreciated in Fig. A.4 and A.5. In the envelope function approximation [218], the band edge wavefunctions are products of Bloch functions (oscillating at the atomic–scale) and slowly varying envelope function, which are of sinusoidal type in the quantum wells [31]. The envelope function tends to zero at the surface and has l nodes inside the slab for VBM$-l$ and CBM$+l$ states. There are also pseudo–nodes with smaller periodicity length along the slab, due to the Bloch function oscillation.

We see that, regardless of surface termination, the variation of slab state energies due to QC with respect to the slab thickness (see Fig. 3.5) is almost the same for calculations without (top) and with SOC (bottom). The main difference between calculations without and with SOC (beyond states energies changes and decreased band gap) is in CBM (and higher states) squared wavefunction shapes. The wavefunctions with SOC have smoother profiles.

The VBM and CBM confined states energies in Fig. 3.5, exhibit QC behaviour, as expected, in all cases. The CBM and VBM exhibit up (positive effective mass) and down (negative effective mass) energy shift, respectively, for thinner slabs. While the energy convergence is faster in VBM case, CBM presents QC even for the thickest calculated slab. This explains the VBM–CBM band gap over–estimation (respect to bulk band gap) in all cases (see Fig. 3.6). When $n < 4$, some VBM or CBM energies do not present smooth behaviour, and the slabs are too thin to host bulk–like states. This shows the bulk–inner slab description is poor at this regime. Also, the two–step procedure VBM and CBM are not well described in this ultrathin slab regime. For $n = 4$, the energies are roughly converged, and for $n \geq 6$ are tightly converged, in all cases. The two–step procedure is, in principle, free of QC. This conception was checked, and for $n \geq 6$, the VBM and CBM present asymptotic behaviour.

Finally, the surface states (MAPI(001)–PbI_2 slab models) exhibit energy splitting, in the thinner regime. When the slab is sufficiently thick ($n = 6$ and $n = 7$, for calculations without and with SOC, respectively), they are degenerated. This behaviour shows that splitting is due to surface state interaction (repulsion, like for the He_2 dimer) through inner slab space, and no through vacuum space.

The last parameter studied is the surface energy. Fig. 3.7 displays the surface energy as a function of the slab thickness. For a $\beta = PbI_2$, or MAI surface type, this energy can be computed as

$$S^n_\beta = \frac{1}{2A_{xy}}\left(E^n_{slab,\beta} - \frac{n}{2}E_{MAPI} - E_\beta\right) \quad , \tag{3.1}$$

where $E^n_{slab,\beta}$ is the total energy of an n–stoichiometric units slab with two surfaces of type β, E_{MAPI} is the total energy of tetragonal bulk MAPI, and E_β is the total energy of solid bulk PbI_2 or MAI. The latter is the sum of chemical potentials of the out–of–stoichiometry species in β–rich condition. The double surface counting is corrected with the $\frac{1}{2}$ factor, and normalized with respect to surface area A_{xy}. Error bars were conservatively defined as the sum of error from each calculation parameter. For further details see Appendix A.3.

The surface energy, for both surface types, and for calculations without and with SOC, are converged for all thicknesses, as shown Fig. 3.7. In MAPI(001)–MAI case, the surface energy presents periodic oscillations, for even and odd number of stoichiometric units. This is due to the existence of small dipoles asymmetries, between MA^+ in both surfaces, but these differences are within the error bars. About 99 % of the error is associated with **k**–point grid, and the rest associated with cutoff, see Appendix A.3. Also, the negative value in surface energy is explained

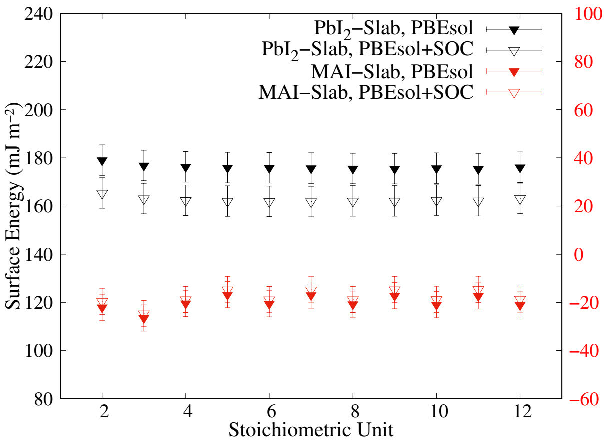

Figure 3.7: Convergence of MAPI(001)–PbI$_2$ and MAPI(001)–MAI surface energy with respect to slab thickness.

by MA$^+$ inversion, and independent of MAI bulk reference [219–221]. Before geometrical relaxation, the surface energy is positive as expected ($\sim$ 110 mJ m^{-2}).
In MAPI(001)–PbI$_2$ case, the surface energy behaves smoothly because both surfaces are highly symmetric for even and odd number of stoichiometric units. The higher surface energy in this case is explained by the contribution of surface states. We have used the PbI$_2$ bulk structure of Ref. [222]. The inclusion of SOC in the calculations does not significantly change the surface energies for both surface types. SOC has a small effect in total energies, reinforcing not having included it in the atomic relaxation calculations. In MAPI(001)–MAI case, SOC effect is negligible. While, in MAPI(001)–PbI$_2$ case, surface energy has rigid downshifts. As this case has surface states located in lead and iodine atoms (heavier atoms), is understandable that SOC shifts are not totally negligible.

For all the thickness range considered, the geometrical parameters undergo minimal variations, matching the constancy of the surface energies.

3.2.2 Square Well Approximation and Quantum Confinement

As has been discussed before, inner slab states present QC. They are 2–D delocalized states in (001) plane, but confined along [001] direction (z axis). Moreover, the trends in the electronic state energies can be fitted with an infinite potential well model. Other considerations follow. The squared wavefunction envelopes, which modulate the Bloch functions, have sinusoidal behaviour. The state energies behaviour seems consistent with a squared hyperbola curve, with asymptotic convergence at high stoichiometric unit number. Also, the *macroscopic* electrostatic potential presents pseudo–square well shape.

Therefore, we propose the following analytical function, based on the infinite potential well energies, to obtain the correct behaviour relative to curvature and thickness dependence

$$E_\alpha(n) = \frac{\gamma}{(n\frac{c}{2} + 2\sigma)^2} + E_\alpha(\infty) \quad , \quad (n \geq 4) \tag{3.2}$$

Table 3.3: Fitted Eq. 3.2 parameters for VBM and CBM (calculations without and with SOC).

α	γ (eV Å^2)	σ (Å)	$E_\alpha(\infty)$ (eV)
	MAPI(001)–PbI$_2$		
CBM	+808.65	12.111	−4.690
VBM	−225.05	12.420	−6.088
CBM$_{SOC}$	+859.81	15.020	−5.219
VBM$_{SOC}$	−392.29	17.935	−5.891
	MAPI(001)–MAI		
CBM	+439.55	5.682	−3.096
VBM	−97.64	10.965	−4.521
CBM$_{SOC}$	+338.31	7.218	−3.639
VBM$_{SOC}$	−181.56	16.131	−4.349

where $E_\alpha(n)$ is the state energy as a function of the number of stoichiometric units n, with α defined in Table 3.3. $c/2$ is the stoichiometric unit thickness (6.745 Å). γ, σ, and $E_\alpha(\infty)$, are the adjustable parameters. The first parameter, γ, is proportional to the curvature of the function. The second, σ, is a correction factor to account the effect of finite and a pseudo–square well. Finally, $E_\alpha(\infty)$ is the asymptotic value of state energy at infinite thickness. The parameter values are shown in Table 3.3. We used the confined state energy data from $n = 4$ to 12 for all fits.

Fig. A.6 shows that the functions $E_\alpha(n)$ fit the data with extreme accuracy, where root mean square of residues and $\bar{\chi}^2$ values are negligible, with orders of 10^{-3} and 10^{-5}, respectively.

The $E_\alpha(\infty)$ values show that the CBM (in all cases) exhibit QC even for the thickest slab models ($n = 12$), while the VBM are less affected, as previously discussed. Furthermore, the two–step process for $n \geq 4$, provides CBM and VBM energies close to $E_\alpha(\infty)$, showing faster convergence than the slab state energies.

The band gap calculated from the asymptotic energy values without SOC are 1.40 and 1.43 eV for PbI$_2$ and MAI surfaces, respectively, which match the value 1.43 eV computed in the bulk system. With SOC, the asymptotic energy values are 0.67 and 0.71 eV for PbI$_2$ and MAI surfaces, respectively, matching the bulk value 0.71 eV.

The SOC correction (Δ_{SOC}) is defined as the difference between state energy function with and without SOC,

$$\Delta_{SOC}(n) = E_{\alpha_{SOC}}(n) - E_\alpha(n) \quad , \tag{3.3}$$

while the QC correction (Δ_{QC}) is defined as the difference between the asymptotic value of state energy and the state energy function,

$$\Delta_{QC}(n) = E_\alpha(\infty) - E_\alpha(n) = \frac{-\gamma}{(n\frac{c}{2} + 2\sigma)^2} \quad . \tag{3.4}$$

Fig. A.7 and A.8 show Eq. 3.3 and 3.4, respectively, using data from Table 3.3. Δ_{SOC} presents near constant behaviour for all cases in the fitting range. Also, the Δ_{SOC} are practically equal to the value computed in the bulk system. Δ_{QC} is the negative of the QC energy.

This correction scheme allows to obtain the QC–free state energies from a thin slab calculation performed with or without SOC.
Currently the use of so–called "quantum well technology" is present in experimental solar cells, such as tandem solar cells [223]. Optimizing the thickness of absorber material making it as thin as possible, the band gap can be controlled to optimize it at the best value enhancing the performance of the solar cell. This enables the use of absorber materials which do not have quite the correct band gap. Moreover, the Ruddlesden–Popper halide perovskites, which are dielectric well structures formed by two–dimensional layers of halide perovskite separated by butylammonium spacer layers, have been studied experimentally and theoretically showing the QC effect on band gap [224].

3.2.3 Convergence Model Criteria

The previous subsections show the convergence studies for slab thickness and vacuum width, using a set of energetic, and states variables. Here, we summarize the most important results and their implications. In all slabs studied as MAPI(001) models, the VBM and CBM state energies present QC (greatest in CBM states), artificially increasing the band gap. We propose a correction scheme (Δ_{SOC} and Δ_{QC}), based on the square well approximation, to obtain energies of QC–free states. The MAPI(001)–PbI_2 models exhibit occupied surface states, caused by cleavage of surface iodine octahedron, which trigger a reduction in band gap. The state energies obtained through the two–step process depend on the *macroscopic* electrostatic potential, and this parameter rapidly converges with the slab thickness. According to this method, the slab requires a minimum thickness of $n = 4$, but $n = 6$ is considered the optimal thickness to obtain state energies numerically close to the converged eigenvalues. Two–step process does not show the existence of in–gap surface states. The surface energies depend weakly on the slab thickness. Also, all parameters present weak dependence on the vacuum width.

3.2.4 Surface Structure and Thermal Motion

It is well known that distortion effects suffered by MAPI perovskites, unlike the low temperature orthorhombic phase, should be considered to adequately estimate their electronic properties. Many times, the calculations show that a single conformation, usually those with greater symmetry, unequivocally represents the minimum of internal energy. However, thermal motion actually breaks this symmetry and the system must be represented by a set of distorted conformations representative of the phase.

We simulate dynamic trajectories of the $(2 \times 2) \times 6$ slabs and with them we assess the distortions by thermal motion. Starting at 600 K in the microcanonical ensemble, our surface models reach equilibrium at 291 and 294 K for MAPI(001)–PbI_2 and MAPI(001)–MAI slabs, respectively. With these trajectories we were able to evaluate the structure of the surfaces, validate our supercell models obtained at 0 K, and calculate the band edge shifts from representative structures of the tetragonal phase surfaces. Finally, we also verify if a small deformation in the *ab* plane of the slab models could affect the band edge states.

We begin the analysis verifying that both static (0 K) and dynamic slab models, preserve the tetragonal phase in the slab interior. As explained in Ref. [45], the tetragonal phase is geometrically described by a set of parameters. These include: (1) dihedral, rotation, apical, and equatorial angles of the inorganic framework (see Table S2 in Ref. [1]), and (2) angles defining the orientation of the MA^+. First, we measured these parameters on the surface and internal layers of the slab models. As reference, we consider reported mean values and their standard deviations for bulk MAPI [45]. The dynamic slab models have the inorganic framework parameters within the reported range for the bulk phase. Thermal motion mainly cancels out the differences in these parameters between the surface layers and bulk (inner) layers. Furthermore, there are no significant differences in the parameters between the two types of slabs. Similar to the dynamic models, the static slab models represent the tetragonal phase, although the apical angle (Pb–I–Pb along the z axis) shows deviations.

The orientation of the MA^+ significantly differs at surface and bulk layers. It allow us to consider the angle between the vector representing the C–N bond and the lattice *ab* plane, called polar angle. Fig. 3.8 shows the distributions of polar angles for all the layers of MAPI(001)–MAI and MAPI(001)–PbI_2 slabs. The distributions indicate that the MA^+ tend to have a preferential dipole orientation at the surface layers that disappears in the bulk. For MAPI(001)–MAI surface, the surface MA^+ has all the CH_3 groups pointing outward (to the vacuum) all the time. On the other hand, for MAPI(001)–PbI_2 surfaces, the sub–surface MA^+ present both orientations, but the higher peak of the distribution corresponds to NH_3^+ groups pointing outward. In this case, it is observed that MA^+ changes its orientations during the trajectory. For inner (bulk) layers under both types of surface, the polar angles are distributed with two almost symmetrical peaks. There is also a surface effect on the inclination of the cation that is independent of the surface termination, the polar angle is 22° in the bulk, while on the surface it is greater than 50° degrees.

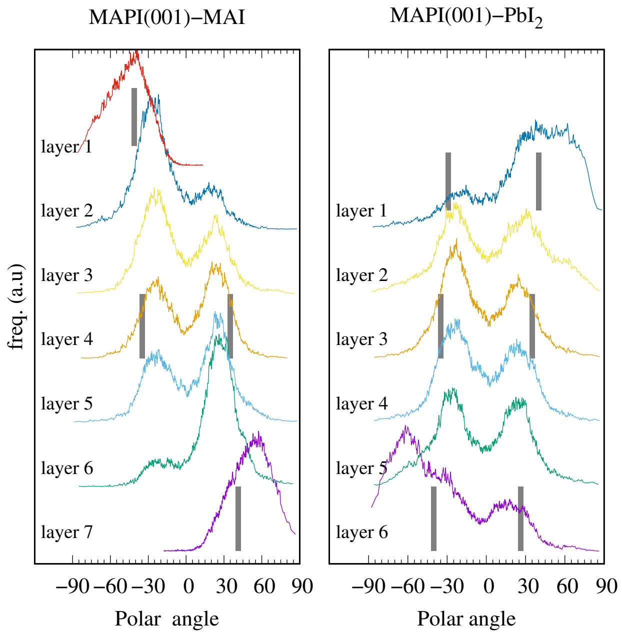

Figure 3.8: Distributions of C–N polar angles for every layer of MAPI(001)–MAI and MAPI(001)–PbI_2 slabs. Vertical lines indicate the average angles for static slab models.

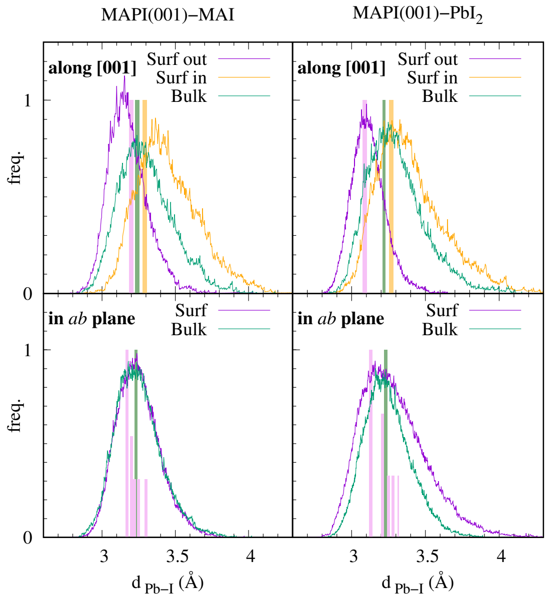

Figure 3.9: Distributions of the Pb–I bond distances along [001] direction and parallel to the *ab* plane, for MAPI(001)–MAI and MAPI(001)–PbI_2 slabs. *Surf out* and *Surf in* refer to the outermost bonds, and the next below, respectively. *Bulk* refers to bonds at slab centers. Vertical lines correspond to the average bond distances of the static slab.

The static model of MAPI(001)–MAI reproduces the preferred MA^+ orientation at the surface, and agrees with previous reports with static [77] and dynamic [76] calculations. These reports linked the inversion of MA^+ at the surface with weak interactions, accounted through vdW functionals and Grimme dispersion correction, respectively. In contrast, we found this MA^+ orientation even without considering the vdW corrections while using PBEsol functional in convergence studies. We realize that this orientation is maintained by electrostatic interactions and mainly by hydrogen bonds of each surface iodine atom with two nearby cations simultaneously. Hence, each surface iodine atom increases its coordination number, which decreases surface energy and increases surface stability compared to other configurations. Under these interactions, the I–I interatomic distances are significantly reduced compared to the other situations. The dynamic model suggests, as will be discussed later that it is possible to observe a pattern of rearrangement of iodine atoms at the surface due to these interactions.

The static model of MAPI(001)–PbI_2 does not reflect the trends of the MA^+ orientations observed during the dynamics. In this case, the model in which no MA^+ layer has a net dipole moment (*unpolarized* slab) corresponds to the conformation of minimum (internal energy). The formation of *polarized* slabs, in which all the cations of the first layer have the NH_3^+ group facing outward, is energetically feasible ($\Delta E = +0.1$ eV/MA^+ with respect to the *unpolarized* slab). In both structures it is observed that NH_3^+ groups form hydrogen bonds creating a network of similar interactions with the nearest iodine atoms. Unlike MAPI(001)–MAI surface, the MA^+ orientation preference observed in this case as *polarized* model, could be justified by the electrostatic interaction between NH_3^+ groups and high electronic density in surface (due to the surface states).

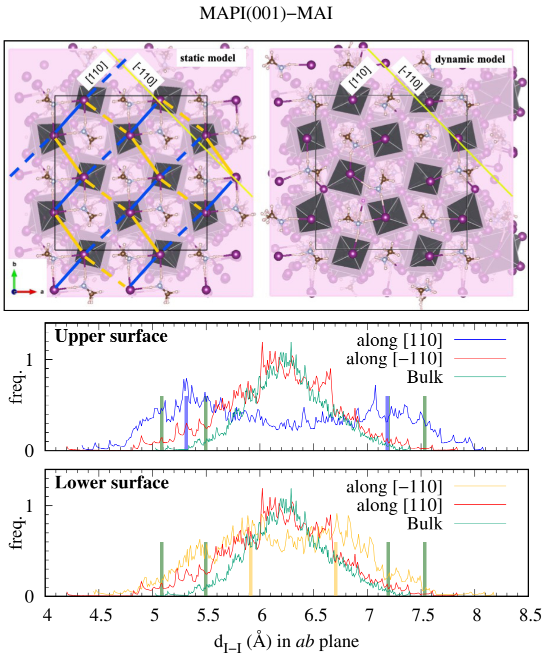

Figure 3.10: Top left: surface layer of relaxed static slab. Top right: MD snapshot of surface layer. Bottom: distribution of I–I distances for iodine atoms in several (001) planes: upper surface, central planes (bulk), and lower surface. Vertical lines are the average I–I distances in static slabs.

Fig. 3.9 shows that both types of MAPI surfaces undergo relaxation along the c axis, but not in the ab plane. There is a reduction in the Pb–I bond distance distribution of the outermost surface layers as compared to the bulk (inner) layers. In the figure, the labels *Surf out* and *Surf in* mean the Pb–I distance distributions in the outermost layer (out) and the next closest to it (in), while *Bulk* label means the average distribution of two layers in the center of the slab. On average, the difference between *Surf out* and *Surf in* is around 0.25 Å on both types of surfaces. However, the distance Pb–I in MAPI(001)–PbI_2 is reduced by 0.16 Å with respect to bulk, while this difference is 0.08 Å for the MAPI(001)–MAI slab. There is no significant difference between the Pb–I average distance in the bulk of both models, as expected. Notice that the corresponding distance of the static models, represented by vertical lines, reproduces the dynamic behaviour in the case of the MAPI(001)–PbI_2 slab. The static model of the MAPI(001)–MAI slab hides this surface relaxation phenomena observed while considering the thermal motion. This means that the static model is one of the possible configurations that represent the surface properties. However, distorted configurations should be also used to model the surface electronic properties.

As noted above, our MAPI(001)–MAI model also shows regular rearrangements of iodine atoms at the surface compared to those in–bulk, which are related to stabilizing interactions with MA^+. According to the I–I distance distributions, the surface layers show iodine arrangements in a certain order depending on the crystallographic orientation on the surface (Fig. 3.10, bottom). In contrast, the iodine atoms in the bulk show a unique (6.2 Å as average), although wide distribution due to thermal motion. During dynamic equilibrium, organic cations experience different orientations within the lattice ab plane, and the I–I distance distributions have maximum at 5.4 / 7.1 Å in the upper surface and at 5.9 / 6.7 Å in the lower surface. Perpendicular to the surface (along [001]), both surfaces show that the I–I distance has a wide distribution at an average of 6.2 Å, as in the bulk. Notice that two different surfaces are obtained for this slab. The surface of the static model (Fig. 3.10, top left), as ideally ordered reference, let to understand that, if two iodine atoms share hydrogen bonds with the same cations, they approach to a distance of 5.4 Å (or move away to 7.1 Å), in average. The rest of the distributions correspond to situations where hydrogen bonds with organic cations are also presented, but without a regular order as in a snapshot of the dynamic (Fig. 3.10, top right). Notice that in the static model the hydrogen bonds are maximized, either at the surface or in the bulk. The iodine arrangement patterns found on the surface are consistent with the results obtained from the *in situ* STM experiment of this type of surface, but for the low temperature orthorhombic phase [67]. Despite the limited size of our models, we believe that our evaluation can contribute to the analysis of surface phenomena in similar experiments in the tetragonal phase.

It should be noted that in convergence study, all models independently of thickness show similar surface structural features as described here for static models. The fact that the geometry of the static models does not show appreciable changes, explains the small variations found in the calculated surface energy based on the thickness of the slabs.

3.2.5 Slab Energy Levels and Band Edge Shifts

Hereinafter, we summarize our results on the electronic properties of modeled MAPI(001)–PbI_2 and MAPI(001)–MAI surfaces. First, the electronic structure of static models is described, for which it is feasible to explore different theoretical approaches. Then, given the dynamic models, we can assess the influence of the structural distortions on the slab energy levels and the band energy shifts that may occur.

Fig. 3.11(a) shows the DOS and the plane PDOS for the MAPI(001)–PbI_2 surface comparing the optB88–vdW and HSE+SOC methods. Based on dynamic analysis, we consider adding a static model of this surface that we call *polarized*. This *polarized* model is a configuration in which the NH_3^+ groups of the surface layers are oriented outward. Fig. 3.11(a) shows the DOS of both models, *unpolarized* (solid lines) and *polarized* (dashed lines), to compare. For both methods the HOCO is a surface state (one spin–degenerate for each surface). The valence band confined states are below in energy, close to the bulk VBM, as expected from Fig. 3.5. Method optB88–vdW shows more surface states with energies close to VBM, while with HSE+SOC these surface states are a bit deeper in energy, but still close to the VBM. The DOS rises more abruptly near the CBM with optB88–vdW, because the lack of SOC causes the conduction bands to be flat in some directions. The QC is apparent on the conduction bands DOS, the first peak is higher than the bulk CBM, and it is absent in the PDOS on the surface plane. The DOS of the *polarized* model is quite similar to the corresponding *unpolarized* one, except that the states of the former are shifted to higher energies (blue–shifted). Table 3.4 presents a comparison of the energy levels obtained with the different approaches: (1) all with the vdW (optB88–vdW) functional, (2) mixed approach combining vdW and hybrid functional with SOC, and (3) all with the hybrid functional with SOC. Let us recall that in the mixed approach, the SCF slab calculation have been performed with the vdW functional, from which the term $\bar{V}(z_{in})$ in Eq. 2.29 is taken, while the bulk VBM and CBM energies $\left(E_{\alpha}^{3D} - \bar{V}^{3D}\right)$ are taken from a

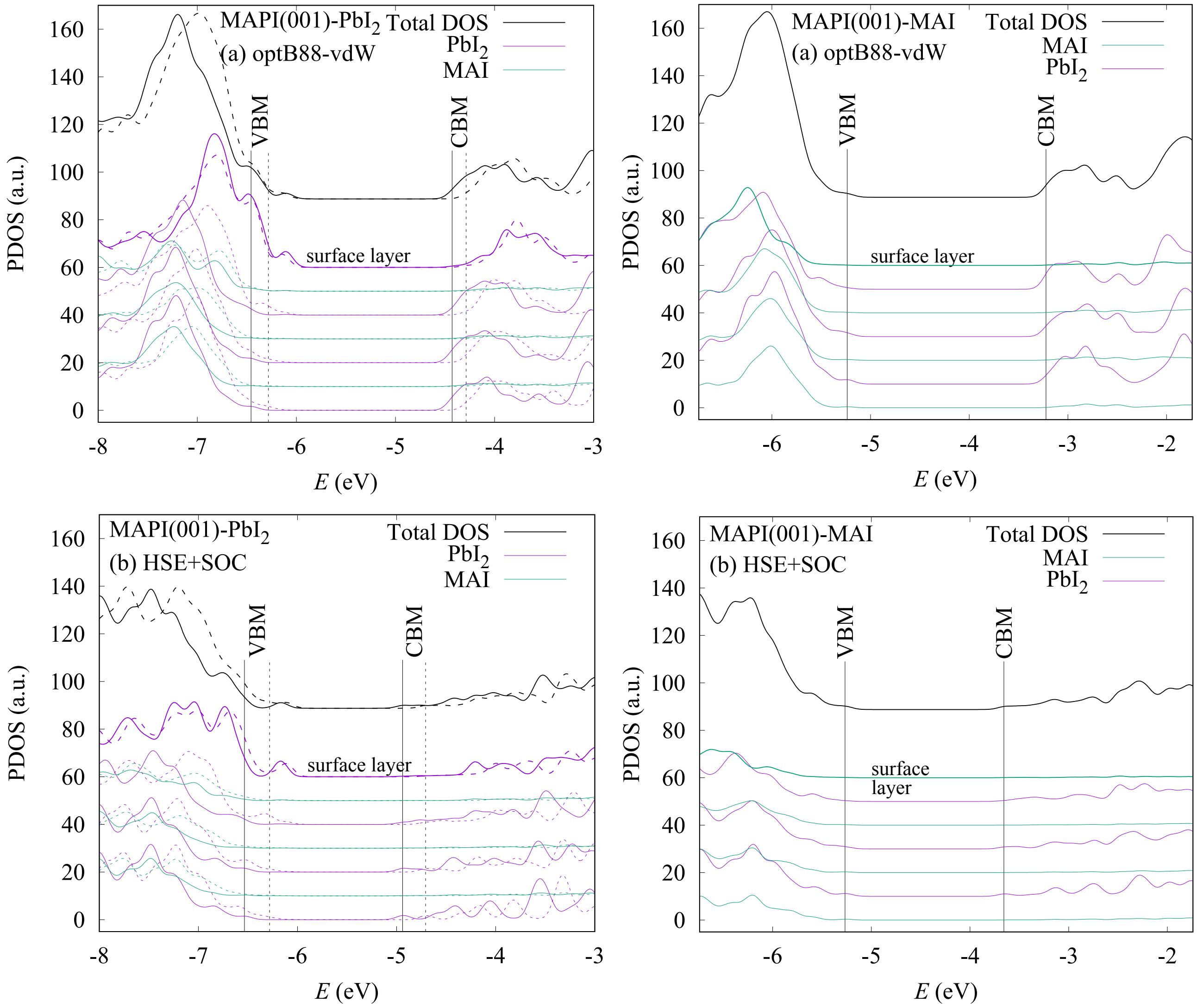

(a) MAPI(001)–PbI$_2$

(b) MAPI(001)–MAI

Figure 3.11: Projected DOS on PbI$_2$ and MAI layers from surface to interior, for: (a) MAPI(001)–PbI$_2$ *unpolarized* (solid lines) and *polarized* (dashed lines) and (b) MAPI(001)–MAI. Calculations performed with optB88–vdW (top) and HSE+SOC (bottom) methods. The energies of bulk VBM and CBM are indicated.

hybrid functional calculation HSE+SOC. Also, shown are the energies of the slab quantum confined frontier orbitals $E^{slab}_{VBM,CBM}$, and the energy of the highest occupied surface state E_{surf} (HOCO), both with the vdW and the hybrid functional. The differences between (2) and (3), are due only to $\bar{V}(z_{in})$, which turn out to be smaller than 0.05 eV, this is a minor difference. Also, for the sake of completeness, we include also results obtained with QE for vdW functional. The differences of (2) and (3) with (1) are large for the VBM and CBM, which is well understood in terms of the famous gap error and the above discussion. Notably, the surface state energy is similar with both functionals. It would be wrong to obtain E_{surf} by applying a correction to the vdW value.

There is other difference between optB88–vdW and HSE+SOC. For a slab made with a

Table 3.4: Band edges, and slab energy levels with respect to the vacuum level for a slab MAPI(001)–PbI_2 and MAPI(001)–MAI. E_{surf} is the energy of top surface states (HOCO). E^{slab}_{VBM} and E^{slab}_{CBM} are the energies of the first quantum confined states[a] of the valence and conduction bands, respectively.

Method	E_{VBM}	E_{CBM}	E_{surf}	E^{slab}_{VBM}	E^{slab}_{CBM}
			MAPI(001)–PbI_2 *unpolarized* (*polarized*)		
optB88–vdW (QE)[c]	−6.49 (−6.22)	−4.60 (−4.33)	−6.13 (−6.06)	−6.48 (−6.22)	−4.51 (−4.29)
optB88–vdW (VASP)[c]	−6.48 (−6.27)	−4.53 (−4.31)	−6.11 (−6.14)	−6.46 (−6.28)	−4.43 (−4.29)
HSE+SOC (VASP)[b]	−6.61 (−6.39)	−5.11 (−4.90)	–	–	–
HSE+SOC (VASP)[c]	−6.56 (−6.27)	−5.07 (−4.78)	−6.18 (−6.12)	−6.54 (−6.28)	−4.94 (−4.71)
			MAPI(001)–MAI		
optB88–vdW (QE)[c]	−5.22	−3.33	–	−5.23	−3.28
optB88–vdW (VASP)[c]	−5.23	−3.27	–	−5.24	−3.19
HSE+SOC (VASP)[b]	−5.35	−3.86	–	–	–
HSE+SOC (VASP)[c]	−5.25	−3.76	–	−5.27	−3.66

[a] To obtain QC–free energies, the quantum confined correction with SOC for $n = 6$ slab model, must be added. $\Delta_{QC} = 0.07$ and -0.18 eV for VBM and CBM in PbI_2 surface. $\Delta_{QC} = 0.04$ and -0.12 eV for VBM and CBM in MAI surface.

[b] Mixed method

[c] SCF

single in–plane unit cell, as shown in a previous section, the surface orbitals are the HOCO, and HOCO−1, one for each surface, each one being doubly degenerate by spin. As the present slab was built from 2×2 surface, the surface orbitals at $k = 0$ are 8, *i.e.*, from HOCO to HOCO−7. Six of these orbitals correspond to the high symmetry points $X(\frac{1}{2}, 0, 0)$, $M(\frac{1}{2}, \frac{1}{2}, 0)$, and $Y(0, \frac{1}{2}, 0)$ of (1×1) surface slab, which fold into the Γ–point of the (2×2) surface slab. The HOCO−8 is also a surface state, derived from a lower surface band. E^{slab}_{VBM} corresponds to the HOCO−9 for (2×2) in our surface model. In contrast, with HSE+SOC, the (2×2) has the quantum confined VBM as the HOCO−2, the other surface states having lower energy. This suggests a different dispersion of the surface bands with both functionals. In Table 3.4, only the highest surface state energy is shown.

Table 3.4 also shows that the energy difference between the surface states (E_{surf}) of the *unpolarized* and *polarized* slab of MAPI(001)–PbI_2 is negligible. There are also negligible band gap differences between these models for the same theoretical level. However, the energy levels of the slab with respect to vacuum change due to variations in the average electrostatic potential within the models. The shift seems to be as large as 0.25 eV and this could influence band alignments.

The PDOS for the slab MAPI(001)–MAI are shown in Fig. 3.11(b). There are no in–gap surface states, both HOCO, and HOCO−1 are confined states with both functionals. The surface MAI layer has no contributions at the CBM. The PDOS over the CBM shows small differences between the sub–surface PbI_2 layer, and the inner PbI_2 layers. It is apparent that the first peak around −2.9 eV is slightly increased for the sub–surface layer. The difference is better appreciated with the plot of the squared wavefunctions in Fig. 3.12. The HOCO and HOCO−1 are practically equal with both functionals. There is some difference for the conduction band states. With optB88–vdW, all the orbitals from LUCO to LUCO+4 have important contribution

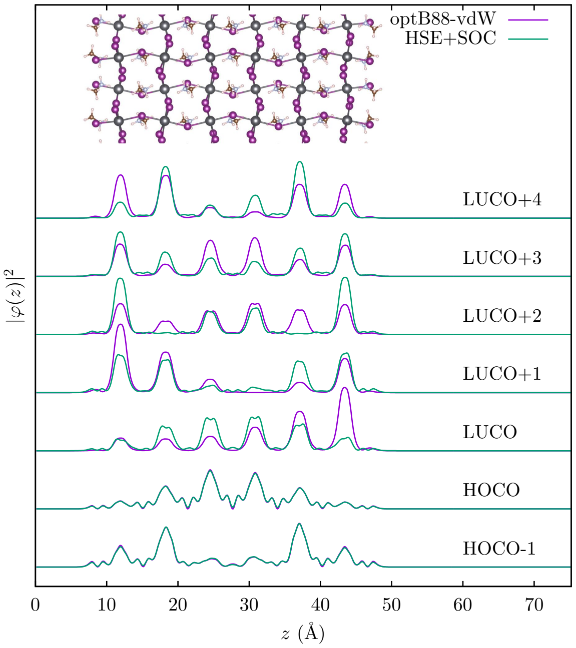

Figure 3.12: Planar–averaged squared wavefunctions for MAPI(001)-MAI, computed with optB88–vdW and HSE+SOC methods. The HOCO, and HOCO−1, are plotted with negative sign.

from the sub–surface PbI_2 layers. In contrast, with HSE+SOC, the LUCO is clearly a confined state, while LUCO+1 to LUCO+3, present mixed confined sub–surface character.

In order to evaluate the shift of slab energy levels due to thermal motion, we use a set of 270 representative configurations of each dynamic slab models, which uncover structural distortions. The SCF calculation of each configuration was computed with the VASP code, with the PBE functional including SOC, which implies a reasonable computational cost to give a correct topological description of the edges of the band. Now we are not interested in the precise values of state energies, but in their distributions (band edge shifts) due to the thermal motion.

Fig. 3.13 shows the distributions of the slab energy levels in the dynamic models, and the energies corresponding to the static models are superimposed to compare. All energies were calculated under the same theoretical approach. In the MAPI(001)–PbI_2 slab, the energy of the surface (E_{surf}) and the conduction band (E^{slab}_{CBM}) states appear uncorrelated at Γ–point (correlation coefficient = 0.12 with linear regression fit). In contrast, the energies of the frontier quantum confined states (E^{slab}_{CBM} vs E^{slab}_{VBM}) of this slab are rather correlated (correlation coefficient = 0.63). This explains the broad distribution obtained for the instantaneous band gap $E^{slab}_{CBM} - E_{surf}$, compared with $E_{CBM^{slab}} - E^{slab}_{VBM}$, see Fig. 3.14. In the MAPI(001)–MAI slab, uncorrelated surface states are not observed either, despite the observed surface relaxation. We verify that this also occurs with the occupied state closer to the valence band of the slab (E^{slab}_{VBM-1}).

The full width at half maximum (FWHM) values of the MAPI(001)–MAI states are larger than those of the MAPI(001)–PbI_2 surface (see Fig. 3.13). Notice that the positions of the band

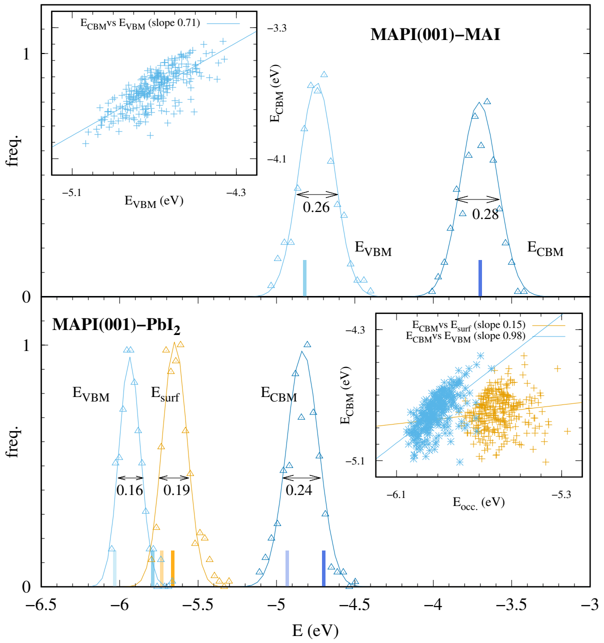

Figure 3.13: Distributions of the slab energy levels for MAPI(001)–MAI (top) and MAPI(001)–PbI_2 (bottom) dynamic models. Vertical bars show static model energy level. For MAPI(001)–PbI_2, the light (dark) bars show the levels of the *unpolarized* (*polarized*) slab. Insets: CBM vs VBM and surface levels, with linear regression.

edges in static models (vertical lines) are close to the center of the distributions obtained in the dynamics. Accordingly, the energy levels of each slab model are expected to suffer broaden deviations, *i.e.*, the standard deviation corresponding to each FWHM, due to the thermal motion. Fig. 3.14 also shows a similar average band gap between the confined states on both surfaces, as expected. With thermal motion, the band gap of the MAI–terminated surface is renormalized by ~ 0.12 eV. Furthermore, it can be seen that a lower band gap could appear if the MAPI(001)–PbI_2 surface state is considered.

Let us note that molecular dynamics breaks the instantaneous symmetry between the slab surfaces, causing differences in the local vacuum level at each side. We have not applied dipole

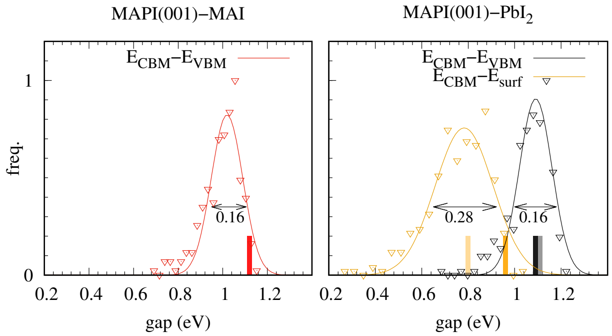

Figure 3.14: Band gap distributions of the surface dynamic models. Vertical bars show static model band gap. For MAPI(001)–PbI_2, the light (dark) bars show the levels of the *unpolarized* (*polarized*) slab.

corrections either during the dynamics with CP2K or for the energy calculation with VASP. Therefore, there is a fluctuating electric field at the vacuum region, which complicates the selection of the vacuum level as reference for the instantaneous surface and band edge energies. The energies shown in Fig. 3.13 are relative to the instantaneous potential at the center of the vacuum region. This approach is roughly equivalent, for average values, to include dipole corrections and to take the average of the local vacuum levels at both surfaces as reference. Alternatively, one could obtain the energies with respect to both vacuum levels. This would double the amount of data, modifying the distributions shown in Fig. 3.13, but not the average values. Fig. S9 in Ref. [1] shows that the electric field in the vacuum region fluctuates in both positive and negative directions, thus not breaking the symmetry if a time–average is considered. Moreover, the fluctuation of the potential at the vacuum center with respect to the supercell mean potential, which is the reference in CP2K and VASP codes, is 0.06 eV.
A typical practice (in static slab calculations) is to freeze one of the slab surfaces, allowing the other surface to relax. In those cases, where the symmetry is broken (both surfaces are different), exists a net dipole along the slab solvable by means of dipole correction. Fig. S10 in Ref. [1] shows a case example, where the averaged electrostatic potential was calculated with, and without dipole corrections. In the first case, there are two vacuum levels, one for each surface. In the second case, there is not an evident vacuum level. It is worth mentioning that: the average value between both vacuum levels, when the dipole correction is applied, is practically the same as the potential in the middle of the vacuum region, when the dipole correction is not applied.

Finally, we also examined how the effect of small stress on the slab can affect the energy of its electronic levels. For this we imposed changes of (±4 %) in the vectors a and b of the supercells, all the details are given in the Supporting Information in Ref. [1]. We found that the MAI–terminated surface is susceptible to these changes and could experience energy level shifts of up to 0.5 eV in the stress range studied. This is an effect to consider when studying interface alignments.

3.2.6 Implications for Band Alignment

The search for companion materials for different layers in electronic devices is guided by Anderson's rule on band alignment with respect to vacuum level [63]. A solar cell that use MAPI as light absorber, requires the ETM and MAPI CBMs to be aligned. Whilst the HTM and MAPI VBMs also need to be aligned. Values of -5.4 and -3.9 eV for the VBM and CBM energies, respectively, were computed in Ref. [225], which have been widely used to search HTM and ETM materials [63–65, 226]. Other values have been measured, showing a distribution of values dependent on the growth technique [79, 227, 228]. A clear correlation of the surface composition with the IP, and EA has been found [63,229,230]. These measurements match our results for the VBM values obtained for surface layers MAI and PbI_2 displayed in Table 3.4, and summarized in Fig. 3.15. The figure presents the results of the best theoretical predictions obtained in this work, which are the states obtained with HSE+SOC(VASP) for the slabs including QC corrections. The surface states of the MAPI(001)–PbI_2 surface in the figure, correspond to SCF calculations. All these theoretical values in the figure include the standard deviation (error bars) as a result of thermal motion. Notice that the expected fluctuations for the VBM and CBM levels could significantly influence the alignment between states with small offset.

The energy levels calculated for the MAI–terminated surface match those reported experimentally for the surfaces obtained with MAI/PbI_2 ratios greater than or equal to 1. In addition, these energies correspond to the trend reported for MAPI obtained by solution preparation methods [62]. On the other hand, the energy levels of the PbI_2–terminated surfaces tend to correspond to those reported for MAPI prepared using coevaporation methods [62]. Thus, our models could represent structural models of MAPI surface depending on the preparation method.

Interestingly, Butler *et al.* [131] made a computational search for HTM and ETM, considering a theoretical value of −5.7 and −4.0 eV for VBM and CBM, respectively [231], but allowing barrier heights of ±0.5 eV, which turns out to be equivalent to allow the VBM of MAPI to fluctuate in the range −6.2 to −5.2 eV. On PbI_2–terminated surfaces, the surface states caused by lead dangling bonds contribute to high reactivity. This reactivity could be used as a driving force for catalytic reactions or to obtain stable interfaces of MAPI with companion materials, *e.g.*, ETM and HTM. If the dangling bonds are not suppressed, they lead to interface localized levels. In solar cells, these states can be harmful recombination centers. Completion of Pb–centered octahedra can eliminate or mitigate these recombination centers [2]. For surfaces in humid environment, water molecules are likely to complete the valences of lead atoms and the surface is passivated [76]. This condition is detrimental to photo–catalytic applications.

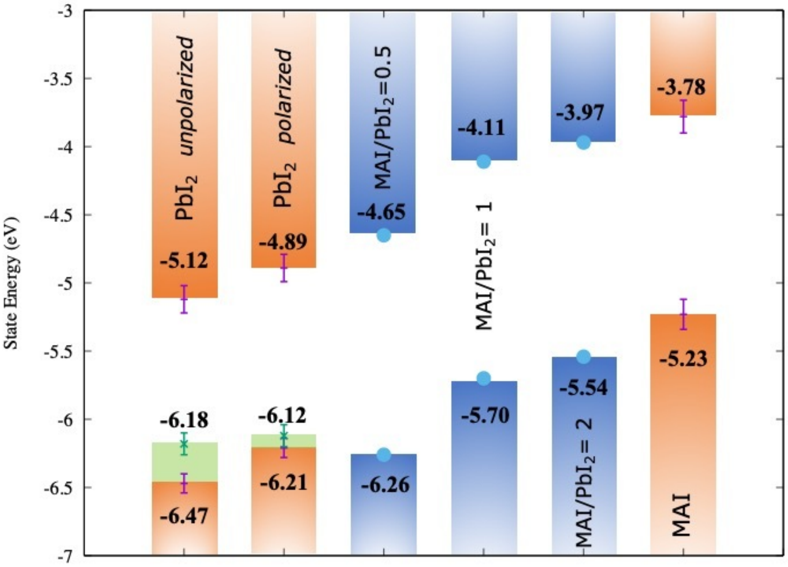

Figure 3.15: MAPI energy levels for alignment; the best theoretical prediction in this work (orange for bulk and green for surface state edges) considering the thermal broadening indicated by error bars, and the experimental data depending on the composition (blue) [63, 229, 230].

Chapter 4

Cu_2O Electronic Structure

Contents

In this chapter we approach different computational methodologies in search of accurate representations of Cu_2O band structure from bulk model and Cu_2O surfaces from slab models. The surface energy levels are modeled by means of a method that aligns the band energies of the bulk with the energy levels of the slab, considering hybrid functionals. Correspondingly, the convergence of these energy levels and SCF energy levels with respect to the size of the slab is also studied. The results of this chapter are not yet published. For computational details, see Appendix A.1.

4.1 Bulk: Structure and Properties

The starting point is the cubic crystal structure of Cu_2O, which is a 6 atom unit cell [90]. This structure is highly symmetric formed by two sublattice of oxygen and copper atoms (see Fig. 1.8). Due to its high symmetry and cubic structure, almost the unique parameter of its structure is the a lattice length. This unit cell was optimized by means of variable–cell relaxation.

4.1.1 How to Proceed to the Computational Study of Cu_2O?

Several computational setups can be used to study the the geometrical and the electronic structure. These different approaches has different strengths and disadvantages for different properties. We focus on two main areas: geometry and band edges.
To define which setup is the optimum in terms of accuracy and computational costs, we performed a study using two different computational setups with PBEsol exchange–correlation functional: USPP and NCPP (see Method I and II in Table A.1). We left out NCPP+SOC setup in this case because the SOC effects slightly changes the geometrical and electronic properties of Cu_2O, as it is expected for non–heavy atoms as is copper and oxygen. As a general rule, USPP requires a smaller PW basis set in comparison to NCPP, enabling faster calculations.

We check the effects and reliability of these three computational setups firstly in geometrical structure of Cu_2O.
For this purpose, we explored the total energy surface adding stress/pressure to the system. Particularly, we enforce the a lattice vector to certain values around ±5 % the equilibrium value.
Latter, the resulting total energy surfaces were fitted using BM equation, setting $V_0 = a_0^3$ and $E_0 = 0$ for both computational setup, in order to compare them in the same–scale. B_0 and B_0' were left as adjustment variables.
Total energy surfaces and BM equation fit for three computational setups are shown in Fig. 4.1A. Quantitative results are shown in Table 4.1.

From Fig. 4.1A is clear that USPP and NCPP setup produce practically the same total energy profile, with a slight (almost unnoticeable) shift of the minimum energy point to larger a lattice lengths when NCPP is used. The data are shown in Table 4.1. In terms of mechanical properties and bulk cell volume, both computational setups show similar deviations underneath with respect to experimental value of a lattice length and over–estimating the bulk modulus. Because our goal is not related with mechanical properties, the bulk modulus error is not

Table 4.1: BM equation fit parameters for Cu_2O bulk cell using USPP, NCPP setup.

Setup	a_0 (Å)	B_0 (Gpa)	B_0'
USPP	4.22	132.73	4.75
NCPP	4.22	130.41	4.76
Exp. [90, 232, 233]	4.27	105.7–112	~ 4.00

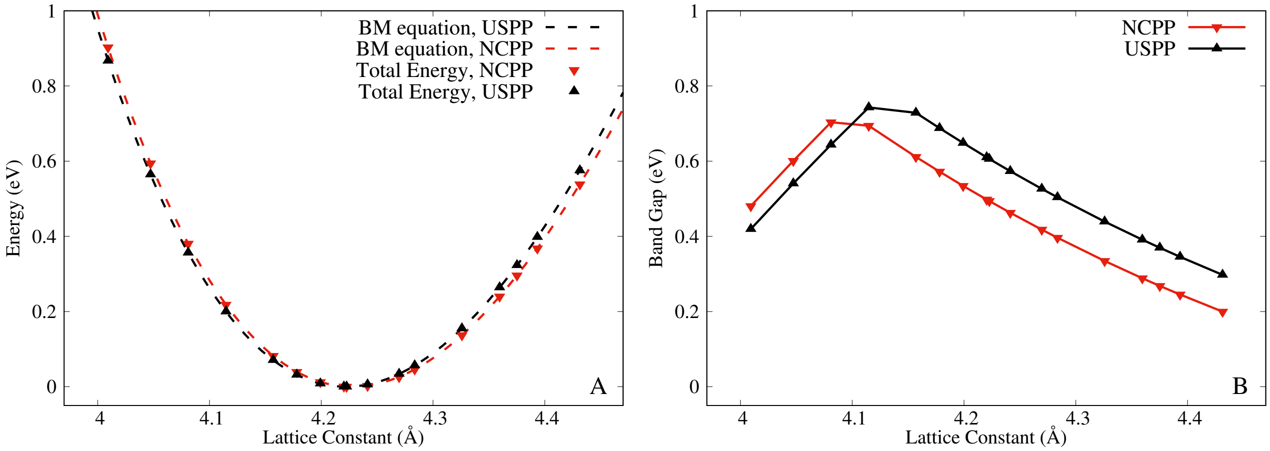

Figure 4.1: Cu$_2$O properties with respect to the lattice constant a. (A) total energy surface and BM equation fit and (B) band gap, for USPP and NCPP setups.

an important issue, meanwhile the atomic and cell geometry are in good agreement with the experimental ones, enabling to use them as representative models.
Taking these results into account is justified to use USPP setup to compute geometry and cell optimization henceforth, without substantial loss of geometrical model accuracy, in the same way as it happened in MAPI case, see Chapter 3.

The second important point is related to the electronic structure of the model: band edges, band gap and band dispersion. Fig. 4.1B shows the band gap, for different values of the lattice constant a of previous systems. Band gap is highly affected by compression and expansion of the cell. The band gap behaves increasing its value when is compressed from $1.05a_0$ to smaller lattice length, passing the lattice value of minimum energy. A change in the behaviour is observed for a values of $\sim$ 4.12 and $\sim$ 4.09 Å for USPP and NCPP setups, respectively, as a cusp–point from where the band gap start to diminish its value when lattice constant is reduced. Both setups show the same trends, just with $\sim$ 0.10 eV band gap difference, almost constant over the entire study range until the cusp–point is reached. As the cusp–point is located at different lattice lengths, the band gap starts to diminish before in USPP setup, reversing the band gap difference once both passed the cusp–point, now with $\sim$ 0.06 eV band gap difference. In both range the difference remains practically constant. In this case, both setups gives incorrect band gap values as it is expected for GGA functionals which underestimates systematically the band gap due to SIE.

To shed deeper insight on the electronic structure, we select five values of lattice parameter and compute band structure in the path M–Γ–X where the VBM, CBM and band gap are located (Γ–point), see Fig. 4.2. We use the minimum energy geometry, two expanded and two compressed cell geometries, using USPP and NCPP setups. Zero energy is defined as E_{VBM} in order to use the same energy–scale to compare the results, as the reference potential is different in each case.
As can be seen, the USPP and NCPP band structure are in practice the same, exhibiting bands with the same distribution, dispersion and intercrossing for each geometry cell. As commented before, NCPP setup gives a smaller band gap value than the USPP setup, which results in a

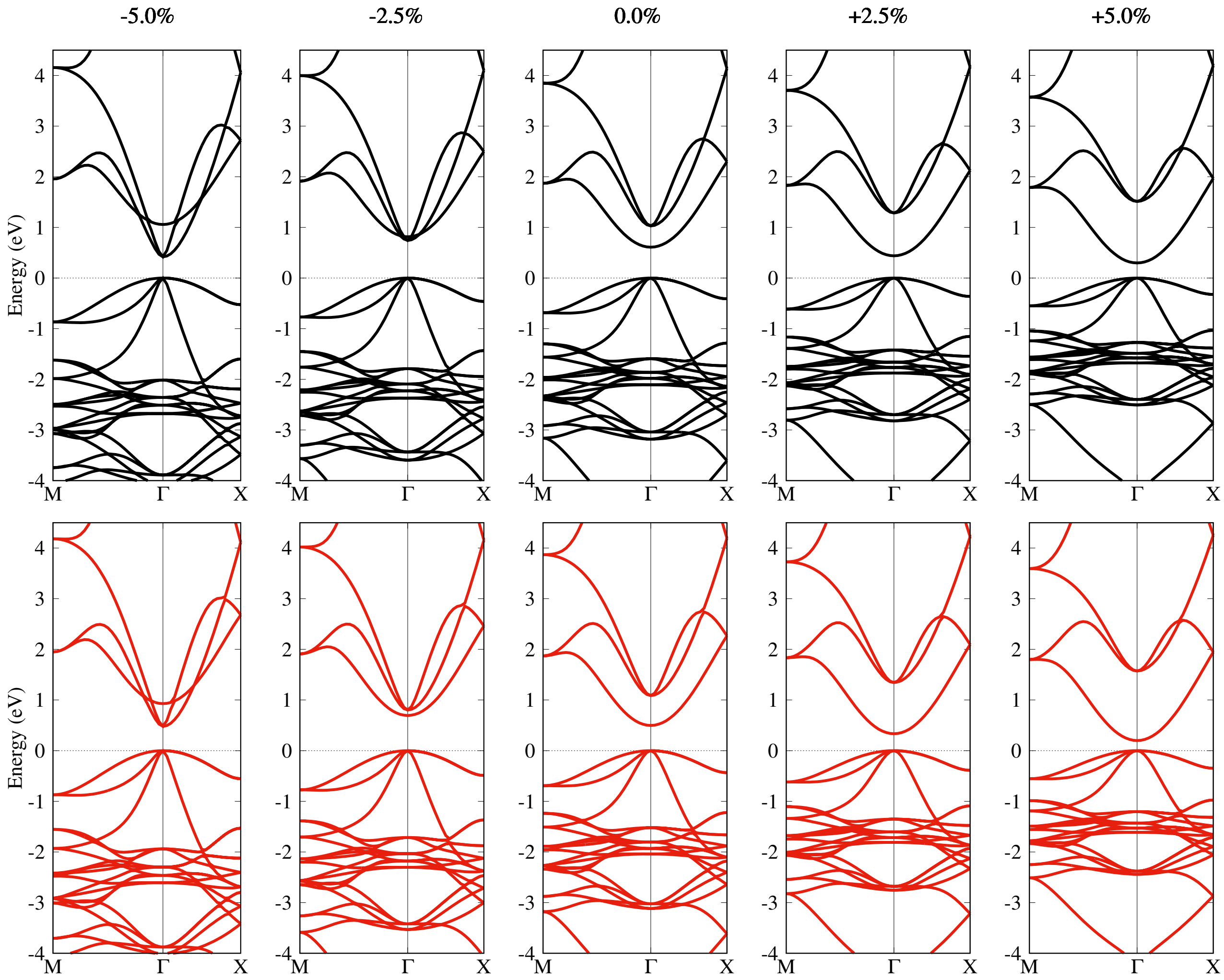

Figure 4.2: Band structure of Cu_2O at minimum energy volume(0.0 %) and different stressed a lattice lengths, using different computation setups: black USPP and red NCPP. **k**–points used: $\Gamma = (0, 0, 0)$, $X = (0, \frac{1}{2}, 0)$ and $M = (\frac{1}{2}, \frac{1}{2}, 0)$, in terms of reciprocal lattice vectors. Zero energy is defined as E_{VBM}.

lower CBM level energy. In addition, it can be seen that close to -2.5 % compression, there is a band swap corresponding to the CBM. The exact compression for which the band swap occurs is between -2.5 % and null stress geometries with the USPP setup, and between -5.0 % and -2.5 % stress geometries with NCPP setup. This band swap corresponding to the CBM is responsible for the cusp–point in the band gap behaviour in both setups
It is worth mentioning that, in this material there is no error cancellation in band gap quantity, then GGA band gap is *de facto* underestimated value. Also, the values of the band edges with respect to the vacuum are in fact bad, because it is impossible to obtain both band edges correctly when the band gap is poorly estimated. Hybrid functionals can be introduced in order to correct the underestimation error in band gap. This is done hereunder.

In conclusion, USPP setup is a reliable framework for obtaining cell geometries. The volume deviation with respect to the experimental value [90] reached -3.5 % for PBEsol functional.

4.1.2 Electronic Structure of Bulk Cu_2O

We proceeded to compute the electronic structure of Cu_2O using NCPP setup for the minimum energy structure obtained with USPP setup, in conjunction with PBEsol functional.
In order to get a detailed electronic structure, we compute band structure with a complete reciprocal space path (X–M–Γ–X–R–Γ–M–R), which pass over all high symmetry points in the Brillouin Zone for simple cubic symmetry. Also we compute the DOS, and, atomic and orbital PDOS using a denser **k**–point grid (see Appendix A.1). Results for NCPP setup are shown in Fig. 4.3.

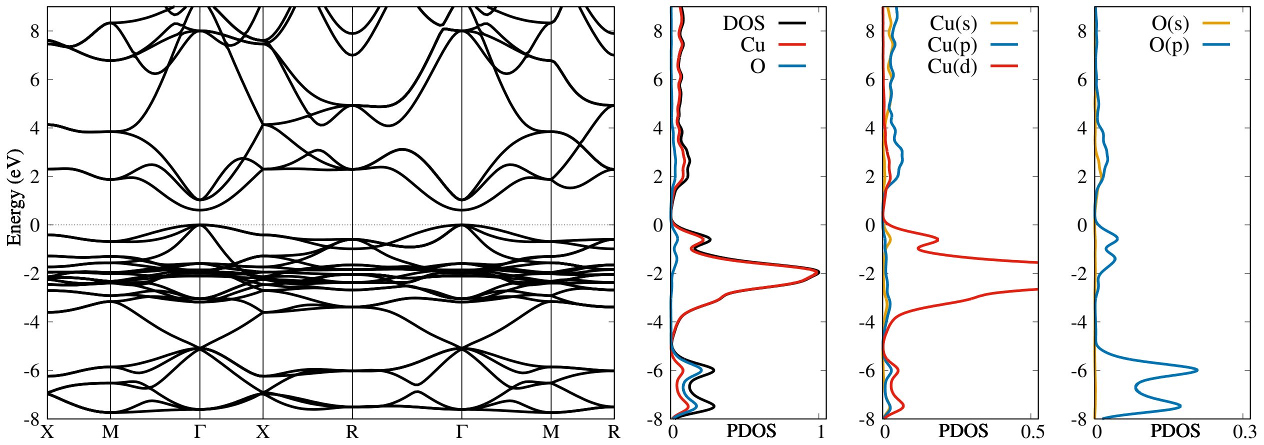

Figure 4.3: Band structure (left panel), and atom– and orbital–PDOS (right panels), of Cu_2O at minimum energy volume. **k**–points used: $\Gamma = (0, 0, 0)$, $X = (0, \frac{1}{2}, 0)$, $M = (\frac{1}{2}, \frac{1}{2}, 0)$ and $R = (\frac{1}{2}, \frac{1}{2}, \frac{1}{2})$, in terms of reciprocal lattice vectors. Zero energy is defined as E_{VBM}.

The band structure (left panel) shows that VBM and CBM are located at Γ–point. The valence bands present two main regions, one from 0.0 to ~ -5.0 eV with high dispersion and band intercrossing, and the second from ~ -5.0 to ~ -8.0 eV with low dispersion and intercrossing. On the other hand, conduction bands show high dispersion and low density as it is expected. The DOS (black line in right panels) and PDOS show that the previous two valence regions are of different nature. The first is composed of copper states, mainly 3d subshell, and the second is mainly composed of oxygen states, 2p subshell entirely, to a smaller composition of copper states, mainly 3d subshell. Conduction states are a mixture of oxygen, 2p subshell, and mainly copper states.
Edges of valence and conduction bands exhibit particular contributions, differing slightly from the inner band composition. The valence band edge is formed mainly by copper 3d subshell states and smaller composition of oxygen 2p subshell states. There is also a small contribution of copper 4s subshell, as a result of the hybridization between $3d_{z^2}$ and 4s subshell. This hybridization is the culprit of copper atom anisotropy, which causes electronic holes in 3d subshell. Conduction band edge, is mainly formed by a mixture of copper states, 4s and 3d subshells, and oxygen states, 2s and 2p subshells.
The band gap at this level of theory is, as previously mentioned, underestimated due to SIE of GGA functional, with a band gap of 0.50 eV (PBEsol), while the experimental value is 2.17 eV. In order to correct the band gap, we explored different hybrid functionals and G_0W_0 over PBEsol reference. It is expected that the inclusion of exact exchange does not change the

Table 4.2: E_{VBM} and E_{CBM} energy corrections for PBEsol computations, using different levels of theory with the minimum energy cell structure. Energy corrections ($E_{\alpha,corr}$ informed as: $E_{VBM}(i) - E_{VBM}$(PBEsol). All values in the Table are in eV.

Functional	HSE	G_0W_0	PBE0(0.098)	PBE0(0.133)	PBE0(0.188)	PBE0
$E_{VBM,corr}$	−0.94	−0.76	−0.42	−0.62	−0.93	−1.31
$E_{CBM,corr}$	+0.56	+0.24	+0.45	+0.56	+0.72	+0.91
E_g	2.00	1.50	1.37	1.68	2.15	2.72

shape of band structure and DOS, destabilizing the conduction bands and stabilizing valence bands, moving them rigidly in energy. This can be checked by comparing Fig. 4.3 and Fig. 3(a) in Ref. [103]. Taking this into account, we proceed to explore corrections for VBM and CBM (at Γ–point). As *macroscopic* electrostatic potential does not change when the functional is changed (see Fig. 2.4), we can compare directly the values of E_{VBM} and E_{CBM} computed with different levels of theory using the same cell structure.

VBM and CBM corrections are very different for different functionals, causing very different values for the band gap, but also the relation between VBM and CBM correction is different, as shown in Table 4.2. Most hybrid functionals stabilize the valence bands rather than destabilize conduction bands, but, PBE0(α) functional with low amounts of exact exchange shows a absolute quantitatively similar effect on both.

It is worth mentioning that, PBE0(0.133) functional corresponds to the use of *macroscopic* dielectric function of Cu_2O (7.5). This functional does not work as it is expected for many materials, were the use of material *macroscopic* dielectric function to determine α produce a reliable electronic structure with coinciding band gap. In this case the band gap is underestimated (less than with GGA) similarly with G_0W_0 results [114], showing Cu_2O electronic structure is a complex case. Traditional hybrid functionals like HSE provides a band gap closer to experimental one, while PBE0 produce a wider band gap far away from experimental band gap. In order to use a tuned PBE0(α) functional, we explore different α values, results are shown in Fig. 4.4. The linear behaviour of band gap with respect to α is consistent with the idea of a rigid displacement of the bands when exact exchange is added. At $\alpha = 0.0$ the hybrid functional turns

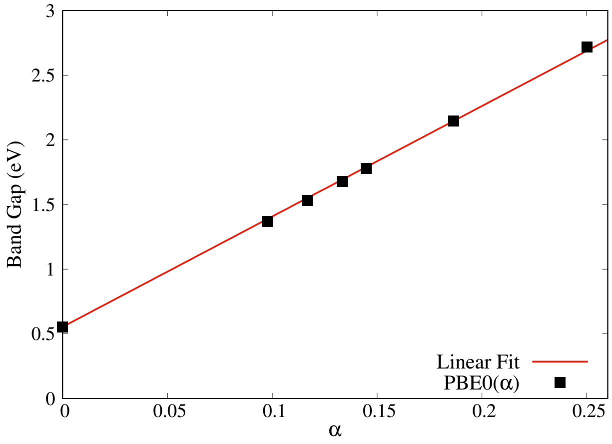

Figure 4.4: Cu_2O band gap using tuned PBE0(α) functionals with different α values.

equal to the pure PBE GGA functional with a band gap of 0.55 eV, similar to the PBEsol one. Meanwhile, when $\alpha = 1.0$ the hybrid functional turns to a HF plus PBE correlation calculation with a band gap of 9.09 eV similar to HF plus LYP correlation calculation in Ref. [110], excessively wide. To obtain the experimental band gap α must be 0.189, close to the SCF α value computed for MAPI electronic structure of 0.188 [44]. Accordingly, we use 0.188 as informed in Table 4.2. This tuned functional produce in practice the exact experimental band gap, and VBM correction is also practically the same as HSE functional and CBM correction is the main source of improvement of PBE0(0.188) over HSE functional.

4.2 Surfaces: Structure, Properties and Thickness Convergence

We modeled Cu_2O surfaces as slab models constructed by replication of the Cu_2O unit cell. Slab models of $Cu_2O(001)$ surfaces were obtained cleaving bulk supercells at selected atomic planes with orientation (001). Let us define the slab stoichiometric unit as a couple of adjacent copper and oxygen (001) planes that span half of a unit cell with thickness $a/2$. Henceforth, the number of stoichiometric units define the slab thickness, as well as the number of copper and oxygen planes. An additional copper or oxygen plane was added to each slab in order to have two symmetric surfaces, breaking the system stoichiometry and also the charge state of surfaces, due to for copper surfaces there are two electrons in excess, making copper atoms at surface a mixture of Cu^+ and Cu^0, and for oxygen surface there are two electrons less, making oxygen atoms at surface behaves as O^-. If electrons are extracted/added to those systems to reach the corresponding oxidation state for each atom, the systems are no longer neutral, which complicates the calculations and makes them almost impossible to perform.

Using two symmetric surfaces enable to avoid internal electric field. Hence, a $Cu_2O(001)$–O slab of n stoichiometric units has a total of n copper layers, and $n + 1$ oxygen layers, while for $Cu_2O(001)$–Cu the numbers are permuted.

The lattice vectors parallel to the surface can be linear combinations of the primitive vectors, allowing for surface reconstruction. Hence, we employ the slab nomenclature $(m \times m) \times n$ for the slab models, were m indicate the unit cell multiplication in each orthogonal direction along the surface. The index n indicates the number of stoichiometric units along the direction [001]. All the atomic coordinates within the slabs were relaxed with the surface cell vectors fixed at their bulk values. The cell vector perpendicular to the surface was also kept fixed.

In order to avoid using dipole correction [216,217], the slabs and their surfaces were constructed and relaxed, canceling the dipoles presented in surfaces, a simple situation to achieve thanks to high symmetry inherent in the system. We did not enforce the use of symmetry elements (mirror planes, inversion, for example) on the calculation, albeit the crystal geometry remained very close to its symmetric structure, which presents these elements of symmetry.

4.2.1 Slab Thickness Convergence

We study the convergence of the electronic state energies, band gap, surface energies, and structural parameters, with respect to the slab thickness, for $(1 \times 1) \times n$ slab. We have classified the different slab states, through inspection of spatial localization of squared wavefunctions, into surface states and bulk confined states (VBM and CBM). The electronic states were studied at the Γ–point, obeying the position of the bulk VBM and CBM (see the band structure diagrams in Fig. 4.3).

The first checked item was the convergence of the energy levels with respect to the slab thickness. Fig. 4.5 shows, for $Cu_2O(001)$–O and $Cu_2O(001)$–Cu slabs, the dependence of the frontier energy levels (relative to the vacuum level). The blue and sky blue symbols correspond to the quantum confined states of CBM, and the VBM. The CBM is the LUCO for both surface types. In $Cu_2O(001)$–O, the HOCO and the next (HOCO-1) are surface states, which

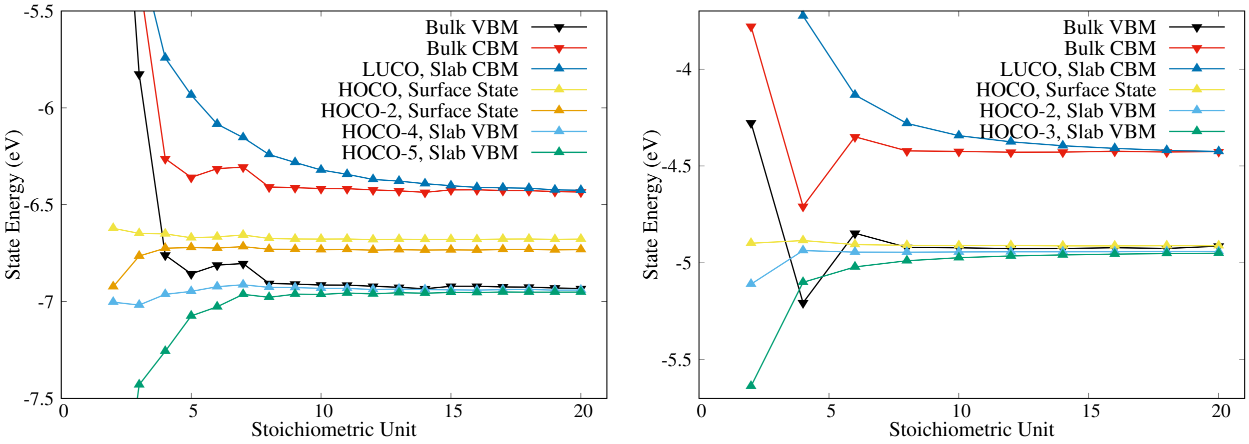

(a) $Cu_2O(001)$–O

(b) $Cu_2O(001)$–Cu

Figure 4.5: Convergence of energy slab levels, at Γ–point, with respect to slab thickness. (a) $Cu_2O(001)$–O and (b) $Cu_2O(001)$–O. PBEsol functional energies with respect to vacuum level.

are doubly degenerate because this slab model has two equivalent surfaces. Also HOCO−2 and HOCO−3 are an extra doubly degenerate set of surface states. Thus, the VBM is the HOCO−4, and HOCO−5 (with the same energy of HOCO−6) converges to the VBM when the slab thickness is enough. This situation resembles to the threefold degenerated bulk Cu_2O VBM, which splits when SOC is used, but in this case the origin of this break is the formation of the slab cutting the bulk material in one direction, breaking the three Cartesian symmetry. The surface states are caused by the breaking of the fourfold coordination of the oxygen atom on the surface, to a twofold one. Because there is only one oxygen per surface, there is not possible a reconstruction to reduce the surface energy.

For $Cu_2O(001)$–O, the HOCO and HOCO−1 are surface states, which are also doubly degenerate because this slab model has two equivalent surfaces. Thus, the VBM is the HOCO−2, and HOCO−3 (with the same energy of HOCO−4) converges to the VBM when the slab thickness is enough large. This situation is analogue to the $Cu_2O(001)$–O case. In this case the surface states are caused by the breaking of the twofold linear coordination of the copper atoms on the surface. Because there are two copper atoms per surface, reconstruction is a possibility. Geometry optimization at surface causes the approximation of copper atoms to shorter distances, 2.34 Å, with respect to in–bulk distance, 2.99 Å. A copper dimer, $(Cu–Cu)^+$ is generated at the surface, and this specie compacts against the bottom layer of oxygen atoms.

The red and black symbols correspond to the CBM and VBM energies, respectively, obtained from the two–step procedure explained in Section 2.5. Its dependence on the slab thickness follows the behaviour of the average electrostatic potential at slab center $\bar{V}(z_{in})$, from which they differ by constant values (Eq. 2.29).

Wavefunctions of $Cu_2O(001)$ (HOCO, LUCO, etc.) exhibit the same characteristics and trends described in MAPI(001) surfaces. For example, surface states are localized mainly on first layer, QC effect are clearly appreciated for VBM and CBM states and they are Bloch states, among others.

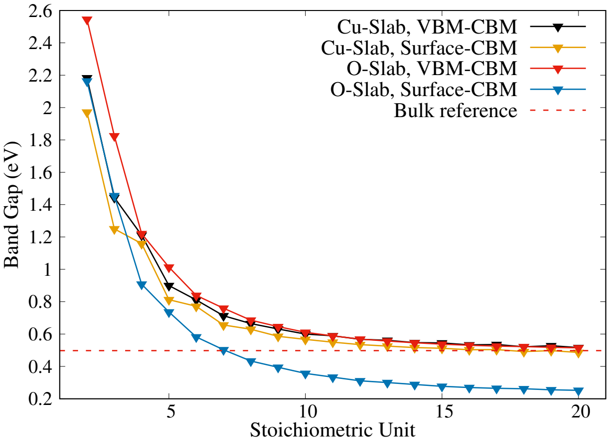

Figure 4.6: Convergence of $Cu_2O(001)$–O and $Cu_2O(001)$–Cu band gap (for inner slab bands and surface slab bands) with respect to slab thickness.

The VBM and CBM confined states energies in Fig. 4.5, exhibit QC behaviour, as expected, in almost all cases. Energy convergence is faster in VBM case with respect to CBM. For sufficiently thick slabs, *e.g.*, 16 stoichiometric units, QC is almost negligible, allowing to obtain SCF states with QC directly, using slab systems computationally tractable. Also band gap converge to bulk band gap for sufficiently thick slabs as it is expected (see Fig. 4.6). When $n < 8$, some VBM or CBM energies do not present smooth behaviour, and the slabs are too thin to host bulk–like states. This shows the bulk–inner slab description is poor at this regime. Also, the two–step procedure VBM and CBM are not well described in this ultrathin slab regime. For $n = 8$, the energies are roughly converged, and for $n \geq 8$ are tightly converged, in all cases. The two–step procedure is, in principle, QC–free. This prognosis was checked, and for $n \geq 8$, the VBM and CBM present asymptotic behaviour.
From Fig. 4.5 and 4.6, is clear that surface states in $Cu_2O(001)$–O are higher in energy with respect to VBM, in comparison to $Cu_2O(001)$–Cu ones, this entails that surface–CBM band gap of $Cu_2O(001)$–O converges to a lower value than bulk band gap, and conversely, in $Cu_2O(001)$–Cu surface states are just above VBM, then surface–CBM and VBM–CBM band gap converges to practically the same value (bulk band gap value) for sufficient slab thickness.

The last parameter studied is the surface energy. Fig. 4.7 displays the surface energy as a function of the slab thickness. For a $\beta =$ oxygen, or copper surface type, this energy can be computed as

$$S_\beta^n = \frac{1}{2A_{xy}}\left(E_{slab,\beta}^n - \frac{n}{2}E_{\mathrm{Cu_2O}} - E_\beta\right) \quad , \tag{4.1}$$

where $E_{slab,\beta}^n$ is the total energy of an n–stoichiometric units slab with two surfaces of type β, $E_{\mathrm{Cu_2O}}$ is the total energy of bulk Cu_2O, and E_β is the total energy of solid bulk metallic copper or gas phase oxygen (triplet state of O_2). The latter is the sum of chemical potentials of the out–of–stoichiometry species in β–rich condition. The double surface counting is corrected with the $\frac{1}{2}$ factor, and normalized with respect to surface area A_{xy}. Error bars were conservatively defined as the sum of error from each calculation parameter. For further details see Appendix A.3.

The surface energy, for both surface types, are converged for almost all thicknesses (the only deviation of the trend is $n = 2$, and an almost converged value is reached for $n = 6$), as shown in Fig. 4.7. About 90 % of the error is associated with **k**–point grid, and the rest associated with

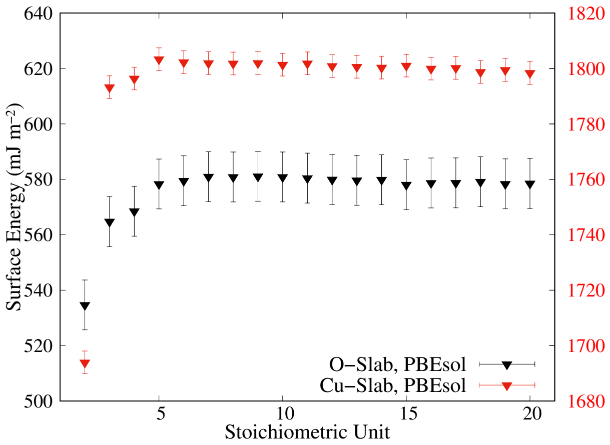

Figure 4.7: Convergence of $Cu_2O(001)$–O and $Cu_2O(001)$–Cu surface energy with respect to slab thickness.

higher cutoff, see Appendix A.3. In both cases, the surface energy behaves smoothly because both surfaces are highly symmetric. Our results show that $Cu_2O(001)$–O has lower surface energy, being more stable than $Cu_2O(001)$–Cu one, in concordance to other studies.

For all the thickness range considered, the geometrical parameters undergo minimal variations, matching the constancy of the surface energies.

4.2.2 Convergence Model Criteria

The previous subsection showed the convergence studies for slab thickness and vacuum width, using a set of energetic, and states variables. Here, we summarize the most important results and their implications. Slabs studied as $Cu_2O(001)$ surface models, do not exhibit QC for VBM and CBM state energies when sufficient slab thickness are used. These slab thickness are computationally affordable, then a model such as square well approximation is not necessary in this case.

Both surface models exhibit occupied surface states, caused by cleavage of bonds at surface copper and oxygen atoms. This triggers a reduction in band gap only for oxygen termination. The state energies obtained through the two–step procedure depend on the *macroscopic* electrostatic potential, and this parameter rapidly converges with the slab thickness. According to this method, the slab requires a minimum thickness of $n = 8$, which is considered the optimal thickness to obtain state energies numerically close to the converged eigenvalues. Two–step procedure cannot show the existence of in–gap surface states. The surface energies depend weakly on the slab thickness. Also, all parameters present weak dependence on the vacuum width.

4.2.3 Vacuum Level Alignment

We did not proceed to study the thermal effects on structural parameters and energy levels. They are left for future work.

We focus on VBM and CBM energy alignment against vacuum level of $Cu_2O(001)$ models, in order to be able to compare these levels with those obtained for MAPI(001) models.
In this sense, we use the simple and direct two–step procedure to obtain VBM and CBM energy alignments against vacuum level, corrected by means of hybrid functionals. Also, in order to have a wider range of possibilities to search for favorable alignments, we construct two extra surface $Cu_2O(001)$ models making vacancies on surfaces, *i.e.*, $Cu_2O(001)$–$O_{0.5}$ and $Cu_2O(001)_{0.5}$. To be able to perform vacancies is necessary to expand the surface into a $(2 \times 2) \times n$ slab. Then $Cu_2O(001)$–O $(2 \times 2) \times n$ slab has four oxygen atoms per surface and $Cu_2O(001)$–Cu $(2 \times 2) \times n$ slab has eight copper atoms per surface. Vacancy models were generated eliminating half of the atoms of each surface. In $Cu_2O(001)$–$O_{0.5}$ oxygen atom vacancies were located in the diagonal lines of the square surface, generating two disconnected lines of oxygen atoms at each surface, and $Cu_2O(001)$–$Cu_{0.5}$ copper atom vacancies were located along one diagonal line of square surface, generating two disconnected lines of copper atoms at each surface.
Results of two–step procedure for the four $Cu_2O(001)$ surface model terminations are shown in Table 4.3.

Table 4.3: Band edge energy levels with respect to the vacuum level for slab $Cu_2O(001)$–O, $Cu_2O(001)$–Cu, $Cu_2O(001)$–$O_{0.5}$ and $Cu_2O(001)$–$Cu_{0.5}$. Energy levels computed with the two–step process over PBEsol SCF calculations and energy corrections of Table 4.2 for different levels of theory with the minimum energy cell structure.* All values in the Table are in eV.

Functional	HSE	G_0W_0	PBE0(0.188)	PBE0
		$Cu_2O(001)$–O		
E_{VBM}	−7.87	−7.69	−7.86	−8.24
E_{CBM}	−5.87	−6.19	−5.72	−5.52
		$Cu_2O(001)$–Cu		
E_{VBM}	−5.85	−5.67	−5.84	−6.22
E_{CBM}	−3.85	−4.17	−3.70	−3.50
		$Cu_2O(001)$–$O_{0.5}$		
E_{VBM}	−6.67	−6.49	−6.66	−7.04
E_{CBM}	−4.67	−4.99	−4.52	−4.32
		$Cu_2O(001)$–$Cu_{0.5}$		
E_{VBM}	−5.55	−5.37	−5.54	−5.92
E_{CBM}	−3.55	−3.87	−3.40	−3.20

* Due to the use of two–step process, band edge energy levels are QC–free in principle.

Chapter 5

$Cu_2O/CH_3NH_3PbI_3$ Interface

Contents

In this chapter we discuss the implications of the alignment between MAPI and Cu_2O bands. The Cu_2O/MAPI interfaces parallel to the planes (001) are investigated. The effect of the stoichiometry at the interfaces atomic planes has been studied. Atomistic models of the interfaces are presented. Their electronic properties are presented by means of PDOS, LDOS, band alignment, charge transfer, interface states, and energy of adhesion. The main results of this chapter are already published in Ref. [2]. For computational details, see Appendix A.1.

5.1 Explicit Interface Construction

5.1.1 Considerations for Good Interfaces

Interfaces in solar cells must present a series of requirements to be efficient, beyond just presenting a favorable band alignment to have barrier–free charge transport. These requirements are: commensurable vectors (epitaxy) to avoid stress and favorable crystal structure and atomic termination in the junctions that prevent dangling bonds, which may generate interfacial/localized energy states in the band gap.

We used these three requirements to conduct a first screening between $Cu_2O(001)$ and MAPI(001) surface models before to proceed to generate and study explicitly their possible interfaces.
Firstly, the epitaxy requisite is satisfied by the equal surface square shape and similar vector lengths of (001) surfaces of both materials ($a_{MAPI} \approx 2a_{\mathrm{Cu_2O}}$), with a mismatch of less 3 %.
Secondly, band alignment at interfaces can be approximated (without taking into account reconstruction effects or dipoles that could be generated at the explicit interface) by means of vacuum level alignment of surface model energy levels. For that, data from Table 4.3 and A.2 are used. Particularly, PBE0(0.188) and PBE0(0.188)+SOC hybrid functional data, respectively, were used here. When Cu_2O surface is $Cu_2O(001)$–O, VBM state is too deep in energy terms (-7.9 eV) to act as hole collector (HTM junction) state with MAPI, due to MAPI VBM energy ranges from -5.3 to -6.6 eV. Therefore, $Cu_2O(001)$–O surface is not a good candidate for interface with MAPI in a solar cell. The other three $Cu_2O(001)$ surface models, *i.e.*, $Cu_2O(001)$–Cu, $Cu_2O(001)$–$Cu_{0.5}$ and $Cu_2O(001)$–$O_{0.5}$, have VBM states (-5.8, -5.5 and -6.7 eV, respectively) into or near MAPI VBM ranges, making them potential candidates for interface with MAPI in a solar cell.
The last requirement is favorable crystal structure and atomic termination in the junctions between both materials. This requirement is related with correct chemical matching of both materials at interface, completing existing dangling bonds (such as lead in PbI_2 MAPI sur-

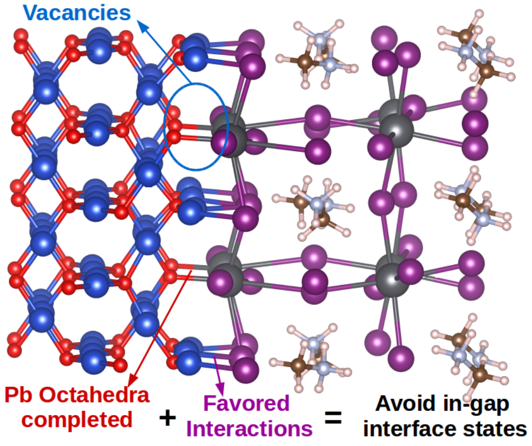

Figure 5.1: Schematic picture of favorable crystal structure and atomic termination in the junctions between both materials, to avoid in–gap states. Cu/PbI explicit interface, see (below) Table 5.1 for interface nomenclature. Image generated with VESTA [50].

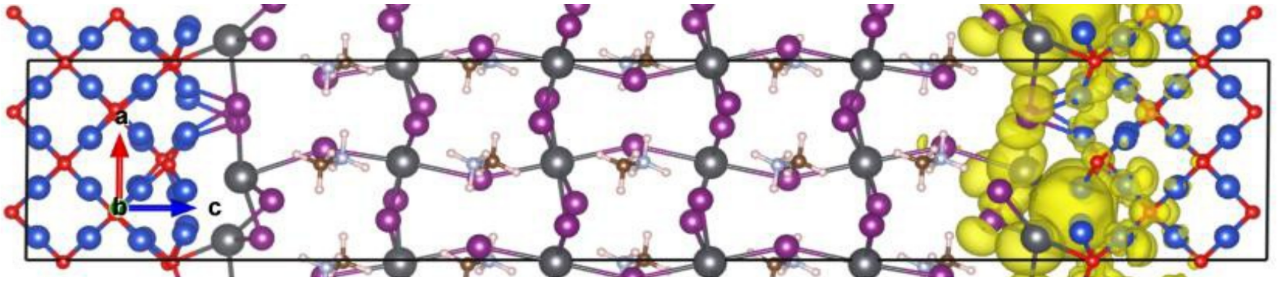

Figure 5.2: Interface state in Cu$_2$O(001)–Cu/PbI$_2$–MAPI(001) explicit interface, corresponding to the HOCO of simulated system. Yellow isosurface represent the squared wavefunction of HOCO. Image generated with VESTA [50].

face), coordination environment of each atom with incomplete coordination sphere and favorable cation–anion interaction, all this in order to avoid in–gap states that can act as trap states for electron or hole carriers. Fig. 5.1 shows schematically this situation in a particular interface that satisfied these requisites.

Particularly, for MAPI(001) and Cu$_2$O(001) surfaces, we have to be concerned about completing the octahedra around lead atom to stabilize and pull the surface state present in MAPI(001)–PbI$_2$ out of the band gap. Also we have to optimize and maximize cation–anion interaction at the interface to improve the adhesion (make a stable interface) between both surfaces. This require to locate the oxygen atoms in Cu$_2$O(001) surfaces near lead atoms and MA$^+$ in MAPI(001) surfaces. Similarly, copper atoms in Cu$_2$O(001) surfaces must be positioned near iodide atoms in MAPI(001) surfaces.
Taking into account that MAPI(001)–PbI$_2$ and MAPI(001)–MAI have two cations at its surface, is necessary to have two accessible anions in Cu$_2$O(001) surfaces. This is satisfied in Cu$_2$O(001)–Cu$_{0.5}$ and Cu$_2$O(001)–O$_{0.5}$ since they were generated for this purpose, with a good cation–anion matching on the whole surface against MAPI(001) surfaces. This requirement is not completely fulfilled in Cu$_2$O(001)–Cu surface model. In fact when Cu$_2$O(001)–Cu model is used to construct explicit interfaces with MAPI(001) surfaces, it is not possible to obtain an interface without interface states above the VBM state of both materials, as shown in Fig. 5.2. Therefore, Cu$_2$O(001)–Cu surface model is not a good candidate for explicit interface construction.

5.1.2 Computational Considerations

The interface can be simulated by means of a supercell that contains both materials joined by interfaces, as can be seen in Fig. 5.3. The bulk calculations of $(E^{(m)}_{VBM,bulk} - \bar{V}^{(m)}_{bulk})$ have been made using unit cells that present the same stress as the middle region of the corresponding slab. Let us note that VASP code sets $\bar{V}^{(m)}_{bulk} = 0$. The Cu$_2$O and MAPI unit cells contain 6 and 48 atoms, respectively, while the slab supercells here considered contain 200–300 atoms. The band edges of bulk materials were calculated using these unit cells with the PBE0(α) hybrid functional, with $\alpha = 0.188$.

Due to PBC, the supercell always contains two interfaces, which should be equal or equivalent by symmetry, in order not to have a *macroscopic* electric field normal to the interface in the bulk materials. In some cases, depending on the crystal symmetry and orientation, it may be impossible to obtain two identical interfaces and stress–free materials. Alternatively, the supercell may contain a vacuum region, in which case there is an interface and two surfaces.

The band gap of stress–free Cu_2O and tetragonal MAPI are 2.08 and 1.77 eV, respectively, which are close to the experimental values of 2.17 eV [103, 106, 107] and 1.60 eV [227]. With this setup, the Cu_2O band gap is slightly underestimated, while the MAPI band gap is slightly over–estimated, both gaps cannot be tuned with the same functional. This affects the band alignment, but also gives the possibility of SCF calculations of interface states. Using a tuned functional for each bulk material allows to obtain the same qualitative band alignment, see supporting information of Ref. [2]. In addition to the band alignments through two–step procedure explained in Section 2.5, the electronic states of the interfaces have been calculated using the PBE0(0.188)+SOC functional. This allows to identify interface states that could act as recombination centers if their energies are within the band gap. The fraction of exact exchange was tuned from standard $\alpha = 0.25$ (PBE0) to $\alpha = 0.188$, to achieve the correct band gap of both materials. This is the PBE0(α) scheme, where the α value has been determined self–consistently [193, 194] for orthorhombic MAPI [44]. It provides closer band gap for both materials, with respect to experimental values, than standard PBE0.

5.1.3 Starting Models

Fig. 5.3 shows the starting interface models for different terminations of $Cu_2O(001)$ and MAPI(001). $Cu_2O(001)$–X (X = Cu, O)) denotes a surface terminated in planes of element X, while $Cu_2O(001)$–$X_{0.5}$ has half of the surface X atoms vacant. The Cu_2O surfaces without vacancies are Tasker class III surfaces [78]. If the $Cu_2O(001)$–Cu or $Cu_2O(001)$–O surfaces are neutral, there are free electrons or holes at the surface. Elimination of these carriers causes the interface to have a net charge, which in turn generates an electrostatic energy, as well as conceptual and computational troubles. The creation of vacancies solves these problems, and turns the Cu_2O surface into Tasker II type [78]. More complex models have been obtained for the Cu_2O surfaces in vacuum [104, 105, 135], including reconstruction and non–stoichiometric compositions. These models have not been included in this work, in an attempt to keep the model complexity to a minimum. X–MAPI(001) (X = MAI, PbI_2)) denotes a surface terminated in planes of X composition. The MAPI surfaces are Tasker class I surfaces [78].
Our interface models have been generated expanding the unit cell of MAPI in tetragonal phase, and a $2 \times 2 \times 1$ supercell of Cu_2O, both in the [001] direction. The structures have been cut at selected atomic planes with orientation (001), and have been placed facing each other. Hence, four interfaces has been studied in detail, as shown in Table 5.1 and Fig. 5.3.

One problem of this method is the difficulty to accommodate two identical interfaces while keeping the continuity of bulk Cu_2O and MAPI lattices. This problem can be mitigated by variable–cell relaxation, with a careful selection of the terminating atomic planes in the starting tetragonal supercells. For the O/MAI, and O/PbI interfaces, the angles between the vectors of the relaxed supercells deviate from the right angle in less than 0.15°. For the Cu/PbI interface deviations in the angles reached 0.9°, but this is still manageable. For the Cu/MAI interface, the angle deviations reached 1.9°, making it difficult to define the reference bulk unit cell of MAPI

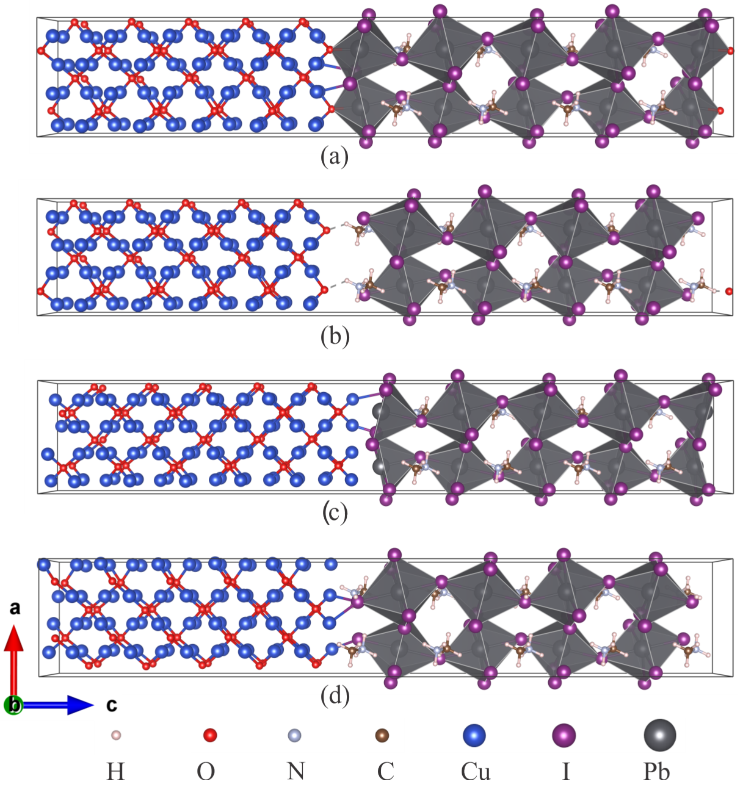

Figure 5.3: Starting supercell models considered for the interface in (001) plane. a) O/PbI, b) O/MAI, c) Cu/PbI, d) Cu/MAI. Images generated with VESTA [50].

and Cu_2O. Therefore, for the Cu/MAI interface, a slab model with a vacuum region ~ 15 Å in width was constructed. Thus, this model contains one single interface and two surfaces. The supercell vectors parallel to the interface were fixed at the average of the relaxed MAPI and Cu_2O lattice constants, *i.e.*, $a = b = 8.625$ Å. The relaxed vectors of the bulk phases are $a_{MAPI} = 8.716$ Å (8.81 Å experimental [49]), and $2a_{Cu_2O} = 8.534$ Å (8.54 experimental [90]). One problem of this model is the appearance of a built–in electric field inside each material, causing the *macroscopic* electrostatic potential to have slopes instead of a plateau in the central region of each material. This is the reason why models without vacuum are preferred. For the Cu/MAI slab model with a vacuum, the built–in electric field was almost completely eliminated by adding hydrogen atoms bound to the undercoordinated oxygen atoms at the Cu_2O surface. All the atoms were allowed to relax.

Table 5.1: Interface nomenclature.

Full name	Abbrv.
$Cu_2O(001)$–$O_{0.5}$|PbI_2–MAPI(001)	O/PbI,
$Cu_2O(001)$–$O_{0.5}$|MAI–MAPI(001)	O/MAI
$Cu_2O(001)$–$Cu_{0.5}$|PbI_2–MAPI(001)	Cu/PbI
$Cu_2O(001)$–$Cu_{0.5}$|MAI–MAPI(001)	Cu/MAI

5.2 Electronic Structure of Explicit Interfaces

5.2.1 Structure of Explicit Interface

The optimized structures of the four interfaces proposed in this study are displayed in Fig. 5.4. The atomic coordinates of the supercell models are given in the supporting information of Ref. [2]. At the O/PbI and Cu/PbI interfaces (Fig. 5.4(a) and (c), respectively), the oxygen atoms are bonded with the lead atoms, with the Pb–O bond length of ~ 2.2 Å, meanwhile the copper atoms are bonded with the iodine atoms, with the Cu–O bond length of ~ 2.6 Å. The strong Pb–O interactions at the interfaces pull the lead atoms from the surface, and the Pb–I bond lengths decrease gradually as their positions vary from the surface region to the MAPI bulk region.

The four proposed interface models do not contain dangling bonds. The creation of oxygen or copper vacancies was crucial in not leaving interfacial atoms with missing bonds. $Cu_2O(001)$ surfaces have reactive oxygens, either due to termination in oxygen planes, or due to the copper vacancies in copper–terminated surfaces. In all models, the reactive oxygens either bind to lead atoms of PbI_2–terminated MAPI, or form hydroxyls capturing hydrogens from MAI–terminated MAPI. In the latter case, the $CH_3NH_3{}^+$ dissociate and the remaining amine groups remain close to the hydroxyls, meeting the hydrogen bonding criteria. An alternate model of the Cu/MAI interface with one single hydroxyl group and one non–dissociated MA^+ was obtained, which has a higher total energy by 0.5 eV. Copper atoms find ionic partners in the iodine atoms of PbI_2

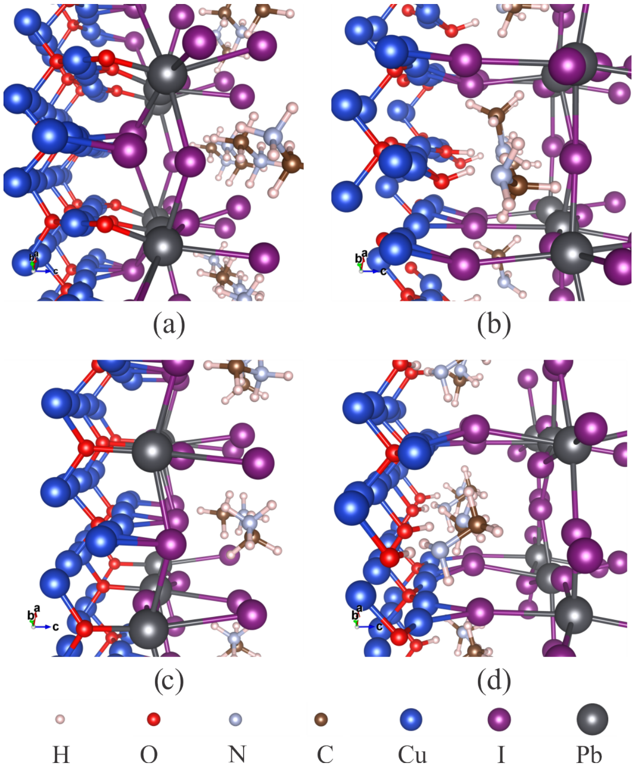
(a) (b) (c) (d)

Figure 5.4: Relaxed interface structures. a) O/PbI, b) O/MAI, c) Cu/PbI, d) Cu/MAI. The VESTA program [50] was used to represent and analyze the interfaces.

Table 5.2: Energy of adhesion E_A and stress energy density E_S for the different interfaces.

System	E_A (J/m^2)	E_S (10^7 J/m^3)	
		Cu_2O	MAPI
O/PbI	−1.19	+0.29	+11.2
O/MAI	−1.01	+0.54	+ 8.6
Cu/PbI	−1.29	+2.10	+ 9.1
Cu/MAI	−1.12	+0.52	+ 6.5

or MAI surface layers. On the other hand, for PbI_2–terminated MAPI, the broken Pb–centered octahedral are completed by the interfacial oxygens. For MAI–terminated MAPI, the broken I–Pb bonds are replaced by ionic bond of iodines with two coppers. At Cu/PbI and O/PbI interfaces, $CH_3NH_3^+$ do not dissociate.

For the sake of evaluating the stability of the structure, the interface energy of adhesion was calculated and summarized in Table 5.2. The energy of adhesion has been calculated as

$$E_A = \frac{1}{N_i}\left(E_{\mathrm{Cu_2O/MAPI}} - E_{\mathrm{Cu_2O}} - E_{\mathrm{MAPI}}\right) \;, \tag{5.1}$$

where $E_{\mathrm{Cu_2O/MAPI}}$, $E_{\mathrm{Cu_2O}}$, and E_{MAPI} are the energies of the three supercells than contain both materials, only the Cu_2O part, and only the MAPI part, respectively. N_i is the number of interfaces present in the supercell, *i.e.*, $N_i = 1$ for the Cu/MAI model with vacuum, and $N_i = 2$ for the other models. The energies of adhesion of the four interfaces are all negative, and are large enough to consider that the four Cu_2O/MAPI interfaces are stable. The Cu/PbI interface displays the strongest adhesion ($E_A = -1.29$ J/m^2). The Cu_2O and MAPI stress energy densities are provided as well. The latter have been calculated for unit cells with three dimensional PBC, with the stressed lattice vectors as in the interface supercell. The stress energy arises from the small lattice mismatch between Cu_2O and MAPI. These values are provided as indication of the degree of deformation that these materials must undergo to couple in lattice–matched interfaces. The precise values depend on the amount of each material that is present in the simulation supercells. Experimentally, this energy depends on grain depth, and can be relaxed by the formation of grain boundaries.

5.2.2 Band Alignment at Interface

The results of the band alignment computed by means of Eq. 2.31 are summarized in Table 5.3. The plane–averaged and *macroscopic* electrostatic potential for the Cu_2O/MAPI interfaces are shown in Fig. S1 of the supporting information in Ref. [2]. For all interfaces, the calculated ΔE_{VBM} and ΔE_{CBM} are in the ranges of [−0.11 eV, +0.85 eV] and [+0.18 eV, +1.13 eV], respectively. Positive values (Type II alignment [31]) allows to separate the electrons and holes at different sides of the interface, which is useful for the interface HTM/absorber in solar cells. However, small negative valence band offsets are still useful, as will be discussed later.

Table 5.3 contains the band gap obtained for bulk MAPI and Cu_2O, in the distorted configurations obtained from the centers of the slabs, using the PBE0(0.188)+SOC functional. The

Table 5.3: Electrostatic potentials at slab centers, VBM, band gap at both sides of the interfaces, and band offsets. All values in the Table are in eV.

Interface	O/PbI	O/MAI	Cu/PbI	Cu/MAI
$\bar{V}_{slab}^{(\mathrm{Cu_2O})}$	-1.67	-1.22	-1.24	-2.96
$\bar{V}_{slab}^{(\mathrm{MAPI})}$	$+1.10$	$+0.65$	$+1.31$	-0.49
$E_{VBM,bulk}^{(\mathrm{Cu_2O})}$	$+3.97$	$+3.95$	$+3.99$	$+3.91$
$E_{VBM,bulk}^{(\mathrm{MAPI})}$	$+1.31$	$+1.23$	$+1.21$	$+1.06$
$E_{g}^{(\mathrm{Cu_2O})}$	$+2.08$	$+2.06$	$+2.02$	$+2.04$
$E_{g}^{(\mathrm{MAPI})}$	$+1.79$	$+1.78$	$+1.82$	$+1.81$
$E_{VBM,slab}^{(\mathrm{Cu_2O})}$	$+2.30$	$+2.73$	$+2.75$	$+0.95$
$E_{VBM,slab}^{(\mathrm{MAPI})}$	$+2.41$	$+1.88$	$+2.52$	$+0.57$
$E_{CBM,slab}^{(\mathrm{Cu_2O})}$	$+4.37$	$+4.79$	$+4.76$	$+2.99$
$E_{CBM,slab}^{(\mathrm{MAPI})}$	$+4.21$	$+3.67$	$+4.34$	$+2.40$
$(\Delta E_{VBM})_{int}$	-0.11	$+0.85$	$+0.23$	$+0.38$
$(\Delta E_{CBM})_{int}$	$+0.18$	$+1.13$	$+0.43$	$+0.61$

variation in the band gap is caused by the stress induced to accommodate the latticed mismatch and bond matching across the interface. The stress has been simulated by defining the bulk lattice vectors from interatomic distances at the slab centers. These band gap variations are small enough not to invalidate the results, and can be easily assimilated as local fluctuations.

To evaluate the error due to a particular choice of functional, Table S2 in supporting information of Ref. [2] shows the values obtained using the HSE functional [192], including the SOC. The results are similar, although one can appreciate slightly smaller band offsets with the HSE+SOC functional. The difference is explained by the fact that the different fractions of exact exchange were used for each material, tuned to reproduce the bulk band gap. Thus, with the HSE+SOC calculation, the MAPI VBM is somewhat higher, while the $\mathrm{Cu_2O}$ VBM is lower. However, the differences are not larger than other sources of error in our computational setup, such as the supercell–dependent stress above discussed. Therefore, the results with PBE0(0.188)+SOC and HSE+SOC are qualitatively equivalent. To investigate the existence of electronic states localized at the interfaces, we have made calculation of the interfaces with the hybrid functional PBE0(0.188)+SOC. The energies and isosurfaces of the frontier orbitals (squared), at Γ–point, are shown in Fig. S2–S5 in supporting information of Ref. [2]. According to their localization, these orbitals can be classified as localized at $\mathrm{Cu_2O}$, MAPI, or at the interfaces. The highest and lowest energies of the occupied and unoccupied states, respectively, localized at either $\mathrm{Cu_2O}$ or MAPI, define the respective valence and conduction band edges ($E_{VBM,slab}^{(\mathrm{Cu_2O})}$, etc). Their squared wavefunction isosurfaces can be identified among the set of orbitals represented in Fig. S2–S5 in supporting information of Ref. [2]. The band edges, band gap, and band alignment inferred from these numbers are summarized in Table 5.4. Due to the small thickness of the slabs that can be computed, the band gap and the individual band edges are modified by the QC effect. The band edges in Table 5.3 are free of QC effects, hence the

Table 5.4: Band edges, band gap, and band offsets obtained from the SCF slab calculation with PBE0(0.188)+SOC. All values in the Table are in eV. $E_{g,slab}^{(m)} = E_{CBM,slab}^{(m)} - E_{VBM,slab}^{(m)}$.

Interface	O/PbI	O/MAI	Cu/PbI	Cu/MAI
$E_{VBM,slab}^{(\mathrm{Cu_2O})}$	+2.29	+2.66	+2.66	+0.88
$E_{VBM,slab}^{(\mathrm{MAPI})}$	+2.38	+1.74	+2.44	+0.36
$E_{CBM,slab}^{(\mathrm{Cu_2O})}$	+4.50	+4.92	+4.89	+3.09
$E_{CBM,slab}^{(\mathrm{MAPI})}$	+4.41	+3.72	+4.47	+2.49
$E_{g,slab}^{(\mathrm{Cu_2O})}$	+2.21	+2.25	+2.23	+2.21
$E_{g,slab}^{(\mathrm{MAPI})}$	+2.03	+1.98	+2.03	+2.13
$(\Delta E_{VBM})_{int}$	−0.09	+0.92	+0.22	+0.52
$(\Delta E_{CBM})_{int}$	+0.09	+1.19	+0.42	+0.60

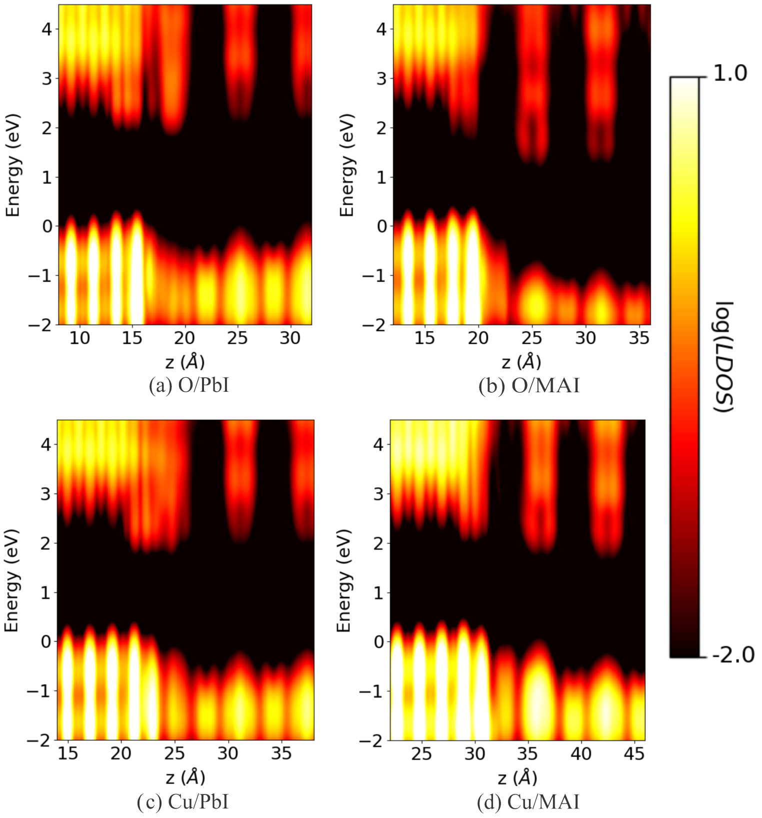

(a) O/PbI

(b) O/MAI

(c) Cu/PbI

(d) Cu/MAI

Figure 5.5: Logarithm of LDOS×V_{cell}–averaged in the xy plane calculated between the MAPI and the Cu_2O interfaces.

band alignment of Table 5.3 are better estimators, in principle. From Fig. S2 and S4 in supporting information of Ref. [2], one can see that the LUCOs in O/PbI and Cu/PbI are interface states. Fig. S4 shows that the two interfaces of the Cu/PbI model, have localized states with different energies, revealing some asymmetry in the achieved model. This asymmetry is evident in Fig. S6 in supporting information of Ref. [2]. The in–gap interface states are dangerous for the photovoltaic conversion, they can trap photo–excited electrons and holes, facilitating recombination [234, 235]. The energy and space dependence of the set of one–electron wavefunctions and energy eigenvalues can be combined in the LDOS using DensityTool [3]. Fig. 5.5 shows the LDOS at the interface region; full LDOS data are shown in Fig. S6 in supporting information of Ref. [2]. An energy smearing of 0.27 eV was used to compute the LDOS. The LDOS display the band alignment according to the values of Table 5.4, and the interface states Fig. 5.5(b and d) suggest that the O/MAI and Cu/MAI interface also present interface states with energies near the CBM. However, these interface states are higher in energy than the MAPI CBM (are not in–gap interface states), allowing electrons in these states to return to MAPI. Therefore, holes can be transferred from MAPI to Cu_2O without being trapped, although they can be attracted and recombine with electrons trapped at O/PbI and Cu/PbI interfaces.

The LDOS at MAPI near the band edges is much smaller than the LDOS at Cu_2O, causing the former not to be discernible in the Fig. 5.5. The band edges are better shown by the site PDOS. The atomic PDOS have been added up by atomic layers parallel to the interfaces, and are shown in Fig. 5.6 and Fig. S2–S5 in supporting information of Ref. [2]. There, one can appreciate the small PDOS at MAPI near the band edges.

In Fig. 5.5 and 5.6 the energy zero has been set at the HOCO energy. For the Cu/MAI model, the HOCO–1 energy has been used, as the HOCO is a surface state at the surface with vacuum with no interest for our study. For every interface model, Fig. 5.6 shows the PDOS (from the PBE0(0.188)+SOC calculation) for the interface and the first three sub–interface layers. It can be observed that the band gap varies non–monotonically across the interface due to the local variation of the band edges. For the O/PbI interface (Fig. 5.6(a)), the valence and conduction manifold near the Fermi level is almost completely occupied by states lying on the PbI_2 layers. However, for the O/MAI, Cu/PbI, and Cu/MAI interfaces Fig. 5.6(b–d)), this behaviour is changed. The larger contribution to the valence manifold near the Fermi level is due to the Cu_2O states, while the conduction manifold is conformed of MAPI states. Such behaviours results from complex rehybridizations of the valence orbitals upon formation across the interface and from changes in the local electrostatic potential due to the deviation from the bulk environment at the interface, which lead to the interface electron depletion or accumulation. Also, the proton transfer in the O/MAI and Cu/MAI favors the stabilization of the interface oxygen orbitals. Besides, the projection of interface states over the interfacial layers is present for the O/PbI model as expected, but there is no visible projection for the Cu/PbI model. As mentioned above, the Cu/PbI model presents two different interfaces states (as shown in Fig. S4 and S6 in supporting information of Ref. [2]), the one with in–gap energy is not localized at the layers corresponding to the PDOS of Fig. 5.6. In contrast with the conduction band interface states, there are not in–gap valence band interface states for any model, as shown in Fig. 5.5, 5.6, and S1–S4 in supporting information of Ref. [2].

A word of caution is in order, concerning the above discussed trap states in O/PbI and Cu/PbI models. The QC energy shift is present on the VBM and CBM states, mainly in $E_{CBM}^{(MAPI)}$. For a MAPI–in–vacuum slab that has the same thickness as our models in Chapter 3 and Ref. [1], the QC energy shift is 0.24 eV. A QC–free (< 0.05 eV) MAPI slab would be at least three times thicker, which is computationally not affordable. The subtraction of 0.24 eV from $E_{CBM}^{(MAPI)}$ (of Table 5.4) lowers the CBM to 4.17 and 4.23 eV, for O/PbI and Cu/PbI models, respectively. Embedding MAPI in Cu_2O may alter the QC shift. Because of this, an independent estimation is obtained comparing the $E_{CBM}^{(MAPI)}$ values of Table 5.3 and Table 5.4.

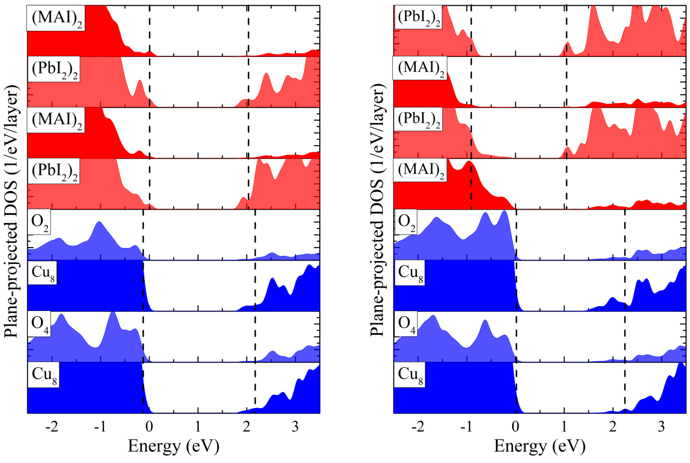

(a) O/PbI (b) O/MAI

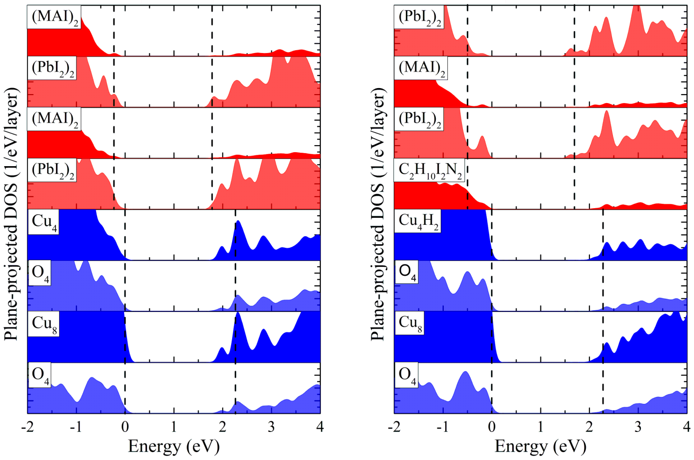

(c) Cu/PbI (d) Cu/MAI

Figure 5.6: PDOS projected on the atomic planes near each interface proposed in this study: (a) O/PbI, (b) O/MAI, (c) Cu/PbI, (d) Cu/MAI. The dotted vertical lines corresponds to the VBM and the CBM for each material.

With both procedures, $E_{CBM}^{(MAPI)}$ has lower energy than the interface state of O/PbI, but it is still higher than interface state in the Cu/PbI interface. In brief, the in–gap interface states of O/PbI in Table 5.4 are likely to be artifacts of a thin model. For Cu/PbI, one of the interface states cannot be removed from the gap with a thicker model. However, the energy difference is small, and it can be blurred by the thermal motion [1, 45].

5.2.3 Charge Distribution at Interface

To analyze the spatial charge redistribution across the Cu_2O/MAPI interfaces, we have computed the Bader atom charges [236] using Henkelman's Group program [237]. The Bader atom charge is the total (including the core) electric charge within the atom boundary, which is established by the topological properties of the electron density. Fig. 5.7 shows the Bader charges summed by layer near the interfaces. In the partition of Cu_2O in layers, the 2:1 stoichiometry

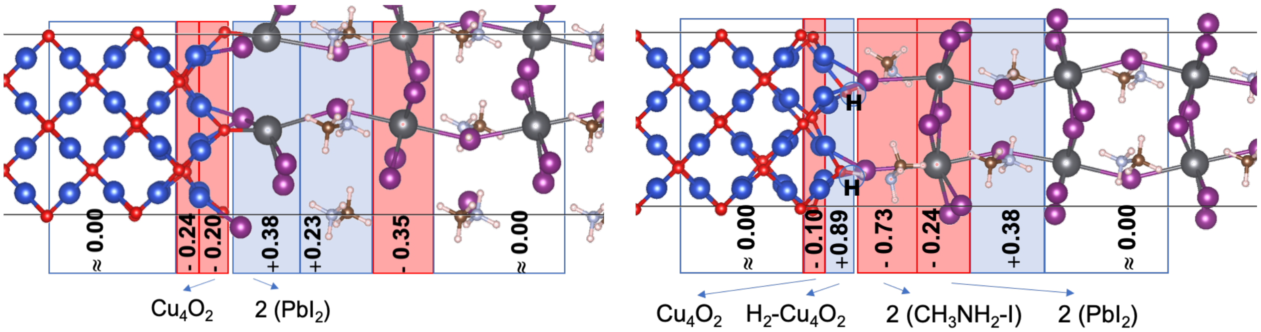

(a) O/PbI

(b) O/MAI

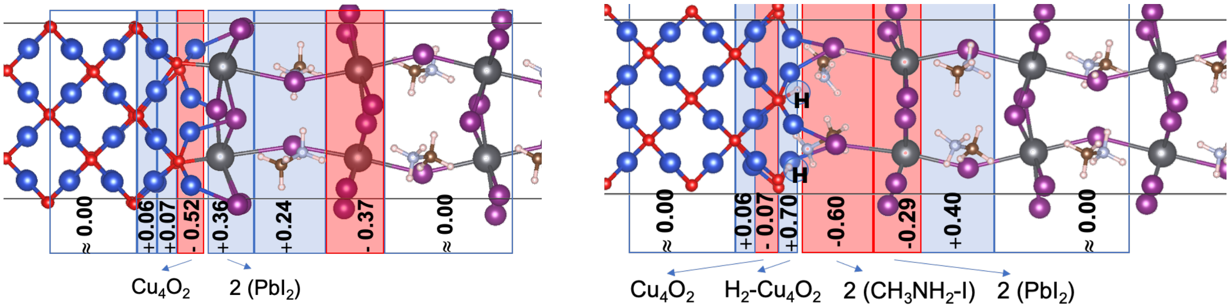

(c) Cu/PbI

(d) Cu/MAI

Figure 5.7: Bader charges (e) summed by layers for the four interface models: (a) O/PbI, (b) O/MAI, (c) Cu/PbI, (d) Cu/MAI.

has been respected. For layer boundaries coincident with copper or oxygen planes, as in Fig. 5.7, the Bader charges of the boundary atoms are equally distributed to each layer on both sides of the boundary. For the O/MAI and Cu/MAI interfaces, the Bader charges of the two hydrogens of hydroxyl groups sum $+1.28e$. They are formally included in the Cu_4O_2 layer in Fig. 5.7, to assess how charges are organized at the interface after dissociation or deprotonation of the MA^+. According to the above described partition, each interface formation involves a net electron transfer from the MAPI to Cu_2O, even in the case of MAI–terminated interfaces, where two protons (per interface) are also transferred, each one with $+0.64e$ Bader charge. This electron transfer is localized at very few layers near the interfaces. The inside of Cu_2O and MAPI remain neutral. The inner layers of the MAPI slab are neutralized when considering the charge of a stoichiometric MAPI unit: a PbI_2 layer and a MAI layer (see Fig. S12 in supporting information of Ref. [2]).

The charge separation described for the formed interfaces suggests the formation of interface dipoles. However, the way of partitioning the charges between the bulk and the surface regions is not unique, and this selection can significantly affect the magnitude of the estimated dipole. Instead, we perform a qualitative analysis with the charge by layers scheme. Fig. 5.7 shows that dipoles are oriented in opposite directions depending on the MAPI surface composition and their particular electron and proton transfer.

It is not obvious that Bader charges describe electron charge transfer, rather than the adjustment of the atom boundaries. As complement to the previous analysis, the electron charge density difference $\Delta\rho(x, y, z)$ has been computed by subtracting from the electron density of

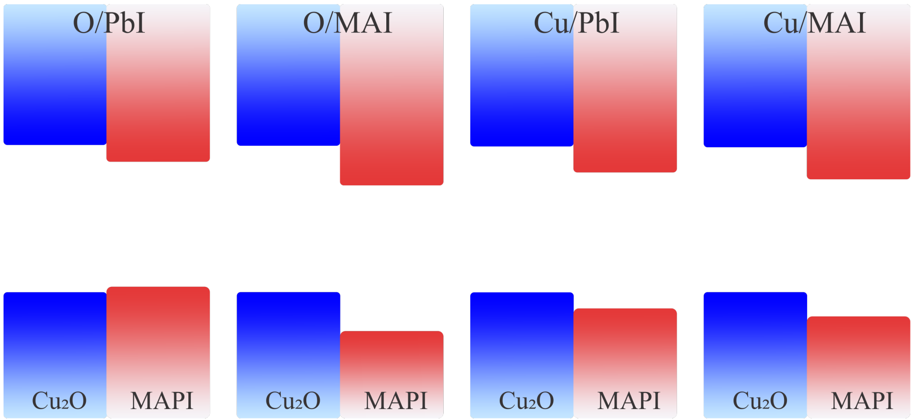

Figure 5.8: Predicted band alignment between the MAPI and the Cu_2O. The band offsets correspond to those reported in Table 5.3.

a Cu_2O/MAPI heterostructure, the densities of the only–Cu_2O, and only–MAPI slabs. In the last two, the atoms were kept fixed at the same coordinates as in the interface. An isosurface representation of $\Delta\rho(x, y, z)$ can be seen in Fig. S7–S11 in supporting information of Ref. [2] for each interface model. There, it can be appreciated that redistribution of charge density occurs primarily in the interface region, in agreement with the Bader charge picture.

Finally, a constructed theoretical band alignment diagram based on the averaged electrostatic potential for the Cu_2O/MAPI interfaces is shown in Fig. 5.8. According to our results, when light is irradiated in a Cu_2O/MAPI interface, electrons are excited to the conduction band on the MAPI side of the interface; simultaneously, photo–excited holes are left in their valence band. The holes in the valence band of the MAPI side can be transferred to the valence band on the Cu_2O side, since the latter VBM is higher. The negative band offset found for the O/PbI interface seems unfavorable for the hole transfer, but it does not necessarily decrease solar cell performance, as it will be discussed below, in Subsection 5.2.5

5.2.4 Connection with Experimental Literature

Most of the best performing HOIHP–based solar cells that use copper oxide as HTM have been prepared growing the perovskite over a copper oxide ultrathin films named CuO_x rather than Cu_2O. No crystallographic characterization of the CuO_x films of the HOIHP–based solar cells has been provided, presumably due to its ultrasmall thickness. X–ray photoelectron spectroscopy (XPS) shows a variable relative amount of Cu^+ and Cu^{+2} species on exposed CuO_x, with Cu^+ content in the range 63–86 % [144, 148–151]. Cu^+ and Cu^{+2} are typically associated with Cu_2O and CuO, respectively. There is another crystalline phase, paramelaconite (Cu_4O_3) [103] which has equal amounts of Cu^+ and Cu^{+2}. A disordered paramelaconite phase exists [238] with approximate stoichiometry $Cu_{64}O_{57}$ having 78 % Cu^{+2}, and 22 % Cu^+, close to the ratio reported in Ref. [148]. The band gap of CuO and Cu_4O_3, being smaller than 1.7 eV [103], are too low to act as HTM while blocking the conduction electrons. Therefore, these phases cannot be the HTM material present in working solar cells, but they are likely to be present at the exposed surfaces of Cu_2O. Non–Cu_2O surfaces could remain or be removed during perovskite deposition, although no evidence is available yet. Anticipating the possibility of measuring a depth profile of Cu^+ content across the interface, we show in Fig. 5.9 the simulated core level shifts (CLS) for all copper atoms present in our interface models. In all cases, there are small shifts at the interfaces, that are much smaller than the expected CLS between different degrees of oxidation. Hence, only Cu^+ is present in our interfaces, and cannot appear like Cu^{+2} in XPS measurements. The CLS have been simulated as the variations in the electrostatic potential energy averaged inside small atom–centered spheres of 1.94 Å in radius.

In other group of solar cells, Cu_2O nanocubes have been prepared in solution and deposited upon perovskite surfaces. The cubical shape implies (001) surfaces. Lui *et al.* [141] achieved a high 18.9 % efficiency using Cu_2O nanocubes deposited from solution on a mixed perovskite $Cs_{0.05}FA_{0.81}MA_{0.14}PbI_{2.55}Br_{0.45}$. These nanocube surfaces were modified with silane coupling agents, in principle intended to make the nanocrystals soluble. Elseman *et al.* [142] also obtained efficient solar cells (17.4 % PCE) with this method. They obtained Cu_2O nanocubes without surfactants and deposited them on MAPI. This is probably the system most related with our interface models.

Nejand *et al.* [146] grew Cu_2O directly over MAPI. In that work, prior to Cu_2O growth, the perovskite surface was treated with a solution of MAI in 2–propanol. This had the main effect of controlling the surface smoothness, and possibly also favored a MAI–terminated surface. For this system, our Cu/MAI and O/MAI models could be relevant.

The literature discussed has focused on the manufacturing of the solar cells and the performance optimization, but there are no characterization of the interface properties. We think that solar cell development need to be supported by experiments that can prove the chemical and spectral properties (*e.g.*, UPS, XPS) as function of depth in the devices or as a function of layer thickness during incremental deposition [63]. A critical knowledge to compare with experiments is the characterization of the copper oxide phase, and the atomic planes present at the interfaces.

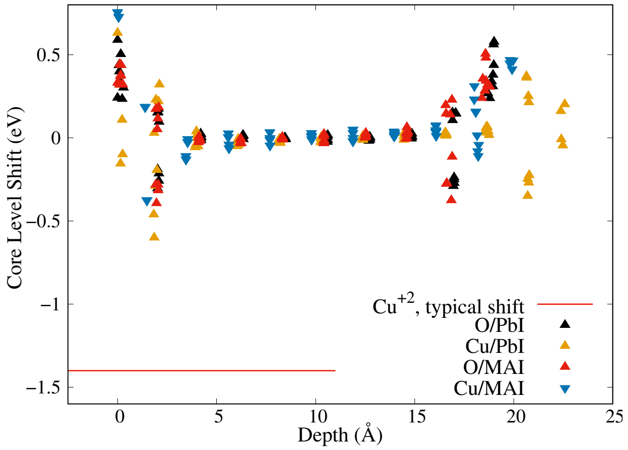

Figure 5.9: Copper core level shifts, with respect to Cu^+ core level binding energies (middle Cu_2O copper atoms), along the interface depth coordinate.

5.2.5 Recommendations for Improved Solar Cell Performance

Let us discuss which of the interfaces studied here can be better for solar cell performance. Device simulations [159, 163] show that small negative offsets $(\Delta E_{VBM})_{int} > -0.3$ eV do not affect substantially the solar cell performance, but positive offsets always decrease the PCE. Based on these results, the O/PbI and Cu/PbI interfaces could be the best for solar cell performance. However, as shown in Fig. 5.5, there are interface states that could trap conduction electrons, and become recombination centers. This could explain why a PCE higher than 20 % has not been reached. In fact, the idea of avoiding traps at the Cu_2O/MAPI interface has been proved experimentally, by means of creating a buffer layer of spiro–OMeTAD between MAPI and Cu_2O [153, 155, 156].

Let us consider the effects of the small, but not negligible lattice mismatch between Cu_2O and MAPI, which is 2 % with our computational setup. For sufficiently thick films, the stress energy (see Table 5.2) can surpass the energy gain associated with the energy of adhesion. The stress energy can be released by means of dislocations at the interface (non–epitaxial growth) or, inside MAPI or Cu_2O. In practice, the Cu_2O layer thickness has been treated as an optimization parameter, with values ranging between 4 nm [147] and 100 nm [146]. The lattice mismatch can be reduced by introduction of bromine in the perovskite. Compositions $MAPb(I_{1-x}Br_x)_3$, with $x \sim 0.2$ have shorter lattice parameter, and have been predicted [239] and verified to improve solar cell stability [240,241]. Therefore, the combination of Cu_2O as HTM with $MAPb(I_{1-x}Br_x)_3$ as photon absorber may be a fruitful path to improve HOIHP–based solar cells performance.

Finally, let us consider the implications of MA^+ dissociation in Cu/MAI and O/MAI interfaces. The preparation of this kind of interface requires a previously deprotonated Cu_2O surface. If aqueous solution methods are used, this requires pH higher than the Cu_2O isoelectric point, for which values of 7.5 [128] and 10.2 [242] have been determined. Therefore, our interface models are relevant for cases when copper oxide is grown in basic pH, such as in Ref. [151]. The dissociation of surface ${CH_3NH_3}^+$ has been associated with fast degradation of MAPI deposited on ZnO [243] and Al_2O_3 [244]. This fact anticipates a disadvantage for solar cells that include this type of interface, regardless of the alignment of their energy levels. However, ${CH_3NH_3}^+$ dissociation at the interface is not sufficient to degrade MAPI, in absence of a mass transport mechanism. In fact, the fast degradation of MAPI on ZnO and Al_2O_3 has not been observed for Cu_2O and CuO_x.

Chapter 6

Concluding Remarks

In order to put this thesis in a general context, it is important to consider the topics that motivate it. Climate change is an immediate problem that humankind must address in order of reducing/deleting the use of fossil fuels and transitioning to renewable energy sources, such as solar energy. Photovoltaic solar cells are a competitive alternative as energy production source. Hybrid organic–inorganic halide perovskite–based solar cells have shown high efficiencies, but exhibit poor stability, not allowing to impulse them to the large–scale market. The study of new hole transport materials, such as Cu_2O, and their interfaces is an important and necessary step to tune up these emerging technologies.

This thesis address the band alignment evaluation between MAPI as light absorber material and Cu_2O as hole transport material, contributing to the knowledge of this type of solar cells and materials, and providing information for more efficient solar cells.

Using Density Functional Theory with Periodic Boundary Condition, we have explored the electronic structure of MAPI and Cu_2O to achieve a detailed insight about energy levels and structure of their surfaces and possible interfaces. First we made a convergence study of the calculation parameters for both materials (Appendix A.2). With these parameters we performed a study of bulk an surface models for both materials (Chapter 3 and 4), describing their geometric structure, band structure, density of states, and projected density of states, among other properties. We compared and discussed advantages and disadvantages of two different approaches to obtain band edge alignment between materials: a) two–step procedure and b) direct self–consistent field calculations. Also, we explored different hybrid (tuned) functionals to obtain a good electronic structure description of MAPI and Cu_2O at the same level of theory. Using this data and chemical insight, we have proposed different atomic–scale models of (001) Cu_2O/MAPI interfaces (Chapter 5), addressing directly the main concern and objective of this thesis: the band alignment evaluation between MAPI and Cu_2O.

With respect to the Density Functional Theory methodology, our calculations proved the feasibility of the two–step procedure to refer the bulk VBM and CBM energy levels to the energy–scale of the slab. The efficiency of this procedure allowed to include the effects of higher precision methods, *i.e.*, hybrid functionals and quasiparticle models, to estimate the energy levels of the surfaces. In this line, it was also possible to assess the error in energy levels caused by Quantum Confinement in thin slab models. Here, we proposed an analytical function to directly obtain this error as a function of the thickness of the slab in the case of MAPI.

It is also essential to consider possible surface states (which can only be addressed with self–consistent field calculation) that may arise from the incomplete coordination sphere of surface lead atoms and copper/oxygen surfaces. These states can modify the optical properties and reactivity of the surface, and even provide new applications. Furthermore, in the case of MAPI, our results showed that the surface energy levels are also sensitive to the thermal motion of the structure. In fact, the dynamic models of the MAPI surfaces showed that this effect would make it possible to overcome energy barriers of up to 0.14 eV and this would decide the charge transport at the interface.

Finally, four atomic–scale models have been obtained for the Cu_2O/MAPI interfaces. The atomic coordinates, electronic states, and band alignments have been obtained and studied. The interface models differ in the ending atomic layers that join the two materials, which could be controlled with the growth conditions. The formation of copper and oxygen vacancies at the interface layer allowed to avoid dangling bonds and deep in–gap electronic states, which is essential for applications in HOIHP–based solar cells. The calculated band alignment is favorable for the photovoltaic conversion using Cu_2O as Hole Transport Material. According to our computed band alignment, and considering device simulations, the O/PbI and Cu/PbI interfaces present the best valence band alignments for solar cells. However, there are interface states with energy close to the conduction band minimum of both materials, which could trap electrons and become recombination centers.

Modification of the interface composition or the formation of a buffer layer is a promising pathway to improve solar cell performance, which require further research.

Appendix A

Supporting Information

A.1 Computational Details

Different setups of DFT calculations have been used throughout this thesis. Table A.1 summarizes them, namely Method I, II, III, IV and V.

In Chapter 3 and 4, bulk and slab relaxations were performed using Method I. Total energies, forces and stress tensors were obtained from DFT calculations, as implemented in the Quantum ESPRESSO code [200,201]. The unit cells were optimized by means of variable–cell relaxation. The lattice vectors were orthogonalized, neglecting small deviations from right angles. Two exchange–correlation functionals were used, the improved GGA PBEsol [183] and the non–local vdW correlation optB88–vdW (vdW) [186,187]. The Brillouin zone was sampled using a Γ–centered $3\times3\times2$ and $6\times6\times6$ **k**–point grid for MAPI and Cu_2O, respectively. The SOC was not included here because its effect on the geometries is insignificant. All the atomic coordinates within the slabs were relaxed with the a and b cell vectors fixed at their bulk values. The cell vector perpendicular to the surface was also kept fixed. Hybrid functionals were used to compute energy level corrections to VBM and CBM of bulk materials. The convergence study was made with Methods I for relaxations and II for electronic structure, over: MAI– and PbI_2–terminated MAPI slabs, and O– and Cu–terminated Cu_2O slabs, respectively. The electronic state energies were computed for $(1\times1)\times n$ slab without and with SOC (for MAPI slabs and Cu_2O/MAPI interfaces), using a Γ–centered $3\times3\times1$ and $6\times6\times1$ **k**–point grid for MAPI and Cu_2O, respectively. For DOS and PDOS calculations, an 4/3 enhanced **k**–points grid was used to obtain smoothed and continuous profiles. This corresponds to Γ–centered $4\times4\times3$ and $8\times8\times8$ **k**–point grids for bulk MAPI and Cu_2O, respectively, and their respective grids for slabs systems. Method II and III were used to compute the electronic structure of the slabs and bulks. Once the thickness convergence criteria were established, the surface physical properties were studied in MAPI using two, MAI– and PbI_2– terminated, $(2\times2)\times6$ slabs with a vacuum width of 35 Å, and the Γ–point (owing to the high computational demands). For these *production* slabs, the atomic coordinates were relaxed using the vdW functional. To obtain accurate band energies in the bulk crystal, the HSE hybrid functional [191,192] was employed for MAPI slabs. The band edges were aligned with respect to out–of–surface vacuum level using a two–step procedure. In addition, SCF slab calculations with vdW and the HSE hybrid functional were performed with the VASP code [202–204].

In Chapter 3 Method IV was used for AIMD. To assess the effect of thermal motion on the surface properties, AIMD simulations were performed with the CP2K code [205, 206], for the $(2 \times 2) \times 6$ MAPI slabs. We took advantage of the efficiency of this code by using the hybrid Gaussian and Plane Wave method (GPW) to represent the wavefunctions and electronic density, and the approach to extrapolate the density matrix implemented in the DFT QuickStep module [252]. Force evaluations were performed using the PBE functional with the Grimme

Table A.1: Details of DFT calculations with different codes.

Method	I	II	III	IV	V
Code	QE	QE	VASP	CP2K	VASP
Core	USPP[a]	NCPP[a]	PAW[a]	Dual–SGPP[a]	PAW[a]
Library	GBRV[b]	ONCV[c]	VASP	GTH[d]	VASP
Valence shell	H(1s)	H(1s)	H(1s)	H(1s)	H(1s)
	C(2s,2p)	C(2s,2p)	C(2s,2p)	C(2s,2p)	C(2s,2p)
	N(2s,2p)	N(2s,2p)	N(2s,2p)	N(2s,2p)	N(2s,2p)
	I(5s,5p)	I(4d,5s,5p)	I(5s,5p)	I(5s,5p)	I(5s,5p)
	Pb(5d,6s,6p)	Pb(5d,6s,6p)	Pb(6s,6p)	Pb(6s,6p)	Pb(6s,6p)
	Cu(3d,4s)	Cu(3p,3d,4s)	Cu(3d,4s)	–	Cu(3d,4s)
	O(2s,2p)	O(2s,2p)	O(2s,2p)	–	O(2s,2p)
Basis type	PW	PW	PAW	Gaussian	PAW
WFN cutoff	50 Ry	80 Ry	295 eV	–	400 eV
Basis set	–	–	–	DZVP[e]	–
Density cutoff	300 Ry	320 Ry	2655 eV	400 Ry	3600 eV
Functionals	PBEsol	PBEsol	PBE	PBE–D3[f]	PBE–D3(BJ)[f]
	optB88–vdW	optB88–vdW	optB88–vdW		
		HSE	HSE		
		PBE0	HSE(α)		
		PBE0(α)	PBE0(α)		
Conv. threshold	10^{-8} Ry	10^{-6} Ry	10^{-4} eV	10^{-6}	10^{-4} eV
Relax. threshold	10^{-6} Ry	–	–	–	–
Force threshold	10^{-4} Ry/bohr	–	–	–	0.05 eV/Å
SOC	no	yes	yes	no	no

Notes:

[a] USPP: UltraSoft Pseudo–Potentials. NCPP: Norm–Conserved Pseudo–Potentials. PAW: Projector Augmented Wave [245, 246], soft potentials were used for carbon, nitrogen and oxygen atoms. Dual–SGPP: Dual–Space Gaussian Pseudo–Potentials.

[b] PP GBRV library [247].

[c] PP SG–15 ONCV library [248, 249]. Full relativistic PPs were created using the code ONCVPSP and the SG–15 library parameters.

[d] PP GTH library [250].

[e] Short range DZVP–MOLOPT basis sets [251].

[f] Zero–damped Grimme's dispersion correction (–D3) [184] and Becke–Johnson–damped Grimme's dispersion correction (–D3(BJ)) [185].

correction scheme (DFT–D3) to account for vdW interactions [184]. BOMD, microcanonical ensemble, and PBC were used. The simulations started from the relaxed slab structures, with initial temperature of 600 K. A time step of 0.5 fs was used to integrate the Newton equations of motion. The thermalization time was 5 ps. Afterwards, the *production* runs were extended up to 40 ps. To obtain statistical information of electronic structure along the dynamics, 270 representative configurations were extracted of each dynamic slab model, and computed using PBE+SOC functional with the VASP code.

In Chapter 5 the relaxations were performed using Method V. Method III was used to compute the electronic structure on interface systems. It is worth mentioning that two parameter changes were performed in Method III: firstly, we increased the WFN and density cutoffs to 400 eV and 3600 eV, respectively, owing to higher requirements of copper and oxygen PPs. Secondly, the Brillouin zone was sampled using a Γ–centered $2 \times 2 \times 1$ $\mathbf{k}$–point grid for interface systems (instead of $3 \times 3 \times 1$ for MAPI and double sized Cu_2O bulk cells), with the aim of maintaining a balance between precision and computational resource requirements. Convergence tests with $3 \times 3 \times 1$ were made.
Particularly, we used the PBE0 [189, 190] hybrid functional with SOC, since this method is necessary to reproduce the band gap, and the conduction band dispersion of MAPI [44]. The fraction of exact exchange was tuned from standard $\alpha = 0.25$ (PBE0) to $\alpha = 0.188$, to achieve the correct band gap of both materials. This is the PBE0(α) scheme, where the α value has been determined self–consistently [193,194] for orthorhombic MAPI [44]. It provides closer band gap for both materials, with respect to experimental values, than standard PBE0.

The cutoff values for different sets of PPs and basis sets were defined by means of: Method III and V using the maximum cutoff values informed in VASP library. Method IV using a balanced values which are a good compromise between accuracy and speed for the dynamics, from GTH library. Method I and II, where GBRV and ONCV libraries were used, required a detailed study to define them, see next subsection. Also, the Brillouin zone sampling was determined by convergence study for each material, see next Section A.2.

A.2 Study of Convergence for Unit Cell Calculations

For PPs from GBRV and ONCV libraries, which are used in Method I and II, the cutoff parameter values were set after a convergence study. The **k**–point grid was also set in the same way.

To determine the optimal values for the WFN cutoff, density cutoff and **k**–points sampling for both sets of PPs, the following convergence were defined: 10 meV Atom^{-1} for total energies, 10 meV Å^{-1} for total forces and 1 kbar for cell pressure.
The values of the parameters chosen are those that allow obtaining these magnitudes within the convergence criteria, compared with the most accurate calculations for the MAPI and Cu_2O unit cells. The most accurate calculation was established as follows: 200 Ry WFN cutoff, 600 Ry density cutoff, and Γ–centered $12 \times 12 \times 8$ and $20 \times 20 \times 20$ **k**–point grid, for MAPI and Cu_2O, respectively.
The optimal WFN and density cutoff values were set in order to satisfy all convergence criteria for both materials at the same time, for each PP set. Meanwhile, the **k**–point sampling of Brillouin zone, was set for each material independently, satisfying all convergence criteria as well. The convergence study for total energy criterion is shown in Fig. A.1. This convergence level requires:

- USPP: 50 Ry WFN cutoff, 300 Ry density cutoff, and Γ–centered $3 \times 3 \times 2$ and $6 \times 6 \times 6$ **k**–point grid, for MAPI and Cu_2O, respectively.
- NCPP: 80 Ry WFN cutoff, 320 Ry density cutoff, and Γ–centered $3 \times 3 \times 2$ and $6 \times 6 \times 6$ **k**–point grid, for MAPI and Cu_2O, respectively.

Fig. A.1(A) shows total energies in terms of WFN cutoff. Total energies are subjected for the variational principle on the PW basis set size and completeness. The NCPP needs higher values to reach similar convergence criterion, compared to USPP.
The final selected density cutoff were defined as 6 times, and 4 times the WFN cutoff, for USPP and NCPP, respectively. Regardless of whether the density cutoff converges for lower values (see Fig. A.1(B)), a minimal ratio is recommended between the WFN and density cutoffs, to achieve a consistent description of wavefunctions and density and to avoid inconsistencies in non–well behaved states. For NCPP this ratio is 4, while for USPP is between 6 and 12, due to the minor requirement of WFN cutoff on USPP scheme, which does not decrease the density cutoff requirements (the minimum, 6 times, is adequate for systems under study).
The **k**–point sampling grid, as Fig. A.1(C) shows, does not depend on PPs. It depends on electronic structure and band dispersion in reciprocal space, which is system dependent.

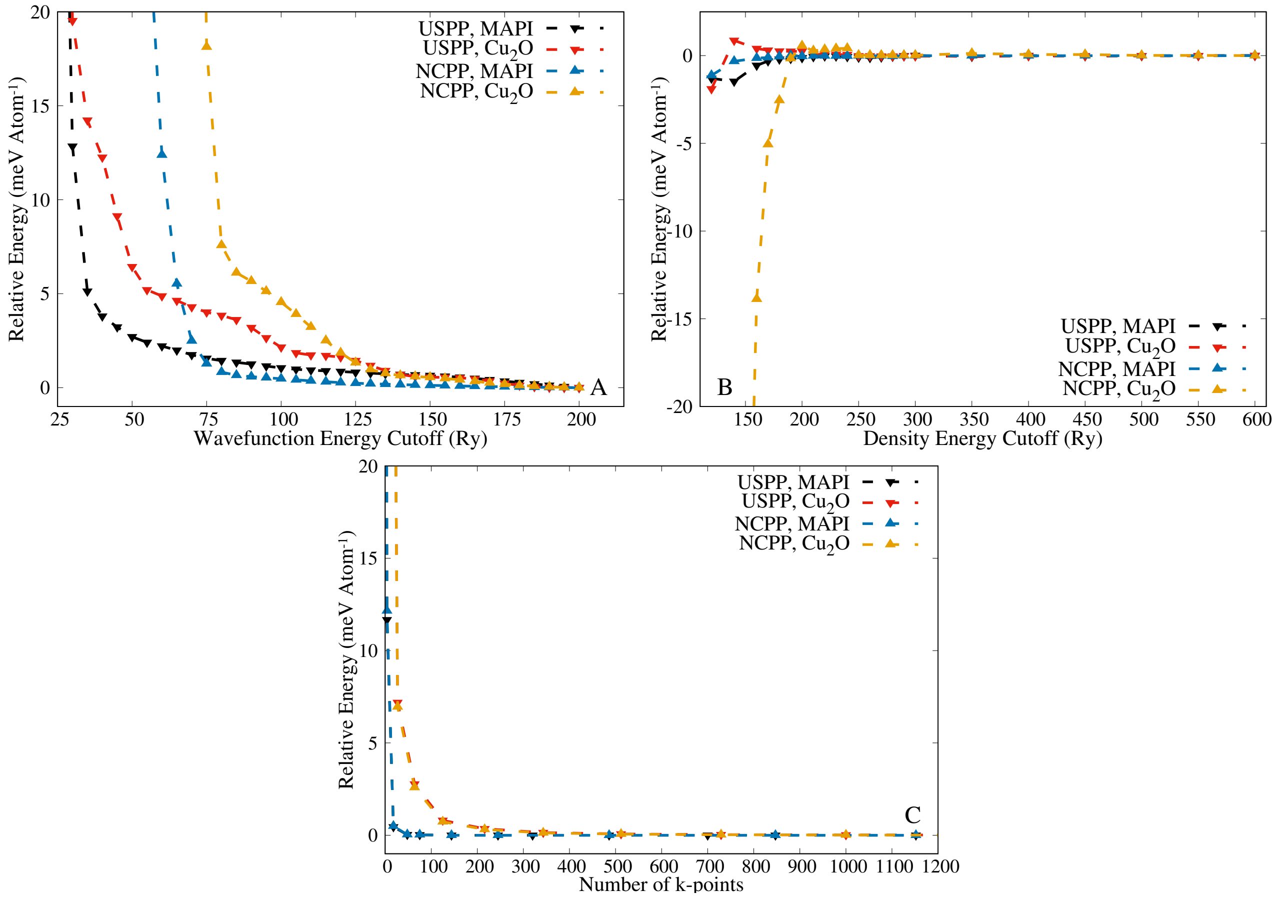

Figure A.1: Convergence study of total energy criterion with respect to: (A) WFN cutoff, (B) density cutoff, and (C) **k**–point sampling (informed as the total number of **k**–points in the grid), for MAPI and Cu_2O.

A.3 Study of Convergence for Surface Energy Calculations

In the last section, the WFN cutoff, density cutoff, and **k**–points sampling were optimized with respect to total energies, total forces and cell pressures. These parameters were defined using convergence criteria. In particular total energy criterion of 10 meV Atom^{-1}.
This error in total energies, due to the selected parameters, could affect other energy quantities, as the surface energy, but in a different manner. Total energies obeys the variational principle. Meanwhile, surface energy is defined as a difference of total energies, this quantity is not variationally converged and the error compensation among total energies could reduce the error in surface energy determination.

In this way, a convergence study of surface energy was performed. O– and Cu–terminated Cu_2O, and MAI– and PbI_2–terminated MAPI $(1 \times 1) \times 5$ slabs were the selected systems. The most accurate calculation was established as 200 Ry WFN cutoff, 600 Ry density cutoff, and Γ–centered $12 \times 12 \times 1$ and $20 \times 20 \times 1$ **k**–point grid, for MAPI and Cu_2O, respectively. Additionally, a vacuum width study was carried out, to analyze the effect of long range replica interaction.
Fig. A.2 shows the relative surface energies for all surface systems, with respect to the most

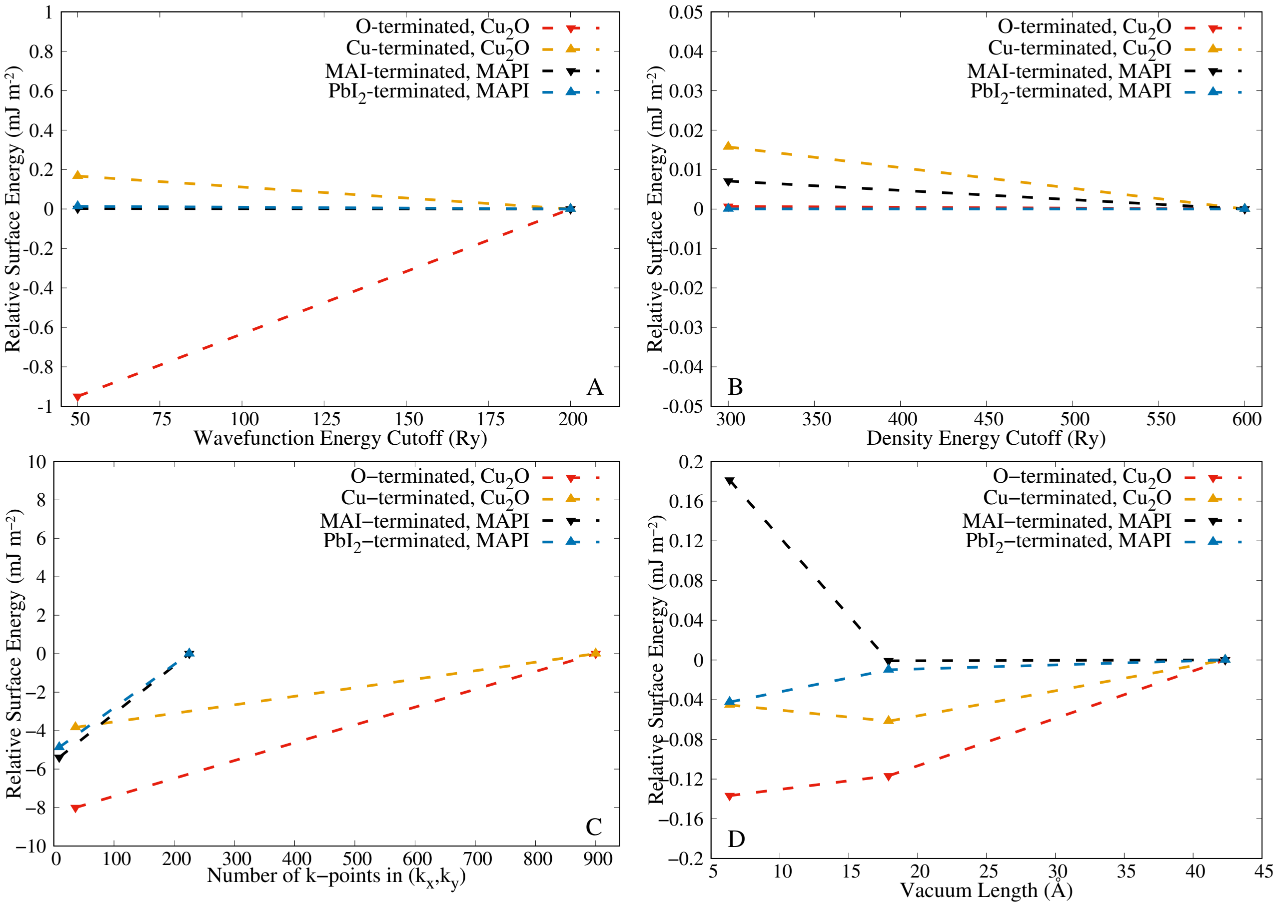

Figure A.2: Convergence study of surface energy with respect to: (A) WFN cutoff, (B) density cutoff, (C) **k**–point sampling (informed as the number of **k**–points in the k_x and k_y grid), and (D) vacuum width, for MAPI and Cu_2O surface systems.

accurate calculation. The main source of surface energy error was the **k**–point sampling. Meanwhile, the error due to WFN cutoff was one order of magnitude less. The other parameters display negligible effects on surface energy.

The surface energy error determinations were conservative defined as the sum of error from each parameter to ensure an error upper bound. Surface energy error were: 9.0, 4.1, 5.4, and 6.3 mJ m^{-2} for O–, Cu–, MAI–, and PbI_2–surface systems, respectively. Meanwhile, the contribution of the **k**–point sampling to the total error was: 88.9, 94.0, 99.5, and 99.1 %, respectively. The surface energy errors in all cases are sufficiently small, compared to surface energy for each system (578, 1803, −19, and 176 mJ m^{-2} for O–, Cu–, MAI–, and PbI_2–surface systems, respectively), thereby enabling to determine the surface energies.

A.4 Vacuum width convergence

The convergence of the state and surface energies with respect to the width of the vacuum region was studied using MAI– and PbI_2– terminated MAPI $(1 \times 1) \times 5$ slabs. We use the parameter setup of Method I for this purpose. We have considered three vacuum thickness: 6.4, 17.9, and 42.3 Å. To begin with, we have verified that the relaxed atomic positions do not change with the vacuum width.

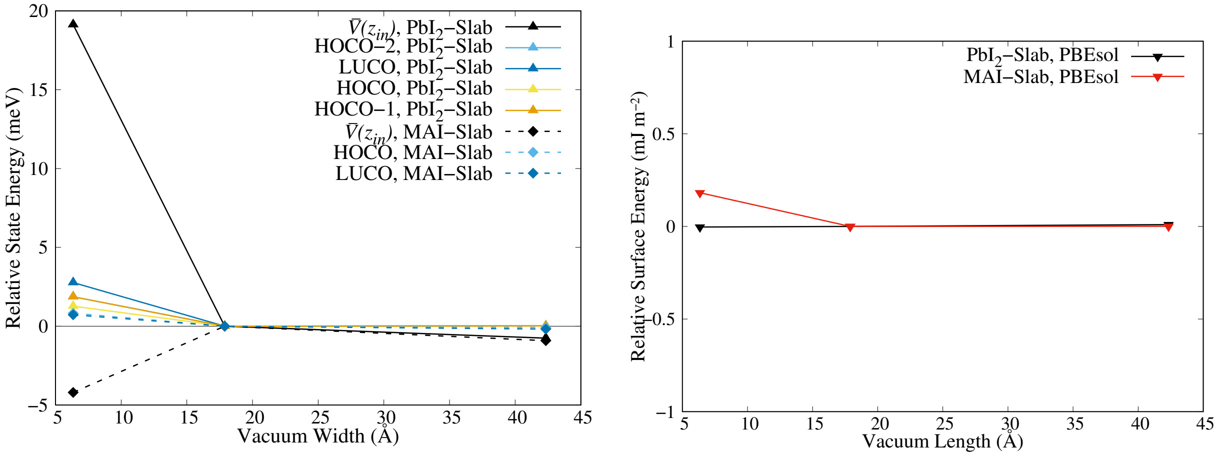

(a) States energy

(b) Surface energy

Figure A.3: Convergence of MAPI(001)–PbI_2 and MAPI(001)–MAI with respect to vacuum thickness, relative to standard vacuum thickness: (a) States energy (in meV), (b) Surface energy.

Fig. A.3(a) shows the behaviour of the slab state energies and the *macroscopic* electrostatic potential ($\bar{V}(z_{in})$), and Fig. A.3(b) the surface energies. The variations of all state energy magnitudes are smaller than 20 meV, which is negligible. As shown, the surface energy variation are negligible (< 0.2 mJ m^{-2}), being much smaller than the surface energy error (see Appendix A.3).

A.5 Supplementary Information: Chapter 3

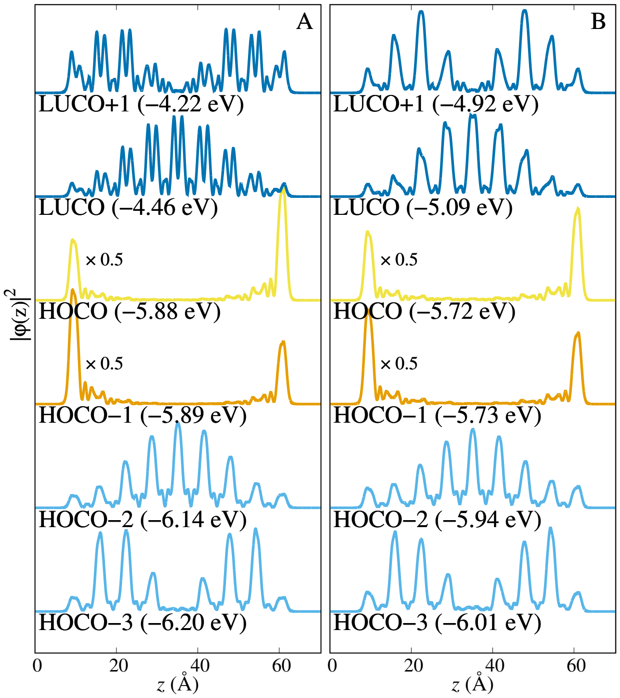

Figure A.4: Plane–averaged wavefunctions for the frontier orbitals shown in Fig. 3.5(a) and their energies with respect to vacuum level of (1 × 1) × 8 MAPI(001)–PbI$_2$. (A) PBEsol, (B) PBEsol+SOC.

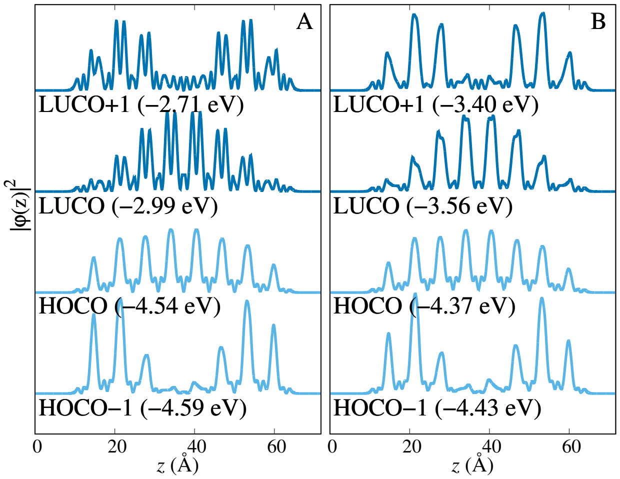

Figure A.5: Plane–averaged wavefunctions for the frontier orbitals shown in Fig. 3.5(b) and their energies with respect to vacuum level of (1 × 1) × 8 MAPI(001)–MAI. (A) PBEsol, (B) PBEsol+SOC.

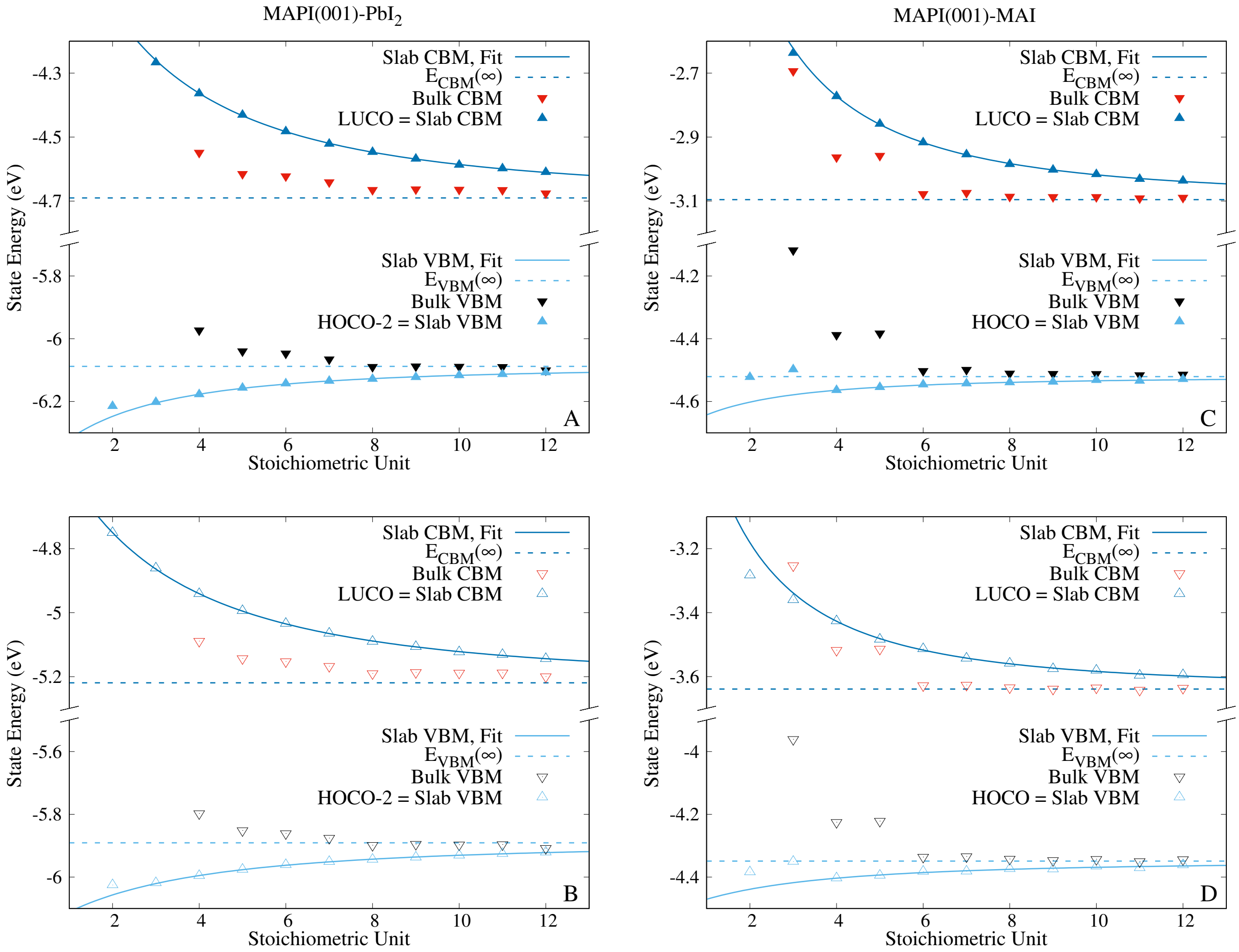

Figure A.6: Same as main text Fig. 3.5 (without surface states), including the $E_\alpha(n)$ and the asymptotic fit energy for each slab level shown. (A) and (C) PBEsol. (B) and (D) PBEsol+SOC.

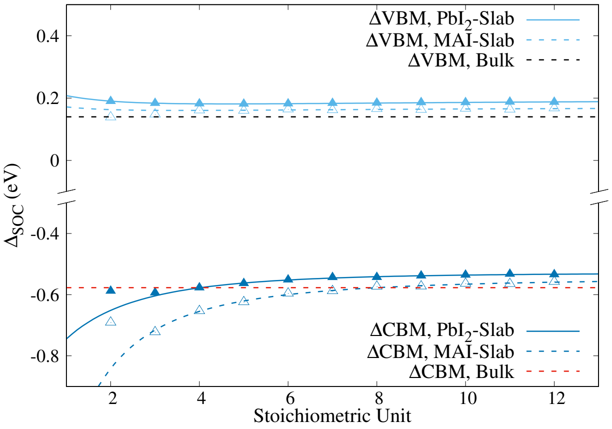

Figure A.7: SOC correction, computed as main text Eq. 3.3. Points calculated with slab energy data.

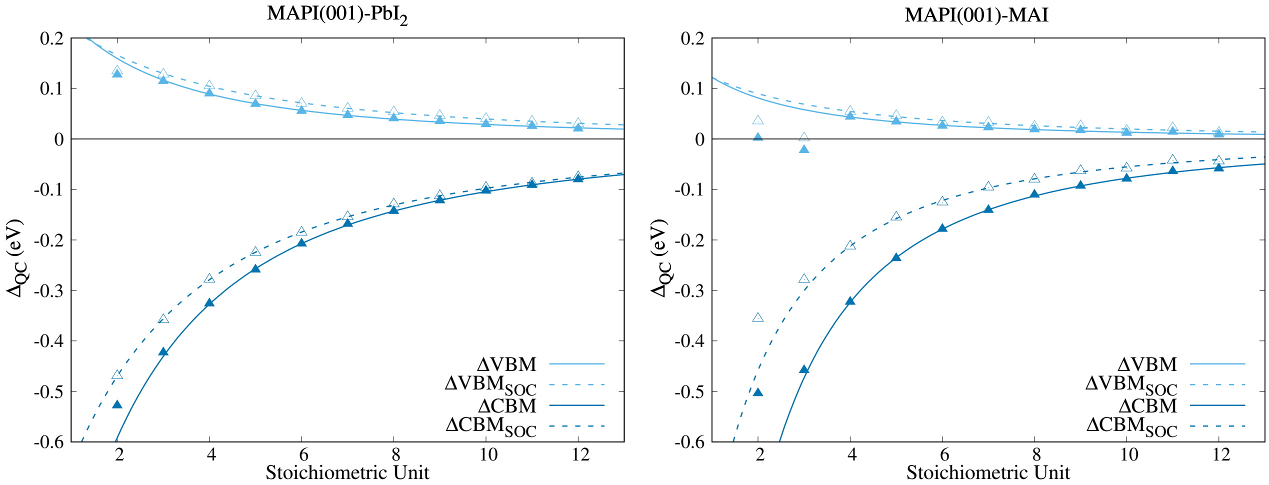

Figure A.8: QC correction, computed as main text Eq. 3.4. Points calculated with slab energy data.

Table A.2: Band edge energy levels with respect to the vacuum level for slab MAPI(001)–PbI$_2$ and MAPI(001)–MAI. Energy levels computed with the two–step process over PBEsol SCF calculations and energy corrections of Table 3.2 for different levels of theory with the minimum energy cell structure.* All values in the Table are in eV.

Functional	HSE+SOC	G_0W_0+SOC	PBE0(0.188)+SOC	PBE0+SOC
MAPI(001)–PbI$_2$ *unpolarized* (*polarized*)				
E_{VBM}	-6.55 (-6.30)	-7.53 (-7.28)	-6.60 (-6.35)	-6.86 (-6.61)
E_{CBM}	-5.31 (-5.06)	-5.52 (-5.27)	-5.06 (-4.81)	-5.06 (-4.81)
MAPI(001)–MAI				
E_{VBM}	-5.26	-6.24	-5.31	-5.57
E_{CBM}	-4.02	-4.23	-3.77	-3.77

* Due to the use of two–step process, band edge energy levels are free of QC in principle.

Bibliography

[1] L. Lodeiro, F. Barría-Cáceres, K. Jiménez, R. Contreras, A. L. Montero-Alejo, and E. Menéndez-Proupin, "Methodological Issues in First-Principle Calculations of $CH_3NH_3PbI_3$ Perovskite Surfaces: Quantum Confinement and Thermal Motion," *ACS Omega*, vol. 5, no. 45, pp. 29477–29491, 2020.

[2] J. E. Castellanos-Águila, L. Lodeiro, E. Menéndez-Proupin, A. L. Montero-Alejo, P. Palacios, J. C. Conesa, and P. Wahnón, "Atomic-Scale Model and Electronic Structure of $Cu_2O/CH_3NH_3PbI_3$ Interfaces in Perovskite Solar cells," *ACS Appl. Mater. Interfaces*, vol. 12, no. 40, pp. 44648–44657, 2020.

[3] L. Lodeiro and T. Rauch, "DensityTool: A Post-Processing Tool for Space- and Spin-Resolved Density of States from VASP," *Comput. Phys. Commun.*, vol. 277, p. 108384, 2022.

[4] P. Forster, V. Ramaswamy, P. Artaxo, T. Berntsen, R. Betts, D. Fahey, J. Haywood, J. Lean, D. Lowe, G. Myhre, J. Nganga, R. Prinn, G. Raga, M. Schulz, and R. V. Dorland, *Changes in Atmospheric Constituents and in Radiative Forcing. Climate Change 2007: The Physical Science Basis. Contribution of Working Group I to the Fourth Assessment Report of the IPCC.* Cambridge: Cambridge University Press, 2008.

[5] J. Hansen, P. Kharecha, M. Sato, V. Masson-Delmotte, F. Ackerman, D. J. Beerling, P. J. Hearty, O. Hoegh-Guldberg, S.-L. Hsu, C. Parmesan, J. Rockstrom, E. J. Rohling, J. Sachs, P. Smith, K. Steffen, L. Van Susteren, K. von Schuckmann, and J. C. Zachos, "Assessing "Dangerous Climate Change": Required Reduction of Carbon Emissions to Protect Young People, Future Generations and Nature," *PLOS ONE*, vol. 8, no. 12, pp. 1–26, 2013.

[6] Paris Agreement. Accessed on 15-October-2020.

[7] J. Hansen, M. Sato, P. Kharecha, D. Beerling, R. Berner, V. Masson-Delmotte, M. Pagani, M. Raymo, D. L. Royer, and J. C. Zachos, "Target Atmospheric CO_2: Where Should Humanity Aim?," *Open Atmospheric Sci. J.*, vol. 2, no. 1, pp. 217–231, 2008.

[8] S. J. Davis, K. Caldeira, and H. D. Matthews, "Future CO_2 Emissions and Climate Change from Existing Energy Infrastructure," *Science*, vol. 329, no. 5997, pp. 1330–1333, 2010.

[9] R. M. Varney, S. E. Chadburn, P. Friedlingstein, E. J. Burke, C. D. Koven, G. Hugelius, and P. M. Cox, "A Spatial Emergent Constraint on the Sensitivity of Soil Carbon Turnover to Global Warming," *Nat. Commun.*, vol. 11, no. 1, p. 5544, 2020.

[10] Z. Liu, Z. Deng, S. J. Davis, C. Giron, and P. Ciais, "Monitoring Global Carbon Emissions in 2021," *Nat Rev Earth Environ*, vol. 3, no. 4, pp. 217–219, 2022.

[11] J. F. Brennecke and B. E. Gurkan, "Ionic Liquids for CO_2 Capture and Emission Reduction," *J. Phys. Chem. Lett.*, vol. 1, no. 24, pp. 3459–3464, 2010.

[12] M. I. Hoffert, K. Caldeira, A. K. Jain, E. F. Haites, L. D. Danny Harvey, S. D. Potter, M. E. Schlesinger, S. H. Schneider, R. G. Watts, T. M. L. Wigley, and D. J. Wuebbles, "Energy Implications of Future Stabilization of Atmospheric CO_2 Content," *Nature*, vol. 395, pp. 881–884, 1998.

[13] S. Gallardo-Fuentes, R. Contreras, M. Isaacs, J. Honores, D. Quezada, E. Landaeta, and R. Ormazábal-Toledo, "On the Mechanism of CO_2 Electro-Cycloaddition to Propylene Oxides," *J. CO2 Util.*, vol. 16, pp. 114 – 120, 2016.

[14] I. H. Arellano, J. Huang, and P. Pendleton, "Computational Insights into the Molecular Interaction and Ion-Pair Structures of a Novel Zinc-Functionalized Ionic Liquid, $[Emim][Zn(TFSI)_3]$," *Spectrochim. Acta A*, vol. 153, pp. 6 – 15, 2016.

[15] Z. Xue, Z. Zhang, J. Han, Y. Chen, and T. Mu, "Carbon Dioxide Capture by a Dual Amino Ionic Liquid with Amino-Functionalized Imidazolium Cation and Taurine Anion," *Int. J. Greenh. Gas Control.*, vol. 5, no. 4, pp. 628 – 633, 2011.

[16] E. D. Bates, R. D. Mayton, I. Ntai, and J. H. Davis, "CO_2 Capture by a Task-Specific Ionic Liquid," *J. Am. Chem. Soc.*, vol. 124, no. 6, pp. 926–927, 2002.

[17] E. Torralba-Calleja, J. Skinner, and D. Gutierrez Tauste, "CO_2 Capture in Ionic Liquids: A Review of Solubilities and Experimental Methods," *J. Chem.*, vol. 2013, p. 473584, 2013.

[18] L. Cao, J. Huang, X. Zhang, S. Zhang, J. Gao, and S. Zeng, "Imidazole Tailored Deep Eutectic Solvents for CO_2 Capture Enhanced by Hydrogen Bonds," *Phys. Chem. Chem. Phys.*, vol. 17, pp. 27306–27316, 2015.

[19] X. Li, M. Hou, B. Han, X. Wang, and L. Zou, "Solubility of CO_2 in a Choline Chloride + Urea Eutectic Mixture," *J. Chem. Eng. Data*, vol. 53, no. 2, pp. 548–550, 2008.

[20] I. E. Agency, *Key World Energy Statistics 2018*. IEA, Paris, 2018.

[21] G. Segev, J. W. Beeman, J. B. Greenblatt, and I. D. Sharp, "Hybrid Photoelectrochemical and Photovoltaic Cells for Simultaneous Production of Chemical Fuels and Electrical Power," *Nat. Mater.*, vol. 17, no. 12, pp. 1115–1121, 2018.

[22] IRENA, *Renewable Power Generation Costs in 2018, Abu Dhabi.* International Renewable Energy Agency, 2019.

[23] W. Palz, *Power for the World - The Emergence of Electricity from the Sun.* Belgium: Pan Stanford Publishing, p. 6 ed., 2010.

[24] D. S. Ginley and D. Cahen, *Fundamentals of Materials for Energy and Environmental Sustainability.* Cambridge: Cambridge University Press, 2011.

[25] F. L. Pedrotti, L. S. Pedrotti, and L. M. Pedrott, *Introduction to Optics.* 3 ed., 2013.

[26] G. Grosso and G. P. Parravicini, *Solid State Physics.* London: Academic Press, 2 ed., 2000.

[27] N. Wikimedia Commons, "Band Structure Diagrams for Metal, etc. Inspired by Kittel's Introduction to Solid State Physics 7th Edition, chapter 7.; File:Band filling diagram.svg — Wikimedia Commons, the free media repository," 2014. [Online; Accessed 28-May-2022].

[28] P. Würfel, *Physics of Solar Cells.* Weinheim: Wiley, 2 ed., 2009.

[29] Z. Song, S. C. Watthage, A. B. Phillips, and M. J. Heben, "Pathways Toward High-Performance Perovskite Solar Cells: Review of Recent Advances in Organo-Metal Halide Perovskites for Photovoltaic Applications," *J. Photonics Energy*, vol. 6, no. 2, pp. 1–23, 2016.

[30] Y. Xu and M. A. A. Schoonen, "The Absolute Energy Positions of Conduction and Valence Bands of Selected Semiconducting Minerals," *Am. Mineral.*, vol. 85, no. 3-4, pp. 543–556, 2000.

[31] P. Y. Yu and M. Cardona, *Fundamentals of Semiconductors.* Berlin: Springer, 2 ed., 1996.

[32] P. K. Nayak, G. Garcia-Belmonte, A. Kahn, J. Bisquert, and D. Cahen, "Photovoltaic Efficiency Limits and Material Disorder," *Energy Environ. Sci.*, vol. 5, pp. 6022–6039, 2012.

[33] P. P. Boix, K. Nonomura, N. Mathews, and S. G. Mhaisalkar, "Current Progress and Future Perspectives for Organic/Inorganic Perovskite Solar Cells," *Mater. Today*, vol. 17, no. 1, pp. 16–23, 2014.

[34] G. S. Alzahrani, F. S. Alzahrani, and A. M. Nahhas, "Study of the Specific Factors Effecting the PV Solar Cell's Efficiency in Saudi Arabia," *Sustain. Energy*, vol. 8, no. 1, pp. 6–11, 2020.

[35] W. Shockley and H. J. Queisser, "Detailed Balance Limit of Efficiency of p-n Junction Solar Cells," *J. Appl. Phys.*, vol. 32, no. 3, pp. 510–519, 1961.

[36] NREL Chart on Record Cell Efficiencies. Accessed on 01-April-2022.

[37] C. Fritts, "On a New Form of Selenium Photocell," *Am. J. Sci.*, vol. 26, p. 465, 1883.

[38] D. M. Chapin, C. S. Fuller, and G. L. Pearson, "A New Silicon p-n Junction Photocell for Converting Solar Radiation into Electrical Power," *J. Appl. Phys.*, vol. 25, no. 5, pp. 676–677, 1954.

[39] NREL Champion Module Efficiencies. Accessed on 28-June-2022.

[40] A. Kojima, K. Teshima, Y. Shirai, and T. Miyasaka, "Organometal Halide Perovskites as Visible-Light Sensitizers for Photovoltaic Cells," *J. Am. Chem. Soc.*, vol. 131, pp. 6050–6051, 2009.

[41] E. Menéndez-Proupin, S. Grover, A. L. Montero-Alejo, S. D. Midgley, K. T. Butler, and R. Grau-Crespo, "Mixed-Anion Mixed-Cation Perovskite $(FAPbI_3)_{0.875}(MAPbBr_3)_{0.125}$: An Ab Initio Molecular Dynamics Study," *J. Mater. Chem. A*, vol. 10, pp. 9592–9603, 2022.

[42] P. Sánchez-Palencia, G. García, P. Wahnón, and P. Palacios, "Cation Substitution Effects on the Structural, Electronic and Sun-Light Absorption Features of All-Inorganic Halide Perovskites," *Inorg. Chem. Front.*, vol. 9, pp. 1337–1353, 2022.

[43] S. D. Stranks, G. E. Eperon, G. Grancini, C. Menelaou, M. J. P. Alcocer, T. Leijtens, L. M. Herz, A. Petrozza, and H. J. Snaith, "Electron-Hole Diffusion Lengths Exceeding 1 Micrometer in an Organometal Trihalide Perovskite Absorber," *Science*, vol. 342, no. 6156, pp. 341–344, 2013.

[44] E. Menéndez-Proupin, P. Palacios, P. Wahnón, and J. C. Conesa, "Self-Consistent Relativistic Band Structure of the $CH_3NH_3PbI_3$ Perovskite," *Phys. Rev. B*, vol. 90, p. 045207, 2014.

[45] A. L. Montero-Alejo, E. Menéndez-Proupin, D. Hidalgo-Rojas, P. Palacios, P. Wahnón, and J. C. Conesa, "Modeling of Thermal Effect on the Electronic Properties of Photovoltaic Perovskite $CH_3NH_3PbI_3$: The Case of Tetragonal Phase," *J. Phys. Chem. C*, vol. 120, pp. 7976–7986, 2016.

[46] O. Knop, R. E. Wasylishen, M. A. White, T. S. Cameron, and M. J. M. van Oort, "Alkylammonium Lead Halides. Part 2. $CH_3NH_3PbX_3$ (X = Cl,Br,I) Perovskites: Cuboctahedral Halides Cages with Isotropic Cation Reorientation," *Can. J. Chem.*, vol. 68, pp. 412–422, 1990.

[47] M. T. Weller, O. J. Weber, P. F. Henry, A. M. Di Pumpo, and T. C. Hansen, "Complete Structure and Cation Orientation in the Perovskite Photovoltaic Methylammonium Lead Iodide between 100 and 352 k," *Chem. Commun.*, vol. 51, pp. 4180–4183, 2015.

[48] A. Poglitsch and D. Weber, "Dynamic Disorder in Methylammoniumtrihalogenoplumbates (II) Observed by Millimeter-Wave Spectroscopy," *J. Chem. Phys.*, vol. 87, no. 11, pp. 6373–6378, 1987.

[49] Y. Kawamura, H. Mashiyama, and K. Hasebe, "Structural Study on Cubic-Tetragonal Transition of $CH_3NH_3PbI_3$," *J. Phys. Soc. Jpn.*, vol. 71, pp. 1694–1697, 2002.

[50] K. Momma and F. Izumi, "*VESTA* 3 for Three-Dimensional Visualization of Crystal, Volumetric and Morphology Data," *J. Appl. Crystallogr.*, vol. 44, no. 6, pp. 1272–1276, 2011.

[51] T. Baikie, Y. Fang, J. M. Kadro, M. Schreyer, F. Wei, S. G. Mhaisalkar, M. Graetzel, and T. J. White, "Synthesis and Crystal Chemistry of the Hybrid Perovskite $(CH_3NH_3)PbI_3$ for Solid-State Sensitised Solar Cell Applications," *J. Mater. Chem. A*,

vol. 1, pp. 5628–5641, 2013.

[52] P. Scherpelz, M. Govoni, I. Hamada, and G. Galli, “Implementation and Validation of Fully Relativistic GW Calculations: Spin–Orbit Coupling in Molecules, Nanocrystals, and Solids,” *J. Chem. Theory Comput.*, vol. 12, no. 8, pp. 3523–3544, 2016.

[53] L. Zhang, W. Geng, C.-j. Tong, X. Chen, T. Cao, and M. Chen, “Strain Induced Electronic Structure Variation in Methyl-Ammonium Lead Iodide Perovskite,” *Sci. Rep.*, vol. 8, no. 1, p. 7760, 2018.

[54] T. A. Berhe, W.-N. Su, C.-H. Chen, C.-J. Pan, J.-H. Cheng, H.-M. Chen, M.-C. Tsai, L.-Y. Chen, A. A. Dubale, and B.-J. Hwang, “Organometal Halide Perovskite Solar Cells: Degradation and Stability,” *Energy Environ. Sci.*, vol. 9, pp. 323–356, 2016.

[55] G. Y. Kim, A. Senocrate, T.-Y. Yang, G. Gregori, M. Grätzel, and J. Maier, “Large Tunable Photoeffect on Ion Conduction in Halide Perovskites and Implications for Photodecomposition,” *Nat. Mater.*, vol. 17, pp. 445–449, 2018.

[56] C. C. Stoumpos, C. D. Malliakas, and M. G. Kanatzidis, “Semiconducting Tin and Lead Iodide Perovskites with Organic Cations: Phase Transitions, High Mobilities, and Near-Infrared Photoluminescent Properties,” *Inorg. Chem.*, vol. 52, no. 15, pp. 9019–9038, 2013.

[57] S. Ito, S. Tanaka, K. Manabe, and H. Nishino, “Effects of Surface Blocking Layer of Sb_2S_3 on Nanocrystalline TiO_2 for $CH_3NH_3PbI_3$ Perovskite Solar Cells,” *J. Phys. Chem. C*, vol. 118, no. 30, pp. 16995–17000, 2014.

[58] T. D. Siegler, D. W. Houck, S. H. Cho, D. J. Milliron, and B. A. Korgel, “Bismuth Enhances the Stability of $CH_3NH_3PbI_3$ (mapi) Perovskite under High Humidity,” *J. Phys. Chem. C*, vol. 123, no. 1, pp. 963–970, 2019.

[59] M. Saliba, J.-P. Correa-Baena, C. M. Wolff, M. Stolterfoht, N. Phung, S. Albrecht, D. Neher, and A. Abate, “How to Make over 20 % Efficient Perovskite Solar Cells in Regular (n–i–p) and Inverted (p–i–n) Architectures,” *Chem. Mater.*, vol. 30, no. 13, pp. 4193–4201, 2018.

[60] B. Charles, J. Dillon, O. J. Weber, M. S. Islam, and M. T. Weller, “Understanding the Stability of Mixed A-Cation Lead Iodide Perovskites,” *J. Mater. Chem. A*, vol. 5, pp. 22495–22499, 2017.

[61] F. Palazon, D. Pérez-del Rey, S. Marras, M. Prato, M. Sessolo, H. J. Bolink, and L. Manna, “Coating Evaporated MAPI Thin Films with Organic Molecules: Improved Stability at High Temperature and Implementation in High-Efficiency Solar Cells,” *ACS Energy Lett.*, vol. 3, no. 4, pp. 835–839, 2018.

[62] S. Wang, T. Sakurai, W. Wen, and Y. Qi, “Energy Level Alignment at Interfaces in Metal Halide Perovskite Solar Cells,” *Adv. Mater. Interfaces*, vol. 5, p. 1800260, 2018.

[63] P. Schulz, D. Cahen, and A. Kahn, “Halide Perovskites: Is It All about the Interfaces?,” *Chem. Rev.*, vol. 119, pp. 3349–3417, 2019.

[64] J. Urieta-Mora, I. García-Benito, A. Molina-Ontoria, and N. Martín, “Hole Transporting Materials for Perovskite Solar Cells: A Chemical Approach,” *Chem. Soc. Rev.*, vol. 47, pp. 8541–8571, 2018.

[65] A. Fakharuddin, L. Schmidt-Mende, G. Garcia-Belmonte, R. Jose, and I. Mora-Sero, “Interfaces in Perovskite Solar Cells,” *Adv. Energy Mater.*, vol. 7, p. 1700623, 2017.

[66] O. Fernandez-Delgado, E. Castro, C. R. Ganivet, K. Fosnacht, F. Liu, T. Mates, Y. Liu, X. Wu, and L. Echegoyen, “Variation of Interfacial Interactions in PC_61BM-like Electron-Transporting Compounds for Perovskite Solar Cells,” *ACS Appl. Mater. Interfaces*, vol. 11, pp. 34408–34415, 2019.

[67] L. She, M. Liu, and D. Zhong, “Atomic Structures of $CH_3NH_3PbI_3$(001) Surfaces,” *ACS Nano*, vol. 10, pp. 1126–1131, 2016.

[68] R. Ohmann, L. K. Ono, H.-S. Kim, H. Lin, M. V. Lee, Y. Li, N.-G. Park, and Y. Qi, “Real-Space Imaging of the Atomic Structure of Organic–Inorganic Perovskite,” *J. Am. Chem. Soc.*, vol. 137, pp. 16049–16054, 2015.

[69] L. K. Ono and Y. Qi, “Surface and Interface Aspects of Organometal Halide Perovskite Materials and Solar Cells,” *J. Phys. Chem. Lett.*, vol. 7, pp. 4764–4794, 2016.

[70] L. Qiu, S. He, L. K. Ono, and Y. Qi, “Progress of Surface Science Studies on ABX_3-Based Metal Halide Perovskite Solar Cells,” *Adv. Energy Mater.*, vol. 10, no. 13, p. 1902726, 2020.

[71] Y. Dong, K. Li, W. Luo, C. Zhu, H. Guan, H. Wang, L. Wang, K. Deng, H. Zhou, H. Xie, Y. Bai, Y. Li, and Q. Chen, “The Role of Surface Termination in Halide Perovskites for Efficient Photocatalytic Synthesis,” *Angew. Chemie Int. Ed.*, vol. 59, pp. 12931–12937, 2020.

[72] Y. Wang, B. G. Sumpter, J. Huang, H. Zhang, P. Liu, H. Yang, and H. Zhao, “Density Functional Studies of Stoichiometric Surfaces of Orthorhombic Hybrid Perovskite $CH_3NH_3PbI_3$,” *J. Phys. Chem. C*, vol. 119, pp. 1136–1145, 2015.

[73] A. Torres and L. G. C. Rego, “Surface Effects and Adsorption of Methoxy Anchors on Hybrid Lead Iodide Perovskites: Insights for Spiro-MeOTAD Attachment,” *J. Phys. Chem. C*, vol. 118, pp. 26947–26954, 2014.

[74] J. Haruyama, K. Sodeyama, L. Han, and Y. Tateyama, “Termination Dependence of Tetragonal $CH_3NH_3PbI_3$ Surfaces for Perovskite Solar Cells,” *J. Phys. Chem. Lett.*, vol. 5, pp. 2903–2909, 2014.

[75] W. Geng, C.-J. Tong, Z.-K. Tang, C. Yam, Y.-N. Zhang, W.-M. Lau, and L.-M. Liu, “Effect of Surface Composition on Electronic Properties of Methylammonium Lead Iodide Perovskite,” *J. Materiomics*, vol. 1, pp. 213–220, 2015.

[76] E. Mosconi, J. M. Azpiroz, and F. De Angelis, “Ab Initio Molecular Dynamics Simulations of Methylammonium Lead Iodide Perovskite Degradation by Water,” *Chem. Mater.*, vol. 27, pp. 4885–4892, 2015.

[77] C. Quarti, F. De Angelis, and D. Beljonne, “Influence of Surface Termination on the Energy Level Alignment at the $CH_3NH_3PbI_3$ Perovskite/C_{60} Interface,” *Chem. Mater.*, vol. 29, pp. 958–968, 2017.

[78] P. W. Tasker, “The Stability of Ionic Crystal Surfaces,” *J. Phys. C*, vol. 12, pp. 4977–4984, 1979.

[79] H. Wang, A. Guerrero, A. Bou, A. Al Mayouf, and J. Bisquert, “Kinetic and Material Properties of Interfaces Governing Slow

Response and Long Timescale Phenomena in Perovskite Solar Cells," *Energy Environ. Sci.*, vol. 12, pp. 2054–2079, 2019.

[80] J. A. Christians, R. C. M. Fung, and P. V. Kamat, "An Inorganic Hole Conductor for Organo-Lead Halide Perovskite Solar Cells. Improved Hole Conductivity with Copper Iodide," *J. Am. Chem. Soc.*, vol. 136, no. 2, pp. 758–764, 2014.

[81] P. Qin, S. Tanaka, S. Ito, N. Tetreault, K. Manabe, H. Nishino, M. K. Nazeeruddin, and M. Grätzel, "Inorganic Hole Conductor-Based Lead Halide Perovskite Solar Cells with 12.4 % Conversion Efficiency," *Nat. Commun.*, vol. 5, no. 1, p. 3534, 2014.

[82] W. H. Brattain, "The Copper Oxide Rectifier," *Rev. Mod. Phys.*, vol. 23, pp. 203–212, 1951.

[83] H.-B. Li, W. Wang, X. Xie, Y. Cheng, Z. Zhang, H. Dong, R. Zheng, W.-H. Wang, F. Lu, and H. Liu, "Electronic Structure and Ferromagnetism Modulation in Cu/Cu_2O Interface: Impact of Interfacial Cu Vacancy and Its Diffusion," *Sci. Rep.*, vol. 5, no. 1, p. 15191, 2015.

[84] M. Hara, T. Kondo, M. Komoda, S. Ikeda, J. N. Kondo, K. Domen, M. Hara, K. Shinohara, and A. Tanaka, "Cu_2O as a Photocatalyst for Overall Water Splitting Under Visible Light Irradiation," *Chem. Commun.*, pp. 357–358, 1998.

[85] C.-C. Hu, J.-N. Nian, and H. Teng, "Electrodeposited p-Type Cu_2O as Photocatalyst for H_2 Evolution from Water Reduction in the Presence of WO_3," *Sol. Energy Mater. Sol. Cells*, vol. 92, no. 9, pp. 1071–1076, 2008.

[86] W. Siripala, A. Ivanovskaya, T. F. Jaramillo, S.-H. Baeck, and E. W. McFarland, "A Cu_2O/TiO_2 Heterojunction Thin Film Cathode for Photoelectrocatalysis," *Sol. Energy Mater. Sol. Cells*, vol. 77, no. 3, pp. 229–237, 2003.

[87] L. Olsen, F. Addis, and W. Miller, "Experimental and Theoretical Studies of Cu_2O Solar Cells," *Solar Cells*, vol. 7, no. 3, pp. 247–279, 1982.

[88] S. Shibasaki, Y. Honishi, N. Nakagawa, M. Yamazaki, Y. Mizuno, Y. Nishida, K. Sugimoto, and K. Yamamoto, "Highly Transparent Cu_2O Absorbing Layer for Thin Film Solar Cells," *Appl. Phys. Lett.*, vol. 119, no. 24, p. 242102, 2021.

[89] T. Ito, H. Yamaguchi, K. Okabe, and T. Masumi, "Single-Crystal Growth and Characterization of Cu_2O and CuO," *J. Mater. Sci.*, vol. 33, no. 14, pp. 3555–3566, 1998.

[90] R. Wyckoff, *Crystal Structures.* New York: Wiley, 1st ed., 1965.

[91] P. A. Korzhavyi and B. Johansson, "Literature Review on the Properties of Cuprous Oxide Cu_2O and the Process of Copper Oxidation," *SKB-TR-11-08, Sweden*, 2011.

[92] R. D. Shannon, "Revised Effective Ionic Radii and Systematic Studies of Interatomic Distances in Halides and Chalcogenides," *Acta Crystallogr. Sect. A*, vol. 32, no. 5, pp. 751–767, 1976.

[93] J. M. Zuo, M. Kim, M. O'Keeffe, and J. C. H. Spence, "Direct Observation of d-Orbital Holes and Cu–Cu Bonding in Cu_2O," *Nature*, vol. 401, no. 6748, p. 49, 1999.

[94] J. M. Zuo, "Measurements of Electron Densities in Solids: a Real-Space View of Electronic Structure and Bonding in Inorganic Crystals," *Rep. Prog. Phys.*, vol. 67, no. 11, pp. 2053–2103, 2004.

[95] L. Kleinman and K. Mednick, "Self-Consistent Energy Bands of Cu_2O," *Phys. Rev. B*, vol. 21, pp. 1549–1553, 1980.

[96] J. Robertson, "Electronic Structure and X-ray Near-Edge Core Spectra of Cu_2O," *Phys. Rev. B*, vol. 28, pp. 3378–3385, 1983.

[97] R. J. Elliott, "Intensity of Optical Absorption by Excitons," *Phys. Rev.*, vol. 108, pp. 1384–1389, 1957.

[98] R. J. Elliott, "Symmetry of Excitons in Cu_2O," *Phys. Rev.*, vol. 124, pp. 340–345, 1961.

[99] T. Kazimierczuk, D. Fröhlich, S. Scheel, H. Stolz, and M. Bayer, "Giant Rydberg Excitons in the Copper Oxide Cu_2O," *Nature*, vol. 514, no. 7522, pp. 343–347, 2014.

[100] J. Ghijsen, L. H. Tjeng, J. van Elp, H. Eskes, J. Westerink, G. A. Sawatzky, and M. T. Czyzyk, "Electronic Structure of Cu_2O and CuO," *Phys. Rev. B*, vol. 38, pp. 11322–11330, 1988.

[101] P. W. Baumeister, "Optical Absorption of Cuprous Oxide," *Phys. Rev.*, vol. 121, pp. 359–362, 1961.

[102] A. Soon, X.-Y. Cui, B. Delley, S.-H. Wei, and C. Stampfl, "Native Defect-Induced Multifarious Magnetism in Nonstoichiometric Cuprous Oxide: First-Principles Study of Bulk and Surface Properties of $Cu_{2-\delta}O$," *Phys. Rev. B*, vol. 79, p. 035205, 2009.

[103] M. Heinemann, B. Eifert, and C. Heiliger, "Band Structure and Phase Stability of the Copper oxides Cu_2O, CuO, and Cu_4O_3," *Phys. Rev. B*, vol. 87, p. 115111, 2013.

[104] A. Soon, M. Todorova, B. Delley, and C. Stampfl, "Thermodynamic Stability and Structure of Copper Oxide Surfaces: A First-Principles Investigation," *Phys. Rev. B*, vol. 75, p. 125420, 2007.

[105] M. Soldemo, J. H. Stenlid, Z. Besharat, M. Ghadami Yazdi, A. Önsten, C. Leygraf, M. Göthelid, T. Brinck, and J. Weissenrieder, "The Surface Structure of Cu_2O(100)," *J. Phys. Chem. C*, vol. 120, no. 8, pp. 4373–4381, 2016.

[106] B. K. Meyer, A. Polity, D. Reppin, M. Becker, P. Hering, P. J. Klar, T. Sander, C. Reindl, J. Benz, M. Eickhoff, C. Heiliger, M. Heinemann, J. Bläsing, A. Krost, S. Shokovets, C. Müller, and C. Ronning, "Binary Copper Oxide Semiconductors: From Materials Towards Devices," *Phys. Status Solidi B*, vol. 249, no. 8, pp. 1487–1509, 2012.

[107] M. A. Washington, A. Z. Genack, H. Z. Cummins, R. H. Bruce, A. Compaan, and R. A. Forman, "Spectroscopy of Excited Yellow Exciton States in Cu_2O by Forbidden Resonant Raman Scattering," *Phys. Rev. B*, vol. 15, pp. 2145–2153, 1977.

[108] F. L. Weichman, "Some Rationale for the Unusual Behavior of the Dielectric Constant of Cu_2O," *Can. J. Phys.*, vol. 51, no. 6, pp. 680–685, 1973.

[109] M. M. Islam, B. Diawara, V. Maurice, and P. Marcus, "Bulk and Surface Properties of Cu_2O: A First-Principles Investigation," *J. Mol. Struct. THEOCHEM*, vol. 903, no. 1, pp. 41–48, 2009.

[110] E. Ruiz, S. Alvarez, P. Alemany, and R. A. Evarestov, "Electronic Structure and Properties of Cu_2O," *Phys. Rev. B*, vol. 56,

pp. 7189–7196, 1997.

[111] A. Filippetti and V. Fiorentini, "Coexistence of Ionic and Metallic Bonding in Noble-Metal Oxides," *Phys. Rev. B*, vol. 72, p. 035128, 2005.

[112] H. Raebiger, S. Lany, and A. Zunger, "Origins of the p-Type Nature and Cation Deficiency in Cu_2O and Related Materials," *Phys. Rev. B*, vol. 76, p. 045209, 2007.

[113] D. O. Scanlon and G. W. Watson, "Uncovering the Complex Behavior of Hydrogen in Cu_2O," *Phys. Rev. Lett.*, vol. 106, p. 186403, 2011.

[114] F. Bruneval, N. Vast, L. Reining, M. Izquierdo, F. Sirotti, and N. Barrett, "Exchange and Correlation Effects in Electronic Excitations of Cu_2O," *Phys. Rev. Lett.*, vol. 97, p. 267601, 2006.

[115] P. F., W. S., W. G., X. M., W. S.Y., C. L.Y., and J. Y., "Electronic and Optical Properties of Noble Metal Oxides M_2O(M = Cu, Ag and Au): First-Principles Study," *J. Korean Phys. Soc.*, vol. 55, pp. 1243–1249, 2009.

[116] Y. Wang, S. Lany, J. Ghanbaja, Y. Fagot-Revurat, Y. P. Chen, F. Soldera, D. Horwat, F. Mücklich, and J. F. Pierson, "Electronic Structures of Cu_2O, Cu_4O_3, and CuO: A Joint Experimental and Theoretical Study," *Phys. Rev. B*, vol. 94, p. 245418, 2016.

[117] H. Schmalzried, "F. A. Kröger: The Chemistry of Imperfect Crystals, North-Holland Publishing Company-Amsterdam 1964. 1039 Seiten. Preis: hfl. 110.," *Ber. Bunsenges. Phys. Chem.*, vol. 68, no. 6, pp. 608–608, 1964.

[118] Y. Tretyakov, V. Komarov, N. Prosvirnina, and I. Kutsenok, "Nonstoichiometry and Defect Structures in Copper Oxides and Ferrites," *J. Solid State Chem.*, vol. 5, no. 2, pp. 157–167, 1972.

[119] S. B. Zhang, "The Microscopic Origin of the Doping Limits in Semiconductors and Wide-Gap Materials and Recent Developments in Overcoming These Limits: A Review," *J. Phys. Condens. Matter*, vol. 14, no. 34, pp. R881–R903, 2002.

[120] J. W. Hodby, T. E. Jenkins, C. Schwab, H. Tamura, and D. Trivich, "Cyclotron Resonance of Electrons and of Holes in Cuprous Oxide, Cu_2O," *J. Phys. C Solid State Phys.*, vol. 9, no. 8, pp. 1429–1439, 1976.

[121] A. Bose, S. Basu, S. Banerjee, and D. Chakravorty, "Electrical Properties of Compacted Assembly of Copper Oxide Nanoparticles," *J. Appl. Phys.*, vol. 98, no. 7, p. 074307, 2005.

[122] Y. S. Lee, M. T. Winkler, S. C. Siah, R. Brandt, and T. Buonassisi, "Hall Mobility of Cuprous Oxide Thin Films Deposited by Reactive Direct-Current Magnetron Sputtering," *Appl. Phys. Lett.*, vol. 98, no. 19, p. 192115, 2011.

[123] K. Akimoto, S. Ishizuka, M. Yanagita, Y. Nawa, G. K. Paul, and T. Sakurai, "Thin Film Deposition of Cu_2O and Application for Solar Cells," *Sol. Energy*, vol. 80, no. 6, pp. 715–722, 2006.

[124] S. Ishizuka, S. Kato, Y. Okamoto, and K. Akimoto, "Hydrogen Treatment for Polycrystalline Nitrogen-Doped Cu_2O Thin Film," *J. Cryst. Growth*, vol. 237-239, pp. 616–620, 2002.

[125] T. Mahalingam, J. S. P. Chitra, J. P. Chu, H. Moon, H. J. Kwon, and Y. D. Kim, "Photoelectrochemical Solar Cell Studies on Electroplated Cuprous Oxide Thin Films," *J. Mater. Sci.: Mater. Electron*, vol. 17, no. 7, pp. 519–253, 2005.

[126] R. Dong, D. S. Lee, W. F. Xiang, S. J. Oh, D. J. Seong, S. H. Heo, H. J. Choi, M. J. Kwon, S. N. Seo, M. B. Pyun, M. Hasan, and H. Hwang, "Reproducible Hysteresis and Resistive Switching in Metal-Cu_xO-Metal Heterostructures," *Appl. Phys. Lett.*, vol. 90, no. 4, p. 042107, 2007.

[127] J. Kunze, V. Maurice, L. H. Klein, H.-H. Strehblow, and P. Marcus, "In Situ Scanning Tunneling Microscopy Study of the Anodic Oxidation of Cu(111) in 0.1 M NaOH," *J. Phys. Chem. B*, vol. 105, no. 19, pp. 4263–4269, 2001.

[128] G. Salek, C. Tenailleau, P. Dufour, and S. Guillemet-Fritsch, "Room Temperature Inorganic Polycondensation of Oxide (Cu_2O and ZnO) nanoparticles and thin films preparation by the dip-coating technique," *Thin Solid Films*, vol. 589, pp. 872–876, 2015.

[129] Y. Youn, M. Lee, D. Kim, J. K. Jeong, Y. Kang, and S. Han, "Large-Scale Computational Identification of p-Type Oxide Semiconductors by Hierarchical Screening," *Chem. Mater.*, vol. 31, no. 15, pp. 5475–5483, 2019.

[130] M. I. Hossain, F. H. Alharbi, and N. Tabet, "Copper Oxide as Inorganic Hole Transport Material for Lead Halide Perovskite Based Solar Cells," *Sol. Energy*, vol. 120, pp. 370–380, 2015.

[131] K. T. Butler, Y. Kumagai, F. Oba, and A. Walsh, "Screening Procedure for Structurally and Electronically Matched Contact Layers for High-Performance Solar Cells: Hybrid Perovskites," *J. Mater. Chem. C*, vol. 4, pp. 1149–1158, 2016.

[132] F. Caballero-Briones, J. M. Artés, I. Díez-Pérez, P. Gorostiza, and F. Sanz, "Direct Observation of the Valence Band Edge by in Situ ECSTM-ECTS in p-Type Cu_2O Layers Prepared by Copper Anodization," *J. Phys. Chem. C*, vol. 113, no. 3, pp. 1028–1036, 2009.

[133] J. Deuermeier, J. Gassmann, J. Brötz, and A. Klein, "Reactive Magnetron Sputtering of Cu_2O: Dependence on Oxygen Pressure and Interface Formation with Indium Tin Oxide," *J. Appl. Phys.*, vol. 109, no. 11, p. 113704, 2011.

[134] V. Stevanović, S. Lany, D. S. Ginley, W. Tumas, and A. Zunger, "Assessing Capability of Semiconductors to Split Water Using Ionization Potentials and Electron Affinities Only," *Phys. Chem. Chem. Phys.*, vol. 16, pp. 3706–3714, 2014.

[135] L. I. Bendavid and E. A. Carter, "First-Principles Predictions of the Structure, Stability, and Photocatalytic Potential of Cu_2O Surfaces," *J. Phys. Chem. B*, vol. 117, no. 49, pp. 15750–15760, 2013.

[136] M. C. Toroker, D. K. Kanan, N. Alidoust, L. Y. Isseroff, P. Liao, and E. A. Carter, "First Principles Scheme to Evaluate Band Edge Positions in Potential Transition Metal Oxide Photocatalysts and Photoelectrodes," *Phys. Chem. Chem. Phys.*, vol. 13, pp. 16644–16654, 2011.

[137] M. M. Islam, B. Diawara, V. Maurice, and P. Marcus, "Surface Reconstruction Modes of Cu_2O(001) Surface: A First Principles Study," *Surf. Sci.*, vol. 604, no. 17, pp. 1516–1523, 2010.

[138] H. Tissot, C. Wang, J. H. Stenlid, T. Brinck, and J. Weissenrieder, "The Surface Structure of $Cu_2O(100)$: Nature of Defects," *J. Phys. Chem. C*, vol. 123, no. 13, pp. 7696–7704, 2019.

[139] D. Le, S. Stolbov, and T. S. Rahman, "Reactivity of the $Cu_2O(100)$ Surface: Insights from First Principles Calculations," *Surf. Sci.*, vol. 603, no. 10, pp. 1637–1645, 2009.

[140] Y. Su, H. Li, H. Ma, J. Robertson, and A. Nathan, "Controlling Surface Termination and Facet Orientation in Cu_2O Nanoparticles for High Photocatalytic Activity: A Combined Experimental and Density Functional Theory Study," *ACS Appl. Mater. Interfaces*, vol. 9, pp. 8100–8106, 2017.

[141] C. Liu, X. Zhou, S. Chen, X. Zhao, S. Dai, and B. Xu, "Hydrophobic Cu_2O Quantum Dots Enabled by Surfactant Modification as Top Hole-Transport Materials for Efficient Perovskite Solar Cells," *Adv. Sci.*, vol. 6, no. 7, p. 1801169, 2019.

[142] A. M. Elseman, M. S. Selim, L. Luo, C. Y. Xu, G. Wang, Y. Jiang, D. B. Liu, L. P. Liao, Z. Hao, and Q. L. Song, "Efficient and Stable Planar n-i-p Perovskite Solar Cells with Negligible Hysteresis through Solution-Processed Cu_2O Nanocubes as a Low-Cost Hole-Transport Material," *ChemSusChem*, vol. 12, no. 16, pp. 3808–3816, 2019.

[143] C. Zuo and L. Ding, "Solution-Processed Cu_2O and CuO as Hole Transport Materials for Efficient Perovskite Solar Cells," *Small*, vol. 11, pp. 5528–5532, 2015.

[144] W. Yu, F. Li, H. Wang, E. Alarousu, Y. Chen, B. Lin, L. Wang, M. N. Hedhili, Y. Li, K. Wu, X. Wang, O. F. Mohammed, and T. Wu, "Ultrathin Cu_2O as an Efficient Inorganic Hole Transporting Material for Perovskite Solar Cells," *Nanoscale*, vol. 8, no. 11, pp. 6173–6179, 2016.

[145] S. Chatterjee and A. J. Pal, "Introducing Cu_2O Thin Films as a Hole-Transport Layer in Efficient Planar Perovskite Solar Cell Structures," *J. Phys. Chem. C*, vol. 120, no. 3, pp. 1428–1437, 2016.

[146] B. A. Nejand, V. Ahmadi, S. Gharibzadeh, and H. R. Shahverdi, "Cuprous Oxide as a Potential Low-Cost Hole-Transport Material for Stable Perovskite Solar Cells," *ChemSusChem*, vol. 9, no. 3, pp. 302–313, 2016.

[147] W. Sun, Y. Li, S. Ye, H. Rao, W. Yan, H. Peng, Y. Li, Z. Liu, S. Wang, Z. Chen, L. Xiao, Z. Bian, and C. Huang, "High-Performance Inverted Planar Heterojunction Perovskite Solar Cells Based on a Solution-Processed CuO_x Hole Transport Layer," *Nanoscale*, vol. 8, pp. 10806–10813, 2016.

[148] Z.-K. Yu, W.-F. Fu, W.-Q. Liu, Z.-Q. Zhang, Y.-J. Liu, J.-L. Yan, T. Ye, W.-T. Yang, H.-Y. Li, and H.-Z. Chen, "Solution-Processed CuO_x as an Efficient Hole-Extraction Layer for Inverted Planar Heterojunction Perovskite Solar Cells," *Chin. Chem. Lett.*, vol. 28, no. 1, pp. 13–18, 2017.

[149] Z. Zhang, S. Chen, P. Li, H. Li, J. Wu, P. Hu, and J. Wang, "Aerosol-Assisted Chemical Vapor Deposition of Ultra-Thin CuO_x Films as Hole Transport Material for Planar Perovskite Solar Cells," *Funct. Mater. Lett.*, vol. 11, no. 2, p. 1850035, 2018.

[150] X. Miao, S. Wang, W. Sun, Y. Zhu, C. Du, R. Ma, and C. Wang, "Effect of Cu_2O Content in Electrodeposited CuO_x Film on Perovskite Solar Cells," *Nano*, vol. 14, no. 10, p. 1950126, 2019.

[151] X. Miao, S. Wang, W. Sun, Y. Zhu, C. Du, R. Ma, and C. Wang, "Room-Temperature Electrochemical Deposition of Ultrathin CuO_x Film as Hole Transport Layer for Perovskite Solar Cells," *Scr. Mater.*, vol. 165, pp. 134–139, 2019.

[152] J. Kim, Y. Takiguchi, and S. Miyajima, "Characterization of p-Type Nitrogen-Doped Cuprous Oxide/n-Type Hydrogenated Microcrystalline Silicon Tunnel Recombination Junction for Perovskite/Crystalline Silicon Tandem Solar Cells," *Jpn. J. Appl. Phys.*, vol. 57, no. 8, SI, p. 08RB05, 2018.

[153] G. Han, W. H. Du, B.-L. An, A. Bruno, S. W. Leow, C. Soci, S. Zhang, S. G. Mhaisalkar, and N. Mathews, "Nitrogen Doped Cuprous Oxide as Low Cost Hole-Transporting Material for Perovskite Solar Cells," *Scr. Mater.*, vol. 153, pp. 104–108, 2018.

[154] H. Rao, S. Ye, W. Sun, W. Yan, Y. Li, H. Peng, Z. Liu, Z. Bian, Y. Li, and C. Huang, "A 19.0 % Efficiency Achieved in CuO_x Based Inverted $CH_3NH_3PbI_{3-x}Cl_x$ Solar Cells by an Effective Cl Doping Method," *Nano Energy*, vol. 27, pp. 51 – 57, 2016.

[155] Y.-J. Chen, M.-H. Li, J.-C.-A. Huang, and P. Chen, "Cu/Cu_2O Nanocomposite Films as a p-Type Modified Layer for Efficient Perovskite Solar Cells," *Sci. Rep.*, vol. 8, p. 7646, 2018.

[156] Y.-J. Chen, M.-H. Li, J.-C.-A. Huang, and P. Chen, "The Cu/Cu_2O Nanocomposite as a p-Type Transparent-Conductive-Oxide for Efficient Bifacial-Illuminated Perovskite Solar Cells," *J. Mater. Chem. C*, vol. 6, no. 23, pp. 6280–6286, 2018.

[157] M.-H. Li, J.-H. Yum, S.-J. Moon, and P. Chen, "Inorganic p-Type Semiconductors: Their Applications and Progress in Dye-Sensitized Solar Cells and Perovskite Solar Cells," *Energies*, vol. 9, no. 5, p. 331, 2016.

[158] M. Bidikoudi and E. Kymakis, "Novel Approaches and Scalability Prospects of Copper Based Hole Transporting Materials for Planar Perovskite Solar Cells," *J. Mater. Chem. C*, vol. 7, no. 44, pp. 13680–13708, 2019.

[159] Y. Wang, Z. Xia, J. Liang, X. Wang, Y. Liu, C. Liu, S. Zhang, and H. Zhou, "Towards Printed Perovskite Solar Cells with Cuprous Oxide Hole Transporting Layers: A Theoretical Design," *Semicond. Sci. Technol.*, vol. 30, p. 054004, 2015.

[160] G. A. Casas, M. A. Cappelletti, A. P. Cédola, B. Marí Soucase, and E. L. Peltzer y Blancá, "Analysis of the Power Conversion Efficiency of Perovskite Solar Cells with Different Materials as Hole-Transport Layer by Numerical Simulations," *Superlattices Microstruct.*, vol. 107, pp. 136 – 143, 2017.

[161] L. Lin, L. Jiang, P. Li, B. Fan, and Y. Qiu, "A Modeled Perovskite Solar Cell Structure with a Cu_2O Hole-Transporting Layer Enabling over 20 % Efficiency by Low-Cost Low-Temperature Processing," *J. Phys. Chem. Solids*, vol. 124, pp. 205–211, 2019.

[162] M. Shasti and A. Mortezaali, "Numerical Study of Cu_2O, $SrCu_2O_2$, and $CuAlO_2$ as Hole-Transport Materials for Application in Perovskite Solar Cells," *Phys. Status Solidi A*, vol. 216, no. 18, p. 1900337, 2019.

[163] S. Z. Haider, H. Anwar, Y. Jamil, and M. Shahid, "A Comparative Study of Interface Engineering with Different Hole Transport Materials for High-Performance Perovskite Solar Cells," *J. Phys. Chem. Solids*, vol. 136, p. 109147, 2020.

[164] M. Born and R. Oppenheimer, "Zur Quantentheorie der Molekeln," *Ann. Phys. (Berl.)*, vol. 389, no. 20, pp. 457–484, 1927.

[165] A. Szabo and N. S. Ostlund, *Modern Quantum Chemistry: Introduction to Advanced Electronic Structure Theory*. New York: McGraw-Hill, 1st ed., 1989.

[166] W. Kolos and L. Wolniewicz, "Improved Theoretical Ground-State Energy of the Hydrogen Molecule," *J. Chem. Phys.*, vol. 49, no. 1, pp. 404–410, 1968.

[167] A. S. Davydov, *Quantum Mechanics*. London: Pergamon, 1st ed., 1965.

[168] I. B. Bersuker, *The Jahn-Teller Effect*. Cambridge: Cambridge University Press, 1st ed., 2006.

[169] V. Fock, "Näherungsmethode zur Lösung des Quantenmechanischen Mehrkörperproblems," *Z. Phys.*, vol. 61, no. 1, p. 126–148, 1930.

[170] D. R. Hartree, "The Wave Mechanics of an Atom with a Non-Coulomb Central Field. Part I. Theory and Methods," *Math. Proc. Camb. Philos. Soc.*, vol. 24, no. 1, p. 89–110, 1928.

[171] W. Kohn and L. J. Sham, "Self-Consistent Equations Including Exchange and Correlation Effects," *Phys. Rev.*, vol. 140, pp. A1133–A1138, 1965.

[172] P. Hohenberg and W. Kohn, "Inhomogeneous Electron Gas," *Phys. Rev.*, vol. 136, pp. B864–B871, 1964.

[173] R. Parr and W. Yang, *Density-Functional Theory of Atoms and Molecules*. Oxford: Oxford University Press, 1st ed., 1989.

[174] L. Hedin, "New Method for Calculating the One-Particle Green's Function with Application to the Electron-Gas Problem," *Phys. Rev.*, vol. 139, pp. A796–A823, 1965.

[175] M. S. Hybertsen and S. G. Louie, "First-Principles Theory of Quasiparticles: Calculation of Band Gaps in Semiconductors and Insulators," *Phys. Rev. Lett.*, vol. 55, pp. 1418–1421, 1985.

[176] D. M. Ceperley and B. J. Alder, "Ground State of the Electron Gas by a Stochastic Method," *Phys. Rev. Lett.*, vol. 45, pp. 566–569, 1980.

[177] J. P. Perdew and A. Zunger, "Self-Interaction Correction to Density-Functional Approximations for Many-Electron Systems," *Phys. Rev. B*, vol. 23, pp. 5048–5079, 1981.

[178] S. H. Vosko, L. Wilk, and M. Nusair, "Accurate Spin-Dependent Electron Liquid Correlation Energies for Local Spin Density Calculations: A Critical Analysis," *Can. J. Phys.*, vol. 58, no. 8, pp. 1200–1211, 1980.

[179] J. P. Perdew and Y. Wang, "Accurate and Simple Analytic Representation of the Electron-Gas Correlation Energy," *Phys. Rev. B*, vol. 45, pp. 13244–13249, 1992.

[180] J. P. Perdew, K. Burke, and M. Ernzerhof, "Generalized Gradient Approximation Made Simple," *Phys. Rev. Lett.*, vol. 77, pp. 3865–3868, 1996.

[181] A. D. Becke, "Density-Functional Exchange-Energy Approximation with Correct Asymptotic Behavior," *Phys. Rev. A*, vol. 38, pp. 3098–3100, 1988.

[182] C. Lee, W. Yang, and R. G. Parr, "Development of the Colle-Salvetti Correlation-Energy Formula into a Functional of the Electron Density," *Phys. Rev. B*, vol. 37, pp. 785–789, 1988.

[183] J. P. Perdew, A. Ruzsinszky, G. I. Csonka, O. A. Vydrov, G. E. Scuseria, L. A. Constantin, X. Zhou, and K. Burke, "Restoring the Density-Gradient Expansion for Exchange in Solids and Surfaces," *Phys. Rev. Lett.*, vol. 100, p. 136406, 2008.

[184] S. Grimme, J. Antony, S. Ehrlich, and H. Krieg, "A Consistent and Accurate Ab Initio Parametrization of Density Functional Dispersion Correction (DFT-D) for the 94 Elements H–Pu," *J. Chem. Phys.*, vol. 132, no. 15, p. 154104, 2010.

[185] S. Grimme, S. Ehrlich, and L. Goerigk, "Effect of the Damping Function in Dispersion Corrected Density Functional Theory," *J. Comput. Chem.*, vol. 32, no. 7, pp. 1456–1465, 2011.

[186] J. Klimeš, D. R. Bowler, and A. Michaelides, "Van der Waals Density Functionals Applied to Solids," *Phys. Rev. B*, vol. 83, p. 195131, 2011.

[187] J. Klimeš, D. R. Bowler, and A. Michaelides, "Chemical Accuracy for the Van der Waals Density Functional," *J. Phys.: Condens. Matter*, vol. 22, no. 2, p. 022201, 2010.

[188] S. L. Dudarev, G. A. Botton, S. Y. Savrasov, C. J. Humphreys, and A. P. Sutton, "Electron-Energy-Loss Spectra and the Structural Stability of Nickel Oxide: An LSDA+U Study," *Phys. Rev. B*, vol. 57, pp. 1505–1509, 1998.

[189] J. P. Perdew, M. Ernzerhof, and K. Burke, "Rationale for Mixing Exact Exchange with Density Functional Approximations," *J. Chem. Phys.*, vol. 105, no. 22, pp. 9982–9985, 1996.

[190] C. Adamo and V. Barone, "Toward Reliable Density Functional Methods without Adjustable Parameters: The PBE0 Model," *J. Chem. Phys.*, vol. 110, no. 13, pp. 6158–6170, 1999.

[191] J. Heyd, G. E. Scuseria, and M. Ernzerhof, "Hybrid Functionals Based on a Screened Coulomb Potential," *J. Chem. Phys.*, vol. 118, pp. 8207–8215, 2003.

[192] J. Heyd, G. E. Scuseria, and M. Ernzerhof, "Erratum: "Hybrid Functionals Based on a Screened Coulomb Potential" [J. Chem. Phys. 118, 8207 (2003)]," *J. Chem. Phys.*, vol. 124, p. 219906, 2006.

[193] M. A. L. Marques, J. Vidal, M. J. T. Oliveira, L. Reining, and S. Botti, "Density-Based Mixing Parameter for Hybrid Functionals," *Phys. Rev. B*, vol. 83, p. 035119, 2011.

[194] J. H. Skone, M. Govoni, and G. Galli, "Self-Consistent Hybrid Functional for Condensed Systems," *Phys. Rev. B*, vol. 89, p. 195112, 2014.

[195] N. P. Brawand, M. Vörös, M. Govoni, and G. Galli, "Generalization of Dielectric-Dependent Hybrid Functionals to Finite Systems," *Phys. Rev. X*, vol. 6, p. 041002, 2016.

[196] J. C. Conesa, “Modeling with Hybrid Density Functional Theory the Electronic Band Alignment at the Zinc Oxide–Anatase Interface,” *J. Phys. Chem. C*, vol. 116, no. 35, pp. 18884–18890, 2012.

[197] J. F. Janak, “Proof that $\frac{\partial E}{\partial n_i} = \epsilon$ in Density-Functional Theory,” *Phys. Rev. B*, vol. 18, pp. 7165–7168, 1978.

[198] F. Bloch, “Über die Quantenmechanik der Elektronen in Kristallgittern,” *Z. Phys.*, vol. 52, p. 555, 1929.

[199] H. J. Monkhorst and J. D. Pack, “Special Points for Brillouin-Zone Integrations,” *Phys. Rev. B*, vol. 13, pp. 5188–5192, 1976.

[200] P. Giannozzi, O. Andreussi, T. Brumme, O. Bunau, M. B. Nardelli, M. Calandra, R. Car, C. Cavazzoni, D. Ceresoli, M. Cococcioni, N. Colonna, I. Carnimeo, A. D. Corso, S. de Gironcoli, P. Delugas, R. A. DiStasio, A. Ferretti, A. Floris, G. Fratesi, G. Fugallo, R. Gebauer, U. Gerstmann, F. Giustino, T. Gorni, J. Jia, M. Kawamura, H.-Y. Ko, A. Kokalj, E. Küçükbenli, M. Lazzeri, M. Marsili, N. Marzari, F. Mauri, N. L. Nguyen, H.-V. Nguyen, A. O. de-la Roza, L. Paulatto, S. Poncé, D. Rocca, R. Sabatini, B. Santra, M. Schlipf, A. P. Seitsonen, A. Smogunov, I. Timrov, T. Thonhauser, P. Umari, N. Vast, X. Wu, and S. Baroni, “Advanced Capabilities for Materials Modelling with Quantum ESPRESSO,” *J. Phys. Condens. Matter*, vol. 29, no. 46, p. 465901, 2017.

[201] P. Giannozzi, S. Baroni, N. Bonini, M. Calandra, R. Car, C. Cavazzoni, D. Ceresoli, G. L. Chiarotti, M. Cococcioni, I. Dabo, A. D. Corso, S. de Gironcoli, S. Fabris, G. Fratesi, R. Gebauer, U. Gerstmann, C. Gougoussis, A. Kokalj, M. Lazzeri, L. Martin-Samos, N. Marzari, F. Mauri, R. Mazzarello, S. Paolini, A. Pasquarello, L. Paulatto, C. Sbraccia, S. Scandolo, G. Sclauzero, A. P. Seitsonen, A. Smogunov, P. Umari, and R. M. Wentzcovitch, “Quantum ESPRESSO: A Modular and Open-Source Software Project for Quantum Simulations of Materials,” *J. Phys. Condens. Matter*, vol. 21, no. 39, p. 395502, 2009.

[202] G. Kresse and J. Furthmüller, “Efficiency of Ab-Initio Total Energy Calculations for Metals and Semiconductors Using a Plane-Wave Basis Set,” *Comput. Mater. Sci.*, vol. 6, p. 15, 1996.

[203] G. Kresse and J. Furthmüller, “Efficient Iterative Schemes for Ab Initio Total-Energy Calculations Using a Plane-Wave Basis Set,” *Phys. Rev. B*, vol. 54, pp. 11169–11186, 1996.

[204] G. Kresse and D. Joubert, “From Ultrasoft Pseudopotentials to the Projector Augmented-Wave Method,” *Phys. Rev. B*, vol. 59, pp. 1758–1775, 1999.

[205] J. Hutter, M. Iannuzzi, F. Schiffmann, and J. VandeVondele, “CP2K: Atomistic Simulations of Condensed Matter Systems,” *Wiley Interdiscip. Rev.: Comput. Mol. Sci.*, vol. 4, no. 1, pp. 15–25, 2014.

[206] The CP2K Developers Group (2019). CP2K is Freely Available from https://www.cp2k.org.

[207] F. Birch, “Finite Elastic Strain of Cubic Crystals,” *Phys. Rev.*, vol. 71, pp. 809–824, 1947.

[208] F. D. Murnaghan, “The Compressibility of Media under Extreme Pressures,” *Proc. Natl. Acad. Sci. U.S.A.*, vol. 30, no. 9, pp. 244–247, 1944.

[209] A. Baldereschi, S. Baroni, and R. Resta, “Band Offsets in Lattice-Matched Heterojunctions: A Model and First-Principles Calculations for GaAs/AlAs,” *Phys. Rev. Lett.*, vol. 61, pp. 734–737, 1988.

[210] R. G. Dandrea, C. B. Duke, and A. Zunger, “Interfacial Atomic Structure and Band Offsets at Semiconductor Heterojunctions,” *J. Vac. Sci. Technol. B*, vol. 10, pp. 1744–1753, 1992.

[211] R. G. Dandrea and C. B. Duke, “Calculation of the Schottky Barrier Height at the Al/GaAs(001) Heterojunction: Effect of Interfacial Atomic Relaxations,” *J. Vac. Sci. Technol. A*, vol. 11, pp. 848–853, 1993.

[212] T. Das, X. Rocquefelte, and S. Jobic, “Ab Initio Positioning of the Valence and Conduction Bands of bulk Photocatalysts: Proposition of Absolute Reference Energy,” *J. Phys. Chem. C*, vol. 124, no. 36, pp. 19426–19434, 2020.

[213] R. Tran, X.-G. Li, J. H. Montoya, D. Winston, K. A. Persson, and S. P. Ong, “Anisotropic Work Function of Elemental Crystals,” *Surf. Sci.*, vol. 687, pp. 48 – 55, 2019.

[214] A. L. Montero-Alejo, E. Menéndez-Proupin, P. Palacios, P. Wahnón, and J. C. Conesa, “Ferroelectric Domains May Lead to Two-Dimensional Confinement of Holes, but not of Electrons, in $CH_3NH_3PbI_3$ Perovskite,” *J. Phys. Chem. C*, vol. 121, no. 48, pp. 26698–26705, 2017.

[215] Y. Rakita, S. R. Cohen, N. K. Kedem, G. Hodes, and D. Cahen, “Mechanical Properties of APbX3 (A = Cs or CH_3NH_3; X = I or Br) Perovskite Single Crystals,” *MRS Commun.*, vol. 5, no. 4, p. 623–629, 2015.

[216] J. Neugebauer and M. Scheffler, “Adsorbate-Substrate and Adsorbate-Adsorbate Interactions of Na and K Adlayers on Al(111),” *Phys. Rev. B*, vol. 46, pp. 16067–16080, 1992.

[217] L. Bengtsson, “Dipole Correction for Surface Supercell Calculations,” *Phys. Rev. B*, vol. 59, pp. 12301–12304, 1999.

[218] J. M. Luttinger and W. Kohn, “Motion of Electrons and Holes in Perturbed Periodic Fields,” *Phys. Rev.*, vol. 97, pp. 869–883, 1955.

[219] O. Yamamuro, T. Matsuo, H. Suga, W. I. F. David, R. M. Ibberson, and A. J. Leadbetter, “Neutron Diffraction and Calorimetric Studies of Methylammonium Iodide,” *Acta Crystallogr. Sect. B*, vol. 48, pp. 329–336, 1992.

[220] K. Persson, “Materials Data on H_6CIN (SG:11) by Materials Project,” 4 2016.

[221] K. Persson, “Materials Data on H_6CIN (SG:11) by Materials Project,” 4 2016.

[222] B. Palosz, W. Steurer, and H. Schulz, “The Structure of PbI_2 Polytypes 2H and 4H: A Study of the 2H - 4H Transition,” *J. Phys.: Condens. Matter*, vol. 2, pp. 5285–5295, 1990.

[223] R. M. France, J. F. Geisz, T. Song, W. Olavarria, M. Young, A. Kibbler, and M. A. Steiner, “Triple-Junction Solar Cells with 39.5 % Terrestrial and 34.2 % Space Efficiency Enabled by Thick Quantum Well Superlattices,” *Joule*, vol. 6, no. 5, pp. 1121–1135, 2022.

[224] J.-C. Blancon, A. V. Stier, H. Tsai, W. Nie, C. C. Stoumpos, B. Traoré, L. Pedesseau, M. Kepenekian, F. Katsutani, G. T. Noe, J. Kono, S. Tretiak, S. A. Crooker, C. Katan, M. G. Kanatzidis, J. J. Crochet, J. Even, and A. D. Mohite, "Scaling Law for Excitons in 2D Perovskite Quantum Wells," *Nat. Commun.*, vol. 9, p. 2254, 2018.

[225] J. Even, L. Pedesseau, J.-M. Jancu, and C. Katan, "Importance of Spin–Orbit Coupling in Hybrid Organic/Inorganic Perovskites for Photovoltaic Applications," *J. Phys. Chem. Lett.*, vol. 4, no. 17, pp. 2999–3005, 2013.

[226] Y. Wang, Y. Yue, X. Yang, and L. Han, "Toward Long-Term Stable and Highly Efficient Perovskite Solar Cells via Effective Charge Transporting Materials," *Adv. Energy Mater.*, vol. 8, p. 1800249, 2018.

[227] J. Endres, D. A. Egger, M. Kulbak, R. A. Kerner, L. Zhao, S. H. Silver, G. Hodes, B. P. Rand, D. Cahen, L. Kronik, and A. Kahn, "Valence and Conduction Band Densities of States of Metal Halide Perovskites: A Combined Experimental-Theoretical Study," *J. Phys. Chem. Lett.*, vol. 7, pp. 2722–2729, 2016.

[228] S. Olthof and K. Meerholz, "Substrate-Dependent Electronic Structure and Film Formation of $MAPbI_3$ Perovskites," *Sci. Rep.*, vol. 7, p. 40267, 2016.

[229] T. G. Kim, S. W. Seo, H. Kwon, J. Hahn, and J. W. Kim, "Influence of Halide Precursor Type and Its Composition on the Electronic Properties of Vacuum Deposited Perovskite Films," *Phys. Chem. Chem. Phys.*, vol. 17, pp. 24342–24348, 2015.

[230] J. Emara, T. Schnier, N. Pourdavoud, T. Riedl, K. Meerholz, and S. Olthof, "Impact of Film Stoichiometry on the Ionization Energy and Electronic Structure of $CH_3NH_3PbI_3$ Perovskites," *Adv. Mater.*, vol. 28, no. 3, pp. 553–559, 2016.

[231] J. Frost, K. Butler, and A. Walsh, "Band Alignment of the Hybrid Halide Perovskites $CH_3NH_3PbCl_3$, $CH_3NH_3PbBr_3$ and $CH_3NH_3PbI_3$," *Mater. Horiz.*, vol. 2, pp. 228–231, 2015.

[232] J. Hallberg and R. C. Hanson, "The Elastic Constants of Cuprous Cxide," *Phys. Status Solidi B*, vol. 42, no. 1, pp. 305–310, 1970.

[233] M. M. Beg and S. M. Shapiro, "Study of Phonon Dispersion Relations in Cuprous Oxide by Inelastic Neutron Scattering," *Phys. Rev. B*, vol. 13, pp. 1728–1734, 1976.

[234] H. Kobayashi, A. Asano, M. Takahashi, K. Yoneda, and Y. Todokoro, "Decrease in Gap States at Ultrathin SiO_2/Si Interfaces by Crown-Ether Cyanide Treatment," *Appl. Phys. Lett.*, vol. 77, no. 26, pp. 4392–4394, 2000.

[235] R. A. Street, M. Schoendorf, A. Roy, and J. H. Lee, "Interface State Recombination in Organic Solar Cells," *Phys. Rev. B*, vol. 81, p. 205307, 2010.

[236] R. F. W. Bader, *Atoms in Molecules: A Quantum Theory.* Clarendon Press, Oxford, 1990.

[237] W. Tang, E. Sanville, and G. Henkelman, "A Grid-Based Bader Analysis Algorithm without Lattice Bias," *J. Phys.: Condens. Matter*, vol. 21, p. 084204, 2009.

[238] N. Datta and J. W. Jeffery, "The Crystal Structure of Paramelaconite, $Cu^{2+}_{12}Cu^{+}_{4}O_{14}$," *Acta Crystallogr. Sect. B*, vol. 34, pp. 22–26, 1978.

[239] U.-G. Jong, C.-J. Yu, J.-S. Ri, N.-H. Kim, and G.-C. Ri, "Influence of Halide Composition on the Structural, Electronic, and Optical Properties of Mixed $CH_3NH_3Pb(I_{1-x}Br_x)_3$ Perovskites Calculated Using the Virtual Crystal Approximation Method," *Phys. Rev. B*, vol. 94, p. 125139, 2016.

[240] N. J. Jeon, J. H. Noh, Y. C. Kim, W. S. Yang, S. Ryu, and S. I. Seok, "Solvent Engineering for High-Performance Inorganic–Organic Hybrid Perovskite Solar Cells," *Nat. Mater.*, vol. 13, p. 897–903, 2014.

[241] H. F. Zarick, N. Soetan, W. R. Erwin, and R. Bardhan, "Mixed Halide Hybrid Perovskites: A Paradigm Shift in Photovoltaics," *J. Mater. Chem. A*, vol. 6, pp. 5507–5537, 2018.

[242] M. Wang, Y. Liu, D. Li, J. Tang, and W. Huang, "Isoelectric Point-Controlled Preferential Photodeposition of Platinum on Cu_2O-TiO_2 Composite Surfaces," *Chin. Chem. Lett.*, vol. 30, no. 5, pp. 985 – 988, 2019.

[243] J. Yang, B. D. Siempelkamp, E. Mosconi, F. De Angelis, and T. L. Kelly, "Origin of the Thermal Instability in $CH_3NH_3PbI_3$ Thin Films Deposited on ZnO," *Chem. Mater.*, vol. 27, no. 12, pp. 4229–4236, 2015.

[244] A. Akbari, J. Hashemi, E. Mosconi, F. De Angelis, and M. Hakala, "First Principles Modelling of Perovskite Solar Cells Based on TiO_2 and Al_2O_3: Stability and Interfacial Electronic Structure," *J. Mater. Chem. A*, vol. 5, pp. 2339–2345, 2017.

[245] P. E. Blöchl, "Projector Augmented-Wave Method," *Phys. Rev. B*, vol. 50, pp. 17953–17979, 1994.

[246] G. Kresse and D. Joubert, "From Ultrasoft Pseudopotentials to the Projector Augmented Wave Method," *Phys. Rev. B*, vol. 59, pp. 1758–1775, 1999.

[247] K. F. Garrity, J. W. Bennett, K. M. Rabe, and D. Vanderbilt, "Pseudopotentials for High-Throughput DFT Calculations," *Comput. Mater. Sci.*, vol. 81, pp. 446 – 452, 2014.

[248] D. R. Hamann, "Optimized Norm-Conserving Vanderbilt Pseudopotentials," *Phys. Rev. B*, vol. 88, p. 085117, 2013.

[249] M. Schlipf and F. Gygi, "Optimization Algorithm for the Generation of ONCV Pseudopotentials," *Comput. Phys. Commun.*, vol. 196, pp. 36 – 44, 2015.

[250] S. Goedecker, M. Teter, and J. Hutter, "Separable Dual-Space Gaussian Pseudopotentials," *Phys. Rev. B*, vol. 54, pp. 1703–1710, 1996.

[251] J. VandeVondele and J. Hutter, "Gaussian Basis Sets for Accurate Calculations on Molecular Systems in Gas and Condensed Phases," *J. Chem. Phys.*, vol. 127, p. 114105, 2007.

[252] J. VandeVondele, M. Krack, F. Mohamed, M. Parrinello, T. Chassaing, and J. Hutter, "Quickstep: Fast and Accurate Density Functional Calculations Using a Mixed Gaussian and Plane Waves Approach," *Comput. Phys. Commun.*, vol. 167, no. 2, pp. 103 – 128, 2005.